Kinetic Characterisation of Disease Causing Mutations in the Embryonic and β-Cardiac Myosin Motor Domain

A Thesis submitted to the University of Kent for the degree of

Doctor of Philosophy in Biochemistry

in the Faculty of Science, Technology and Medical Studies

2016

Jonathan Walklate

Department of Biosciences

I would like to dedicate this thesis to my loving wife Joss who has kept me going through the years.

Declaration

The two manifolds for the stopped-flow spectrometer were designed by my supervisor Professor Michael A. Geeves and Ted King. This was a collaborative project between TgK scientific and our laboratory. Myosin and actin purification used for these investigations were carried out by Sam Lynn or Dr Nancy Adamek.

The investigation into the wild type embryonic myosin (Chapter 4), the three Freeman-Sheldon Syndrome mutations in embryonic myosin (Chapter 5) and the juvenile hypertrophic cardiomyopathy mutation (Chapter 6) was part of a collaboration between Professor Leslie A. Leinwand from the University of Colorado, USA and our laboratory. Her PhD student Carlos Vera, Dr. Stephen Langers, and technician Ariana Combs cloned the sequences, grew the viruses, transfected and grew the C2C12 cells and shipped cell pellets for purification. Carlos Vera also conducted all the ATPase assays presented here.

No part of this thesis has been submitted in support of an application for any degree or qualification of the University of Kent or any other University or Institute of learning.

Jonathan Walklate

June 2016

Acknowledgements

I wish to thank Professor Michael A. Geeves for giving me the opportunity to study for this PhD and for his continued guidance and support throughout. I would also like to thank the NIH for providing me with funding for this PhD.

A special thank you to my collaborators in the Leinwand laboratory. Professor Leslie Leinwand for allowing me to visit her laboratory and her support. Stephen Langers and Ariana Combs for producing the recombinant protein. Special thanks to Carlos Vera who has shared the joys and tribulations of this project.

I would also like to thank from the bottom of my heart my colleagues in the Geeves lab (past and present) who helped, encouraged and supported me through this PhD: Dr Nancy Adamek, Dr Marieke Bloemink, Dr Dave Pearson, Dr Anja Schmidtmann, Dr Miro Janco, Dr Zoltan Ujfalusi, Dr Alice Racca, Sam Lynn, Cassidy Mackenzie, Rory Parsons, Sarah Jeanfavre, and Michael Coghlan. I would also like to thank the other members of the MADCAP groups from the Mulvihill, Kad, Toseland, and Goult laboratories. I would also like to thank the members of my postgraduate committee Professor David Brown and Dr Tobias von der Haar.

Finally I would like to thank my family and my fiancée Jocelyn Rebera for all of their love and support.

Table of Contents

Abstract

Myosin myopathies are a growing area of research not only to understand the nature of the disease and how it can occur, but also to gain insight into how the myosin molecule works. Point mutations are a great way of examining how regions of myosin interact, however, given that there are over 800 amino acids in the motor domain alone, pinpointing key residues can be challenging. The missense mutations in the myosin molecule that lead to disease are ideal then to investigate residue changes that will have an effect on the function of the motor. The expression of recombinant skeletal myosin class II molecules has only recently become possible.

Previous studies into the function of the embryonic myosin isoform have shown it to be a slow type myosin similar to the β-cardiac isoform. Here stopped-flow kinetic analysis of recombinant embryonic myosin S1 showed it has a tight ADP affinity and slow ADP release, characteristic of the β-cardiac myosin. Analysis of the three most common mutations in the embryonic myosin that cause Freeman-Sheldon syndrome (R672H, R672C, and T178I) showed a significantly reduced ATP hydrolysis, and ATPase V_{max} and K_M. Modelling of the cycle found that the mutations will be detached from actin for longer due to reduced ATP hydrolysis rate and a slower estimated phosphate release step.

Another more common myopathy is hypertrophic cardiomyopathy (HCM) which can be cause by mutations in a multitude of sarcomeric proteins, most notably the β-cardiac myosin. HCM is usually found in adolescents and young adults; however cases are beginning to emerge involving young children. Stopped-flow kinetic analysis of one of these mutations, H251N, shows more significant effects on the myosin function than 'adult' HCM mutations, including; a weaker ADP affinity, tighter ATP affinity, and slower detachment from actin rate constant. However the difference in severity is not apparently clear from the stopped-flow data alone.

These results highlight new key areas on the myosin molecule that are essential for its correct function. The myosin motor is an intricate machine with multiple parts that need further investigation to truly understand its function and the impact of disease causing mutations

Abbreviations

[ ]	indicates a concentration
Å	angstrom
°C	degree Celsius
A	actin
Acto.myosin	actin-myosin complex
ADP, D	adenosine 5’ diphosphate
A.M	actin-myosin complex
A.M.D	actin-myosin-ADP complex
A.M.D.P	actin-myosin-ADP-phosphate complex
A.M.T	actin-myosin-ATP complex
ATP, T	adenosine 5’ triphosphate
Ca^{2+}	calcium ion
cm, mm, µm, nm	centimetre, millimetre, micrometre, nanometre
C-terminal	carboxy terminal
DA	distal arthrogryposis
DA2A	distal arthrogryposis 2A
DCM	dilated cardiomyopathy
dH_2O	distilled water
DTT	dithiothreitol
EDTA	ethlenediaminetetraacetic acid
ELC	essential light chain
F-actin	filamentous actin
FPLC	fast protein liquid chromatography
FSS	Freeman-Sheldon syndrome

g, mg	gram, milligram
G-actin	globular actin
h	hour
HCM	hypertrophic cardiomyopathy
HEPES	N-(2-hydroxyethyl) piperazine N'-(2-ethanesulfonic) acid
HMM	heavy meromyosin
k	rate constant
k_{obs}	observed rate constant
kDa	kilo Dalton
L50	lower 50 kDa domain of myosin
L, mL, µL	litre, millilitre, microlitre
LDH	lactate dehydrogenase
LVH	left ventricle hypertrophy
M, mM, µM, nM	molar, millimolar, micromolar, nanomolar
MDa	mega Dalton
M.D.P	myosin-ADP-phosphate complex
Min	minute
Mg^{2+}	magnesium ion
M.T	myosin-ATP complex
MOPS	N-(2-morpholino) propanesulfonic acid
mRNA	messenger ribonucleic acid
MVM	micro-volume manifold
MyBP-C	myosin binding protein C
MYH	myosin heavy chain gene
MyHC	myosin heavy chain

MyHC-α	myosin heavy chain α
MyHC-β	myosin heavy chain β
MyHC-emb	myosin heavy chain embryonic
MyHC-eo	myosin heavy chain extraocular
MyHC-IIa	myosin heavy chain IIa
MyHC-IIb	myosin heavy chain IIb
MyHC-IIx	myosin heavy chain IIx
MyHC-peri	myosin heavy chain perinatal
N-terminal	amino terminal
NAD	nicotinamide adenine dinucleotide
NADH	nicotinamide adenine dinucleotide plus a proton
PEEK	polyether ether ketone
PEP	phosphoenolpyruvate
Pi	inorganic phosphate
PK	pyruvate kinase
PMSF	phenylmethylsulfonyl fluoride
Pyrene actin	actin labelled with pyrene at residue Cysteine-374
RLC	regulatory light chain
rpm	rotations per minute
RT	room temperature
S1	subfragment 1 of myosin
S2	subfragment 2 of myosin
SCD	sudden cardiac death
SDS-PAGE	sodium docecylsulfate polyacrylamide gel electrophoresis
SHS	Sheldon-Hall syndrome

Tm	tropomyosin
Tn	troponin
TnC	troponin C
TnI	troponin I
TnT	troponin T
Tris	2-amino-2-(hydroxylmethyl)-1,3-propanediol
U50	upper 50 kDa domain of myosin
v/v	volume per volume
w/w	% weight per weight

1. Introduction

Myosin is a motor protein found in almost all cells of the human body. The myosin family is large with 35 subgroups which play different roles including muscle contraction, cargo movement and strain sensors. As a major component of muscle tissue their correct function is essential for working muscle. Muscle myopathies are a group of diseases that lead to muscle weakness. A leading cause of muscle myopathies are mutations in myosin and other sarcomeric proteins. Using kinetic measurements such as stopped-flow spectroscopy and ATPase assays it is possible to determine how the myosin cross-bridge cycle is affected by myosin mutations. By understanding the effects of the mutations on myosin function our understanding of how the residues within the myosin molecule interact and work together will increase.

1.1. General biochemistry and biophysical characteristics of myosin

1.1.1. Myosin

Myosin is a ubiquitous actin associated motor protein found in cells from the nucleus (de Lanerolle, Serebryannyy 2011) to the cytoskeleton (Coluccio 2008). The myosin family is large with approximately 35 subgroups (Odronitz, Kollmar 2007). The myosin class II group includes; non-muscle, smooth muscle and striated muscle myosins (Figure 1.1). Myosin is a molecular motor that uses chemical energy from hydrolysis of ATP to ADP + inorganic phosphate (P_i) to move along actin filaments. In most cells the job of myosin is to move cargo around the cell or act as strain sensors, while in smooth and striated muscle the myosin is used for muscle contraction.

All myosins are composed of three function groups: head, neck, and tail domains. The head domain is also referred to as the motor domain due to its catalytic activity. The motor domain contains the nucleotide binding pocket, actin binding interface, as well as a converter region linking to the lever arm which moves the myosin along the actin. The neck region (lever arm) is a long variable helix which contains a number of IQ motifs. IQ

motifs get their name from the sequence (IQXXXRGXXXR, (Cheney, Mooseker 1992)) and bind either light chains or calmodulin. The tail domain of myosins is very variable in both length and sequence. The major roles of the tail are cellular localisation and function of the myosin, i.e. carrying cargo or filament assembly.

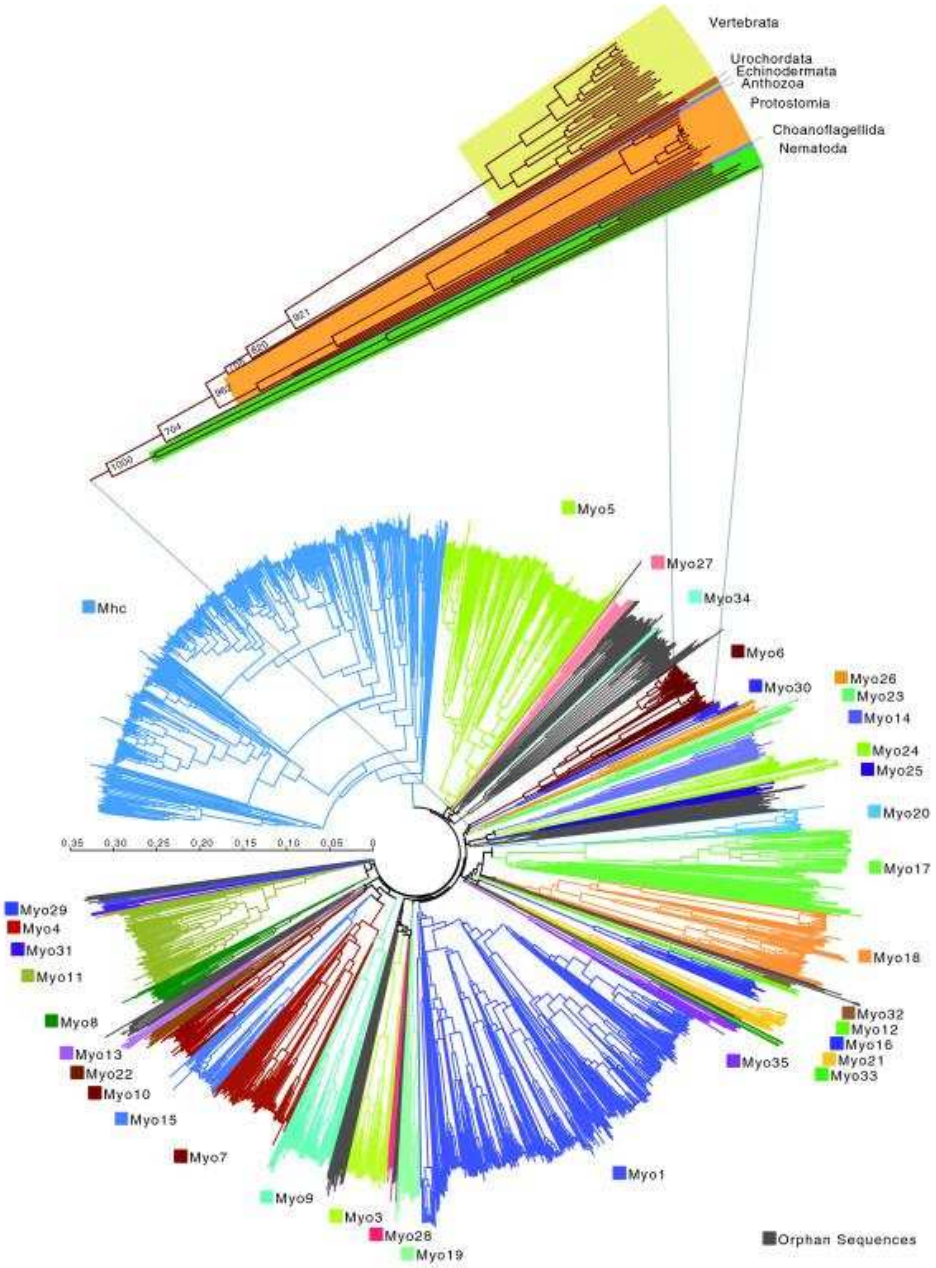

Figure 1.1 – Phylogenetic tree of 1,984 myosin motor domains divided into 35 subgroups. The expanded view shows the sequences of myosin class-VI and distribution within taxa. The scale bar represents estimated amino acid substitutions per site. Figure from (Odronitz, Kollmar 2007).

Myosins can be subdivided into two groups: conventional and unconventional. Conventional myosins encompass the myosin-II myosins while unconventional myosins contain the rest of the myosins.

1.1.2. Myosin class II

Conventional myosin class II (myosin-II) is probably the most recognisable as it is the protein responsible for muscle contraction. Myosin-II is a hexameric protein composed of: 2 heavy chains, 2 essential light chains (ELC), and 2 regulatory light chains (RLC). The C-terminus of the heavy chain is termed the tail domain which forms a coiled-coil with the other myosin heavy chain (Figure 1.2). The N-terminus of myosin contains a globular head domain which contains the nucleotide binding pocket and actin binding region. The head of myosin is referred to as the motor domain and binds to actin.

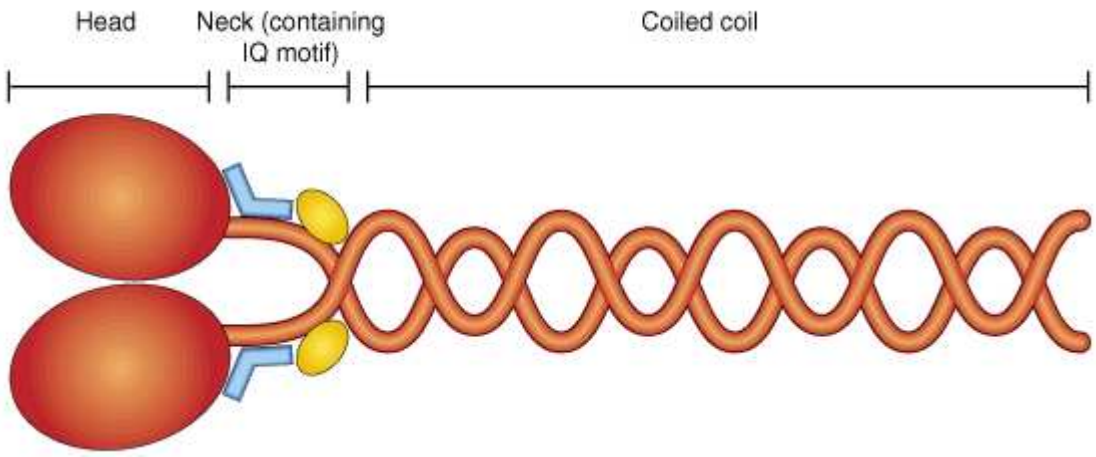

Figure 1.2 – Cartoon representation of the myosin-II hexamer. The tail domain of myosin forms a coiled-coil around a second myosin tail. The myosin heads are located at the N-terminus of the molecule containing the motor domain. Between the tail and head domains is the neck region where the light chains bind. The tails in this figure look as though they are one on top of the other when in reality they are wrapped around each other. Figure from (Mulvihill, Hyams 2001).

1.1.3. Protein structure

When subjected to proteolytic digest by α-chymotrypsin the myosin molecule can be divided into two sections: the light meromyosin (LMM) and heavy meromyosin (HMM,

Figure 1.3). LMM is composed of just the coiled-coil tail domains, while the HMM contains the globular head domain, lever arm (neck) and some of the coiled-coil tails. Further digestion of the HMM with α-chymotrypsin or papain cleaves the protein at the end of the lever arm. This results in two domains termed subfragment 1 (S1) and subfragment 2 (S2). S2 contains the tail domains of the HMM and the RLC while S1 contains the motor domain as well as the lever arm with the ELC on its IQ motif (Figure 1.3). A benefit of using the S1 and HMM is that the entire motor domain is intact and is more soluble in lower ionic strength buffers. Since S1 is just a single motor domain the kinetics can be easier to interpret.

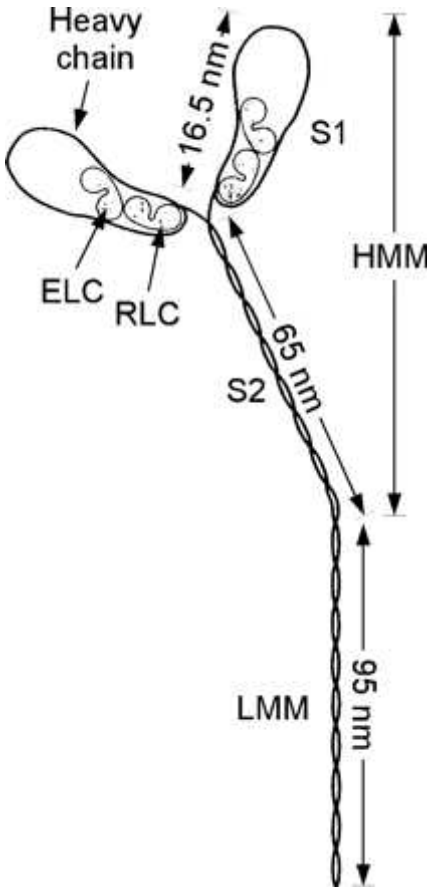

Figure 1.3 – Diagram of myosin which can be digested into light meromyosin (LMM) and heavy meromyosin (HMM). The HMM can be further digested to an S1 and S2 domain. The S1 domain contains the motor domain and the essential and regulatory light chains. Figure from (Hooper, Thuma 2005).

A benefit of the S1 domain is that it can be crystallised unlike full length myosin. The first crystal structure of S1 solved (Figure 1.4) was of chicken skeletal myosin in high salt with a bound sulphate rather than a nucleotide (Rayment, Rypniewski et al. 1993).

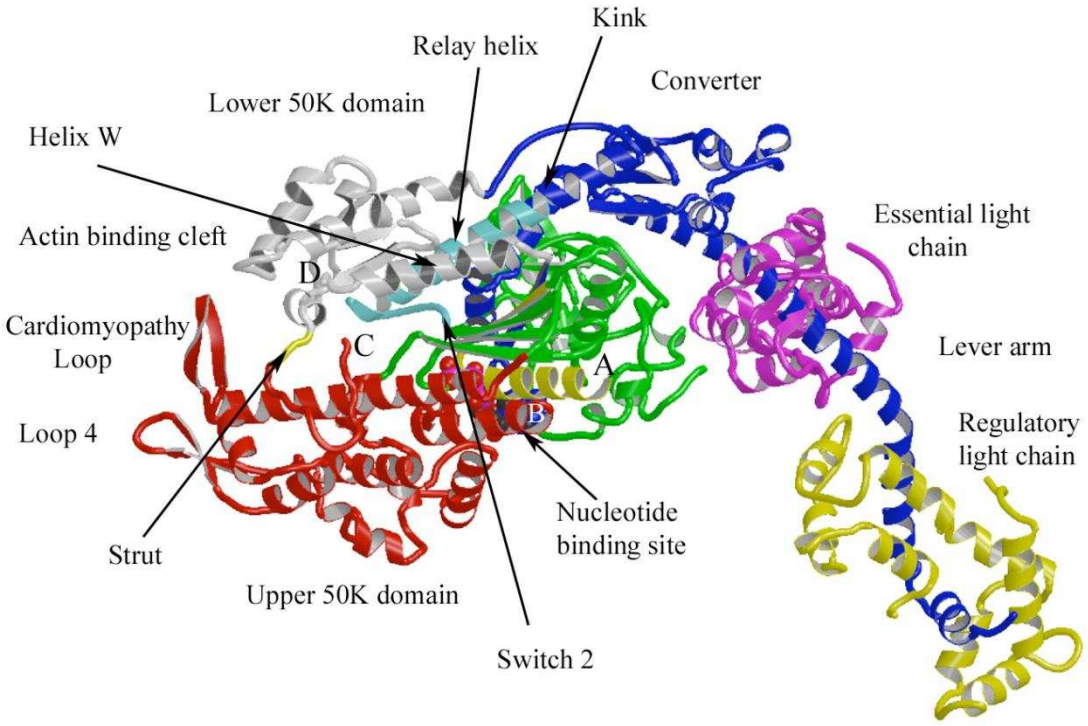

Figure 1.4 – Post-rigor crystal structure of the myosin motor domain (Rayment, Rypniewski et al. 1993). The N-terminus is shown in green, upper 50 kDa domain in red and lower 50 kDa domain in grey. The nucleotide binding P-loop and neighbouring helix are shown in yellow. A and B mark the start and end point of loop 1, C and D show where loop 2 would be. The light blue shows switch 2 of the nucleotide pocket and the relay helix. The dark blue shows the converter and the lever arm. The essential and regulatory light chains are shown in magenta and yellow respectively.

With further proteolytic digestion the S1 domain can be broken down into 3 fragments named after their apparent molecular weights: the N-terminal 25 kDa, central 50 kDa, and C-terminal 20 kDa. It was thought that these fragments were representative of subdomains, however it appears the cleavage sites are related to two flexible loop regions (loop 1 and loop 2, Figure 1.4). The central 50 kDa fragment spans two structural domains: the upper 50 kDa (U50) and lower 50 kDa (L50) which are separated by the actin binding cleft and actin binding region. The L50 is sometimes called the actin binding domain since it is formed of a major part of the actin binding sites (Geeves, Fedorov et al. 2005). The N-terminus of the 25 kDa fragment is close to the lever arm and contains the SH3-like β-barrel (Figure 1.5) which has an unknown function. The 25 kDa and U50 domains form one large structural domain which includes 6 of the 7 strands of the central β-sheet that runs through the middle of the protein. This β-sheet separates the actin and

nucleotide binding sites by 40-50 Å (Geeves, Fedorov et al. 2005). The U50 domain contains the nucleotide binding pocket made up by the P-loop, switch 1 and switch 2 with the latter acting as γ-phosphate sensors. These switches move together when ATP is present and move away when ADP is bound.

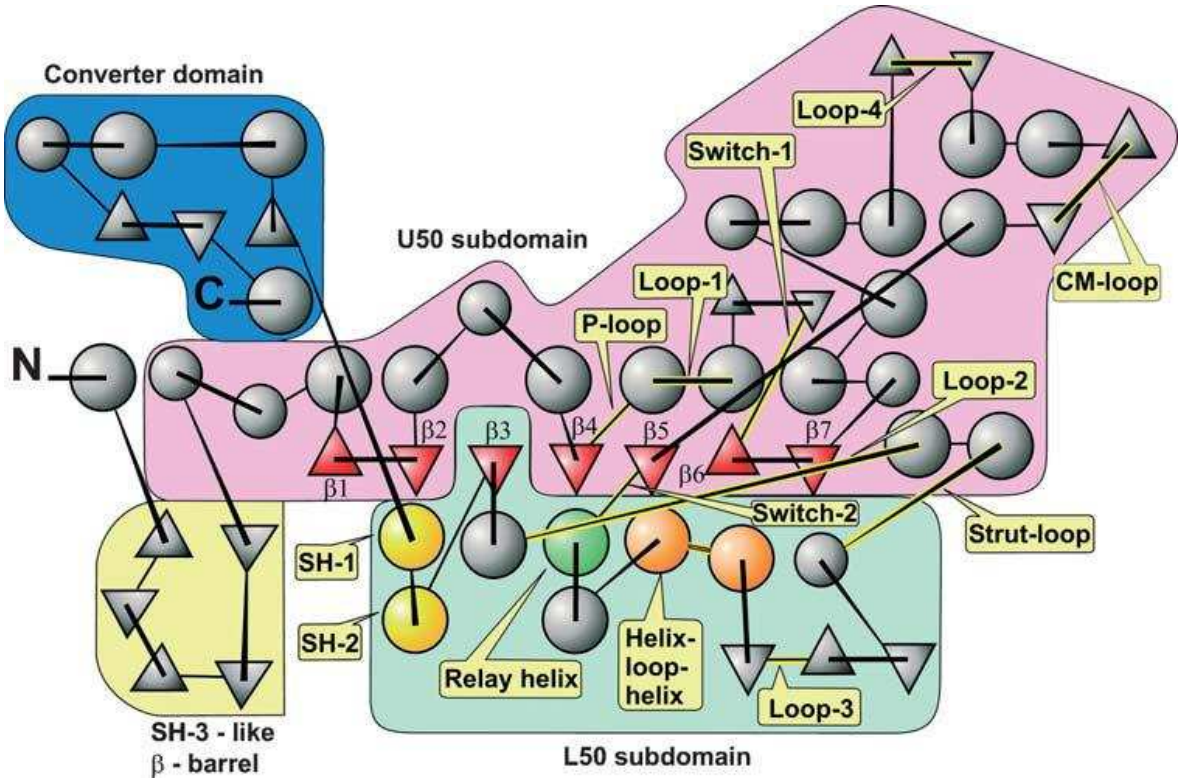

Figure 1.5 – Topological map of the myosin motor domain. Helices are shown as circles while β strands are shown as triangles. The N-terminal SH-3 – like β – barrel is coloured yellow, U50 subdomain – pink, L50 subdomain – light green, converter domain – blue. The central β-sheet is shown by red triangles, Relay helix by a green circle, and SH1-SH2 by yellow circles. Figure from (Geeves, Fedorov et al. 2005).

The 20 kDa fragment begins with a long helix that runs from loop 2 to the 3rd strand in the β sheet which is followed by a broken helix. Both segments of this broken helix contain reactive thiol groups and therefore this region is referred to as the SH1-SH2 helix. Following this is a compact area known as the converter domain (Dominquez, Freyzon et al. 1998). This is located close to the essential light chain binding site and is critical for communication between the active sites and the lever arm.

The relay helix is another area of interest found in the L50 subdomain (Figure 1.5). Throughout the cross bridge cycle the relay helix bends and straightens. This bending leads to a 60° rotation of the converter domain relative to the rest of the motor domain

which in turn rotates the lever arm 60°. A loop at the end of the relay helix (relay loop) contains a tryptophan (W508). Upon ATP binding the C-terminus of the relay helix moves relative to the rest of the molecule. When excited at the correct wavelength the fluorescence of this tryptophan can be measured to observe ATP binding and sometimes hydrolysis.

The binding of myosin to actin is coordinated by several regions including: loop 3 and the helix-loop-helix of the L50, the cardiomyopathy loop and loop 4 of the U50 and loops 1 and 2 which link the U50 and L50. The helix-loop-helix motif has a number of hydrophobic residues flanked by ionic and polar groups. Loop 2 has been found to have different amino acid sequences in different myosins and has been shown to be involved in weak and strong actin binding interactions (Furch, Geeves et al. 1998, Van Dijk, Furch et al. 1999b). Loop 3 contains positively charged residues involved in electrostatic interactions with F-actin (Van Dijk, Furch et al. 1999a). Although in atomic models of the F-actin.myosin complex loop 4 does not appear to interact, some unconventional myosins have an extended loop 4 with a high density of charged amino acids, which may stabilise the complex (Kliche, Fujita-Becker et al. 2001). The cardiomyopathy loop is important for normal myosin function. This was the location of the first missense point mutation, R403Q, in β-myosin that was linked familial hypertrophic cardiomyopathy (HCM, Chapter 1.3.4, (Geisterfer-Lowrance, Kass et al. 1990)).

1.1.4. Structure and proteins of the sarcomere

The sarcomere is the basic contractile unit of skeletal and cardiac muscle. This highly ordered structure contains myosin, actin, tropomyosin, troponin, and other actin or myosin associated proteins (Clark, McElhinny et al. 2002). Electron microscopy of the muscle fibre reveals some of the ultrastructure of the sarcomere showing alternating light and dark bands (Figure 1.6).

The light bands are also referred to as I-bands (isotropic bands) which are composed of just the thin filaments (actin, tropomyosin, and troponin complex). These filaments are anchored into the Z-disc (from the German ‘Zweischenscheibe’ meaning the disc in

between). The Z-disc can be seen as a thick band running vertically in the middle of the I-band (Figure 1.6).

The dark bands, also referred to as the A-bands (anisotropic bands), are composed of the thin filaments and thick filaments (myosin, light chains, and myosin binding protein-C). The thick filaments are aligned by the M-line (from the German 'Mittelscheibe' meaning disc in the middle) which links the thick filament in the centre of the sarcomere. This can be seen as a slightly darker band running vertically through the middle of the A-band (Figure 1.6).

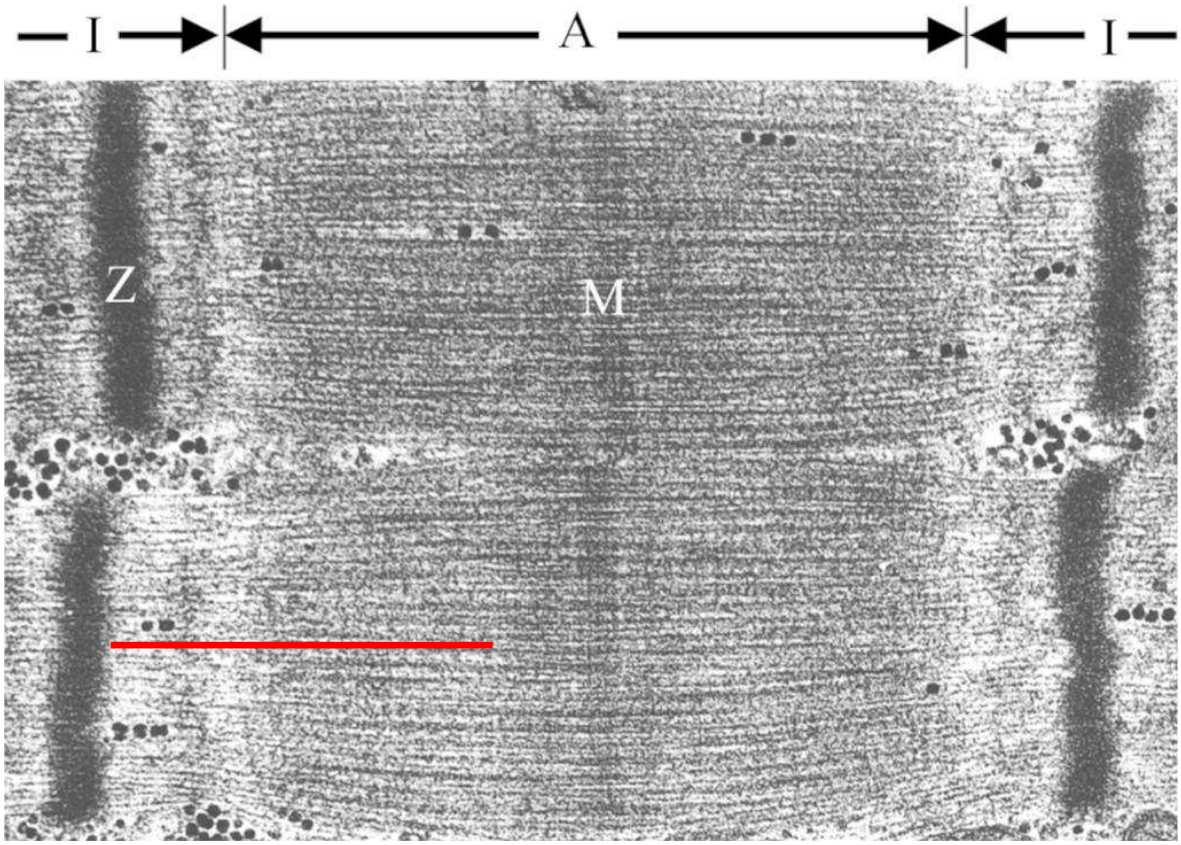

Figure 1.6 – Electron micrograph of the sarcomere in the skeletal muscle showing the ultrastructure from an unidentified species. The A-band (A) in this image corresponds to the overlap of the thick filament and thin filament. The I-band (I) contains just the thin filaments, there is no overlap with the thick filament. The Z-disc (Z) is the thick band in the middle of the I-band where actin filaments attach. The M-line (M) is the band in the middle of the A-band. Unfortunately in this figure the ends of the thin filaments cannot be seen very clearly. The red line indicates where the actin filaments would be. Figure from (Tajsharghi 2008).

Precise alignment of the actin and myosin is required for the function of skeletal and cardiac muscle. To achieve this, a wide variety of accessory proteins are needed. The Z-disc which anchors the actin is composed mainly of α-actinin by cross-linking into a lattice to hold the actin filaments in place (Maruyama, Ebashi 1965, Blanchard, Ohanian et al.

1989). Titin is a huge protein sometimes referred to as the third filament of the sarcomere (Figure 1.7). Spanning from the Z disc to the M-line titin is longer than 1 µm; the molecular weight is predicted to be 3 MDa and composed of 244 immunoglobulin and fibronectin type 3 domains. The roles of titin in the sarcomere are filament assembly, maintaining resting tension and elasticity (Labeit, Kolmerer 1995). Myosin binding protein-C (MyBP-C) forms 7 strips that run parallel to the M-line (Tajsharghi 2008) (Figure 1.7) interacting with both the thick and thin filament (Figure 1.8). These stripes appear at regular intervals of 43 nm in the C-zone of the A-band (Morimoto 2007). The exact function of MyBP-C is unknown however due to the interaction with both thick and thin filaments it is thought to align the filaments in the A-band (Clark, McElhinny et al. 2002).

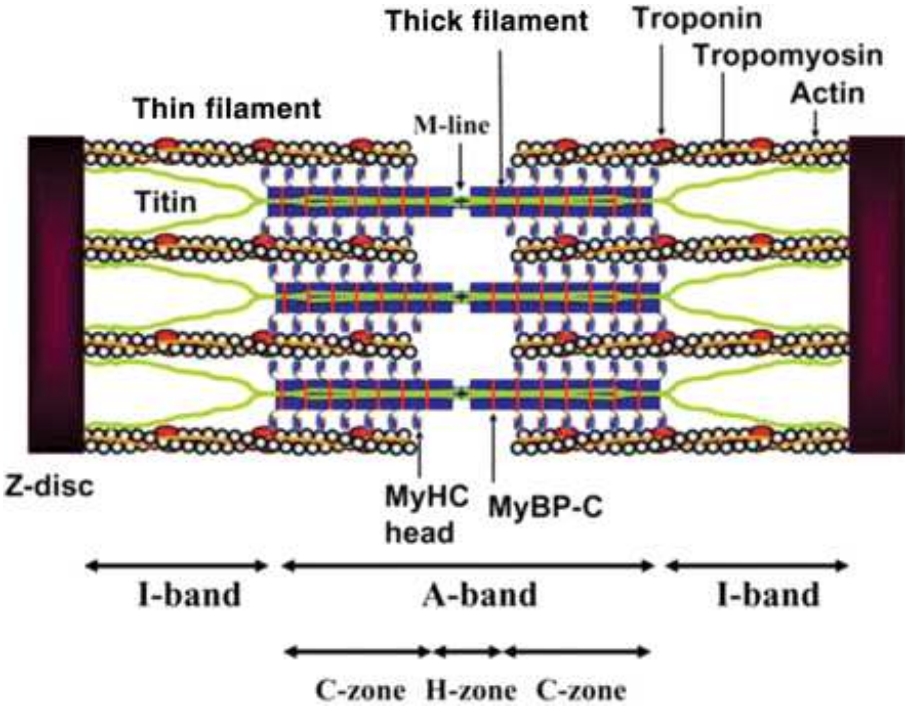

Figure 1.7 – Schematic drawing of the sarcomere structure. Actin filaments (thin filaments) protrude from the Z-disc towards the middle of the sarcomere. Tropomyosin coils around the actin filaments blocking the myosin binding sites of actin. Troponin T, I, and C form a troponin complex (shown as troponin) and binds two thirds of the way along tropomyosin. Myosin (MyHC) tails form filaments (thick filaments) that run parallel to the actin from the M-line towards the Z-discs, however they do not reach the Z-disc. Titin is a huge protein that spans from the Z-disc to the M-line making it half the length of the sarcomere. Myosin binding protein-C (MyBP-C) binds to myosin forming 7-9 transverse stripes across the myosin filaments. In reality the MyBP-C does not cover the entirety of the thick filament and is especially not present in the bare zone. However this cartoon demonstrates the general location of the sarcomeric proteins. The locations of the H and C zone are also a general location and not an accurate representation. Figure from (Morimoto 2007).

The presence of MyBP-C reduces the concentration of myosin needed for polymerisation.

Polymerisation in the presence of MyBP-C leads to longer filaments of a more uniform length compared to those formed in the absence of MyBP-C (Koretz 1979, Davis 1988).

The major component of the thick filament is myosin which has been described already. The major components of the thin filaments are actin, nebulin (not discussed here), tropomyosin, and the troponin complex (Figure 1.8).

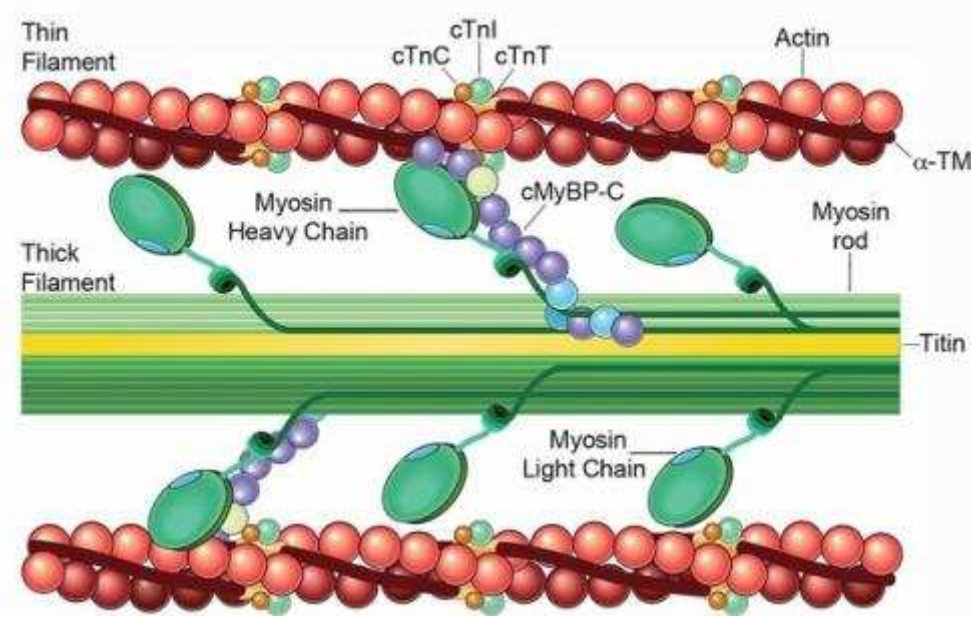

Figure 1.8 – Close up schematic diagram of part of the sarcomere. Actin (red) forms the thin filament with tropomyosin (dark) coiled around it. The troponin complex is shown as the three component parts: troponin T , troponin I, and troponin C. Thick filament proteins myosin (green) and myosin binding protein-C (blue) and titin (yellow) are also shown. Figure from (Lynch and Sadayappan 2014).

Globular actin (G-actin) is a protein composed of 4 subdomains (Figure 1.9) which surround the binding pocket for a nucleotide (ATP or ADP) and a divalent cation (Mg^{2+} or Ca^{+2}, (Gordon, Homsher et al. 2000)). The sequence of actin is highly conserved, for example the amino-acid sequence in human skeletal muscle is 87% identical to yeast actin. This high level of conservation is possibly due to over 50 specific actin binding proteins being identified in lower and higher eukaryotes (Geeves, Fedorov et al. 2005).

G-actin can spontaneously polymerise into filaments (F-actin) which forms the backbone to the thin filament. F-actin appears to form a helix as the filamentous actin twists (Figure 1.8). The helix repeats every 13 actin molecules or every 360 Å. The larger subdomains 3 and 4 are located internally in the double helix and interact with subdomain 3 and 4 of the actin in the opposite filament. Subdomains 1 and 2 however are on the outer side of

the filament and so are exposed to the solvent. These also interact with myosin, in particular the N- and C-terminal ends of actin which are found in subdomain 1. Each actin interacts with 4 other molecules; one before, one after, and two on the other long-pitch helical strand. These interactions are predicted to bind through 10 surface loops and 2 α-helices (Milligan 1996). The total area on the actin surface where myosin binds is approximately 2000 $Å^2$ (Geeves, Fedorov et al. 2005).

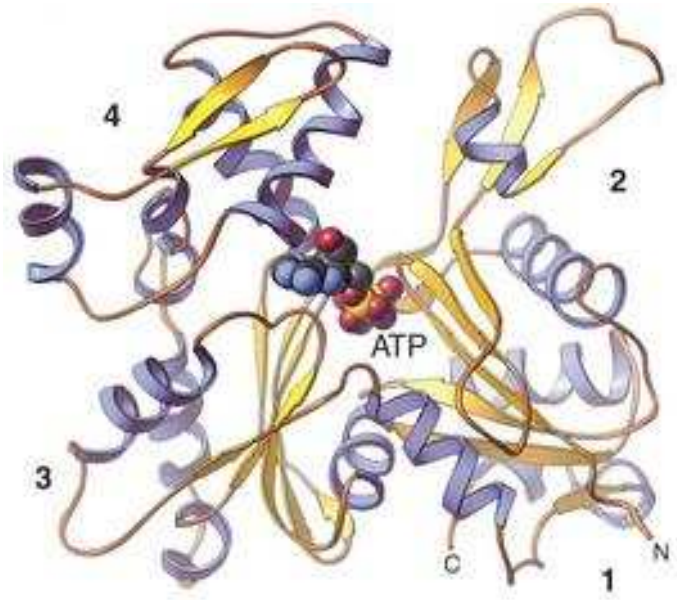

Figure 1.9 – Crystal structure of actin monomer (G-actin). G-actin contains 4 sub-domains (numbered 1-4), a nucleotide, and domains that can bind divalent cations. Figure adapted from (Clinicgate, 2015).

Tropomyosin (Tm) is an extended molecule (~42 nm long) that binds to actin (Figure 1.8). It is formed of an α-helical coiled-coil of either: α,α homodimers in cardiac muscle in large mammals or α,β heterodimers (α and β are different isoforms of tropomysoin) in skeletal muscle and cardiac muscle of small mammals (Tobacman 1996). Tm is stabilised by hydrophobic interactions of non-polar residues in each of the two chains making it more energetically favourable for the two chains to form a coil around each other. Tm is 284 residues long and spans 7 actin monomers on each strand of the F-actin (Gordon, Homsher et al. 2000, Schmidt, Lehman et al. 2015). There is a 14 residue quasi-equivalent repeat in the structure of Tm and it is thought that the overlap between each successive Tm increases the binding affinity of Tm to actin. This was determined by deleting some of these repeats which had little effect (Landis, Bobkova et al. 1997, Hitchcock-DeGregori,

An 1996) whereas deletion of the overlap region showed a reduction of Tm affinity (Mak, Smillie 1981). Tm regulates the binding of myosin to actin through the troponin complex. Upon S1 binding to actin Tm's affinity for actin increases (Cassell, Tobacman 1996, Eaton 1976) and flexibility decreases (Szczesna, Fajer 1995) which helps to push myosin off of actin when the myosin is in the weakly attached state after the power stroke. These effects are greater in cardiac Tm compared to skeletal (Chandy, Lo et al. 1999).

Troponin (Tn) is a complex of three subunits: troponin I (TnI), troponin C (TnC) and troponin T (TnT). TnI binds to actin, inhibiting the actomyosin ATPase in a Ca^{2+}-insensitive manner, TnC binds Ca^{2+}, and TnT links the Tm and Tn complex together (Greaser, Gergely 1973, Mak, Smillie 1981).

TnI is a subunit of the Tn that holds the complex together and onto actin by binding actin, TnC, and TnT. Many of these interactions are regulated by Ca^{2+}. TnI binds to the N-terminal region of actin (Syska, Wilkinson et al. 1976) and can inhibit myosin binding, hence the name TnI (inhibitory troponin). However this inhibitory effect is not responsible for the regulation of actin since it is only present in a 1:7 ratio to actin. Binding occurs between TnI and TnC dependent upon the presence of Mg^{2+} or Ca^{2+} (Ingraham, Swenson 1984). Upon Ca^{2+} binding to TnC this interaction between TnI-TnC weakens the binding of TnI to actin, to the point where in isolated TnI-TnC bound to actin, the binding of Ca^{2+} abolishes this interaction (Potter, Gergely 1974).

TnC is the calcium binding subunit of the troponin and senses Ca^{2+} in muscle regulation. When TnC is removed from the muscle it becomes insensitive to Ca^{2+} activation (Moss, Giulian et al. 1985) while added to reconstituted fibres restores Ca^{2+} sensitivity. TnC contains two globular domains at the N- and C-terminal domains connected by a long helix. Each globular domain contains two possible Ca^{2+} binding sites in the form of E-F hands (helix-loop-helix motif). The C-terminal end has high affinity for both Ca^{2+} and Mg^{2+} and while under relaxed conditions Mg^{2+} is usually bound. This E-F hand also enhances the binding of TnI to TnC and TnC to the thin filament (Zot, Potter 1982). The N-terminus on the other hand is much more selective for Ca^{2+} binding over Mg^{2+} (Potter, Gergely 1974). Removal of this domain renders muscle fibres insensitive to Ca^{2+} activation (Sheng, Strauss et al. 1990, Sorenson, da Silva et al. 1995).

The TnT subunit is involved in holding the Tn complex together and onto Tm by binding to TnI, TnC, Tm, and actin. However the role of TnT is not only to bind the complex and Tm to actin, it also aids in cooperative activation of the thin filament (Gordon, Homsher et al. 2000). The C-terminal end of TnT binds to TnC, TnI, and Tm while the N-terminal end binds to Tm at the region of overlap which is responsible for Tm affinity to actin (Mak, Smillie 1981, White, Cohen et al. 1987). This region of overlap is the most flexible part of Tm and so the TnT is in a position to influence this flexibility. TnT isoforms contain hyper variable region and some are formed from alternate splice variants (Breitbart, Nguyen et al. 1985, Smillie, Golosinska et al. 1988) which gives different TnT isoforms a diverse function.

1.1.5. Cross-bridge cycle

The idea of a cross-bridge cycle by which myosin binds to actin, hydrolyses ATP and walks its way along actin had been around since the 1950's. However it was Lymm and Taylor who first proposed a correlation between enzymatic and structural changes within the myosin (Lymm, Taylor 1971). Myosin on its own will bind and hydrolyse ATP to ADP, however this basal activity is very slow. Actin activates the myosin cross-bridge cycle acting a competitor to the nucleotide. Compared to the cycle shown below (Figure 1.10) the Lymm and Taylor model is a very simple only containing 4 steps. The model used for assays in this thesis (Figure 1.10) has a total of 7 steps. In the first step ATP binds to myosin in a rigor complex with actin (A.M.T). A rigor complex is unlikely to exist in a living muscle due to the abundance of nucleotide (Geeves, Holmes 2005). Geeves and Holmes stated that, in the second step the myosin.ATP complex (M.T) dissociates from the actin. This is caused by switch 1 (Figure 1.5) closing around ATP which pulls the upper 50 kDa domain away from the lower 50 kDa domain opening the actin binding cleft which releases actin from myosin (Geeves, Holmes 2005). In the third step two separate but important events happen. Firstly the switch 2 is brought into proximity of the bound ATP which results in the rotation of the converter/light-chain binding domain which completes the recovery stroke.

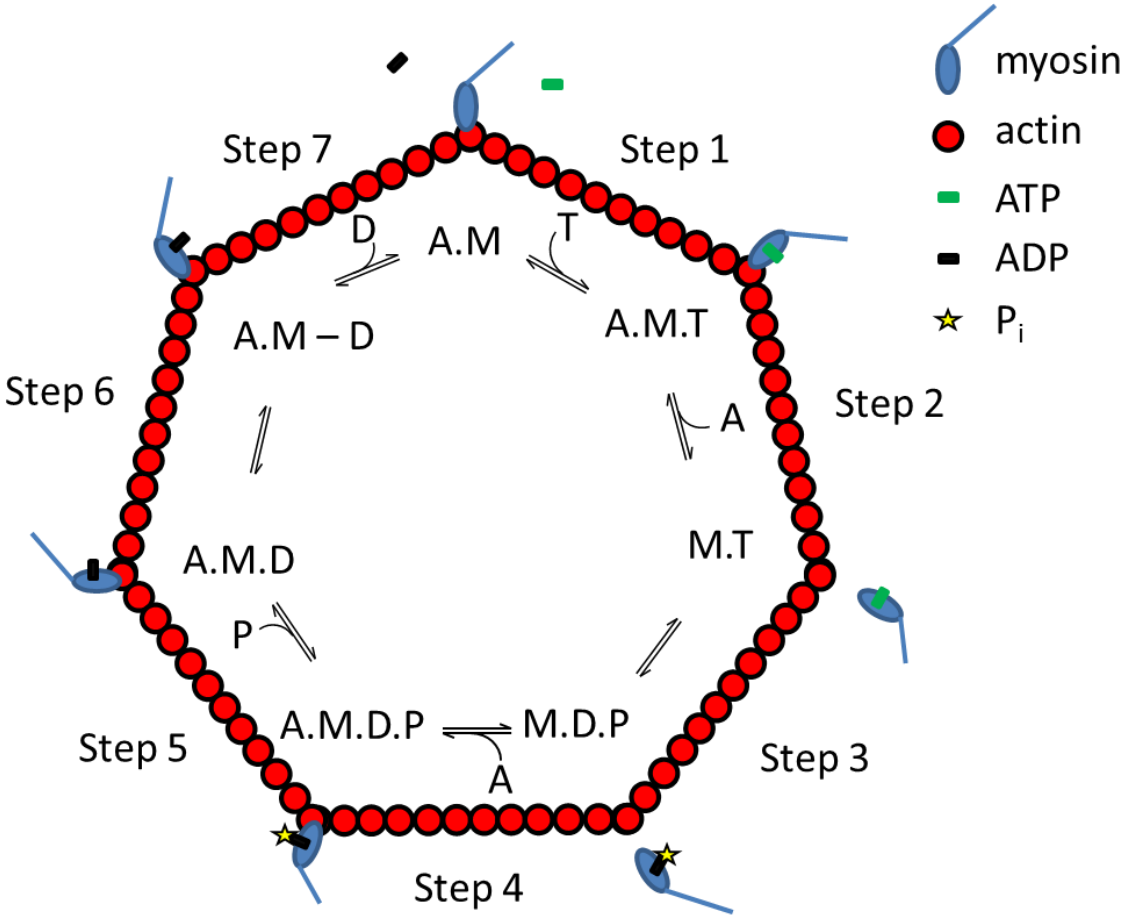

Figure 1.10 – ATP induced actomyosin cross-bridge cycle. Step 1 – myosin is bound to actin in a rigor bond (A.M) and ATP can bind to form an actomyosin.ATP complex (A.M.T). Step 2 – the binding of ATP causing a dissociation of myosin from actin resulting in a myosin.ATP complex (M.T). Step 3 – Unbound from actin myosin hydrolyses the ATP to ADP and inorganic phosphate (P_i) to form a myosin.ADP.P_i complex (M.D.P). The myosin also primes itself for a new power stroke, this is called the recovery stroke. Step 4 – the M.D.P complex rebinds to actin to form an actomyosin.ADP.P_i complex (A.M.D.P). Step 5 – P_i is released and the myosin goes through the power stroke pulling actin along relative to the myosin. It is not clear which occurs first so they have been shown to occur at the same time. Step 6 – the ADP goes from a strong binding to a weaker binding affinity (A.M – D). Step 7 – ADP is released and the myosin returns to the rigor state.

This is necessary for priming the myosin to execute its power stroke and move actin. The second event is the hydrolysis of ATP to ADP. This only occurs after switch 1 and switch 2 are 'closed' and forms a stable myosin.ADP.P_i complex (M.D.P). The forth step is actin rebinding which involves the lower 50 kDa domain binding to actin and the upper 50 kDa domain binds and closes the cleft. The closing of the cleft leads into step 5 where P_i is released and the relay helix rotates releasing the kink and generates the force needed to produce the power stroke which moves the load 5-10 nm. The strain in the converter

domain dissipates by the sliding movement. It is at this point that the nucleotide pocket opens in step 6. In the seventh and final step ADP is released due to a weak affinity and is replaced by a new ATP if there is one available.

It is worth noting that the order of phosphate release and power stroke is not defined and remains under debate. Also if the force produced in step 5 is not significant enough to move the load no sliding will take place and will be inhibited until the load is less or more myosins bind to actin to move the load. The movement of the relay helix against load is strongly inhibited 5-100 fold depending upon the myosin.

1.2. Myosin isoforms

1.2.1. Myosin heavy chain isoform genes

The myosin class II family contains numerous proteins that share a common shape and function, located on different genes with small sequence changes. There are at least 13 different myosin class II heavy chain isoforms in humans. These can be divided into 3 classes: smooth muscle, striated muscle, and non-muscle myosins (Table 1.1). Of these 13 isoforms, 9 are striated muscle myosin which will be the focus of this section. These 8 isoforms are: MyHC-IIa, MyHC-IIb, MyHC-IIx, MyHC-α, MyHC-β, MyHC-extraocular, MyHC-embryonic, and MyHC-perinatal.

1.2.1.1. Adult skeletal isoforms

There are three skeletal 'adult' myosin isoforms; MyHC-IIx, MyHC-IIa, and MyHC-IIb. These are encoded by the genes *MYH1*, *MYH2*, and *MYH4* respectively found on chromosome 17 at position 13.1. MyHC-IIb can be detected at the mRNA and protein level in small mammals, such as mice. Only the mRNA is detectable in a small subset of adult human muscles, with no expression of the protein (Smerdu, Karsch-Mizrachi et al. 1994, Ennion, Sant'ana Pereira et al. 1995, Sant'ana Pereira, Ennion et al. 1997, Wu, Crumley et al. 2000, Horton, Brandon et al. 2001, Allen, Harrison et al. 2001). However the gene is intact and using a recombinant system a functioning protein can be expressed (Bloemink, Deacon et al. 2013). These isoforms are expressed after birth in the fast 2A and 2B fibres (Smerdu, Karsch-Mizrachi et al. 1994) and kinetic characterisation has shown the ADP release rate (thought to be the rate limiting step for velocity) to be very fast (>1,000 s^{-1}) for all three recombinant human isoforms (Bloemink, Deacon et al. 2013).

Gene	Protein	Class	Expression	Function
MYH1	MyHC-IIx	Striated muscle	skeletal muscle post birth	contraction of skeletal muscle
MYH2	MyHC-IIa	Striated muscle	skeletal muscle post birth	contraction of skeletal muscle
MYH3	MyHC-emb	Striated muscle	embryo skeletal muscle and regenerating muscle	contraction of skeletal muscle
MYH4	MyHC-IIb	Striated muscle	skeletal muscle post birth	contraction of skeletal muscle
MYH6	MyHC-α	Striated muscle	cardiac muscle	contraction of cardic muscle
MYH7	MyHC-β	Striated muscle	cardiac muscle and slow skeletal	contraction of cardic muscle
MYH7b	MyHC-7B	Striated muscle	Unknown	Slow twich muslce
MYH8	MyHC-peri	Striated muscle	embryo skeletal muscle and regenerating muscle	contraction of skeletal muscle
MYH9	NMMHC-IIa	Non-muscle	cell cytoplasm	cytokinesis, cell motility, maintaining cell shape
MYH10	NMMHC-IIb	Non-muscle	cell cytoplasm	cytokinesis, cell motility, maintaining cell shape
MYH11	SMMHC	Smooth muscle	smooth muscles	contraction of smooth muscle
MYH13	MyHC-eo	Striated muscle	specialised muscles including extraocular	contraction of extraocular and laryngeal muscle
MYH14	NMMHC-IIc	Non-muscle	cell cytoplasm	cytokinesis, cell motility, maintaining cell shape

Table 1.1 – Summary of the myosin class II genes and the proteins they encode. They have been grouped into three different classes: smooth muscle, striated muscle, and non-muscle.

1.2.1.2. Cardiac isoforms

There are two cardiac myosin isoforms expressed in the myocardium; MyHC-α and MyHC-β. These isoforms are encoded by the genes *MYH6* and *MYH7* respectively found on chromosome 14 at position 12. These genes are; regulated during development, distributed in the heart, and react to hormones, stress, and exercise differently (Table 1.2).

MyHC-α is the major isoform expressed in the atria of all mammals and ventricles of small mammals (Lompré, Nadal-Ginard et al. 1984) however is expressed at low levels in the ventricles of larger mammals including humans.

MyHC-β is in abundance in the ventricles of mammals during development and is the major isoform present in the ventricles of large mammals including humans. MyHC-β is also the slow skeletal isoform found in fibres such as the soleus muscle (Weiss, Leinwand 1996).

	MYH6	*MYH7*
+ T3	↑	↓
- T3	↓	↑
Exercise	↑	↓
Pressure overload	↓	↑
Aging	↓	↑

Table 1.1 – Directional regulation response of cardiac *MYH* genes. T3 = triiodothyronine thyroid hormone. Adapted from (Weiss, Leinwand 1996)

Investigations using recombinant MyHC-α and MyHC-β found the MyHC-α to have a 10-fold faster ADP release rate than MyHC-β. A fast ADP release rate is indicative of a fast type myosin and therefore the MyHC-α was found to be a fast type myosin while MyHC-β was a slow type (Deacon, Bloemink et al. 2012).

1.2.1.3. Extraocular isoform

The MyHC-eo is a specialised isoform that is thought to be very fast due to its expression in the fast twitch fibres in the extraocular and laryngeal muscles (Sartore, Mascarello et al. 1987, Lucas, Rughani et al. 1995, Brueckner, Itkis et al. 1996). ATPase kinetics using a recombinant-GFP construct found the MyHC-eo to have a V_{max} similar to the adult skeletal isoforms (Resnicow, Deacon et al. 2010) and stopped-flow spectroscopy found the ADP affinity to be weak and ADP release rate to be fast (>1100 s^{-1}) which is characteristic of a fast type myosin (Bloemink, Deacon et al. 2013).

1.2.1.4. Developmental isoforms

There are two developmental isoforms, MyHC-emb and MyHC-peri, which are encoded for by the genes *MYH3* and *MYH8* respectively. MyHC-emb is thought to be a slow type myosin similar to the MyHC-β, while the MyHC-peri is likely to be a fast type isoform. Both isoforms are expressed in the developing embryo along with MyHC-β. They are down-regulated after birth and replaced with the adult isoforms, however they are upregulated during muscle damage and repair. Some work has been conducted on the kinetics of the two isoforms which found the V_{max} of the MyHC-peri to be close to the adult isoforms while the MyHC-emb was at the slower end (Resnicow, Deacon et al. 2010). The MyHC-emb will be described in more detail in Chapter 4.

1.2.2. Sequence identity

Mammalian *MYH* genes share a similar intron/exon organisation and are highly conserved in terms of their primary structure. It has been suggested from evolutionary comparisons of the mammalian *MYH* genes that this gene family arose from multiple duplications of an ancestral *MYH* gene (Stedman, Eller et al. 1990, Moore, Tidyman et al. 1993). Most of these genes are large at approximately 30 kb, encoded on 40-41 exons with the coding region beginning at exon 3 (Strehler, Strehler-Page et al. 1986). The striated muscle *MYH* genes are highly conserved (Table 1.3) with a 77-95 % sequence identity.

MyHC-β	MyHC-β							
MyHC-α	92.82	MyHC-α						
MyHC-IIx	81.14	80.38	MyHC-IIx					
MyHC-IIa	81.03	80.43	94.84	MyHC-IIa				
MyHC-IIb	80.67	80.23	94.07	91.95	MyHC-IIb			
MyHC-peri	78.89	78.94	83.88	84.61	83.21	MyHC-peri		
MyHC-emb	80.75	80.25	92.25	92.76	90.39	84.55	MyHC-emb	
MyHC-eo	77.12	77.25	82.02	82.68	81.68	79.07	81.76	MyHC-eo

Table 1.2 – Sequence identities of whole human myosin isoforms

This conservation is even greater when comparing the sequence identities of the same myosin isoform between species (Table 1.4). A comparison of the sequence of *MYH3* and *MYH7* in mice, rat, human, cow, and elephant show very high similarity (>95%).

MYH7

Mouse	Mouse				
Rat	99.17	Rat			
Human	97.52	97.21	Human		
Cow	97.31	96.95	97.57	Cow	
Elephant	96.65	96.23	97.07	97.28	Elephant

MYH3

Mouse	Mouse				
Rat	99.59	Rat			
Human	98.2	98.25	Human		
Cow	97.11	97.16	98.04	Cow	
Elephant	97.53	97.58	97.94	97.22	Elephant

Table 1.3 – Sequence identities of whole myosin (*MYH7* or *MYH3*) from different species.

The 5' and 3' untranslated regions (UTRs) of the *MYH* sequences are less conserved than the rest of the sequence and as such can be targets for gene specific probes (Lyons, Schiaffino et al. 1990, Lyons, Ontell et al. 1990). However when the UTRs of the same isoform are compared across species there is greater conservation (Periasamy, Wieczorek et al. 1984, Saez, Leinwand 1986).

1.2.3. Sequence differences relate to functional divergence

While the sequence identities of the 8 skeletal myosin isoforms are very similar there are still areas of divergence. Two of these regions within the myosin head where there is divergence are loop-1 and loop-2 (Figure 1.11).

There has been much interest in the variable loop-2 region with mutagenic studies altering the sequence of the loop. Lengthing the loop with no change in charge has no measurable effect on actomyosin ATPase, rate of ATP binding or the binding affinities of myosin for actin. Insertion of upto 11 uncharged amino acids only decreases the thermal stability of the myosin slightly (Ponomarev, Furch et al. 2000). Replacing the loop of smooth-muscle HMM with the loop of either skeletal or cardiac myosin prevented HMM regulation similar to the donor myosins. There was however no change in the actin affinity or the maximum rate of turn over in the presence of actin (Rovner, Freyzon et al. 1995). Similarly insertion of loop-2 regions from various species inserted into the *Dictyostelium* myosin-II backbone had similar ATPase activity as the donor myosin (Uyeda, Ruppel et al. 1994).

1.2.4. Expression of isoforms

The expression pattern of the two developmental myosin isoforms has been well characterised in the mouse and rat models with MyHC-emb appearing 9.5 days post coitum (dpc) and MyHC-peri 10.5 dpc in the mouse (Lyons, Ontell et al. 1990). The proximal ends of the developmental myosin genes contain E-boxes stimulating muscle commitment and differentiation in response to MyoD and Myf5 binding (Beylkin, Allen et al. 2006, Konig, Burkman et al. 2002). Along with these two developmental isoforms, a myosin indistinguishable from MyHC-β is expressed. It was suggested that the myosin expressed differs from the adult form (Hughes, Cho et al. 1993); however this has yet to be proven. It has also been suggested that this isoform is the slow tonic myosin coded for by *MYH7b* (Rossi, Mammucari et al. 2010), however this is only detected at low levels or in rare fibres. For the time being then it appears the three isoforms expressed during development are: MyHC-emb, MyHC-peri, and MyHC-β.

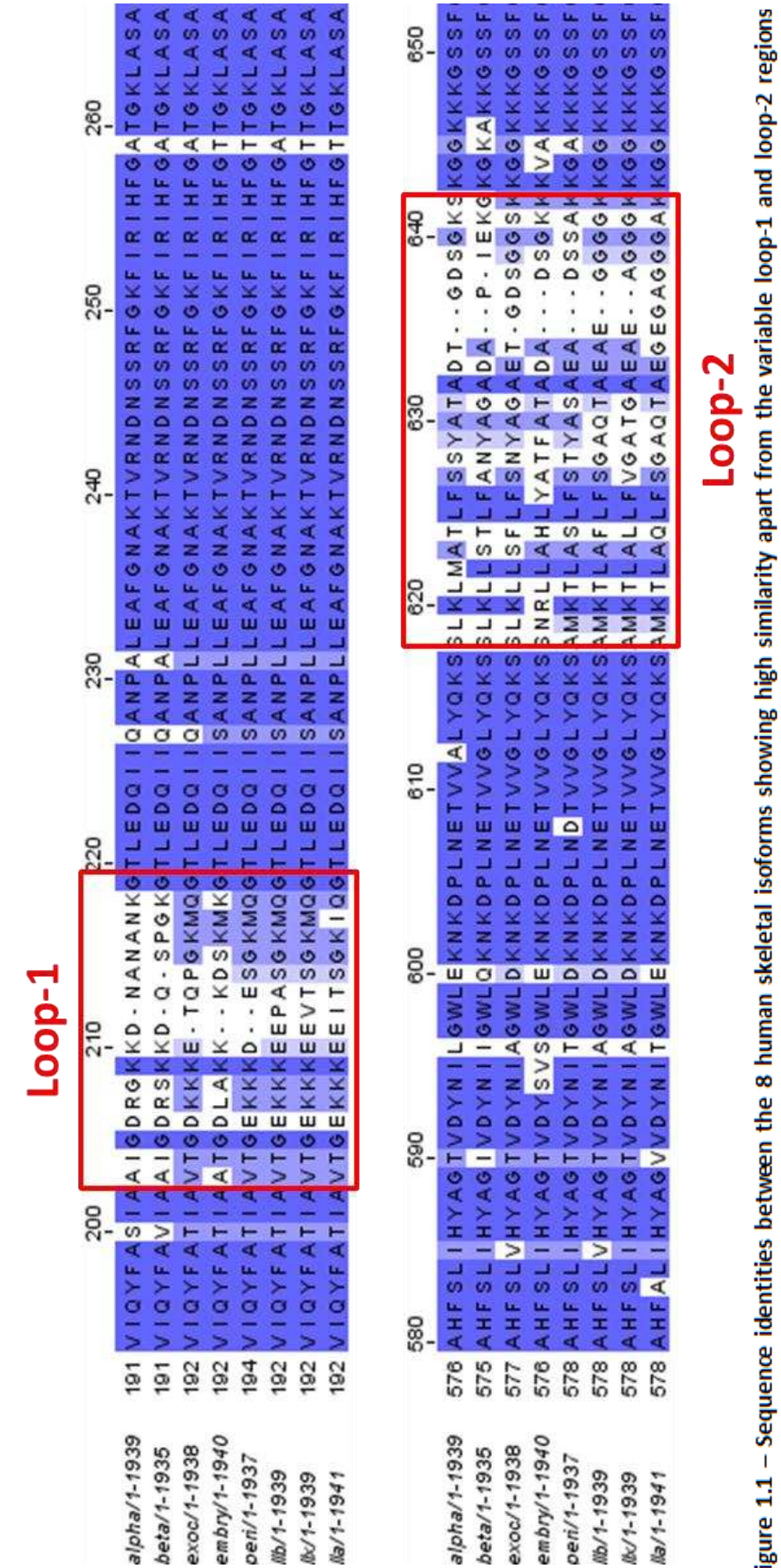

igure 1.1 – Sequence identities between the 8 human skeletal isoforms showing high similarity apart from the variable loop-1 and loop-2 regions ighlighted

In rats, MyHC-emb and MyHC-β are expressed in the first muscle fibres to form (primary generation fibres (Narusawa, Fitzsimons et al. 1987, Rubinstein, Kelly 1981)). The second fibres to be expressed (secondary generation fibres) express MyHC-emb and MyHC-peri (Condon, Silberstein et al. 1990). The developmental isoforms disappear at the same time as the adult skeletal myosin isoforms (MyHC-IIa, MyHC-IIx, and MyHC-IIb) are expressed. In rats the adult skeletal myosins are detected a few days after birth (DeNardi, Ausoni et al. 1993) while in mice the transcripts can be detected before birth (Lu, Allen et al. 1999). The timing of the downregulation of the developmental isoforms appears to be dependent on the body muscle at both the mRNA (Lu, Allen et al. 1999) and protein (Agbulut, Noirez et al. 2003) level.

The switch from developmental to adult isoforms can be modulated by neural influences and extrinsic hormones. Thyroid hormone is required for the switch from MyHC-emb/MyHC-peri to adult fast myosin. Hyperthyroidism can lead to precocious expression of the fast myosins, while hypothyroidism can delay the switch (Butler-Browne, Herlicoviez et al. 1984, Gambke, Lyons et al. 1983, Russell, Cambon et al. 1988). Neural activity does not seem to be necessary for transition from developmental to fast isoforms (Gambke, Lyons et al. 1983, Butler-Browne, Bugaisky et al. 1982), however it does appear to be required to promote MyHC-β expression in the soleus muscle in place of MyHC-emb (Narusawa, Fitzsimons et al. 1987).

The details of the switch from developmental to adult isoforms remain to be established, however probably involves specific sequence regulation of the *MYH* gene cluster where they are in the order: *MYH3-MYH2-MYH1-MYH4-MYH8-MYH13*. It has been reported that there is a long non-coding antisense RNA controlled by thyroid hormone that regulates the transition during postnatal development and hypothyroidism. This RNA is transcribed from a site between the *MYH4* and *MYH8* genes and appears to repress the *MYH8* gene (Pandorf, Jiang et al. 2012).

There appears to also be an enhancer between the *MYH3* and *MYH2* genes (Sakakibara, Santolini et al. 2014) which upregulates the expression of the fast myosin genes and suppress *MYH7*. Whether there are other locations that control the developmental switch is not clear.

1.3. Myopathies

Myopathies are muscular and neuromuscular disorders which present with muscle weakness due to dysfunction of the muscle fibre. Other symptoms can include muscle cramps, stiffness, and spasm. Myopathies are grouped as: congenital myopathies; muscular dystrophies; mitochondrial myopathies; glycogen storage disease of muscle; myoglobinurias (myoglobin in the urine); dermatomyositis (inflammation of the skin and muscle tissue); myositis ossificans (bone growth in the muscle); familial periodic paralysis; polymyositis (inflammation and degradation of the muscle); inclusion body myositis (inflammatory disease of the muscle); and related myopathies; neuromyotonia (inflammatory disease of the peripheral nerves); stiff-man syndrome; and common cramps and stiffness (National Institutes of Health 2015). This thesis will focus on the congenital myopathies.

The first myopathy described to be cause by a mutation in a *MYH* gene was in 1990 in a case of familial hypertrophic cardiomyopathy (Geisterfer-Lowrance, Kass et al. 1990). The first skeletal myopathy causing *MYH* mutation was identified in 2000 (Martinsson, Oldfors et al. 2000).

There are at least 5 *MYH* genes that have been found to cause myopathies including: *MYH2*, *MYH3*, *MYH6*, *MYH7*, and *MYH8*.

1.3.1. Hypertrophic cardiomyopathy

Cardiomyopathy is a collection of diseases of the heart muscle including: hypertrophic cardiomyopathy (HCM), dilated cardiomyopathy (DCM), and arrhythmogenic right ventricular cardiomyopathy (ARVC). These are the three most common types of cardiomyopathy. Mutations in 10 cardiac sarcomeric proteins have been linked to this disease (Table 1.5) with mutations in β-cardiac myosin (MyHC-β) and myosin binding protein-C (MyBP-C) being the two major causes (Figure 1.12).

More than 300 mutations have been identified in MyHC-β (Seidman, Seidman 2001, Buvoli, Hamady et al. 2008, Walsh, Rutland et al. 2010, Colegrave, Peckham 2014), the

majority of which are found within the motor domain. Hypertrophic cardiomyopathy is a disease of the heart leading to left ventricle hypertrophy (LVH, Figure 1.13). This is a thickening on the heart muscle and a reduction of the volume within the ventricle. This results in less oxygenated blood being pumped at a much higher force which becomes dangerous during intense exercise.

Chromosomal Locus	Gene	Protein
1q32	**TNNT2**	**Cardiac troponin T** (Thierfelder, Watkins et al. 1994)
2q31	**TTN**	**Titin** (Satoh, Takahashi et al. 1999)
3p21	**MYL3**	**Essential myosin light chain** (Poetter, Jiang et al. 1996)
3p21-p14	**TNNC1**	**Cardiac troponin C** (Hoffman, Schmidt-Traub et al. 2001)
11p11	**MYBPC3**	**Cardiac myosin binding protein-C** (Bonne, Carrier et al. 1995, Watkins, Conner et al. 1995)
12q23-q24	**MYL2**	**Regulatory myosin light chain** (Poetter, Jiang et al. 1996)
14q12	**MYH7**	**β-Myosin heavy chain** (Geisterfer-Lowrance, Kass et al. 1990)
15q14	**ACTC**	**Cardiac actin** (Olson, Doan et al. 2000)
15q22	**TPM1**	**α-Tropomyosin** (Thierfelder, Watkins et al. 1994)
19q13	**TNNI3**	**Cardiac troponin I** (Kimura, Harada et al. 1997)

Table 1.5 – Sarcomeric proteins with mutations associated with cardiomyopathies. The chromosomal locus and gene are also given.

This makes HCM a leading cause of sudden cardiac death (SCD) in young adults and athletes effecting <1% of the general population (Fatkin, Graham 2002). While the major causes of HCM in adults are mutations in sarcomeric proteins it is less clear what the causes are in infants and children.

Generally speaking the presence of a sarcomeric gene mutation leads patients to present with symptoms earlier, have a higher prevalence of family history of HCM and sudden cardiac death (SCD) than those who have no mutation (Lopes, Zekavati et al. 2013, Olivotto, Girolami et al. 2008). The trend also appears that those with a sarcomeric protein mutation have more severe hypertrophy, microvascular dysfunction and myocardial fibrosis (Olivotto, Girolami et al. 2011). There is also the suggestion that the patients with sarcomeric mutations have a poorer prognosis, however due to small sample sizes no clear conclusion can yet be drawn (Watkins, Conner et al. 1995, Pasguale,

Syrris et al. 2012, Moolman, Corfield et al. 1997, Anan, Shono et al. 1998, Torricelli, Girolami et al. 2003, Nakajima-Taniguchi, Matsui et al. 1997, Lopes, Rahman et al. 2013). Mutations in multiple sarcomeric proteins are present in up to 5% of individuals, with a more severe phenotype that presents earlier (Ingles, Doolan et al. 2005, Richard, Charron et al. 2003, Girolami, Ho et al. 2010).

In adults, HCM is defined by a wall thickness of ≥15 mm in one or more segments on the left ventricle. In children the diagnosis requires a left ventricle wall thickness greater than 2 standard deviations from the predicated mean (Elliott, Anastasakis et al. 2014). The wall thickness can be measured by a variety of imaging techniques including: echocardiography, cardiac magnetic resonance imaging, or computed tomography. Other tests may include taking family history and genetic testing (Elliott, Anastasakis et al. 2014).

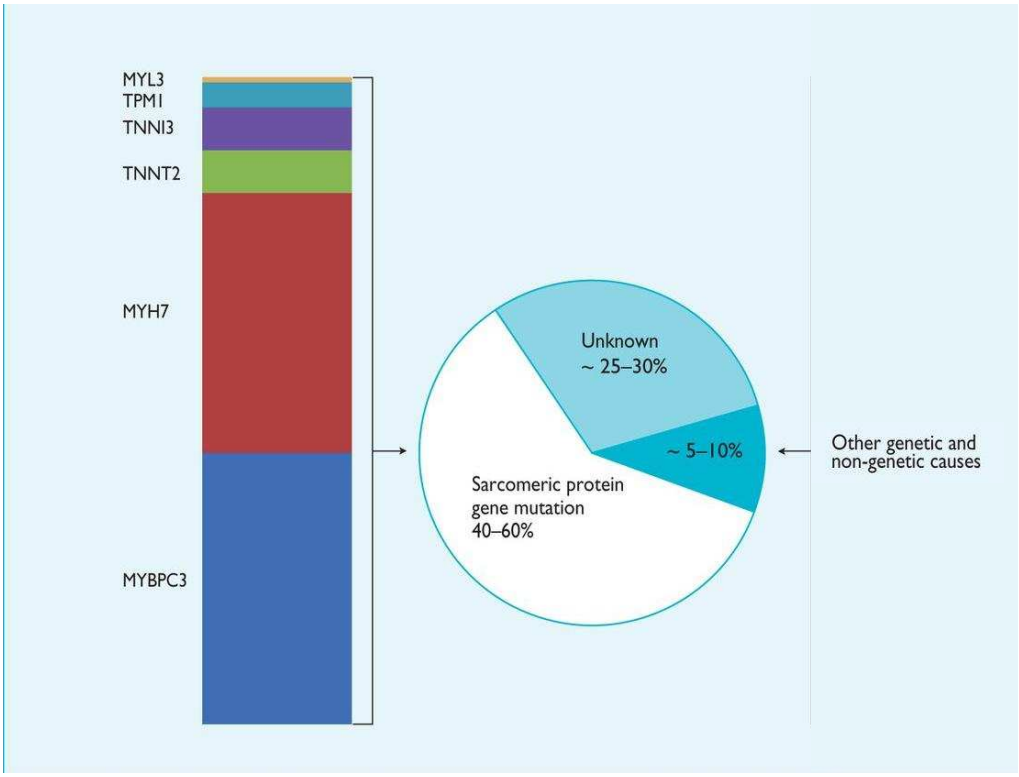

Figure 1.11 – The major causes of cardiomyopathy in adolescents and adults are mutations in the sarcomeric proteins. Of the 40-60 % of sarcomeric protein gene mutations the majority are caused by mutations in either MYH7 or MYBPC3. Figure adapted from (Elliott, Anastasakis et al. 2014).

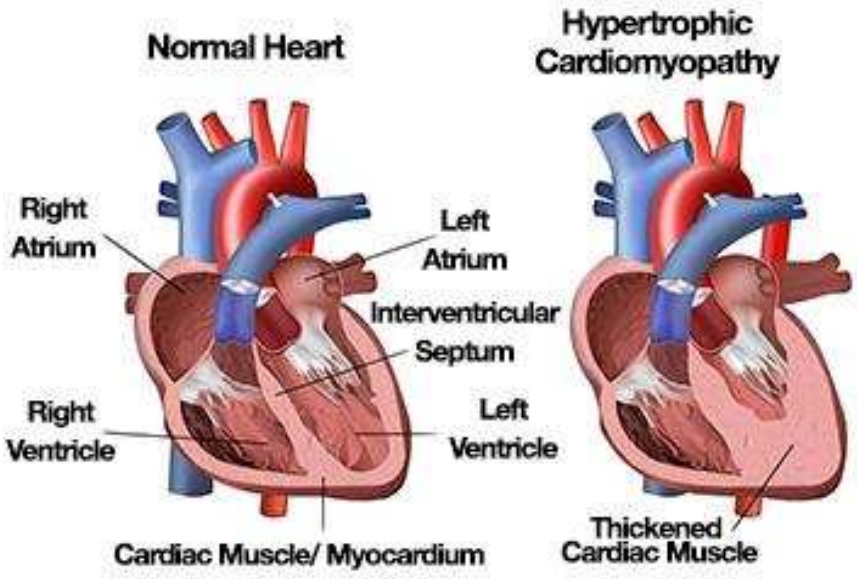

Figure 1.12 – Diagram of the normal (left) and hypertrophic (right) heart. The muscle of the left ventricle becomes much thicker reducing the ventricular volume. Figure from (Bajona, Turer 2015).

Histological studies on the myocardium from hypertrophic cardiomyopathy patients (Figure 1.14) show the large structure changes in the diseased heart. The histological sample in figure 1.14 shows the hallmarks of HCM: regions of myocyte disarray (Davies 1984), fibrosis (Anderson, Sutton et al. 1979), and small vessel disease (Maron, Wolfson et al. 1986). Myocyte disarray can be characterised by the disorganisation of the myocytes, however this is not specific just to HCM (Almaas, Amlie 2010). The amount of fibrosis is linked with small-vessel disease, increased septal thickness, cardiac mass, increasing age, end-stage heart failure progression and sudden cardiac death (SCD (Varnava, Elliott et al. 2001, Basso, Thiene et al. 2000)).

Due to MyHC-β being expressed in the skeletal muscle as well as the cardiac, studies have investigated the skeletal muscle of HCM patients. *In vitro* motility assays have demonstrated impaired function due to the mutated protein presence (Cuda, Fananapazir et al. 1993). However histological staining has shown HCM mutations in MyHC-β has very little effect on the skeletal muscle (Oldfors 2007).

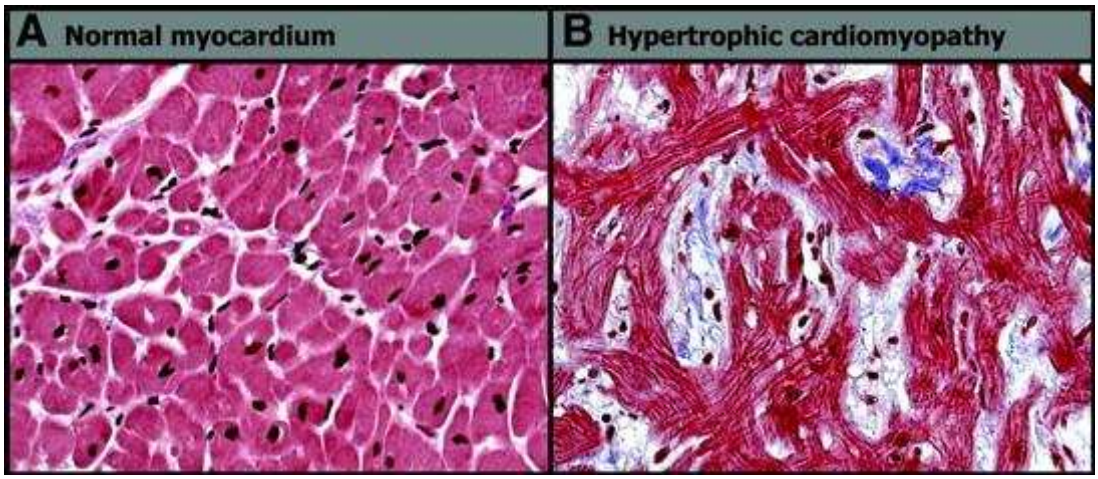

Figure 1.13 – Example histological images of the myocardium in either a normal (A) and hypertrophic cardiomyopathy (B) sample. The hypertrophic cardiomyocytes show myofibre disarray and fibrosis. Figure adapted from (Yilmaz, Kindermann et al. 2010)

1.3.2. Freeman-Sheldon Syndrome

There are two groups of congenital contractures (over contracted joints from birth) observed in children; isolated congenital contracture (eg clubfoot) and multiple congenital contractures (arthrogryposis). 1 in 3,000 children are born with arthrogryposis, often the cases are sporadic. However children with arthrogryposis are usually found to have an underlying inherited syndrome (Bamshad, Jorde et al. 1996, Bamshad, Bohnsack et al. 1996, Hall, Reed et al. 1982, Krakowiak, O'Quinn et al. 1997). The most common of the inherited arthrogryposis syndromes affect the distal limbs (hands and feet) leading to camptodactyly and club foot. There are 10 of these distal arthrogryposis (DA) syndromes (Bamshad, Jorde et al. 1996).

Freeman-Sheldon Syndrome (FSS) or DA2A is the most severe but very rare distal arthrogryposis syndrome which causes contractures of the orofacial muscles (Freeman, Sheldon 1938). This causes a pinching of the lips and reduces the mouth opening, hence the other name of FSS 'whistling face syndrome' (Figure 1.15A). There appears to be no gender preference (Gross-Kieselstein, Abrahamov et al. 1971). The only treatment for individuals with FSS is surgery to try and correct the over contracted joints, however this leads to a high risk of mortality due to difficulty supplying air to the patient (intubating)

while under anaesthetic (Yamamoto, Osuga et al. 1994) as well as the general risks of anaesthetics.

A reason why the entire musculature system of the mouth is involved in this myopathy is unclear. Biopsies of the orbicularis oris (muscle around the mouth), masseter (lower jaw muscle), buccinators (muscle within the cheek) and risorius (the muscle of facial expression) muscles show atrophy of the fibres and adipose infiltration, as well as fibrosis, variation in fibre diameter and central migration of the nucleus (Ferrari, Bettuzzi et al. 2008, Burian 1962, Malkawi, Tarawneh 1983).

DA syndromes are characterised as a group of similar disorders characterised by multiple congenital contractures of the upper and lower limbs (Hall, Reed et al. 1982, Bamshad, Jorde et al. 1996, Beals 2005, Hall 2014). This results in contractures of the hands (Figure 1.15B) and feet (Figure 1.15C). Unlike other DA syndromes the facial muscles of FSS patients are severely contracted resulting in a small oral opening resembling a whistling face (Freeman, Sheldon 1938, Stevenson, Carey et al. 2006).

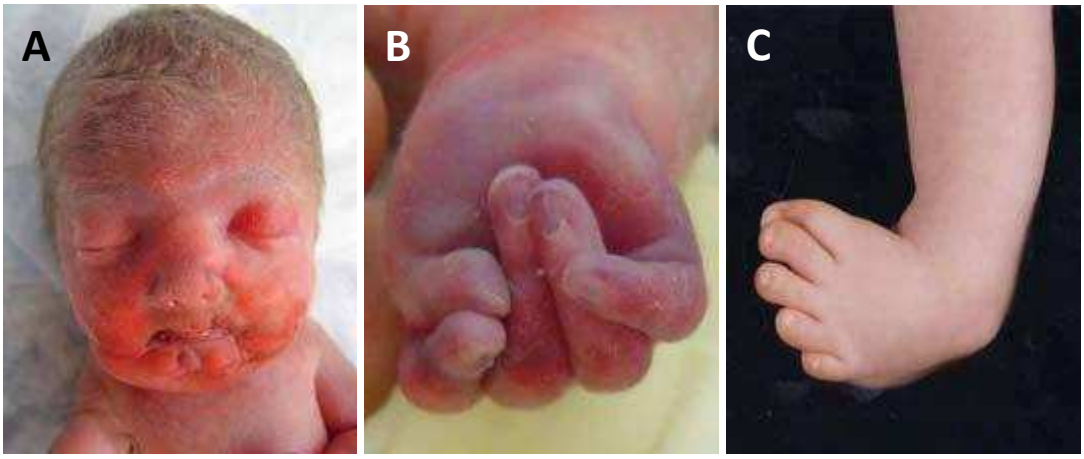

Figure 1.14 – Clinical characteristics of Freeman-Sheldon syndrome. (A) Child with a severe contracture of the facial muscles giving the phenotypic whistling face. (B) and (C) A common phenotype among DA syndrome patients is contracted hands (Camptodactyly) and feet (club foot). Figure from (Toydemir, Rutherford et al. 2006)

Unlike the most common DA syndrome Sheldon-Hall syndrome (SHS) the only known cause for FSS is a mutation in the embryonic myosin gene, *MYH3* (Figure 1.16(Beck, McMillin et al. 2014)). Analysis by Beck *et al*. revealed that the 3 most common mutations that cause FSS were: Threonine-178-Isoleucine (T178I), Arginine-672-Cysteine (R672C), and Arginine-672-Histidine (R672H). These were ranked in order of severity with T178I being the most, R672C the least and R672H intermediately severe. This was determined

by ranking the affected areas using a severity score with T178I ranking highest in all areas. Curvature of the spine (scoliosis), while found in all three mutants with no varying severity was observed in only the T178I mutants before the age of 3 months (Figure 1.17).

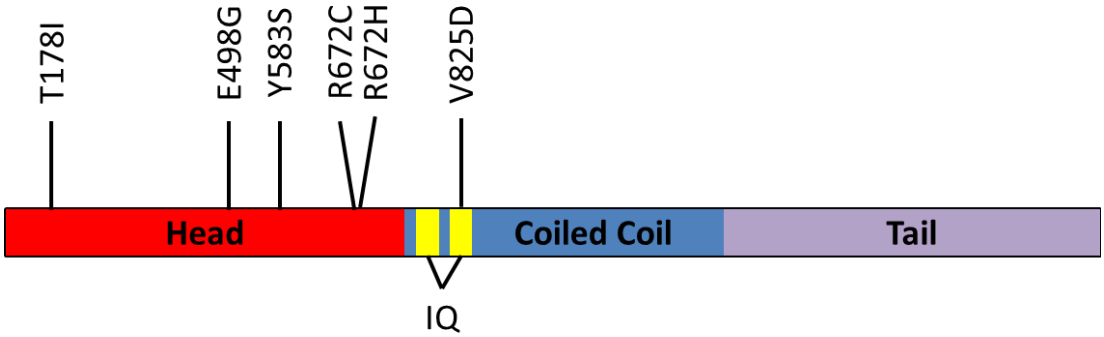

Figure 1.15 – Location of mutations on the myosin molecule in *MYH3* that cause FSS. They are all located in the head and IQ domains. Figure adapted from (Toydemir, Rutherford et al. 2006).

Figure 1.16 – Radiograph of an individual with a T178I mutation in the embryonic myosin showing the severe curvature of the spine. Figure from (Beck, McMillin et al. 2014).

It is worth noting that this myopathy while caused by a mutation in the embryonic myosin persists beyond the developmental stage where embryonic myosin is expressed.

Histological samples from a FSS patient at 15 months showed an abnormally large number of fibres (>20% of all fibres) expressing the perinatal myosin isoform (Figure 1.18). This was compared to samples from 8 controls aged 10-15 months where there were only the occasional fibres (0-2% of all fibres) expressing the perinatal isoform (Tajsharghi, Kimber et al. 2008).

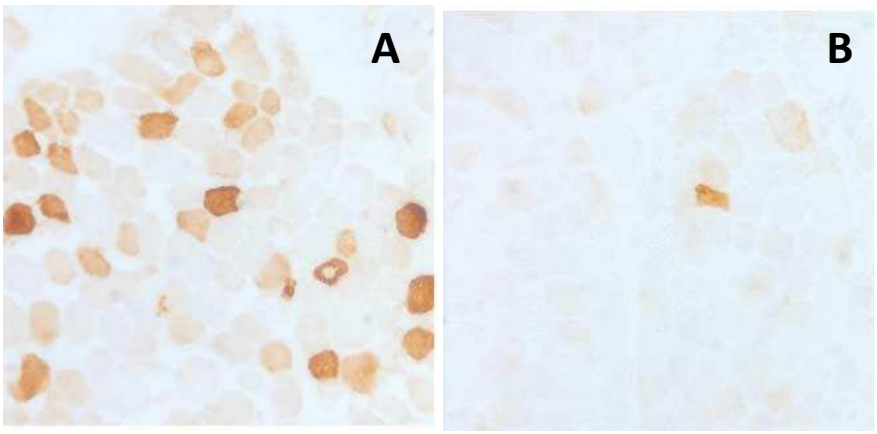

Figure 1.17 – Histological samples stained for the perinatal myosin isoform while the unstained fibres are expressing the adult fibres. (A) Muscle biopsy from a FSS patient's tibialis anterior muscle at 15 months. (B) A specimen from a healthy control subject at 11 months showing only a few scattered fibres expressing perinatal myosin. Figure from (Tajsharghi, Kimber et al. 2008).

A study into force production and relaxation of myofibrils from a R672C patient showed that the specific force was greatly reduced. While the absolute force was increased on the wild type the cell diameters were much greater and appeared hypertrophic. The relaxation time was also found to be prolonged and the relaxation of the myofibrils never reached completion (Racca, Beck et al. 2015).

1.3.3. Other myopathies

Mutations in the *MYH2* gene that encodes the MyHC-IIa myosin isoform lead to autosomal dominant myopathy with congenital joint contractures, ophthalmoplegia (paralysis of eye muscles) and rimmed vacuoles. It is also known as 'autosomal dominant myosin heavy chain IIa myopathy (E706K)' and 'Hereditary inclusion body myopathy type 3' (Oldfors 2007). Clinical characteristics of this myopathy include: congenital joint contractures, ophthalmoplegia, mild proximal muscle weakness during childhood, and impaired movement in middle age. Children with this disease have either no or very few

and small type 2A muscle fibres (Martinsson, Oldfors et al. 2000, Darin, Kyllerman et al. 1998, Tajsharghi, Thornell et al. 2002). Adults on the other hand, show dystrophic changes with fibre thickness variation and increased interstitial fat and connective tissue.

Hypertrophic cardiomyopathy is not the only disease caused by a mutation in the *MYH7* gene. Dilated cardiomyopathy (DCM) can also be caused by mutations in the *MYH7* however unlike the LVH seen for HCM the left ventricle wall becomes thinner and the volume within the ventricle increases. With this the ventricle becomes stretched or 'baggy' and the muscle itself becomes weaker and not able to pump blood around the body efficiently (British Heart Foundation 2016).

A second disease associated with a mutation in the *MYH7* gene is Laing early onset distal myopathy (Laing, Laing et al. 1995). The clinical findings are initially muscle weakness of the ankle dorsiflexors and big toe extension. Onset is usually during the first or second year of life with slow progression leading to weakness of the wrists and fingers. Weakness spreads to the majority of the body however most patients remain mobile throughout their lives. One oddity of this disease is that it is a mutation in the *MYH7* gene however only one case has shown heart failure (Hedera, Petty et al. 2003).

Another disease associated with a mutation in the developmental myosins is Trismus-pseudocamptodacyly syndrome (DA7) caused by a mutation of R674Q in the perinatal myosin gene *MYH8* (Oldfors 2007, Veugelers, Bressan et al. 2004, Toydemir, Chen et al. 2006). This arginine is paralogous to the R672 that can be mutated in embryonic myosin to cause FSS (Toydemir, Rutherford et al. 2006). Symptoms of this myopathy include problems opening the mouth (trismus), short finger flexor tendons leading to involuntary movement of the fingers when the wrist is bent (pseudocamptodactyly) and short leg muscles resulting in foot deformity (Hall, Reed et al. 1982).

Myopathies are complex diseases where little is known how the mutations can cause the severe phenotypes that present. Animal models can only work so far, especially with the cardiomyopathies since mice and rats have a different ratio of MyHC-α and MyHC-β in the atria and ventricles. In fact mice have almost entirely MyHC-α in the ventricle which becomes problematic when investigating human diseases. For example the mutation of R403Q in MyHC-α behaves the opposite to the mutation in MyHC-β (Lowey, Lesko et al. 2008).

Recombinant myosin II is hard to obtain since chaperones are needed for the protein to fold correctly. Using a cell line derived from mouse myoblasts, studies were conducted to investigate the roles of these chaperones (Srikakulam, Winkelmann 1999). A by-product of this was an expression system that could be used to produce recombinant myosin or S1. Using adenovirus' to infect these cells it was possible to produce the human myosin isoforms and mutations for kinetic study (Resnicow, Deacon et al. 2010, Deacon, Bloemink et al. 2012, Bloemink, Deacon et al. 2013, Bloemink, Deacon et al. 2014, Nag, Sommese et al. 2015). It is with this method that was used here to characterise the embryonic myosin isoform as well as disease causing mutations in the MyHC-emb and MyHC-β.

1.4. Stopped-flow Spectroscopy

Stopped-flow spectroscopy is a method of measuring kinetic parameters over very small time scales allowing fast reactions to be monitored. There are advantages to this method over conventional steady state assay in that intermediate products can be observed and their lifetimes measured.

1.4.1. How it works

The stopped-flow spectrometer used in this thesis was produced by TgK Scientific. With this set up there are two drive syringes that are filled with the separate reactants (Figure 1.19). With use of a pneumatic ram the plungers of the syringes are pushed rapidly and simultaneously to expel the reactants by a drive plate. The reactants flow rapidly into the mixing chamber prior to the observation cell where the reaction is measured. The mixing time depends upon the rate at which the samples were pushed and the internal volume of the observation cell.

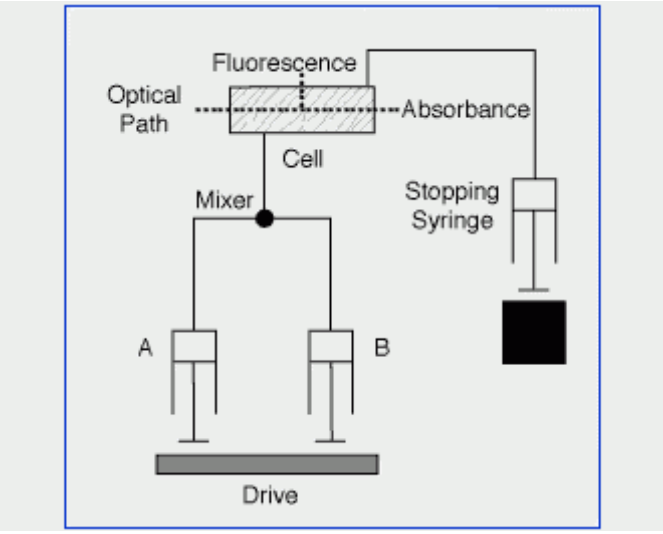

Figure 1.18 – Schematic of the single mixing stopped-flow. Figure from (TgK Scientific 2016)

The stopped-flow can either be used to measure fluorescence or absorbance. For absorbance the optical light path should be used opposite the detector, while for fluorescence the detector needs to be 90° from the light source or the emitted light will be lost in the excitation light.

When the reactants reach the observation cell its volume displaces the previous reactants which travel down a separate waste tube to a third syringe, the stopping syringe. As this fills the plunger strikes a backstop which is linked to a trigger. When this is activated the drive plate stops pushing the two drive syringes ensuring an exact volume of both reactants is mixed. It is always important to remember that the concentration of the reactants inside the observation cell is half of that in the drive syringes.

1.4.2. Uses

As mentioned above, stopped-flow can be used to great effect at measuring very rapid kinetics on millisecond time scales. It also lends itself to be used with either fluorescence or absorbance. While the use of steady state kinetics is invaluable to determine the overall behaviour or a reaction, in this case myosin – the ATPase cycle, transient kinetics determined from the stopped-flow can give insights into the intermediates formed throughout the cycle (De La Cruz, E. M., Ostap 2009).

Transient kinetics rather simply only needs 3 things: (1) a signal/chemical/optical change that can be measured, (2) rapid physical or chemical change that disrupts equilibrium e.g. a concentration or temperature change, (3) the ability to measure the formation of a new equilibrium with appropriate time resolution (De La Cruz, E. M., Ostap 2009).

Stopped-flow therefore lends itself perfectly to measure the rapid kinetics of myosin which can bind ATP, detach from actin, hydrolyse ATP, rebind to actin, and release the products of hydrolysis in milliseconds. Pyrene is fluorescent tag can be chemically attached to actin to allow measurement of the ATPase cycle. When bound to actin the myosin molecule can quench the fluorescence of the pyrene. The increase in fluorescence associated with the myosin dissociation lends itself to measuring the ATPase cycle. By using this increase in fluorescence steps proceeding the dissociation (such as ADP release and ATP binding) and the dissociation step can be measured. Scheme 1.1 show the constants throughout the ATPase cycle that will be discussed in this thesis.

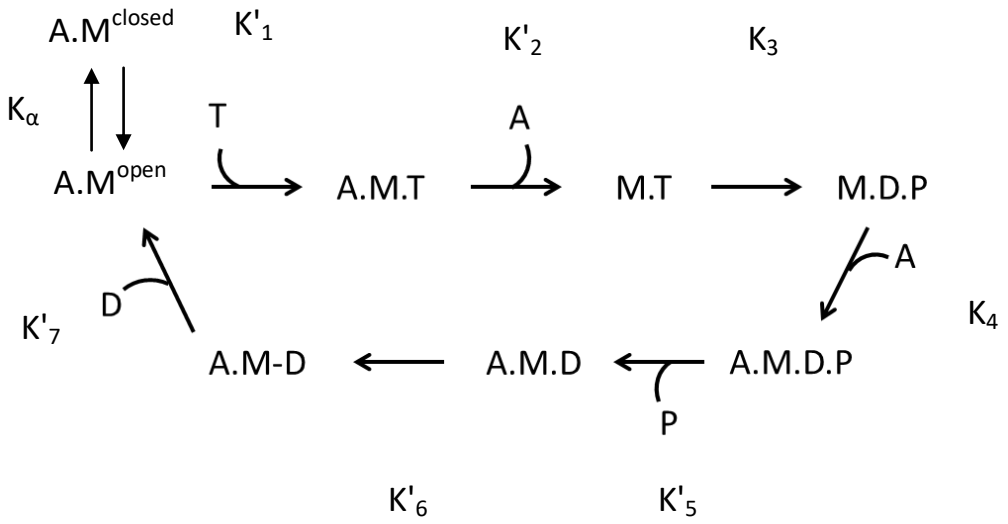

Scheme 1.1 – Myosin ATPase cycle used for the data in table 4.1 and figure 4.9. A = actin, M = myosin, T = ATP, D = ADP, P = phosphate, '.' = tightly bound, '-' = weakly bound. $K_i = k_{+i}/k_{-i}$ for example $K_1 = k_{+1}/k_{-1}$.

The values of K'_1 and K'_2 have significance in highlighting myosins that bind ATP weakly or tightly and quickly or slowly. For example myosins that bind ATP weakly and slowly do so because they have a large and weak K'_1. As such the physiological ATP concentrations can be nonsaturating. Some myosins can which between an open and closed nucleotide pocket (Scheme 1.1). The K'_1 can be shifted due to allosteric communication in actin-attached myosin VI dimmers. Intramolecular load can affect the k'_{+2} of some myosins (De La Cruz, E. M., Ostap 2009).

ATP binding to myosin can be followed by intrinsic tryptophan fluorescence. For most myosins ATP binds rapidly and irreversibly and release phosphate very slowly. Interpretation of this data is straight forward and can be due to one of two things.

1. In a system where there is only a single fluorescence change. ATP induces a change originating from the population of Myosin.ADP.P_i state. The transients are well described by a single exponential and plot of the observed rate constant versus the ATp concentration is hyperbolic with the maximum rate being the sum of the forward and reverse rates of ATP hydrolysis ($k_{+3} + k_{-3}$) (De La Cruz, E. M., Ostap 2009).
2. In a system where there are multiple fluorescence changes. Where the transients are well described by a double exponential the faster state can be described as the

fluorescence change upon ATP binding or population of M*.ATP (where * denotes a fluorescence change) and the slower component is caused by the population of M**.ADP.P_i. In some cases the faster phase can be too fast to be measured by stopped-flow spectroscopy and appears as a single exponetial (De La Cruz, E. M., Ostap 2009).

ADP binding to actomyosin can also be measured using stopped-flow spectroscopy to determine the ADP affinity. Acto.S1 is rapidly mixed with a constant ATP and varied concentrations of ADP. The transients can be described one of two ways:

1. If mixing of the solutions follows a single exponential at all ADP concentrations it is indicative of ADP binding in a rapid equilibrium. As the ADP concentration increases the observed rate constant should become slower.
2. When ADP release is slower than ATP binding and not in rapid equilibrium the transients can be well described by double exponentials with fast and slow phases depending on the ADP concentration when the ATP concentration is held constant. The ADP dependence of the fast phase may depend hyperbolically on the ADP concentration which indicates that ADP binding, much like ATP binding occurs via a teo-step binding process (De La Cruz, E. M., Ostap 2009).

1.4.3. Limitations

While stopped-flow seems ideal for measuring the rapid kinetics of chemical and biochemical reactions there are some drawbacks that need to be considered. The ability to measure a reaction is limited by the dead time which is determined by the end of the mixing and the start of the measurement. In order to reduce the dead time a smaller observation cell can be used to reduce the dead time to below 1 millisecond. Two other limitations are the volume and concentration protein needed to make these measurements.

The concentration of reactants is very dependent on the signal to noise seen in the transients. Some fluorophores behave very well and will provide large amplitudes while others may only give a flat transient. A second consideration is the concentration of the

substrate compared to protein. A substrate concentration is usually 3-fold greater than the enzyme to satisfy a pseudo-first order reaction making analysis simpler than a second-order reaction.

The volume of reactants needed for the stopped-flow assays is a rather fixed volume. Enough volume has to be pushed through the system in each 'shot' to displace the previous 'shot' to avoid any error in mixing. A rule of thumb used is a shot volume 3 times the observation cell volume; therefore for a 5 µL cell as little as 15 µL shot volumes are needed. However using a smaller observation cell can compromise the amplitude and reduce the signal to noise in transients. These are issues that should be addressed to help those wanting to use stopped-flow for the powerful technique it is at determining kinetic parameters but are held back by having low yields or expensive protein.

Another limitation of this method is that the system needs to be kept at a reasonable temperature to prevent leaks from occurring. For example if the temperature were to be changed from 2 °C to 45 °C, the contraction and expansion of the valves would lead to a leak in the system. While specialised equipment exists to measure kinetics at the extremes of temperature, there is no simple solution that allows a broad range of temperatures to be used without having to change cooling or heating equipment. This is therefore something that should be addressed.

1.5. Aim of the project

1. The first aim of this thesis is to develop a modification to the stopped-flow instrument that would allow the assays to be conducted at a constant temperature that is different to the main water bath. This would need to be a simple design that could be adapted to instruments by different manufacturers and could heat or cool the samples before mixing. Most stopped-flow assays are conducted at 20 °C or below to reduce expansion or contraction of valves and therefore cause leaks in the system. Using an external thermal control before mixing will allow biological assays to be conducted at physiological temperatures (e.g. 37 °C) when possible. Investigating this prototype in its efficacy at heating and cooling samples before mixing to a desired temperature will be essential to determine if it is working as designed. Studies have

already shown how temperature affects the ATP induced dissociation of myosin S1 from pyrene-labelled actin (Millar, Geeves 1983, Iorga, Adamek et al. 2007). Comparing the new method to the published data will show how effective this manifold is at adjusting the temperature before mixing rather than having no manifold present.

2. The second aim is to address the largest limiting factor of using stopped-flow, which is the volume of sample needed. By developing an adaptation to the stopped-flow between the drive syringes and observation cell it could be possible to reduce the volume of sample needed. Some protein samples can be very precious, whether due to a low expression, or an expensive process to produce them. Wasting large quantities of these proteins on preparing the system before data collection begins is not desirable. This may even be such a limiting factor that stopped-flow cannot be used and answers to very important kinetic questions not found. This manifold therefore would open the option to used stopped-flow to researchers not previously able to use it.
3. To investigate the effects of the three most common causes of Freeman-Sheldon syndrome on the embryonic myosin, the wild type MyHC-emb will firstly need to be kinetically characterised. Using the recombinant expression system wild type MyHC-emb S1 will be expressed and used in stopped-flow and ATPase assays. This will be compared to the MyHC-β, because both are thought to be slow type myosins, and therefore have similar kinetic features. Using the same recombinant expression system the three mutations; T178I, R672C, and R672H will be individually investigated. The aim is to find a common change in the kinetic parameters compared to the wild type MyHC-emb. The X-ray crystallography structures of the scallop myosin will be used to build homology models of the MyHC-emb as the S1 goes through the cross-bridge cycle. The scallop structures will also be investigated to validate the interactions observed. The mutations will then be inserted into the structures to investigate whether any interactions seen in the wild type myosin are lost. This could give a molecular explanation to how the mutations can affect the cross-bridge kinetics or cause the myopathy.
4. Finally I will investigate the kinetic parameters of the hypertrophic cardiomyopathy mutation that has been identified as a cause of juvenile HCM. A couple of adult HCM

mutations have been characterised previously and showed very small changes in the kinetics (Nag, Sommese et al. 2015, Bloemink, Deacon et al. 2014). Since juvenile HCM presents itself earlier there is the possibility that the mutations are more severe. The aim of this investigation is to observe whether the juvenile HCM mutation H251N is more severe than the adult HCM mutations.

The overall aims of this thesis are to provide better understanding of myosin myopathies. Also to provide new modifications to stopped-flow spectrometers, this will allow future investigations to be conducted in a simple and cost effective manner.

2 Materials and methods

2.1 Materials

2.1.1 Chemicals

ATP	Boehringer
ADP	Boehringer
Pyrene	Molecular Probes
EDTA free protease inhibitor	Roche

All other chemicals and reagents used, including distilled water, were supplied from Melford laboratories, Sigma-Aldrich, or Fisher chemicals. Stock solutions were made using the chemicals for use in buffers.

2.1.2 Buffers

5X SDS-PAGE sample buffer:

0.625 M Tris base, 40 % Glycerol, 10 % SDS, 10% 2 mercaptoethanol, 0.005% Bromophenol Blue

Rabbit S1 digestion buffe:

125 mM KCl, 10 mM KPi (pH 6.2 at RT), 2 mM EDTA, 2 mM DTT

Guba-Straub:

100 mM KH_2PO_4, 50 mM K_2HPO_4, 300 mM KCl, pH 6.6 (at RT)

Myosin storage buffer:

500 mM KCl, 10 mM KPi pH 6.5, and 1 mM DTT + equal volume of glycerol

Lysis buffer:

20 mM Imidazole, 100 mM NaCl, 50 mM Tris pH 7.4, 1 x EDTA free protease inhibitor, 3 mM ATP, 0.5% Tween-20, 1 mM DTT

His-Trap buffer A:

50 mM Tri , 500 mM NaCl, 0.05 % Tween-20, 1 mM DTT, pH 7.0

His-Trap buffer B:

50 mM Tris pH 7.0, 500 mM NaCl, 0.05% Tween-20, 1 mM DTT, 1 M Imidazole, pH 7.0

Acetone powder resuspension buffer:

10 mM $NaHCO_3$, 10 mM Na_2CO_3, and 0.1 mM $CaCl_2$

Actin buffer:

10 mM Tris, 0.5 mM ATP, 0.2 mM CaCl, 1 mM DTT, pH 8.0 (at RT)

Imidazole temperature manifold stopped-flow buffer:

100 mM KCl, 20 mM Imidazole, 1 mM NaN_3, 40 % ethylene glycol, pH 6.5 (at RT)

Cacodylate temperature manifold buffer:

30 – 100 mM KCl, 20 mM cacodylic acid, 5 mM $MgCl_2$, 1 mM NaN_3, (40 % ethylene glycol), pH 7.0 (at RT)

Micro-volume manifold stopped-flow buffer:

100 mM KCl, 25 mM HEPES, 5 mM $MgCl_2$, pH 7.0 (at RT)

Recombinant S1 stopped-flow buffer:

25 mM KCl, 20 mM MOPS, 5 mM $MgCl_2$, 1 mM DTT, pH 7.0 (at RT)

NADH-coupled ATPase assay buffer:

12 mM PIPES, 2 mM $MgCl_2$ and 1 mM DTT, pH 6.8 (at RT)

2.1.3 Hardware and apparatus

Stopped-flow SF-61 DX2

TgK (Hi-Tech) Scientific SF-61 DX2:	TgK Scientific, Bradford-on-Avon, UK
Optical filters:	Schott, Germany
Temperature controlled water baths:	K20, Haake, Germany
	RM6, Lauda-Brinkmann, USA
	2219, LKB Bromma, Sweden

UV-Spectrophotometer

Cary 50 UV	Varian, Germany
Quartz cuvettes	Hellma, Germany

Centrifuges

Eppendorf 5415R	Eppendorf, Germany
Beckman J-26 XP	Beckman, USA
Beckman Optima Ultracentrifuge	Beckman, USA

FPLC

Akta FPLC UPC-900, P-920, and FRAC-950	GE Healthcare, UK
HisTrap HP 1 mL columns	GE Healthcare, UK

Miscellaneous

Weighing scales	Sigma-Aldrich
pH-meter	Sigma-Aldrich
Pipettes	Gilson, USA

2.2 Protein preparation and purification

2.2.1 Rabbit myosin and S1 preparation and purification

The preparation of rabbit muscle proteins, rabbit myosin and rabbit myosin subfragment 1 (S1) was kindly performed by Dr. Nancy Adamek and Sam Lynn.

2.2.1.1 Rabbit myosin extraction

The back and leg muscles from two rabbits were dissected immediately post mortem and stored on ice. After removing all fat and ligaments the muscle was minced using a meat mincer and left to stir in 3 L of Guba-Straub for 30 mins at 4 °C. This was then centrifuged at 5 ,000 rpm using a Beckman JA-10 rotor for 30 mins. The supernatant was used for the myosin preparation while the pellet was used to purify actin and thin filament proteins.

Rabbit myosin was prepared by the same method as Margossian and Lowey (Margossian, Lowey 1982). Supernatant was filtered through a cheese cloth to remove large parts of unhomogenised muscle then through homogenised filter paper to remove fat. The filtrate was added rapidly to 30 L of cold water and left overnight at 4 °C to allow the myosin to precipitate. The water was then siphoned off and the precipitated myosin centrifuged for 45 mins at 5 ,000 rpm. The pellet was re-suspended in 1 L 0.5 M KCl and purified further by adding the myosin solution to 10 L of cold water and left overnight at 4 °C to precipitate the myosin. The supernatant was removed and the precipitated myosin centrifuged for 20 mins at 12 ,000 rpm. At this stage the myosin could be stored at -20 °C by dissolving the pellet in myosin storage buffer.

2.2.1.2 Rabbit myosin subfragment 1 (S1) preparation and purification

Fresh myosin or myosin from a glycerol stock was allowed to precipitate in a large volume of distilled water (dH_2O) overnight. The next day the supernatant was siphoned off and

the remainder centrifuged for 45 mins at 5 ,000 rpm. The pellets were dissolved in the rabbit S1 digestion buffer. Assaying the myosin at this point should give a concentration between 10-20 mg/mL for optimal digestion. The mixture was then warmed to 23 °C and 0.1 mg Chymotrypsin per mL of solution was added and left to stir at 23 °C for 10 mins exactly. To stop the digestion 0.5 mM phenylmethylsulfonyl fluoride (PMSF) was added and the solution left to stir for 10 mins. The digested myosin solution was dialysed against 5 mM KPi pH 6.5 for 12 hours. After dialysis the solution was centrifuged for 1 h at 12 ,000 rpm and the S1 was then purified by use of anion-exchange chromatography on a DEAE-sephacel column (500 mL gel bed volume), which had been equilibrated with 50 mM Imidazole pH 7.0. A KCl gradient of 0-250 mM KCl was used to elute the S1. UV spectroscopy was used to determine the final concentration of the S1 using the extinction coefficient at 280 nm $\varepsilon^{1\%} = 7.9\ cm^{-1}$ for S1 and a molecular weight of 115 kDa (Boussouf *et al*, 2007).

An equal amount of sucrose (w/w) of sucrose could be added to S1 and then freeze dried to allow for long term storage. The S1 powder could then be dissolved in one of the stopped-flow buffers and dialysed into the same buffer to remove sucrose. This solution is stable for 2-3 weeks at 4 °C.

2.2.1.3 Recombinant His-tagged human S1 expression

The expression of the recombinant human myosin S1 proteins were kindly performed by Carlos Vera, Stephen Langers, and Ariana Combs as previously described by Resnicow *et al.* 2010 (Resnicow, Deacon et al. 2010).

Shuttle plasmids containing the coding regions of the *MYH3* or *MYH7* genes (Methionine-1 – Serine-843) were constructed upstream of a 6x-Histidine tag. Using the pAdEasy kit (MP Biomedicals), these plasmids were used to construct recombinant replication-deficient adenovirus that expressed either *MYH3* or *MYH7*. The mutations were created using site directed mutagenesis to produce the *MYH3* R672H, R672C, and T178I mutants and the *MYH7* H251N mutant. HEK293 cells were used to amplify the viral particles, and the cell lysates were clarified using caesium chloride gradients with the concentrated virus being stored in a glycol buffer at -20 °C.

For the culturing of C2C12 cells 4-layer Nunc™ cell factory systems (Thermo Fisher) were used to increase culturing capacity. The C2C12 cells needed to be allowed to differentiate from myoblasts to myotubes. To measure the concentration of virus an OD_{260} = 1.1 x 10^{12} particles per mL was used (Mittereder, March et al. 1996). Infected C2C12 cells were incubated for 5 days then frozen into a cell pellet.

2.2.1.4 Recombinant His-tagged human S1 purification

One cell pellet was incubated at 37 °C for 1 min before addition of 3 mL of lysis buffer. When the pellet was fully defrosted the volume was made up to 18 mL with lysis buffer. The sample was then homogenised using a glass homogeniser (Fisher Scientific) to form a homogeneous solution. The cell lysate was centrifuged at 100 ,000 rpm in the Beckman ultracentrifuge for 20 mins to remove the majority of the cell contents. The supernatant was then filtered through a 5 µm Minisart single use syringe filter (Sartorius Stedim Biotech, Germany) then the volume was made up to 18 mL using lysis buffer. 5 M NaCl was added to the solution to bring the final NaCl concentration to 0.5 M. A His-Trap HP 1 mL nickel column was equilibrated with His-Trap buffer A. The recombinant S1 was added to the column, washed with 20 mL of His-Trap buffer A. The recombinant S1 was then eluted using a 0-1 M stepped Imidazole gradient, eluting from the column at around 350 mM Imidazole using His-Trap buffer B. The fractions were run on an SDS-PAGE gel to find the best fractions to pool. Samples were dialysed overnight into the recombinant S1 stopped-flow buffer. The concentration of the S1 was determined using UV spectroscopy (extinction coefficient at 280 nm $\varepsilon^{1\%}$ = 7.9 cm^{-1} and a molecular weight of 115 kDa (Boussouf *et al*, 2007)). Cell pellets weighing approximately 0.6 g derived from 1,500-3,000 mL would yield between 1-2 mL 10-20 µM active S1. Wild type S1 was stable at 4 °C for up to 2 weeks, addition of equal amount of sucrose (w/w) and stored at -20 °C was kinetically active for up to 4 months.

In order to determine the active concentration of S1 an activity test was performed. In order to do this the S1 concentration is then doubled to observe the relative amplitude also doubles or increases. This is repeated until the relative amplitude remains the same.

Dividing the initial concentration by the overall increase in S1 concentration compared to the start gives the concentration of active S1.

2.2.2 Actin purification and preparation

Acetone powder, F-actin, and pyrene-labelled F-actin were kindly prepared by Dr. Nancy Adamek and Sam Lynn.

2.2.2.1 Acetone powder

The pellet obtained from the first centrifugation from the myosin extraction which contained the actin and thin filament proteins was dissolved in 5 L of buffer containing 4 % $NaHCO_3$ and 0.1 mM $CaCl_2$. This was left to stir at 4 °C for 30 mins. The solution was then filtered through a cheese cloth, and the filtrate discarded. The residue from the filtration step was re-suspended in 1 L of acetone powder resuspension buffer. At room temperature, 10 L of water was added, stirred for 1 min and then filtered a second time, again discarding the filtrate. The residue was dissolved in 2.5 L cold acetone and left to stir for 20 mins. This was filtered through cheese cloth and the filtrate discarded. The process of re-suspending in acetone and filtering was repeated 3 further times until the residue becomes fibrous. The residue was then dried between two pieces of blotting paper for 1-2 days. When the powder was dry it was sieved to form a fine powder and could be stored at -20 °C.

2.2.2.2 F-actin preparation

The method of F-actin preparation is based on the method of Lehrer and Kerwar (Lehrer, Kerwar 1972). 1-2 g of acetone powder was dissolved in 200 mL of cold actin buffer and left to stir for 30 mins. Using a double layer of cotton cloth the mixture was filtered under vacuum and the filtrate, which extracts the actin from the acetone powder leaving behind the tropomyosin and troponin, then centrifuged for 1 h at 30,000 rpm. In order to

polymerise the actin 3 M KCl and 1 M $MgCl_2$ was added to give a final concentration of 100 mM KCl and 2 mM $MgCl_2$. This was left to stir for 1 h after which the solution was centrifuged for 3 hours at 30,000 rpm. The pellet was dissolved into a depolymerising buffer containing 5 mM Tris, 0.2 mM CaCl, 1 mM NaN_3, ph 7.5, homogenised, and dialysed for 12 hours against the depolymerisation buffer. Centrifuging the actin the next day at 30,000 rpm for 1 h removed any remaining filamentous actin. Using UV spectroscopy the actin concentration was determined using the extinction coefficient at 280 nm $\varepsilon^{1\%}$ = 11.04 cm^{-1} and molecular weight of 42 kDa (Toseland and Fili, 2014) with the final concentration being adjusted to 1 mg/mL. 3 M KCl and 1 M $MgCl_2$ was added to the actin to give a concentration of 100 mM KCl and 2 mM $MgCl_2$ and left at room temperature to polymerise. The polymerised actin was centrifuged for 3 hours at 30,000 rpm. The actin pellet was dissolved, homogenised and dialysed for 12 hours in the appropriate experimental buffer (2-500 mM KCl, 20 mM MOPS, 5 mM $MgCl_2$, pH 7.0). Addition of 1 mM NaN_3 prevented the growth of bacteria. The concentration of F-actin was usually between 100-200 µM and could be stored for at least 2 weeks at 4 °C.

2.2.2.3 Pyrene labelling of F-actin

Preparation of pyrene-labelled actin is based on a method by Criddle *et al* (Criddle, Geeves et al. 1985). Pyrene (5 mg/mL dissolved in DMF) was added stepwise to 1 mg/mL F-actin solution while stirring to a final concentration of 0.8-1 % pyrene. The solution was stirred for 12 hours in the dark and then centrifuged at 8,000 rpm for 1 h to remove residual pyrene which precipitates if unbound to actin. The actin was precipitated by centrifugation at 30,000 rpm for 3 hours. The actin pellet was dissolved, homogenised and dialysed overnight against an appropriate experimental buffer (2-500 mM KCl, 20 mM MOPS, 5 mM $MgCl_2$, pH 7.0). Addition of 1 mM NaN_3 prevented the growth of bacteria. The labelled actin was assayed by actin content (extinction coefficient $\varepsilon^{1\%}$ = 11.04 cm^{-1} and molecular weight of 42 kDa) and pyrene (extinction coefficient at 280 nm $\varepsilon^{1\%}$ = 0.22; at 344 nm $\varepsilon^{1\%}$ = 0.233) (Toseland and Fili, 2014). Given that pyrene absorbs at 280 nm this peak will contain both actin and pyrene. To separate these out and determine the percentage of labelling. By subtracting the value for the 344 nm peak from

the 280 nm peak the concentration of actin can be determined. Then by dividing the pyrene concentration by the actin concentration the percentage of labelling can be determined. The final concentration of labelled actin was usually 100-200 μM and the efficiency of labelling was around 90-100 %.

2.2.2.4 Stabilisation of actin with phalloidin

When the concentration of actin is below 1 μM F-actin begins to depolymerise since the equilibrium between F and G actin is pushed towards G-actin. In order to prevent this in stopped-flow assays the actin can be stabilised by the addition of phalloidin (Kurzawa, Geeves 1996). An equimolar stock of 10 μM actin and phalloidin (from *Amanita phalloides*) was prepared as a concentrated stock from phalloidin powder dissolved in dH_2O. The mixture was incubated over night at 4 °C and used within 2-3 days. This has no effect on the properties of actin other than keeping it in the filamentous form (Kurzawa, Geeves 1996).

2.2.3 SDS-Page gel

Pre-cast polyacrylamide gels NuPAGE® Novex® 4-12 % Bis-Tris Gels (1.0 mm thick, 12 or 15 – well) were used to check protein purity after purification.

Sample buffer (5x) containing 2-mercaptoethanol was added to samples and heated at 95 °C for 10 mins before loading. The gels were run in MOPS buffer (50 mL of NuPAGE® MOPS running buffer (20x) (Life Technologies) mixed with 950 mL dH_2O) at 200 V for 45 mins. The gels were then incubated in Coomassie blue staining solution (1 g Coomassie brilliant blue dissolved in 1 L of: 50 % (v/v) methanol, 10 % (v/v) glacial acetic acid, 40 % (v/v) dH_2O). The gels were then transferred to a destaining solution (7% (v/v) glacial acetic acid, 25 % (v/v) methanol, 68 % (v/v) dH_2O) 2-3 times to reveal the protein bands. Proteins of interest were identified by comparison with PageRuler™ unstained protein ladder ranging from 200 to 10 kDa (Fermentas Life Sciences).

2.3 Kinetic measurements

Stopped-flow is a method employed to allow the measurement of fast reaction kinetics on very short time scales. Due to the reactants being mixed rapidly the reaction can be observed and measured from several milliseconds after mixing until equilibrium is reached.

2.3.1 Fluorescent signals

Intrinsic and extrinsic fluorescence were used to measure the kinetics of the stopped-flow reactions.

Intrinsic fluorescence originates from naturally fluorescent groups like certain amino acids within a protein such as tryptophan. Tryptophan fluorescence is very commonly used as it can respond to changes in the local environment. In the case of the myosin subfragment 1 (S1) there is a tryptophan residue located on the end of the relay helix which moves relative to the rest of the molecule through the ATPase cycle. This can be observed by an increase in fluorescence when ATP binds, however the intensity of this fluorescence can vary between myosin classes and even myosin isoforms. The tryptophan was excited at a wavelength of 295 nm with the emission signal detected above 320 nm via a WG320 cut-off filter.

Extrinsic fluorescence derives from an external fluorophore being attached to a protein of interest. For the assays in this thesis pyrene was chemically linked to actin filaments via a Thio-ether bond to the cysteine-374. The binding of myosin S1 to pyrene-labelled actin quenches the fluorescence . The pyrene-actin was excited at a wavelength of 365 nm and the emission detected above 399 nm through a KV399 cut-off filter.

2.3.2 Stopped-flow

The stopped-flow spectrometer used throughout this thesis was a SF-61 DX2 manufactured by HiTech Scientific which was capable of double mixing but only used for

single mixing. The stopped-flow contains two 700 µL sample syringes driven by air-pressure from an external air pressure pump. Both syringes are triggered simultaneously pushing the reactants into an observation cell which is in the optical light path of a high intensity light source. The light source used for these experiments was a Xenon-Mercury lamp. The wavelength used for excitation could be chosen using a monochromator. The fluorescence of the sample was detected via a photomultiplier placed at a right-angle to the incoming light. When the samples reached the observation cell they were mixed in a 1:1 ratio resulting in the concentration of both reactants being halved. As the solution leaves the observation cell it fills the empty stop syringe which forces the syringe to hit a back-stop which immediately ceases the flow. The samples syringes are temperature controlled by an external water bath.

For assays where millimolar concentrations of ADP were used the ADP was pre-treated with hexokinase and glucose to ensure any ATP contamination in the ADP was converted to ADP and would not affect the assay. During the purification of actin and S1 adenylate cyclase, which converts ADP and inorganic phosphate back to ATP, can be purified. P1, P5-Di(adenosine-5') pentaphosphate (Ap5A) was added to the acto.S1 solutions to inhibit any adenylate cyclase activity.

The concentrations of reactants used in the stopped-flow given are those after mixing unless stated otherwise.

2.3.2.1 Transient Kinetics

First order reactions are dependent upon the concentration of only one reactant. While some other reactants may be present they are zero-order and therefore do not affect the observed rate constant. Scheme 2.1 shows the rate law of a first order reaction with respect to A.

$$A \xrightarrow{k} B$$ **Scheme 2.1**

The rate at which A is lost can be expressed as:

$$-\frac{\mathrm{d[A]_t}}{\mathrm{dt}} = \mathrm{k[A]_t} \qquad \text{Equation 2.1}$$

Where k is the first order rate constant with units of s^{-1}.

Integration of equation 2.1 gives the integrated 1st order rate law:

$$\ln [\mathrm{A}]_\mathrm{t} - \ln[\mathrm{A}]_0 = -\mathrm{kt} \qquad \text{Equation 2.2}$$

Where $[A]_t$ is the concentration of A at time t and $[A]_0$ is the initial concentration of A. A rearrangement of this equation gives:

$$[\mathrm{A}]_\mathrm{t} = [\mathrm{A}]_0 \mathrm{e}^{-\mathrm{kt}} \qquad \text{Equation 2.3}$$

All single exponential transients from the stopped-flow were fit to a single exponential equation derived from equation 2.3 using:

$$F = A(1 - e^{-kt}) + c \qquad \text{Equation 2.4}$$

Where: F = fluorescence, A = amplitude, t = time, k = rate constant, c = fluorescence offset. While all the double exponential transients were fitted to a two exponential equation also based off of equation 2.3:

$$F = A_1(1 - e^{-k_1 t}) + A_2(1 - e^{-k_2 t}) + c \qquad \text{Equation 2.5}$$

Where: F = fluorescence, A = amplitude, t = time, k = rate constant, c = fluorescence offset

When dealing with the stopped-flow second-order 1 step reversible and 2 step reversible reactions are used. However these reactions are complex to work with due to there being two variables involved. Therefore pseudo-first order reactions were employed where one reactant is used in large excess (over 5-fold) over the concentration of the second reactant. This ensures that the concentration of the first reactant stays constant and the reaction does not become second-order.

In a second-order 2 step reversible reaction one of the two steps needs to be faster in order to determine the two steps (Scheme 2.2).

$$A.M + T \underset{k_{-1}}{\overset{k_{+1}}{\rightleftharpoons}} A.M.T \underset{k_{-2}}{\overset{k_{+2}}{\rightleftharpoons}} A + M.T \qquad \textbf{Scheme 2.2}$$

Here we make the assumption that step 1 is very fast and that the k_{-2} value is very small. Therefore:

$$\frac{d[MT]}{dt} = [AMT] \times k_{+2} \qquad \text{Equation 2.6}$$

If we then use the equation to find the total concentration of AM we get:

$$[AM]_{total} = [AM] + [AMT] + [MT] \qquad \text{Equation 2.7}$$

Wanting all the AM functions on one side so need to put AM in terms of AMT and MT:

$$K_1 = \frac{[AMT]}{[AM]\cdot[T]} \qquad \text{rearrange} \qquad [AM] = \frac{[AMT]}{K_1\cdot[T]} \qquad \text{Equation 2.8}$$

If we insert equation 2.8 into equation 2.7 we get:

$$[\mathrm{AM}]_{\mathrm{total}} = \frac{[\mathrm{AMT}]}{\mathrm{K_1}\cdot[\mathrm{T}]} + [\mathrm{AMT}] + [\mathrm{MT}] \qquad \text{Equation 2.9}$$

Solving for AMT gives the equation:

$$[\mathrm{AMT}] = \frac{[\mathrm{AM}]_{\mathrm{total}} - [\mathrm{MT}]}{1 + \frac{1}{\mathrm{K_1}\cdot[\mathrm{T}]}} \qquad \text{Equation 2.10}$$

This can be inserted into equation 2.6 which results in:

$$\frac{\mathrm{d}[\mathrm{MT}]}{\mathrm{dt}} = \left(\frac{[\mathrm{AM}]_{\mathrm{total}} - [\mathrm{MT}]}{1 + \frac{1}{\mathrm{K_1}\cdot[\mathrm{T}]}}\right)\mathrm{k_{+2}} \qquad \text{Equation 2.11}$$

This can be simplified to:

$$\frac{\mathrm{d}[\mathrm{MT}]}{\mathrm{dt}} = \frac{[\mathrm{AM}]_{\mathrm{total}}\cdot\mathrm{K_1k_{+2}}\cdot[\mathrm{T}]}{\mathrm{K_1}[\mathrm{T}]+1} - [\mathrm{MT}]\left(\frac{\mathrm{K_1k_{+2}}\cdot[\mathrm{T}]}{1 + \mathrm{K_1}[\mathrm{T}]}\right) \qquad \text{Equation 2.12}$$

The second part of Equation 2.12 can be simplified to:

$$\mathrm{k_{obs}} = \frac{\mathrm{K_1k_{+2}}[\mathrm{T}]}{1+\mathrm{K_1}[\mathrm{T}]} \qquad \text{Equation 2.13}$$

This hyperbola was used to fit the k_{obs} values from the ATP induced dissociation of S1 from pyrene-labelled actin and ATP binding to S1 when observing the increase in tryptophan fluorescence.

When ADP is added to the system there are three processes that need to be taken into account (Scheme 2.3).

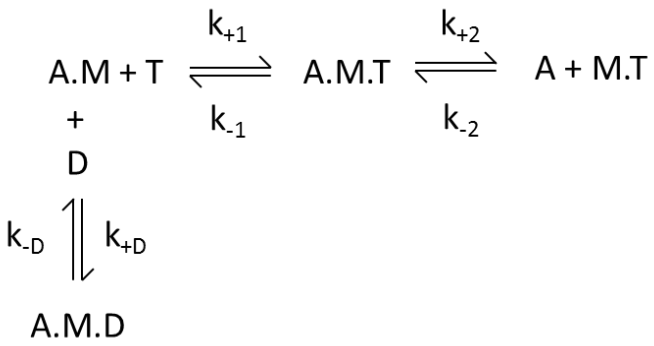

Scheme 2.3

There are two different assumptions that need to be made depending on the behaviour of the S1.

Assumption 1 – Steps 1 and D are fast this gives the same equation as equation 2.13 with the added ADP function:

$$k_{obs} = \frac{K_1 k_{+2} \cdot [T]}{1 + K_1 + \frac{[D]}{K_{[D]}}}$$ Equation 2.14

When the ATP and ADP are in rapid competition for binding and $K_1[ATP] < 1$ then the equation is linear with respect to [ATP].

$$k_{obs} = \frac{K_1 k_{+2} \cdot [T]}{1 + \frac{[D]}{K_{[D]}}}$$ Equation 2.15

If in the absence of ADP $k_{obs} = k_0$ then normalising equation 2.15 would give:

$$k_{rel} = \frac{k_{obs}}{k_0} = \frac{1}{1 + \frac{[D]}{K_{[D]}}}$$ Equation 2.16

This is the normal case for the skeletal myosin class II myosin S1 with actin when using the competition assay.

Assumption 2 – Step D is slow and steps 1 and 2 are fast. In this case we can focus on just the step D (Scheme 2.4). This will result in a fast and a slow phase in the transients.

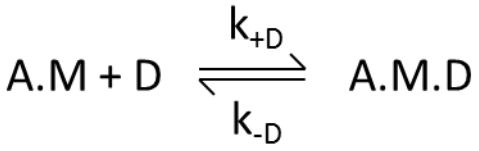

Scheme 2.4

Solving for total AM concentration:

$$[\mathrm{AM}]_{\mathrm{total}} = [\mathrm{AM}] + [\mathrm{AMD}] \qquad \text{Equation 2.17}$$

To get all functions we can use the rate law equation when solving for AMD:

$$[\mathrm{AMD}] = \frac{[\mathrm{AM}]\cdot[\mathrm{D}]}{\mathrm{K_D}} \qquad \text{Equation 2.18}$$

By inserting equation 2.18 into equation 2.17 we get:

$$[\mathrm{AM}] = [\mathrm{AM}]_{\mathrm{total}} \cdot \frac{\mathrm{K_D}}{\mathrm{K_D}+[\mathrm{D}]}$$

$$\frac{[\mathrm{AM}]}{[\mathrm{AM}]_{\mathrm{total}}} = \frac{\mathrm{K_D}}{\mathrm{K_D}+[\mathrm{D}]} \qquad \text{Equation 2.19}$$

When [AM] is proportional to A_{fast} and $[AM]_{total}$ is proportional to A_{max}, Equation 2.19 becomes:

$$\mathrm{A_{fast}} = \frac{\mathrm{A_{max}}\cdot\mathrm{K_D}}{[\mathrm{D}]+\mathrm{K_D}} + \mathrm{A_{min}} \qquad \text{Equation 2.20}$$

Here the A_{min} value only applies if there is a second phase at saturating ADP concentration.

If instead we solve for AM with equation 2.18 rather than AMD we get:

$$[\mathrm{AM}] = \frac{K_D \cdot [\mathrm{AMD}]}{[\mathrm{D}]} \qquad \text{Equation 2.21}$$

When we insert this into equation 2.17 we end up with:

$$[\mathrm{AM}]_{\mathrm{total}} = \frac{K_D \cdot [\mathrm{AMD}]}{[\mathrm{D}]} + [\mathrm{AMD}] \qquad \text{Equation 2.22}$$

Solving for AMD yields:

$$[\mathrm{AMD}] = [\mathrm{AM}]_{\mathrm{total}} \cdot \frac{[\mathrm{D}]}{[\mathrm{D}]+K_D}$$

$$\frac{[\mathrm{AMD}]}{[\mathrm{AM}]_{\mathrm{total}}} = \frac{[\mathrm{D}]}{[\mathrm{D}]+K_D} \qquad \text{Equation 2.23}$$

When [AMD] is proportional to A_{slow} and $[AM]_{total}$ is proportional to A_{max}, Equation 2.23 becomes:

$$A_{\mathrm{slow}} = \frac{A_{\mathrm{max}}[\mathrm{D}]}{K_D+[\mathrm{D}]} + A_{\mathrm{min}} \qquad \text{Equation 2.24}$$

This is a hyperbolic equation that best describes the slow phase of the stopped-flow transients. This biphasic nature is generally seen in the assays for ADP binding to S1 alone without actin.

For actin affinity assays the following equation could be used (Bloemink, Deacon et al. 2014).

$$\alpha = \frac{[M]+K_D+[A]_0 - \sqrt{([M]+K_D+[A]_0)^2 - \frac{4}{[M][A]_0}}}{2[A]_0} \qquad \text{Eq. 2.25}$$

Where: α = fraction of actin bound to S1

[M] = total concentration of myosin or S1

K_D = the dissociation constant of S1 for actin in the presence or absence of ADP

$[A]_0$ = concentration of actin

2.3.2.2 Temperature effect

To investigate the effects of temperature on stopped-flow experiments the assays were repeated in the same conditions with varied temperatures. The thermodynamic parameters, enthalpy and entropy, can be determined by plotting the k_{obs} as a function of temperature.

Plotting the natural log of an equilibrium constant K (lnK) as a function of 1/absolute temperature and can be analysed with the Van't Hoff equation:

$$\ln K = -\frac{\Delta H^\circ}{R} \cdot \frac{1}{T} + \frac{\Delta S^\circ}{R} \qquad \text{where } \Delta G^\circ = \Delta H^\circ - T \cdot \Delta S^\circ \qquad \text{Equation 2.26}$$

Where: R = molar gas constant (8.314 $J.K^{-1}mol^{-1}$), T = Temperature (K), ΔH° = reaction enthalpy (standard state), ΔS° = reaction entropy (standard state)

The intercept of a linear fit of a Van't Hoff plot gives the ΔS° while the slope of the Van't Hoff plot is equal to -ΔH°/R.

An Arrhenius equation can also be used to determine the activation energy of a reaction by investigating the effect of temperature on the rate of reaction.

$$\ln k = \frac{\Delta H^{\ddagger}}{R} \cdot \frac{1}{T} + \frac{\Delta S^{\ddagger}}{R} + \ln\left(\frac{k_B \cdot T}{h}\right) \qquad \text{where } \Delta G° = \Delta H° - T \cdot \Delta S° \qquad \text{Equation 2.27}$$

Where: R = molar gas constant (8.314 $J.K^{-1}mol^{-1}$), T = Temperature (K), $\Delta G^{\ddagger}$ = free energy of activation, $\Delta H^{\ddagger}$ = activation enthalpy, $\Delta S^{\ddagger}$ = activation entropy, k_B = Boltzmann constant (1.3806 x 10^{-23} $J.K^{-1}$), h = Planck's constant (6.626 x 10^{-34} J.s)

In this case $\ln k_{obs}$ is plotted as a function of 1/absolute temperature. The slope of the linear fit is equal to $-\Delta H^{\ddagger}/R$. The activation energy can be easily calculated as it is equal to $\Delta H^{\ddagger}$.

2.3.3 NADH-coupled ATPase assay

The NADH-coupled ATPase assay was conducted by Carlos Vera (University of Colorado, USA).

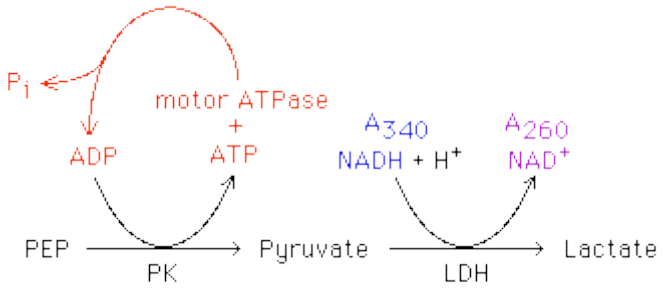

Scheme 2.5

Myosin S1 was added to a mixture of 0.5 mM phosphoenolpyruvate (PEP), 0.05 mg/mL pyruvate kinase (PK), 0.02 mg/mL lactate dehydrogenase (LDH), 0.2 mM NADH, and 0.5 mM ATP. As the myosin hydrolyses ATP to ADP and phosphate, PK transfers a phosphate from PEP to ADP. This creates a new ATP molecule and pyruvate. Therefore the ATP is kept at a relatively constant concentration. LDH converts the pyruvate to lactate by transferring an H^+ from NADH to form NAD^+. Since NADH absorbs at 340 nm the conversion of pyruvate to lactate can be measured. This therefore gives an indirect measurement of the ATPase cycle since ADP concentration drives the formation of pyruvate from PEP. Then in the absence of actin the myosin S1 basal ATPase rate can be measured. Actin is an activator of the ATPase cycle, forcing phosphate and ADP to be

released faster and therefore adding more actin to the mixture increases the ATPase rate. The data can be fit with the Michaelis-Menten equation:

$$v = \frac{V_{max}[S]}{K_M + [S]} \qquad \text{Equation 2.28}$$

Where V_{max} is the maximum rate of the ATPase cycle where the myosin is saturated with actin and K_M is the relationship between the rate of reaction and concentration of actin depends on the affinity of the myosin for actin

The ATPase assays used here were conducted at 25 °C.

3 New methods for measuring kinetic parameters and equilibrium constants

3.1 Temperature manifold

Stopped-flow spectroscopy is a very powerful tool to investigate fast kinetic reactions, being able to measure and record reactions on millisecond time scales. However there are a few draw backs to this method, which include: only being able to operate within a certain temperature window without damaging parts of the machine, and using large volumes of precious sample.

Commercial stopped-flow spectroscopy systems have the capability to be thermostated, usually by an external water bath. This allows reactions to be monitored at a constant temperature. However measuring reactions at temperatures above or below a recommended level can damage the mechanical components of the system. Also adjusting the temperature from one to another can lead to expansion and contraction of drive valves which over time can lead to leaking of these valves resulting in improper mixing i.e. not a 1:1 ratio. Specialist equipment exists provided by manufacturers of stopped-flow systems that allows for very extreme temperatures to be reached, however this is specialised equipment and may not be cost effective. The use of temperature can be valuable when investigating reaction kinetics as at low temperatures it is possible to observe intermediates within a reaction pathway (Travers, Barman 1995, Petsko 2009). A temperature control that can work both above room temperature and close to physiological temperature can be vital in determining the kinetics of a protein and gaining a deeper understanding into its function. As has been shown by Millar and Geeves (Millar, Geeves 1983) that the ATP induced dissociation of myosin S1 from actin is not linear across all temperature points.

The aim of this section is to show using an existing system that a temperature manifold can be used to measure kinetic parameters at temperatures above and below 20 °C. The first aim was to calibrate the efficiency of the thermal transfer. To do this a fluorescent

probe, fluorescein, was be used. From here the shot volumes could be investigated to determine the maximum volume that could be used. From here the manifold would be investigated using the well-established ATP induced dissociation of myosin S1 from actin. This has previously been investigated over a temperature range above and below 0 °C. Using the data from these investigations the design of the temperature manifold could be changed to make it more efficient at adjusting the temperature before mixing, which requires building new prototypes.

The temperature manifold project was published in Analytical Biochemistry in May 2015. This contained just the obtained using ethylene glycol, here a more detailed explanation of how the manifold was tested is given. This includes assays conducted above 0 °C in the absence of ethylene glycol.

Walklate, J., Geeves, M. A. *Temperature manifold for a stopped-flow machine to allow measurements from -10 to +40 °C* Anal. Biochem. 2015. 476: p. 11-16.

3.1.1 Temperature manifold development

In collaboration with TgK Scientific we developed a simple manifold that could be attached to a commercial stopped-flow, in this case a HiTech TgK Scientific SF-61 DX2. Figure 3.1 shows a schematic of the manifold attached to the stopped-flow along with

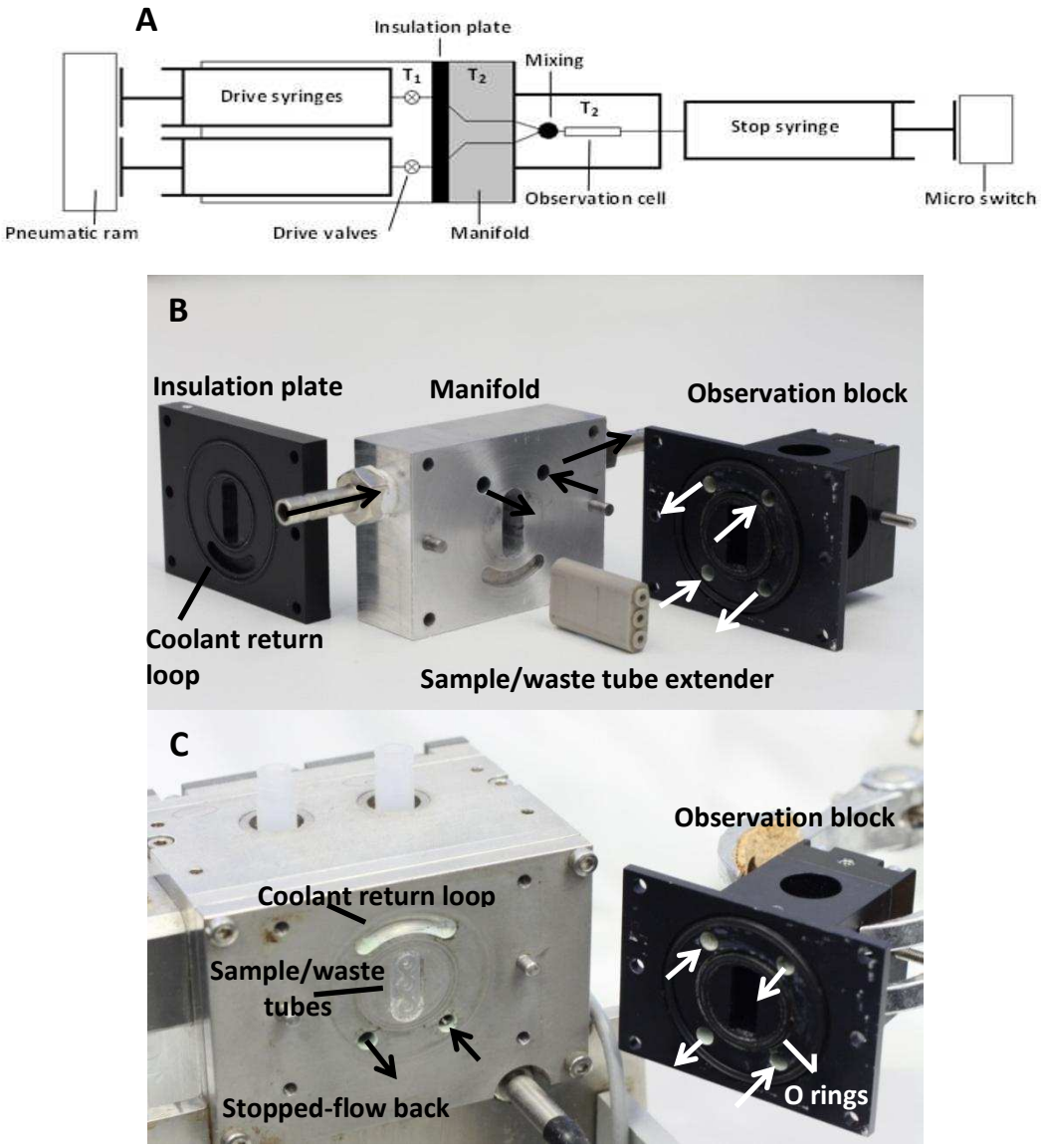

Figure 3.1 – Design of the temperature manifold and how it works in relation to the stopped-flow. (A) A schematic diagram of the stopped-flow with the temperature manifold attachment. (B) The component parts that make up the temperature manifold. The insulation plate, the manifold and the observation block. (C) The interface between the stopped-flow and the observation block.

photos of the manifold component parts and how it fits to the back of the stopped-flow.

The schematic in figure 3.1A shows that the main body of the stopped-flow and the drive syringes which contain the sample prior to being pushed are at the initial temperature T_1. The manifold itself is set at the desired temperature (T_2) and is isolated from the drive block by the insulation plate. The observation cell, where the mixing of the reactants and the reaction is observed is also at T_2.

The insulation plate is a 59 x 45 x 7 mm block of acetal (Figure 3.1B). This has a low-thermoconductivity making it ideal for insulation. The face of this insulation plate has a return loop engraved to return the coolant back into the reservoir. It also has two O-rings to prevent any leaking between coolant and sample. The back of the insulation plate is a flat surface allowing it to join to the back of the manifold.

The manifold itself is made of a 59 x 45 x 20 mm block of aluminium which has a higher-thermoconductivity than acetal and so is better suited for thermal transfer between sample and manifold. The interface between the manifold and the observation block mimics the interface between the stopped-flow and the observation block (Figure 3.1C). Due to the extra space between the back of the stopped-flow and the observation cell an extension tube was required to allow the sample to enter the observation cell and waste to exit. This was made of PEEK (polyether ether ketone) which is inert and is a thermal conductor to acetal.

3.1.2 Calibration of the manifold

In order to calibrate the efficiency of the thermal transfer a fluorescent probe was used. The combination of fluorescein and imidazole was an ideal choice. The pH of imidazole is dependent upon the temperature of its environment, $pK_{Im}/\Delta T = -0.02\ °C^{-1}$ (Burton 2002). The fluorescence of fluorescein however is dependent on the pH of its environment (Chen, Cheng et al. 2008). Therefore as the temperature of the sample changes, so will the pH causing a change in fluorescence from the fluorescein which can be measured. To measure the fluorescence, the fluorescein was excited at 488 nm and detected through an OG530 nm cut-off filter. The buffer used was the imidazole temperature manifold buffer (chapter 2 – 2.1.2 buffers).

It was required to investigate what size shot volumes were suitable and the speed at which the sample got to temperature once pushed. To investigate this 1 µM fluorescein was loaded into both drive syringes and pushed with the manifold being set at different temperatures. The fluorescence was allowed to reach a steady state to determine the fluorescence at different temperatures (Figure 3.2). This was repeated in both the aqueous buffer and the buffer containing 40 % ethylene glycol to measure the difference between the two.

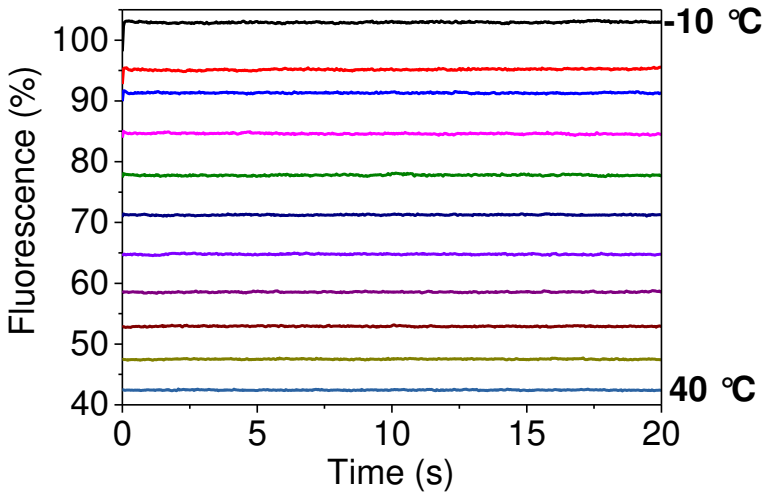

Figure 3.2 – Steady state fluorescence of fluorescein in 5 °C increments from -10 °C to 40 °C

These steady state fluorescence signals were plotted against temperature (Figure 3.3A) which had a linear dependence. The gradient for the aqueous solution was 1.6 %/°C while the buffer containing ethylene glycol had a gradient of 1.2 %/°C.

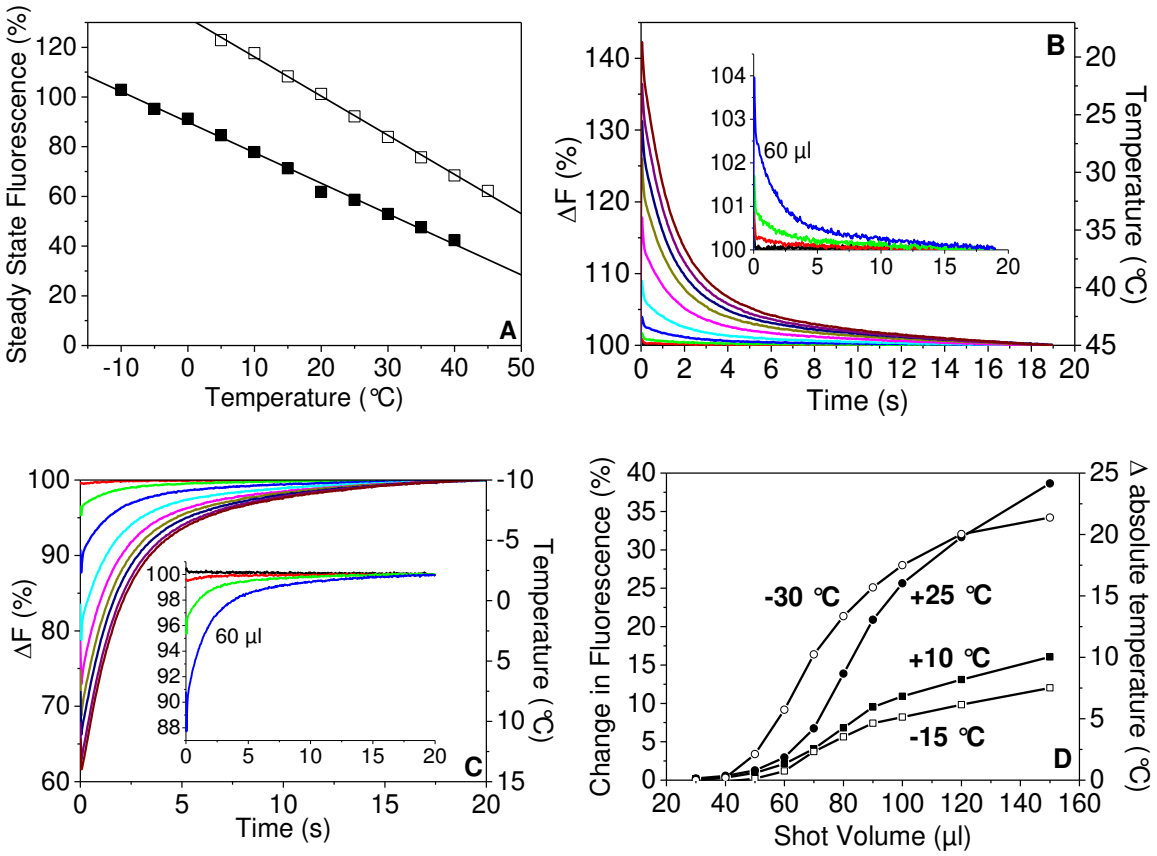

Figure 3.3 – Calibration curves for the temperature manifold. (A) Temperature dependence of fluorescence of 1 µM fluorescein in aqueous solution (open squares) and ethylene glycol (filled square). (B) Varied shot volumes (30 -150 µL) over a 25 °C increase from 20 to 45 °C. (C) Varied shot volumes (same as (B)) over a 30 °C decrease from 20 to -10 °C. (D) The observed fluorescence change for each shot volume at the 4 different temperature changes of +25, +10, -15, and -30 °C to show what temperature the sample is arriving. The change in fluorescence has been converted into a temperature difference.

Using this relationship it was then possible to work out the temperature of the sample based on the fluorescence detected. The next step was to determine the maximum shot volume that could be used to ensure that the sample was at or close to the desired temperature when the reaction was monitored. The shot volume was increased from 30 µL up to 150 µL (including 40, 50, 60, 70, 80, 90, 100, and 120 µL) and the fluorescence was monitored for 20 seconds to allow it to reach a steady state (Figures 3.3B and 3.3C). Figure 3.3B shows how the fluorescence decreases as the temperature increases (from 20-45 °C) but also shows how far away from the desired temperature some shot volumes are at time zero. Figure 3.3C also shows the efficiency of the system at varied shot volumes but this time with a decrease in temperature (from 20 °C to -10 °C). The shot volume assays were repeated 4 times with different temperature changes starting from 20 °C (+10, +25, -15, and -30 °C) to investigate how quickly the temperatures can

equilibrate and what shot volume was best to use. It is worth noting that the assays were carried out in the aqueous buffer, however the 20 °C to -10 °C assay had to contain ethylene glycol since the reaction went below 0 °C. This therefore gave a slightly different shape to the graph in figure 3.3D. Our usual set up when using myosin S1 is to use a shot volume of 60 µL, which can adequately flush out the previous shot from the observation cell. It was therefore encouraging to see that the 60 µL was not very far from the desired temperature.

3.1.3 ATP induced dissociation data at different temperatures

To investigate whether the temperature manifold could work on a real system, the ATP induced dissociation assay was used over a range of different temperatures. This reaction is made of two steps. The first step is the binding of ATP to the actomyosin complex, which is a rapid equilibration of ATP binding. During the second myosin-ATP becomes loosely bound to actin and rapidly dissociates. Previous study (Iorga, Adamek et al. 2007) found that the equilibrium constant of the first step (scheme 3.1, K_1) is thermodynamically unaffected by a change in temperature. The second step (scheme 3.1, k_{+2}) however is strongly affected. The primes (') after the constants indicate that actin is present in the assay.

$$\mathrm{A.M + T} \underset{K_1}{\overset{K'_1}{\rightleftharpoons}} \mathrm{A.M-T} \xrightarrow{k_{+2}} \mathrm{A + M.T}$$

Scheme 3.1 – ATP induced dissociation of myosin from actin. K'_1 denotes the equilibrium constant for ATP binding and k'_{+2} is used to describe the irreversible dissociation of myosin-ATP from actin.

In order to investigate the efficacy of the temperature manifold below 0 °C it was necessary to add 40 % ethylene glycol to prevent the buffer from freezing. However the presence of ethylene glycol weakens the binding of ATP (Millar, Geeves 1983) but leaves the rate of isomerisation unaffected. The buffer used throughout was the cacodylate temperature manifold buffer (Chapter 2.1.2 – section 2.1.2) because cacodylate has a relatively stable pH over a large temperature range and was also used in the previous

investigations (Iorga, Adamek et al. 2007, Millar, Geeves 1983). When used in assays that went below 0 °C, ethylene glycol was added to prevent the buffer from freezing.

The first assay performed was to mix a constant acto.S1 concentration (0.5 µM) against a constant ATP concentration (10 µM) at varied temperatures. Figure 3.4 shows example traces from -6 to +38 °C.

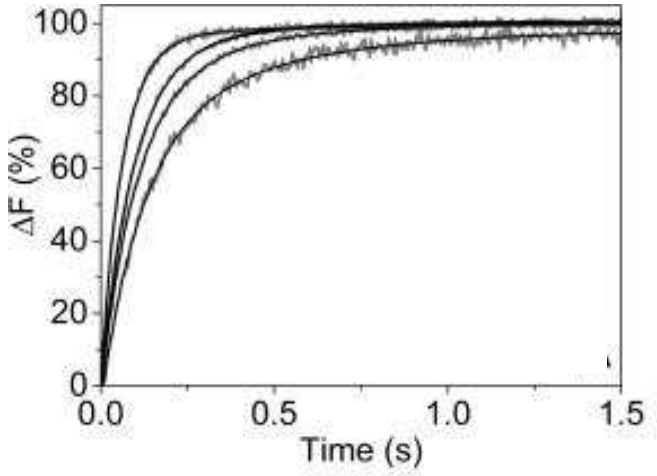

Figure 3.4 – Example traces of ATP induced dissociation at different temperatures. 10 µM ATP was rapidly mixed with 0.5 µM acto.S1. The temperatures shown are -5,7 (slowest transient), -1.4, 3, and 7.3 °C (fastest transient).

All the traces were fit by a single exponential. The observed rate constant (k_{obs}) increased with the temperature as expected.

The next step was to investigate how the temperature of the manifold affected the second order rate constant of ATP binding ($K'_1k'_{+2}$). This is determined by plotting the k_{obs} against the concentration of ATP. At low concentrations of ATP (<100 µM) this can be described by a linear fit which equates to the $K'_1k'_{+2}$.

Figure 3.5A shows the transients of 10 to 50 µM ATP over a temperature range of 6.5 to 37.8 °C in an aqueous solution. The value of $K'_1k'_{+2}$ increased from 2.04 μM^{-1} s^{-1} to 7.66 μM^{-1} s^{-1} indicating that the reaction has a temperature dependence. The values of k_{obs} were then used in an Arrhenius plot to determine the thermodynamic parameters of the reaction (Figure 3.5B).

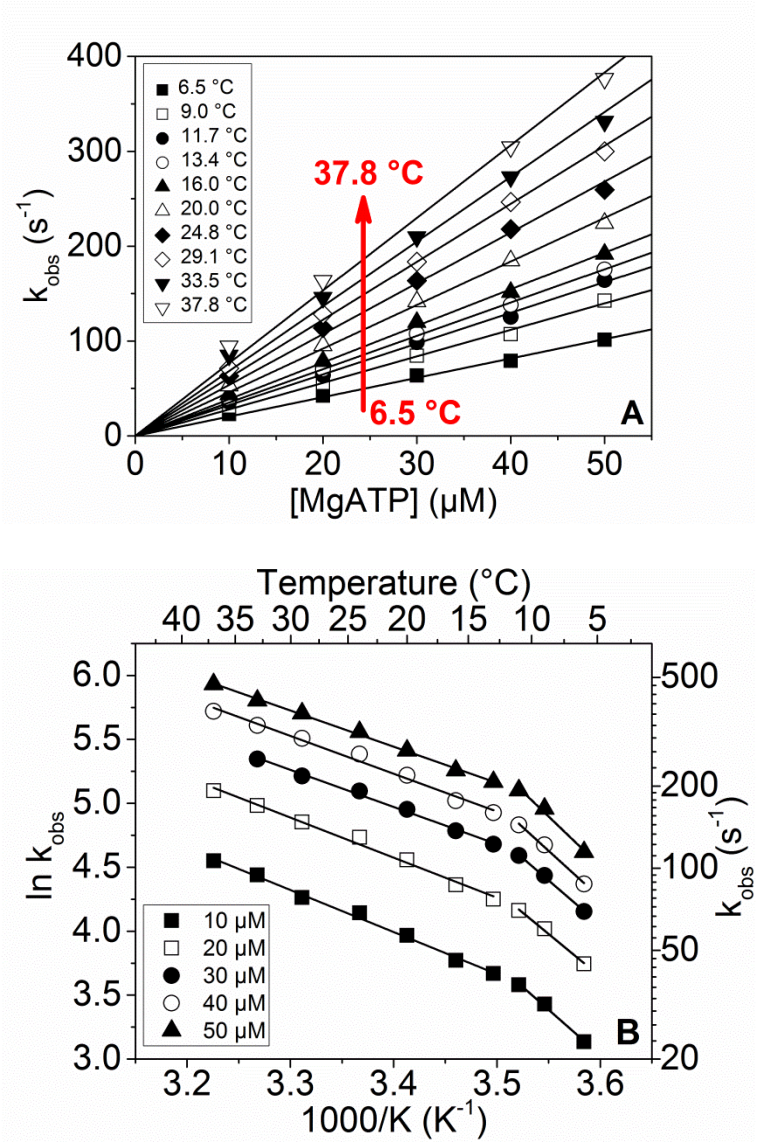

Figure 3.5 – ATP induced dissociation over varied temperatures at low ATP concentrations in an aqueous solution. (A) Linear dependence of k_{obs} at low ATP concentrations from 6.5 to 37.8 °C. (B) Arrhenius plot of the points from panel A to calculate the ΔH^0 of the reaction.

As was expected the linear fits of this plot (Figure 3.5B) were parallel to each other since the activation energy (E_a) remains the same for each concentration of ATP. However upon further examination it was found that the data in the Arrhenius plot did not strictly follow a linear dependence, and could alternatively be fit with a curve as shown here two linear lines with a break point between 11.7 and 13.4 °C. This is comparable to earlier data (Millar, Geeves 1983) and with the general explanation that there is a phase change in the myosin structure causing this nonlinearity of the plot (Anson 1992, Biosca, Travers et al. 1983). The value for the ΔH^0 for figure 3.5B is given in table 3.2.

This assay was then repeated at 5 temperatures, from 6.5 to 16 °C, over an ATP concentration range of 10 to 800 µM (Figure 3.6). At higher concentrations of ATP the plot of k_{obs} becomes hyperbolically dependent and allows for the determination of K'_1 and k'_{+2} by fitting the data with equation 2.13 (Chapter 2.3.2.1). This experiment is only possible at lower temperatures (<20 °C in most cases) as the k_{obs} becomes very fast (>1,000 s^{-1}) at the higher ATP concentrations which becomes hard to measure with current stopped-flow devices. The values for K'_1 (given as $1/K'_1$ to simplify units) and k'_{+2}

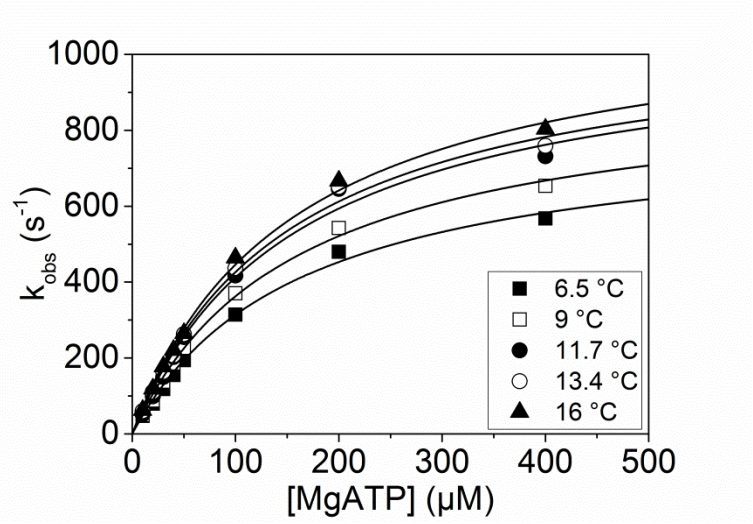

Figure 3.6 – ATP induced dissociation up to high concentrations of ATP from 6.5 to 16 °C.

are summarised in table 3.1.

The values for K'_1 and k'_{+2} were then plotted in a Van't Hoff plot (Figure 3.7A) and Arrhenius plot (Figure 3.7B) respectively to determine the ΔH^0 and ΔS^0 or $\Delta H^‡$ and $\Delta S^‡$ of the reaction which are summarised in table 3.2.

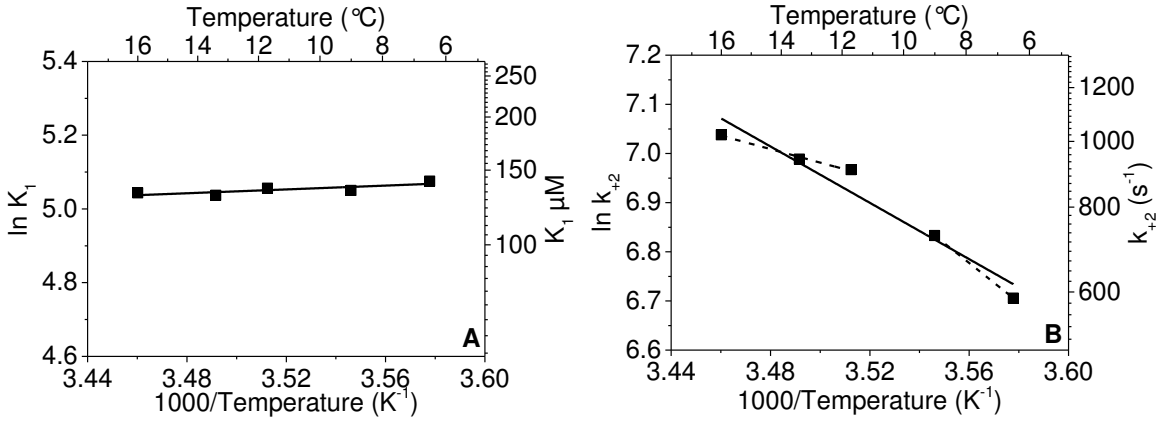

Figure 3.7 – Arrhenius/Van't Hoff plots of the values from figure 3.6. (A) Van't Hoff plot of the $1/K'_1$ values from figure 3.6. (B) Arrhenius plots of the k'_{+2} values from figure 3.6. Two dashed lines have been added to show a potential break point.

To then investigate the capabilities of the manifold at sub-zero temperatures is was necessary to add 40% ethylene glycol to the cacodylate temperature manifold buffer (Chapter 2 – section 2.1.2). This prevented the buffer from freezing at the lower temperatures used, however it also increased the viscosity and as stated earlier (section 3.2.2) the presence of ethylene glycol weakens ATP binding. It was therefore necessary to repeat the above assays with ethylene glycol to compare to previous study (Millar, Geeves 1983).

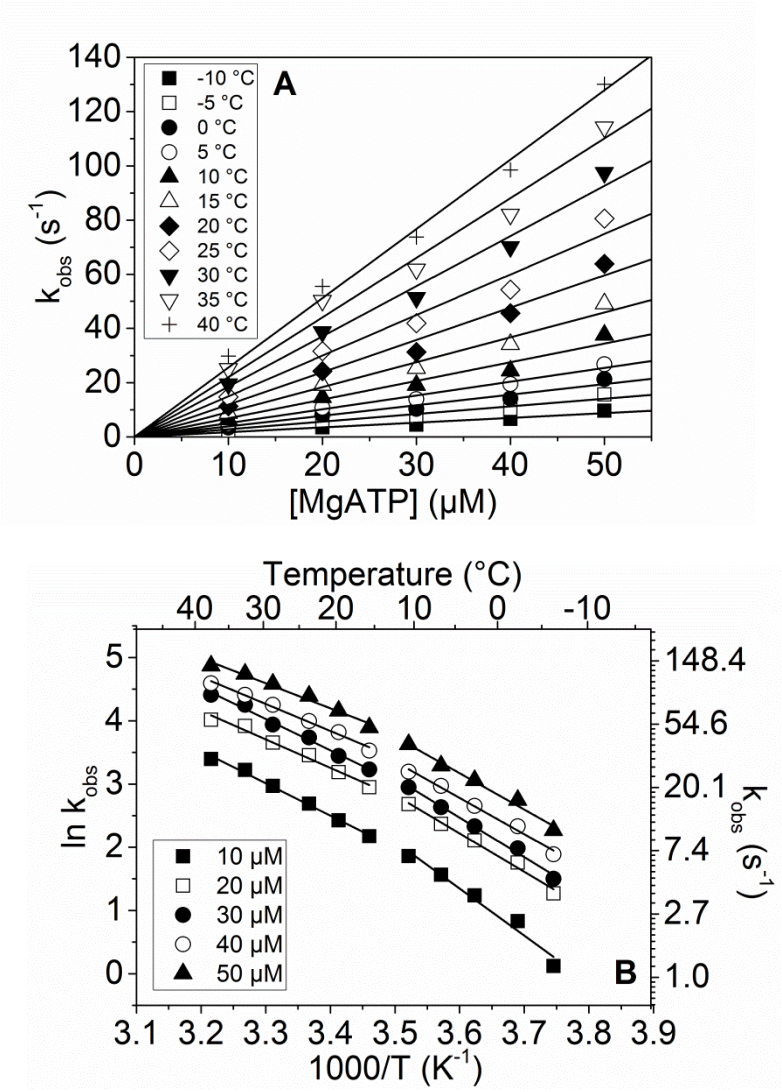

Figure 3.8 – ATP induced dissociation at low ATP concentrations over varied temperatures. (A) Linear dependence of k_{obs} on ATP concentration from -5.7 to +37.8 °C. (B) An Arrhenius plot of the data from panel A to determine the ΔH^0 of the reaction.

Figure 3.8A shows the linear dependence of ATP induced dissociation at low concentrations of ATP over a temperature range of -5.7 to + 37.5 °C. The values for the $K'_1k'_{+2}$ are given in table 3.1. Figure 3.8B shows an Arrhenius plot of the data from the ATP

induced dissociation which again showed a non-linear dependence or a break point between 11.7 and 16 °C. This has therefore been fit with two linear lines, and the ΔH^0 for the two fits are summarised in table 3.2.

As before the ATP induced dissociation assays were then repeated at high ATP concentrations however this could only be done at lower temperatures (-5.7 to 11.7 °C). The k_{obs} again followed a hyperbolic curve (Figure 3.9) allowing for the calculation of K'_1 and k'_{+2}. The values for K'_1 and k'_{+2} are summarised in table 3.1.

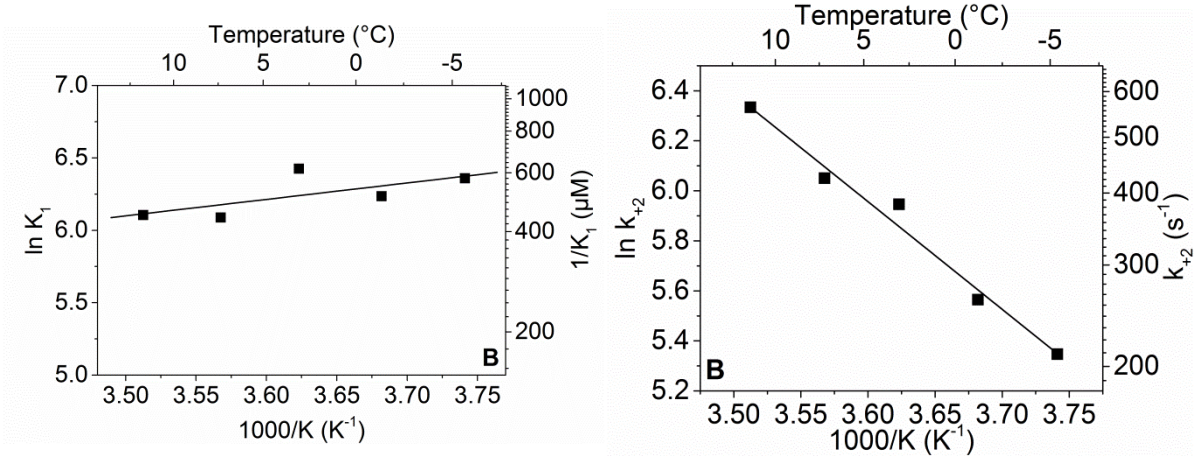

Figure 3.10 – Van't Hoff/Arrhenius plots of the values from figure 3.9. (A) Van't Hoff plot of the $1/K'_1$ values from figure 3.9. (B) Arrhenius plot of the k'_{+2} values from figure 3.9.

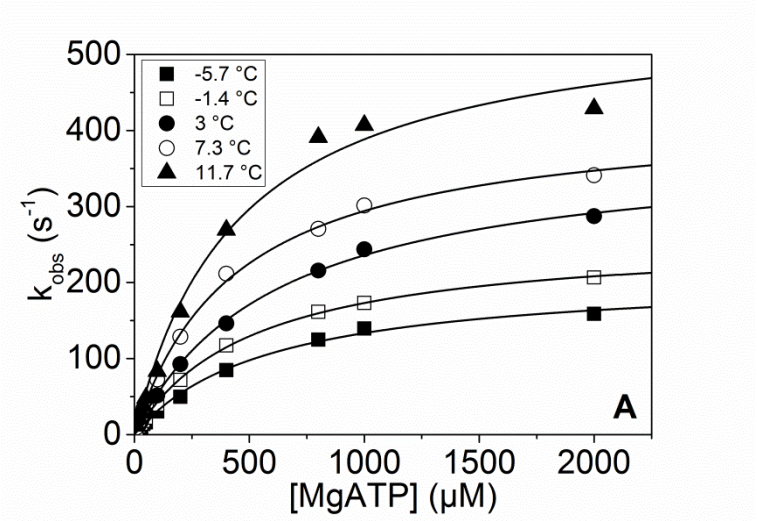

Figure 3.9 – ATP induced dissociation up to a saturating ATP concentration over a temperature range of -5.7 to 11.7 °C.

The values for K'_1 were plotted in a Van't Hoff plot (Figure 3.10A) and the values of k'_{+2} in an Arrhenius plot (Figure 3.10B). From these graphs the ΔH^0 and ΔS^0 or $\Delta H^{\ddagger}$ and $\Delta S^{\ddagger}$ could be determined and is summarised is table 3.2.

Condition	Temperature (°C)	$K'_1k'_{+2}$ (μM^{-1} s^{-1})	$1/K'_1$ (μM)	k'_{+2} (s^{-1})
Aqueous	6.5	2.04 ± 0.03	160 ± 15	817 ± 36
	9.0	2.79 ± 0.04	156 ± 13	928 ± 35
	11.7	3.24 ± 0.04	157 ± 22	1061 ± 70
	13.4	3.51 ± 0.04	154 ± 16	1084 ± 53
	16.0	3.86 ± 0.04	155 ± 12	1139 ± 42
	20.0	4.60 ± 0.07	-	-
	24.8	5.36 ± 0.10	-	-
	29.1	6.11 ± 0.09	-	-
	33.5	6.83 ± 0.15	-	-
	37.8	7.66 ± 0.19	-	-
40 % ethylene glycol	-5.7	0.18 ± 0.01	579 ± 43	210 ± 6.5
	-1.4	0.28 ± 0.01	510 ± 17	261 ± 3.6
	3.0	0.39 ± 0.02	615 ± 29	381 ± 7.6
	7.3	0.51 ± 0.01	439 ± 25	423 ± 9.3
	11.7	0.69 ± 0.03	447 ± 63	562 ± 29
	16.0	0.92 ± 0.03	-	-
	20.0	1.19 ± 0.04	-	-
	24.8	1.50 ± 0.06	-	-
	29.1	1.85 ± 0.05	-	-
	33.5	2.20 ± 0.07	-	-
	37.8	2.56 ± 0.05	-	-

Table 3.1 – Values for $K'_1k'_{+2}$, $1/K'_1$, and k'_{+2} in both conditions at varied temperatures derived from figures 3.5, 3.6, 3.8, and 3.9. Values are those from the fits ± standard error.

		Aqueous buffer	40 % ethylene glycol
Arrhenius plot before break point (-5.7 °C to 10 °C) ($K'_1k'_{+2}$ values)	Gradient (K)	-7.17 ± 0.2	-6.2 ± 0.3
	ΔH^0 (kJ·mol^{-1})	59.6 ± 1.5	51.5 ± 2.5
Arrhenius plot after break point (10 °C to 37.8 °C) ($K'_1k'_{+2}$ values)	Gradient (K)	-3.0 ± 0.08	-4.6 ± 0.2
	ΔH^0 (kJ·mol^{-1})	24.9 ± 0.67	38.2 ± 1.7
Van't Hoff plot (K'_1 values)	Gradient (K)	0.26 ± 0.10	1.14 ± 0.7
	Intercept	4.14 ± 0.37	2.13 ± 2.5
	ΔH^0 (kJ·mol^{-1})	-2.2 ± 0.9	-9.5 ± 5.8
	ΔS^0 (J·K·mol^{-1})	34.4 ± 3.1	17.7 ± 21.0
Arrhenius plot (k'_{+2} values)	Gradient (K)	-2.87 ± 0.4	-4.3 ± 0.3
	Intercept	17.0 ± 1.4	21.5 ± 2.25
	$\Delta H^‡$ (kJ·mol^{-1})	23.9 ± 3.4	35.8 ± 2.9
	$\Delta S^‡$ (J·K·mol^{-1})	141.4 ± 11.8	178.8 ± 10.4

Table 3.2 – Thermodynamic parameters derived from figure 3.5, 3.7, 3.8, and 3.10. Values are those from the fits ± standard error.

3.2 Discussion

With the exception of having to adjust the temperature slightly to get the desired temperature in the observation chamber the temperature manifold appears to work as expected where the sample temperature is rapidly increased/decreased. A correction factor was determined from the temperature induced step ($\Delta T = T_1 - T_2$) versus the temperature immediately after mixing. Therefore the temperature of the reaction ($\Delta T'$) = 0.87 x ΔT, where $\Delta T'$ is the difference between T_2 and the temperature of the sample immediately after mixing. The results obtained from the assays above are very similar to the published data (Iorga, Adamek et al. 2007, Millar, Geeves 1983). For the assays in aqueous solution the values of ΔH^0 and ΔS^0 or $\Delta H^{\ddagger}$ and $\Delta S^{\ddagger}$ can be compared between this study and that of previous work (Iorga, Adamek et al. 2007). Iorga *et al* found that for rabbit psoas S1 the ΔH^0 of K'_1 = -1.9 ± 3.6 kJ.mol^{-1} while here the ΔH^0 = -2.2 ± 0.9 kJ.mol^{-1}. The ΔS^0 = 37.0 ± 12.8 J.K.mol^{-1} while here the value of ΔS^0 = 34.4 ± 3.1 J.K.mol^{-1} for K'_1. The values of both ΔH^0 and ΔS^0 are very similar between the Iorga *et al* data and that shown here with overlapping values when considering the standard error. When comparing the thermodynamic parameters for the k'_{+2} value they are again very similar. The $\Delta H^{\ddagger}$ = 35.7 ± 7.2 kJ.mol^{-1} from Iorga *et al* while here the value of $\Delta H^{\ddagger}$ = 23.9 ± 3.4 kJ.mol^{-1}. The $\Delta S^{\ddagger}$ = 178.7 ± 25.3 J.K.mol^{-1} from Iorga *et al* while here the $\Delta S^{\ddagger}$ = 141.4 ± 11.8. Again the values of $\Delta H^{\ddagger}$ and $\Delta S^{\ddagger}$ are very similar and within each other's range. This gives us great confidence that the manifold is working as expected when using an aqueous solution above 0 °C.

For a comparison between the data presented here and that presented by Millar and Geeves there is a clear similarity in the behaviour of the data presented in the Arrhenius plots. However the values for $\Delta H^{\ddagger}$ are different between the two investigations for reasons unknown. For each ATP concentration there are two distinct linear relationships between rate constant and temperature, one below 10 °C and the other above 10 °C.

The design could be altered as needed to fit other manufactures simply. This will give laboratories that possess stopped-flow equipment, but are not specialising in extreme temperature effects on reaction, an option to explore the effects of temperature on their systems.

3.3 Micro-volume manifold

A limiting factor for many when considering the use of stopped-flow spectroscopy is the large volume of sample needed to obtain consistent reproducible data. One assay using the standard set up would require the use of 300-500 µL of sample per data point. When considering ≈100 µL of samples is used to fill the observation cell and clear the previous reaction this can become very wasteful. Use of a smaller observation cell can alleviate some of these limitations. By reducing the volume of the observation cell, the volume needed to clear the cell also become smaller, as does the volume needed per shot. This does have the drawback that there less fluorescent molecules to fluoresce so the amplitudes will be smaller. Therefore decreasing the volume that is loaded into the system as well as using a smaller cell volume will have a cumulative effect of saving the volume of sample needed.

3.3.1 Micro-volume manifold (MVM) development

The need to reduce the volume of sample needed to perform stopped-flow spectroscopy is very apparent when using samples that are expensive to make and/or yield low amounts of the protein. In collaboration with TgK Scientific we have developed a manifold, similar to the temperature manifold that it is positioned between the back of the stopped-flow and the observation block. The original design was created by Michael Geeves and TgK scientific. The testing of the design and method of loading the micro-volume manifold was performed by myself. The information was then fed back to TgK scientific who redesigned the manifold to the prototype shown in this thesis.

The principle of the design is to reduce the distance between where the sample is loaded and the observation cell. the loading volume can be reduced leading to fewer samples being wasted to set up the stopped-flow. By turning a valve on the MVM the sample could be pulled into the tubing in the stopped-flow spectrometer. Pulling on the stop syringe would normally pull buffer coming from the drive syringe into the stop syringe. However in this case the sample is pulled in instead sandwiched between buffer. When

the sample is loaded it can be pushed into the observation cell by buffer from the drive syringe.

The standard setup requires 3 observation cell volume shots to clear the observation cell of previous reactant/buffer and replace it with the new sample. Since the observation cell is 22.5 µL the volume of sample that should be pushed through the system would have to be 67.5 µL.

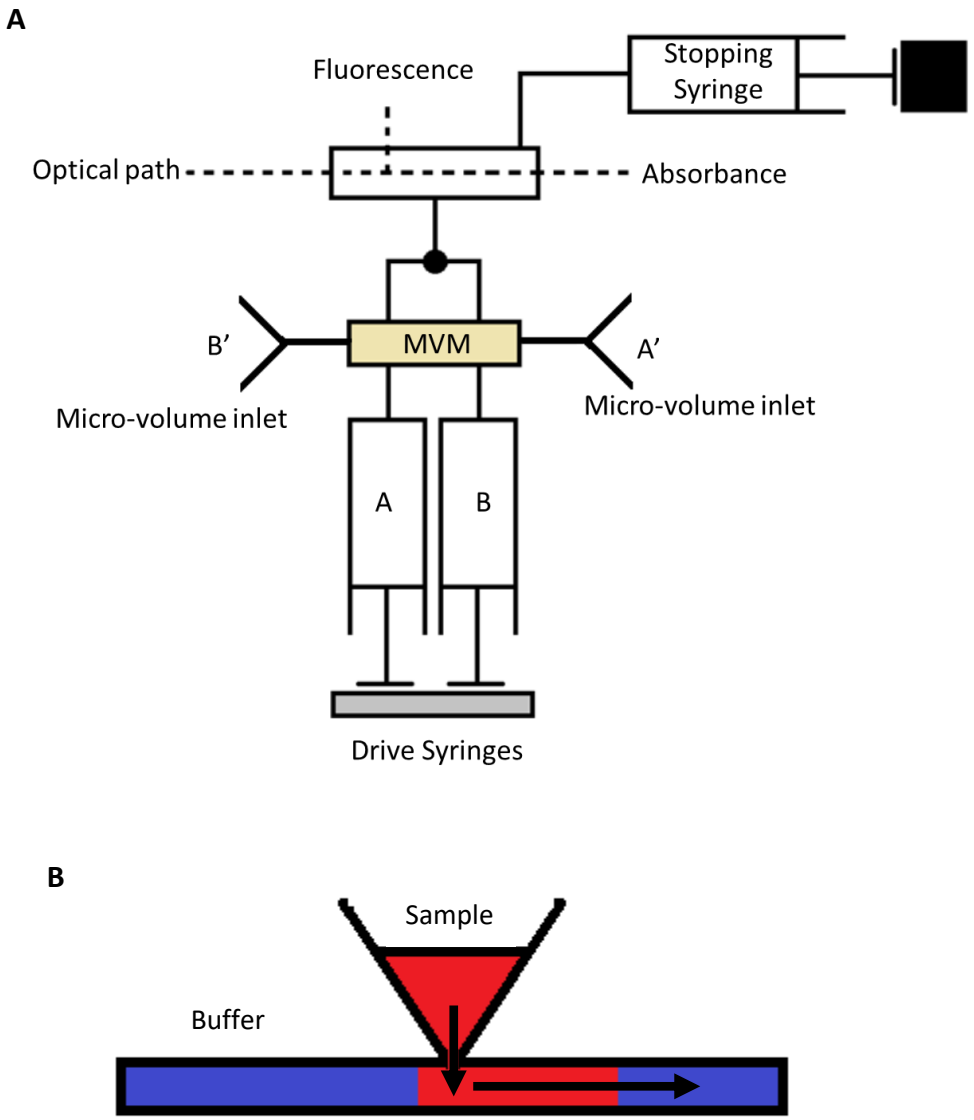

Figure 3.11: A schematic of how the micro-volume manifold fits into the stopped-flow. (A) The inlet cups for the sample on the manifold are represented by two funnel shapes. Given the complexity of the manifold the flow circuit is opposite within the manifold. Therefore the sample that would be added to drive syringe A has to be added on the opposite side, A'. (B) Passage of sample into the tubing in the stopped-flow spectrometer. By turning a valve on the manifold the sample could be pulled into the tubing, then pushed into the observation cell via the drive syringes.

However it is possible to use a shot volume of 60 µL three times to clear the cell giving a total volume wasted of 90 µL from each syringe (30 µL from syringe A + 30 µL from syringe B = 60 µL x 3). Figure 3.11 shows a schematic of where the MVM is positioned in respect to the rest of the stopped-flow and how the sample is loaded.

The MVM is made of a solid block of PEEK (polyether ether ketone) that has two cone shaped cups at the top for loading of the sample in either side (Figure 3.12A). The shape of the loading cups was chosen to reduce the chance of air entering the flow circuit. The manifold fits onto the back of the stopped-flow unit and the observation block attaches to the back of the manifold. Pins on the stopped-flow drive unit interlock with holes in the MVM and pins on the MVM lock into holes on the observation block. This is further secured with screws to help make the seal water tight. The sample and waste tubes are also surrounded by small O rings to form a water tight seal between stopped-flow and manifold and observation cell. On the sides of the MVM (Figure 3.12A and B) are two valves that allow the samples to be loaded and also prevent the sample from flowing straight into the observation cell. Lastly the sample and waste tubes on the MVM create a seal with the tubes on the stopped-flow to transfer sample through the MVM to the observation cell.

Assys using the MVM were compared to the standard set up of the stopped-flow spectrometer. This consisted on the observation block attached to the back of the stopped-flow drive unit without the MVM in place. The temperature was kept constant at 20 °C using an external water bath using a 5 µL observation cell. S1 or acto.S1 was loaded into one drive syringe and ATP into the other. For the MVM assays ATP was still in one of the drive syringes while buffer was loaded into the other drive syringe. S1 or acto.S1 was loaded into the drive unit via the MVM. The temperature could not be maintained by an external water bath and therefore was subject to the temperature of the room which varied between 20-23 °C.

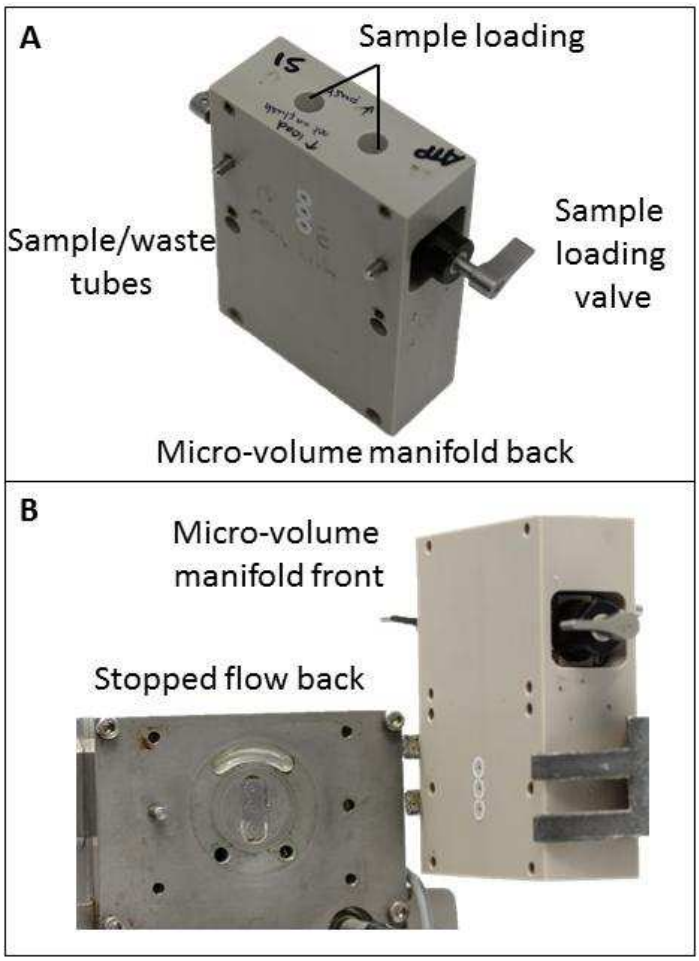

Figure 3.12: The micro-volume manifold and how it joins on to the stopped-flow. (A) A photo of the top, back and side of the MVM. (B) The interaction between the stopped-flow and the MVM.

3.3.2 Load volume calibration

Since the aim of this attachment is to reduce the volume of sample needed a 5 µL observation cell was used. The light path for this observation cell is the same as that of the 22.5 µL cell. This meant that to effectively clear the cell of the previous sample then a minimum of 15 µL would be needed as 3x the observation cell volume can adequately clear the cell of the previous shot. A 20 µL shot volume was used (10 µL from syringes A and B). This required setting the stop syringe to fill up to 20 µL before hitting the back stop and triggering the stopped-flow to start recording the data.

It was necessary to determine what volume to load into the stopped-flow from the MVM. To do this a volume of S1 greater than that loaded (for example 100 µL pipetted, 80 µL

loaded) was pipetted into the cup on the MVM that was labelled S1. This extra volume allowed for any error associated with pipetting and prevented any air being pulled into the system.

The desired volume was then loaded into the stopped-flow (this method is for filling just one side of the MVM). In order to do this; firstly the valve on the manifold must be in the load position with the drive valve in the drive or waste position, not flush. To pull the sample into the system the stop syringe had to be emptied by turning the stop valve to waste (if not already done so) then pushing the syringe up to eject the waste. Next the stop valve needed to be turned to drive and the stop syringe pulled down to the back stop thus filling this syringe. This will have pulled 20 µL of the sample from the manifold into the flow circuit. This process of filling and emptying the stop syringe can be repeated as many times as needed to load the desired volume. The stopped-flow was then used as normal using buffer in the drive syringe used for the S1 which pushed the S1 into the observation cell. 20 'shots' were used to determine whether there was a delay in the sample reaching the observation cell, and also how many traces containing protein could be obtained with the volume loaded.

The tryptophan fluorescence assay was investigated using the MVM setup. It relies on a tryptophan residue at the end of the relay helix in the S1 domain moving relative to the rest of the molecule. The signal from the tryptophan fluorescence is much smaller than that seen for the pyrene-actin (Figure 3.4) and will test the limits of the MVM. Tryptophan fluorescence is also a more widely used fluorophore and therefore is more applicable to most researchers.

80, 100, or 120 µL of rabbit myosin S1 was loaded into the system via the MVM as described above. The drive syringe, which would normally contain the S1, was filled with the micro-volume manifold stopped-flow buffer. The other drive syringe was filled with 20 µM ATP. The stopped-flow was then triggered 20 times to monitor the fluorescence amplitude and determine how many similar transients could be obtained before the S1 was completely washed out (Figure 3.13). As the protein was washed out the fluorescence signal was too. Therefore the fluorescence amplitude decreased as the protein was replaced with buffer.

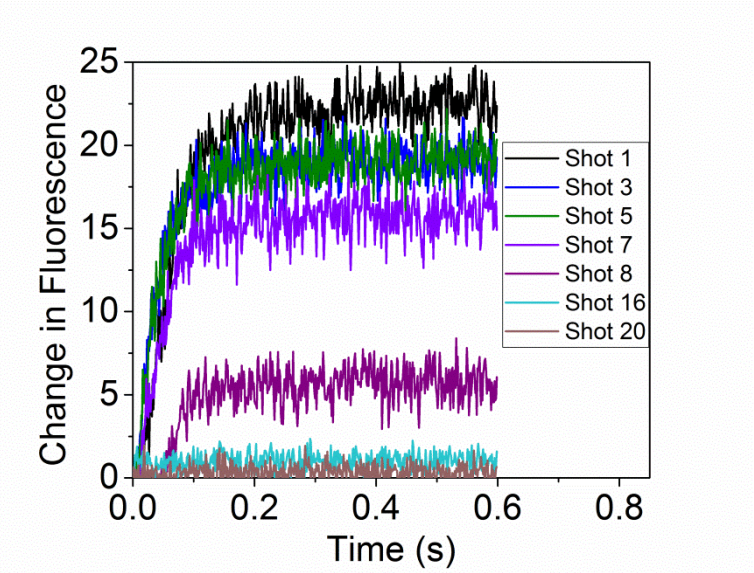

Figure 3.13 – 120 µL 0.5 µM rabbit myosin S1 rapidly mixed with 10 µM ATP. ATP was loaded into the drive syringe as per the standard stopped-flow method while buffer was loaded in the other drive syringe. 120 µL of 1 µM S1 was loaded into the flow circuit via the MVM before 20 'shots' were pushed. A selection has been displayed to show that the initial 6-7 transients contain protein and have high amplitudes. After this the protein concentration rapidly decreases as it is replaced with buffer reducing the fluorescence change to zero.

Figure 3.14 shows a comparison of the parameters from the standard stopped-flow method to the MVM with a load volume of 80, 100, and 120 µL. The values of k_{obs}, amplitude, maximum fluorescence/end point, and relative amplitude would ideally be similar to the standard method. Figure 3.14A shows the observed rate constant (k_{obs}) from the standard method, and the different load volumes. Here the values should all be similar since the concentration of ATP (which k_{obs} is dependent on) is unchanged. However as the S1 is being washed out the trace becomes harder to define and so the k_{obs} will become less reliable. However the values of k_{obs} are similar to the values of the standard method up until shot 15. Figure 3.14B shows the fluorescence amplitudes of the two methods. After 6-7 shots the amplitude begins to reduce to 0 as the S1 is washed out. Figure 3.14C is similar to figure 3.14B but this time shows the maximum fluorescence signal (end point). The amplitudes and end points are larger for the MVM for an unknown reason. Figure 3.14D shows the relative amplitude ((amplitude/end point) x 100) for the two methods. This value is very useful when the end point is moving. Overall the amplitude, end point, and relative amplitude all show that the MVM works for the 3 volumes loaded (80, 100, and 120 µL) up until shot 7. After this they all begin to decrease

which will make fitting the data harder and therefore makes the k_{obs} less reliable. The 80 µL load volume while possible showed some variability in the first few shots for the amplitudes, end points, and relative amplitudes suggesting that not all the sample has reached the observation cell from the first shot. There is therefore still buffer between the sample and the observation cell in the case of 80 µL of sample added. For the 100 and 120 µL load volumes this buffer has passed through the observation cell and from the first shot there is sample in the observation cell. It would then be prudent to use either 100 or 120 µL to load the stopped-flow.

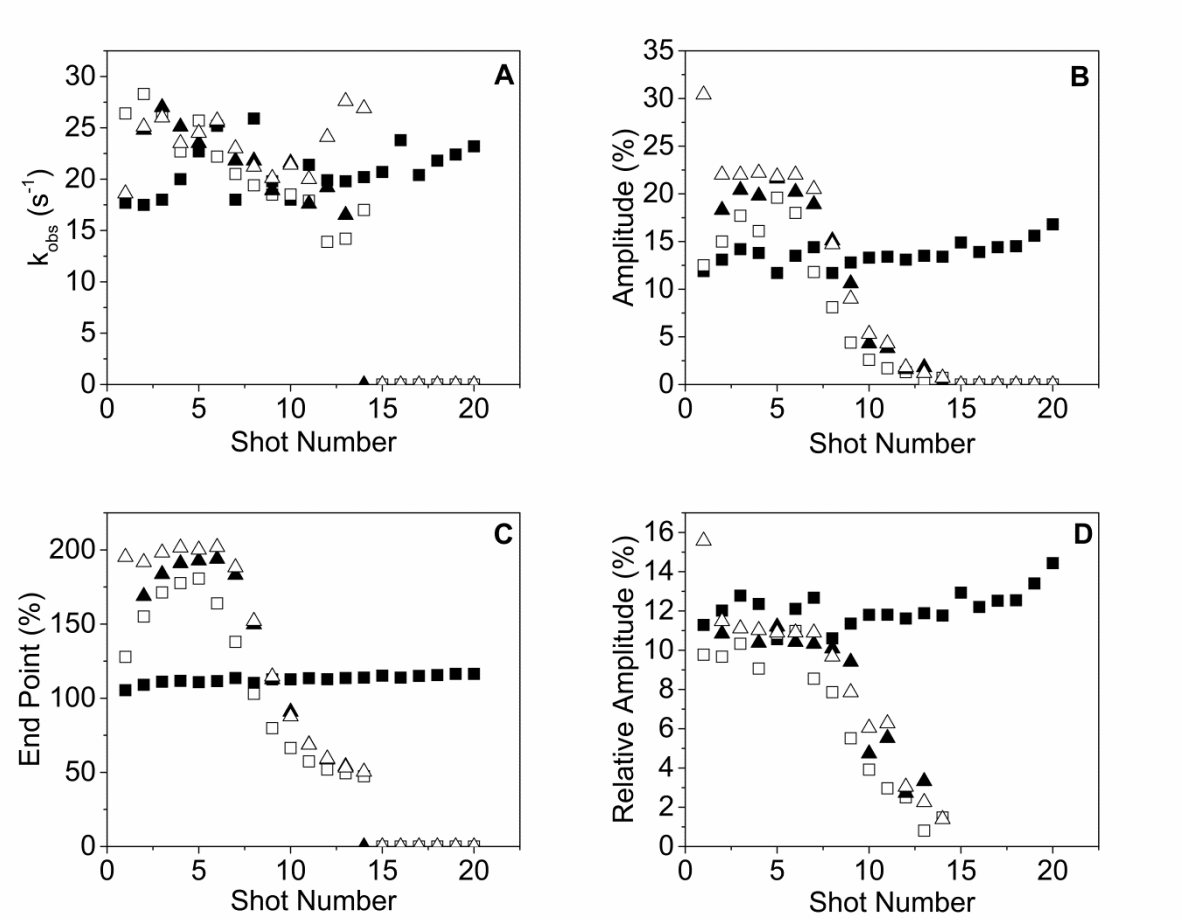

Figure 3.14: Different load volumes of myosin S1 (0.5µM S1) versus 10 µM MgATP. Filled squares – standard method, open squares – 80 µL load volume, filled triangles – 100 µL load volume, open triangles – 120 µL load volume. (A) The observed rate constant over 20 shots for the standard method versus MVM. (B) Fluorescence amplitude over 20 shots for the standard method versus MVM. (C) Maximum fluorescence (end point) for standard method and MVM. (D) The relative fluorescence amplitude ((Fluorescence amplitude/end point) x 100) for the standard method versus MVM.

This test was repeated for its suitability with myosin S1 in complex with pyrene-labelled actin (Figure 3.15). The same load volumes were used as for tryptophan fluorescence assays (80, 100, 120 µL). The k_{obs} values (Figure 3.16A) were higher in the MVM

measurements compared to the standard setup. This was largely due to the MVM not being thermostated with a water bath as the standard method. Given that the room temperature varied and in some instances was warmer than the standard method the reaction had a faster rate constant.

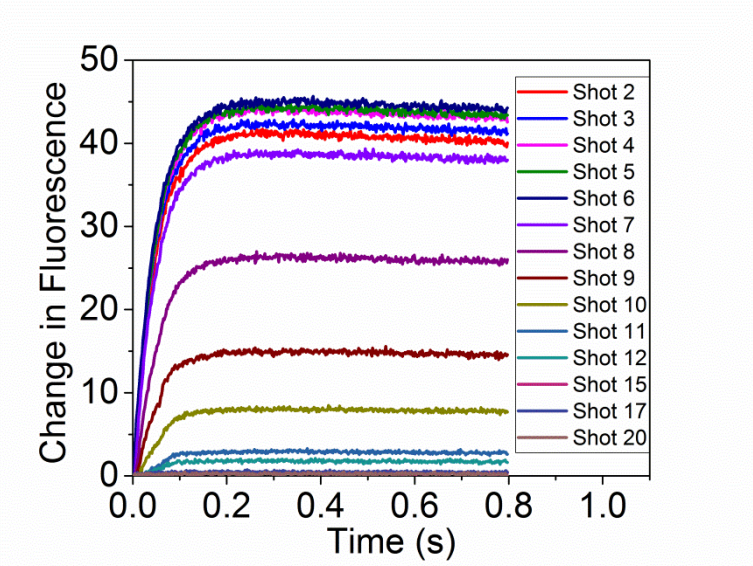

Figure 3.15 – 120 µL 0.5 µM rabbit myosin S1-pyrene actin (pA.S1) rapidly mixed with 10 µM ATP. ATP was loaded into the drive syringe as per the standard stopped-flow method while buffer was loaded into the other drive syringe. 120 µL of 1 µM acto.S1 was loaded into the flow circuit via the MVM before 20 'shots' were pushed. A selection of transients are displayed to show that the protein is present at a high concentration in the first 6-7 shots. The change in fluorescence decreasing shows the acto.S1 washing out of the system and buffer is replacing it.

Figure 3.16B shows the amplitude per shot similar to figure 3.14B. However in this case the amplitude was lower than the standard method, again the reason for this in unknown. Figure 3.16C shows the end points similar to figure 3.14C, and similar to the amplitudes the MVM shots have a lower end point. In both figure 3.16B and C there is a decrease in the fluorescence after shot 7, which is the same observation as for the tryptophan fluorescence. Figure 3.16D shows the relative amplitude of the pyrene-actin.S1 and similar to figure 3.14D the relative amplitude decreases after shot 7.

Both of these figures suggest that it is possible to obtain 7 shots that are similar to the standard setup using the MVM using 80, 100, or 120 µL load volumes. However if the variable being measured is the amplitude as is the case for the actin affinity measurements (K_A) then 120 µL load volume would be best since all 7 shots are very similar.

One potential cause for the difference in k_{obs} for the tryptophan and pyrene fluorescence assays is a lack of thermoregulation in the MVM. The temperature of the assay was dependent upon the temperature of the room and if this increased as the investigation proceeded then the k_{obs} would also increase. The air conditioning of the room was set to 20 °C however this may not have kept the room at a constant temperature.

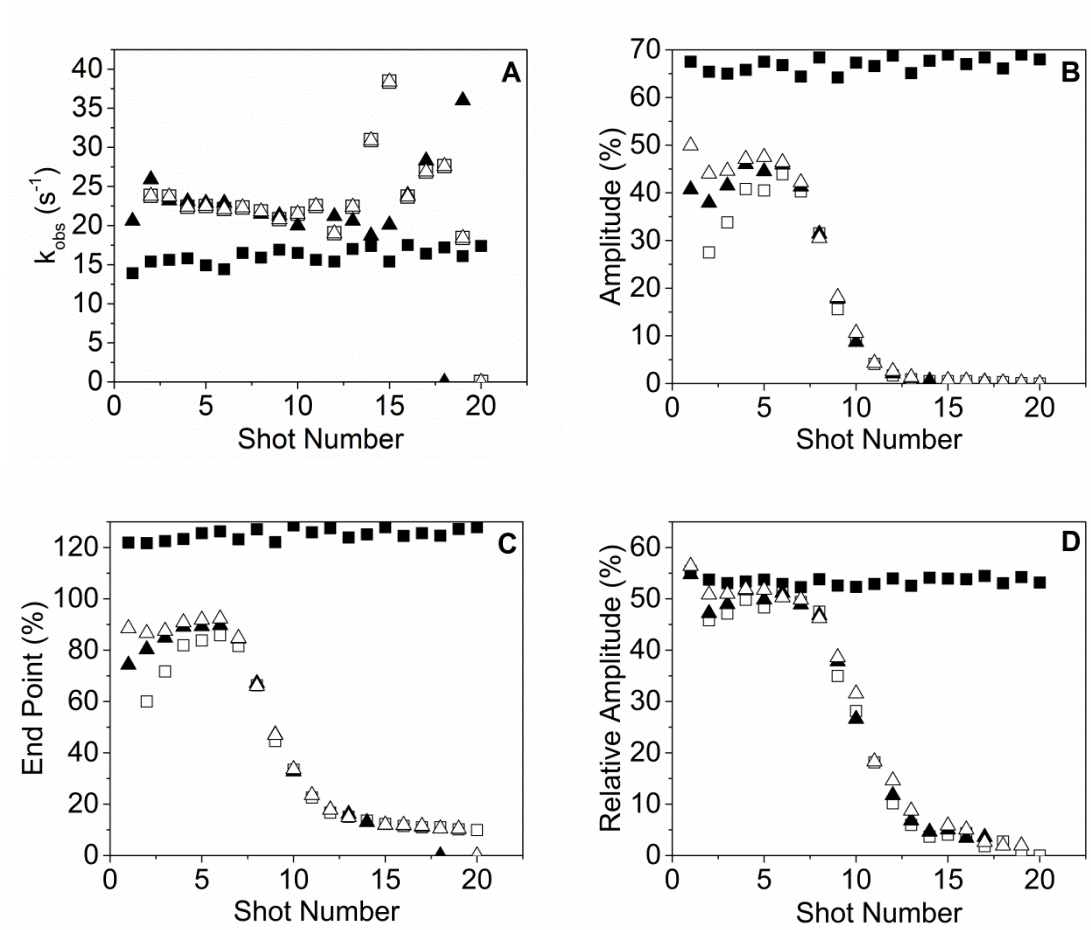

Figure 3.16: Different load volumes of myosin S1-pyrene actin (0.5µM pA.S1) and standard method versus 10 µM MgATP. Filled squares – standard method, open squares – 80 µL load volume, filled triangles – 100 µL load volume, open triangles – 120 µL load volume. (A) The observed rate constant over 20 shots for the standard method versus MVM. (B) Amplitude over 20 shots for the standard method versus MVM. (C) End point for standard method and MVM. (D) The relative fluorescence amplitude for the standard method versus MVM.

3.3.3 Determining the actin affinity using the micro-volume manifold

Having established that the micro-volume manifold worked as intended, it seemed prudent to test its efficacy compared to the standard set up using an established assay.

Kurzawa *et al* (Kurzawa, Geeves 1996) previously demonstrated that the actin affinity of myosin S1 could be determined by using a fixed concentration of actin (30 nM) preincubated with increasing concentrations of S1. This can then be rapidly mixed with ATP in the stopped-flow to induce dissociation. Plotting the relative amplitude against the concentration of S1 before mixing it is possible to determine the actin affinity using equation 2.25 (Chapter 2.3.2.1).

Kurzawa *et al* found the affinity of actin to be 44 nM using their method and could measure the K_A using concentrations as low as 10 nM pyrene-labelled actin. This was possible by using phalloidin which stabilises actin in the F-actin state allowing the ability to work at lower concentrations of F-actin. In the Kurzawa *et al* investigation they used a 20 µL observation cell, while here a 5 µL cell volume was used to reduce the shot volume needed (from 60 µL to 20 µL). The drawback to using the smaller observation cell is the reduced fluorescence amplitude due to the smaller volume of sample and smaller volume of excitation, which will result in less fluorescence emission. Therefore a higher concentration of pyrene-labelled actin was used to acquire adequate fluorescence.

This assay was conducted with the MVM at an actin concentration (before mixing) of 50 nM (Figure 3.17). This was done to assess whether this assay was suitable to be used with the MVM. The concentration of actin was chosen since it was unknown how sensitive the stopped-flow would be with the MVM attached due to any possible dilution of the sample with buffer either side when in the flow circuit. As can be seen from figure 3.17 the first concentration of S1 (10 nM) had a relative amplitude of ≈10 % which increased to ≈45 % at 1 µM S1.

Figure 3.17A shows the traces of S1 (of varied concentrations) preincubated with 50 nM phalloidin-stabilised pyrene-labelled actin after being rapidly mixed with 20 µM MgATP. As more S1 is added to the actin more of the pyrene is quenched before mixing. When ATP binds and induces the dissociation the pyrene is exposed and fluoresces. This leads to an increase in fluorescence as the initial background fluorescence decreases. This figure has been normalised to the same start point to make it easier to see the overall change in fluorescence. In reality they would have the same end points as this is the maximum fluorescence which is dependent on the actin concentration. The relative amplitudes (defined by dividing the change in fluorescence by the end point) were then fit as a

function of S1 concentration (figure 3.17B) which can be described by the quadratic equation (eq. 3.1). Three repeats have been shown here to highlight the reproducibility of the assay. The average value of K_A = 44.8 ± 5.3 nM, very similar to the value determined in Kurzawa *et al*.

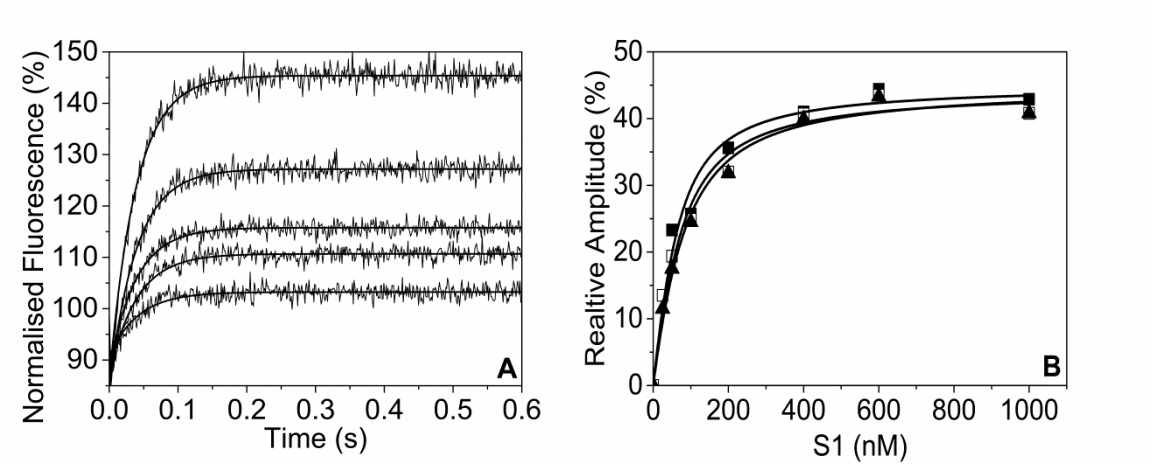

Figure 3.17: Actin affinity of rabbit psoas S1 preincubated with 50 nM actin rapidly mixed with 20 µM MgATP using the MVM. The S1 concentration was varied from 0 to 1 µM. (A) Averaged traces from one assay of the actin affinity. Each trace can be best described by a single exponential which has been shown on the transients. Each transient has been normalised to the start point to make observing the overall change in fluorescence easier. (B) The relative amplitudes were then plot as a function of S1 concentration and fit with the quadratic equation (eq. 3.1). Three repeats have been shown to demonstrate the accuracy of the measurement with the MVM. The individual values of K_A determined are 35.6 ±9.1 nM, 44.8 ± 11.1 nM, and 53.9 ± 9.6 nM. This gave an average K_A = 44.8 ± 5.3 nM. All concentrations given are those before mixing since the actomyosin complex is being measured rather than the rate of dissociation.

Having determined that the MVM was suitable to use for this assay at 50 nM pyrene-labelled actin it seemed necessary to attempt the assay at the actin concentration used for most actin affinity assays, 30 nM. This is the concentration used in the original paper and is the concentration of actin used in chapters 4, 5, and 6 to determine the actin affinities. Figure 3.18A shows the traces from an actin affinity assay similar to figure 3.17A. The relative amplitudes were then plotted against the S1 concentration (Figure 3.18B) similar to figure 3.17B. This gave an average K_A value of 45.5 ± 2.6 nM which is both similar to the value at 50 nM actin and the Kurzawa *et al* value.

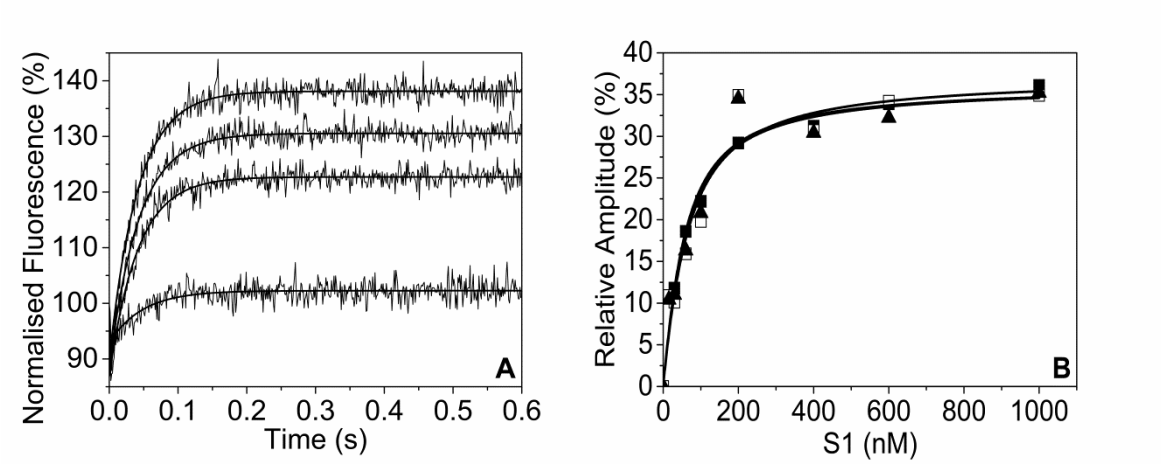

Figure 3.18: Actin affinity of varied rabbit psoas S1 preincubated with 30 nM actin rapidly mixed with 20 µM MgATP using the MVM. The S1 concentration was varied from 0 to 1 µM. (A) Averaged traces from one actin affinity assay. Again each trace was best described by a single exponential which are shown with a solid line. These traces have also been normalised to the start point. (B) Quadratic fit of the relative amplitude versus the S1 concentration. All three repeats have been shown with individual K_A values of 41.7 ± 7.7 nM, 50.5 ± 16.9 nM, and 44.2 ± 13.9 nM. This gave an average K_A value of 45.5 ± 2.6 nM. All concentrations are again those before mixing.

If these assays were to be conducted using the standard method then 3.5 mL of S1 would be needed (500 µL x 7 S1 concentrations). Using the MVM this volume was reduced to just over 1 mL at 1.05 mL (150 µL x 7 S1 concentrations, where 120 µL is loaded with 30 µL spare to prevent air getting into the system). 80 µL load volume could be used however the first shot did not contain the full concentration of protein. Therefore this method is 3 times more efficient and allowed the assay to be repeated in triplicate using the same volume as would be needed for one assay using the standard set up.

3.4 Discussion

3.4.1 Micro-volume Manifold

As stated above the major limiting factor of using stopped-flow spectroscopy assays is the large volume of sample needed. The standard setup would require 300-500 µL of sample to acquire several repeated traces that could be averaged and give a repeatable set of values. Using the micro-volume manifold with a 120 µL load volume (with 150 µL pipetted and 120 µL loaded) allows the operator to use half to a third the sample needed to produce 6-7 similar traces. This could not only save time and sample in running these assays, but also money in producing less of a protein, or being able to do multiple assays from a sample that could only be used on one.

In a similar assay using pyrene-labelled actin at 15 nM, Kurzawa and Geeves (Kurzawa, Geeves 1996) found the actin affinity to be 44 nM. The assays here were conducted with either 50 or 30 nM pyrene actin resulting in a K_A = 44.8 ± 5. nM and 45.5 ± 7.7 nM respectively. This method therefore gives comparable results to not using the MVM whilst using a third of the volume when using 500 µL for the standard setup. The possible limitation of this investigation is the use of the micro-volume observation cell (5 µL). Using a smaller volume of fluorophore will reduce the fluorescence signal which drove the decision to use a higher concentration of pyrene-actin. However given more time it would be useful to investigate whether a concentration as low as 10 nM pyrene-actin could result reliable data.

There are several sources of error with this investigation that Kurzawa and Geeves identified. One error is an incorrect protein concentration calculation which may result from an unknown fraction of inactive protein. Activity test are conducted on the rabbit S1 after it has been dialysed to get a more accurate estimation of the active S1 concentration compared to that measured from UV/vis spectroscopy. A second error could occur as a result of the phalloidin used to keep the actin in the filamentous state. However Kurzawa and Geeves investigated the effects of phalloidin on the K_A when investigated at high actin concentrations (2 µM) where little G-actin is expected. Here they found that the phalloidin had little effect on the K_A (Kurzawa, Geeves 1996).

3.4.2 Conclusions

The MVM is still an early prototype with some issues that would need to be addressed before it could be released as a commercial product. One of these is the lack of a thermostatic control on the manifold which means that the temperature the reaction is recorded at cannot be controlled. However the manifold functions as intended by reducing the volume loaded into the stopped-flow whilst providing data similar to that obtained using the standard setup.

4 Characterisation of wild type embryonic skeletal muscle myosin S1

4.1 Introduction

During mammalian foetal development, three skeletal heavy chain myosin isoforms have been shown to be expressed: embryonic (MyHC-emb), perinatal/neonatal (MyHC-peri), and β-slow/cardiac (MyHC-β) (Schiaffino, Rossi et al. 2015). MyHC-emb was first identified by Whalen *et al*. (Whalen, Schwartz et al. 1979) in 1979 although some earlier studies had hinted at the existence of the developmental myosins. The genes responsible for the expression of MyHC-emb and MyHC-peri are MYH3 and MYH8 respectively (Wydro, Nguyen et al. 1983, Periasamy, Wieczorek et al. 1984) and are located on the same chromosome (11 for mouse, 17 for human) as the adult fast skeletal myosin isoforms (Leinwand, Saez et al. 1983). The sequence identity of the MyHC-peri show high similarities to the adult fast skeletal isoforms (MyHC-IIa, -IIb, and –IIx, Figure 4.1) while the MyHC-emb has the most divergent sequence.

Myosin head domain

MyHC-β	MyHC-β						
MyHC-α	92.22	MyHC-α					
MyHC-IIx	83.12	83.74	MyHC-IIx				
MyHC-IIa	82.85	83.62	94.69	MyHC-IIa			
MyHC-IIb	82.68	83.60	96.13	94.26	MyHC-IIb		
MyHC-peri	83.96	84.29	95.24	95.68	94.24	MyHC-peri	
MyHC-emb	83.21	83.55	87.59	88.62	87.45	89.32	MyHC-emb

Myosin tail domain

MyHC-β	MyHC-β						
MyHC-α	94.43	MyHC-α					
MyHC-IIx	81.77	80.57	MyHC-IIx				
MyHC-IIa	82.22	81.11	95.81	MyHC-IIa			
MyHC-IIb	81.22	80.11	92.98	91.70	MyHC-IIb		
MyHC-peri	80.84	80.00	91.61	91.97	89.05	MyHC-peri	
MyHC-emb	78.98	78.96	83.46	83.82	82.08	83.46	MyHC-emb

Figure 4.1 – Human sequence identities of the two cardiac (MyHC-β and MyHC-α), three adult fast skeletal (MyHC-IIx, MyHC-IIa, and MyHC-IIb) and two developmental (MyHC-peri and MyHC-emb) myosin isoforms. The upper table shows the identities within the head (motor) domain, while the lower tables shows the tail of the molecule.

Little is known about the expression patterns of the developmental isoforms in humans due to the ethical considerations in obtaining samples of foetal muscle tissue. Therefore we have had to rely on animal models as a guide for the expression of these myosins.

MyHC-emb has been identified in birds and fish however the majority of work has been carried out in rats and mice. In the mouse in situ hybridisation has detected transcripts of MyHC-emb from 9.5 days post-coitum (Lyons, Ontell et al. 1990). The upregulation of these genes is thought to be controlled by myogenic factors MyoD and Myf5 which are involved in muscle differentiation (Beylkin, Allen et al. 2006). The expression of MyHC-emb appears to vary depending on the developmental stage of the fibre. For example in rats MyHC-emb is co-expressed with MyHC-β in primary generation fibres (the first fibres formed (Narusawa, Fitzsimons et al. 1987, Rubinstein, Kelly 1981)). However the secondary generation fibres express MyHC-emb and MyHC-peri (Condon, Silberstein et al. 1990).

The developmental isoforms have been shown to be down regulated after birth and replaced by an upregulation of the adult fast isoforms (MyHC-IIx, MyHC-IIa, and MyHC-IIb). In the rat, this occurs a few days after birth (DeNardi, Ausoni et al. 1993), however in the mouse, transcripts can be detected before birth (Lu, Allen et al. 1999). However the levels of protein in new born mice shows the developmental isoforms are still dominant (30 % MyHC-emb and 70 % MyHC-peri) (Agbulut, Noirez et al. 2003).

In humans primary generation fibres form around week 8 while secondary generation fibres emerge around week 10 becoming the dominant fibre at week 21 (Fidzianska 1980). By week 9 the MyHC-emb, MyHC-peri, and MyHC-β transcripts can be detected (Figure 4.2). All the primary fibres express MyHC-emb and MyHC-β (Barbet, Thornell et al. 1991, Draeger, Weeds et al. 1987) initially, with the expression of MyHC-β decreasing from 75 % at week 10 to 3 % at week 21 which correlates with secondary fibres becoming dominant at this time (Cho, Webster et al. 1993). Secondary fibres begin to express MyHC-emb at week 12, and MyHC-peri later (Cho, Webster et al. 1993). Similar to the rat and mouse models the developmental isoforms are downregulated leading up to and after birth and are replaced by the adult fast skeletal isoforms (Figure 4.2).

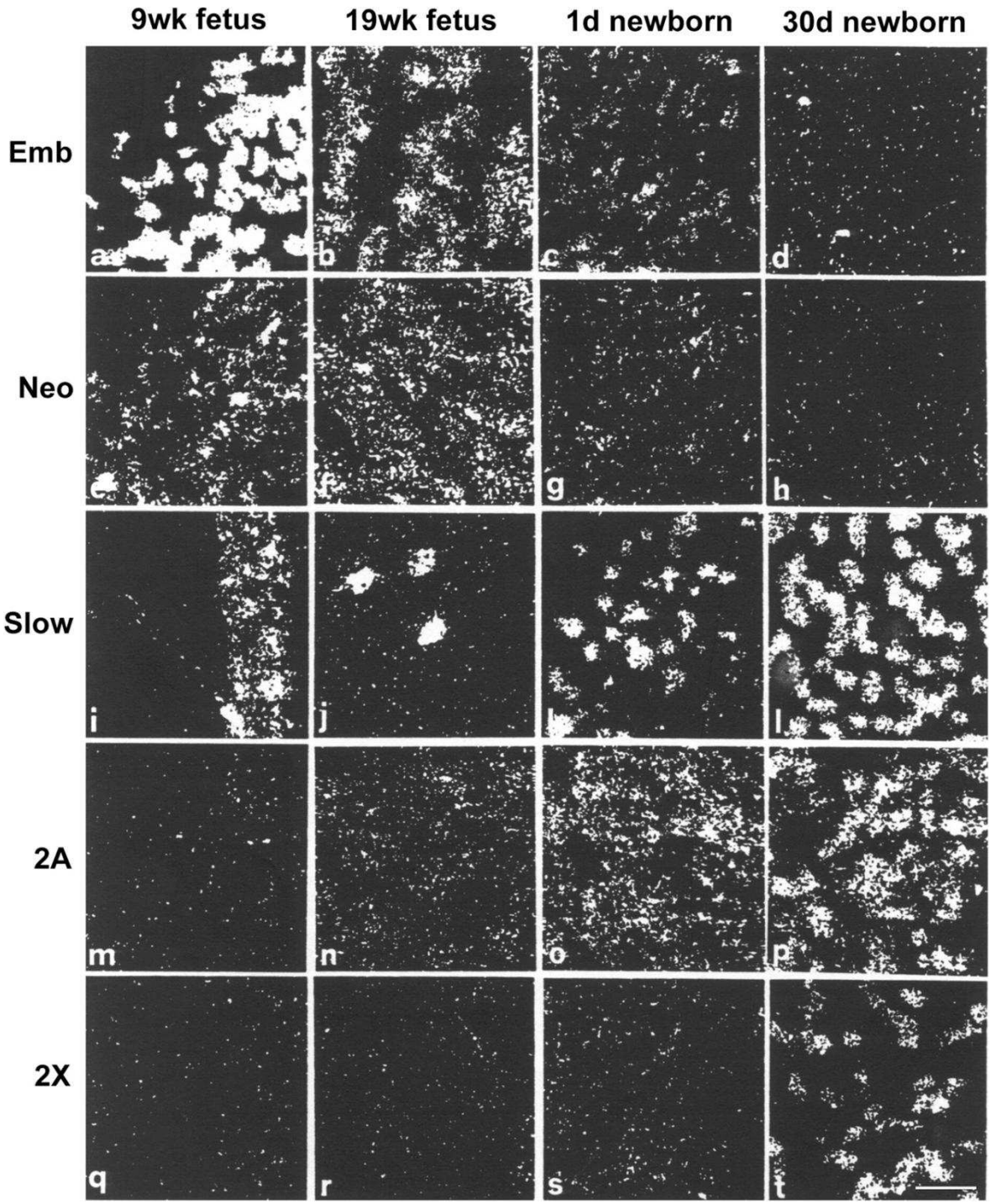

Figure 4.2 – Transcripts of myosin heavy chains in developing human muscle. In situ hybridisation probes were used to detect the following MYH genes: *MYH3* (MyHC-emb, a-d), *MYH8* (MyHC-peri, e-h), *MYH7* (MyHC-β, i-l), *MYH2* (MyHC-IIa, m-p), and *MYH1* (MyHC-IIx, q-t). Quadriceps femoris muscles were from 9- and 19-week old foetuses while vastus lateralis muscles were from 1-day- and 1-month-old new born. Scale bar = 30 µm and is the same across all figures Figure from (Smerdu, 2002).

MyHC-emb is thought to be a slow type myosin similar to MyHC-β due to the actin activated ATPase activity being lower than the adult fast isoforms (Drachman, Johnston 1973, Lowey, Waller et al. 1993). A study by Resnicow *et al*. (Resnicow, Deacon et al.

2010) using the same method as used here for producing recombinant S1 (with a GFP tag) showed however that the ATPase maximum rate (V_{max}) and half maximum rate (K_M) were very similar to the adult fast isoforms.

This is the first study to examine the transient kinetic parameters of the wild type MyHC-emb S1 using a recombinant protein (Chapters 2.2.1.3 and 2.2.1.4). This method allows the examination of a pure homogeneous sample since muscle samples will contain fibres expressing different myosin isoforms which will affect the kinetics. C2C12 cells dervived from a mouse myoblast cell line were grown and transfected with the human MYH3 gene encoding the MyHC-emb S1 domain with a His-tag at the C-terminus by Carlos Vera (University of Colorado, USA). No human light chains were expressed with the S1, as such the endogenous mouse light chains were purified with the S1 (Figure 4.3). The purification was performed using the method in chapter 2 (Chapter 2.2.1.4). Previously protein was purified at Colorado and shipped here to the UK. Purifying the protein in the UK prior to use in the stopped-flow ensured the sample could be used when fully active. An added benefit was an increase in protein yield by removing an additional chromatography step following the cell lysis and nickel chromatography step. Therefore samples of 1-2 mL 2-5 µM myosin S1 was increased to 1-2 mL 10-20 µM myosin S1. This S1 was used for the stopped-flow assays.

Since starting this project collaborators at Colorado have also improved their purification to obtain similar concentrations of myosin S1 without an endogenous mouse myosin contamination. The S1 purified in Colorado was used for the ATPase assays.

The aim of the investigation in this chapter is to characterise the kinetics of the individual steps of the myosin cross-bridge cycle for MyHC-emb. This will help to determine whether the embryonic myosin is a slow type myosin like MyHC-β or fast like the other class II skeletal myosins. Embryonic myosin (MyHC-emb) is thought to be a slow type myosin like the cardiac slow myosin-β. A comparison can be drawn with the MyHC-β isoform since it has recently been characterised under the same experimental conditions (Nag, Sommese et al. 2015). A second aim is to repeat the ATPase assay with the new construct (without GFP) and observe any correlation between the stopped-flow kinetics and steady-state ATPase data. The ATPase data will also help to fill gaps in the stopped-flow data by allowing estimates through modelling. In understanding the MyHC-emb this will help to

evaluate the consequences of disease causing mutations in the myosin molecule (Chapter 5).

The kinetic data on the wild type MyHC-emb was published along with the Freeman Sheldon Syndrome mutations in MyHC-emb data in the Journal of Biological Chemistry in May 2016:

Walklate, J., Vera, C., Bloemink, M. J., Geeves, M. A., Leinwand, L., The most prevalent Freeman-Sheldon syndrome mutations in the embryonic myosin motor share functional defects. The Journal of Biological Chemistry, 2016, **291**, p.10318-10331.

4.2 WT Embryonic myosin stopped-flow kinetics

4.2.1 Purification of recombinant S1

The recombinant S1 was expressed by Carlos Vera (University of Colorado, USA, Chapter 2.2.1.3) then purified from cell pellets using nickel affinity chromatography (Chapter 2.2.1.4) which resulted in a fairly pure solution of S1 (Figure 4.3).

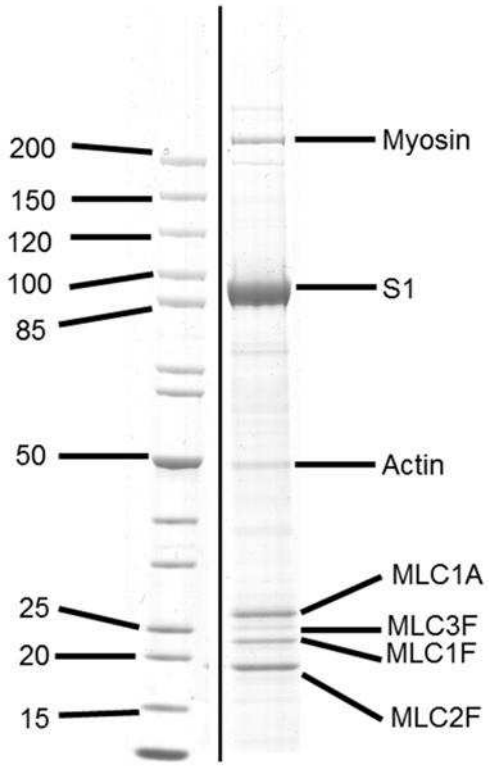

Figure 4.3 – SDS-PAGE of the wild type MyHC-emb purified from recombinant expression in the mouse myoblast cell line C2C12. Molecular weights are displayed on the left hand side from the ladder used. *MLC1A* = myosin light chain 1A, *MLC3F* = myosin light chain 3F, *MLC1F* = myosin light chain 1F, *MLC2F* = myosin light chain 2F.

There was however a small contamination of full length endogenous myosin and an even smaller band of actin present after the column. Densitometry analysis was used to work out the percentage of myosin present in the solution to determine if it would have an effect on the stopped-flow kinetics data (Figure 4.4).

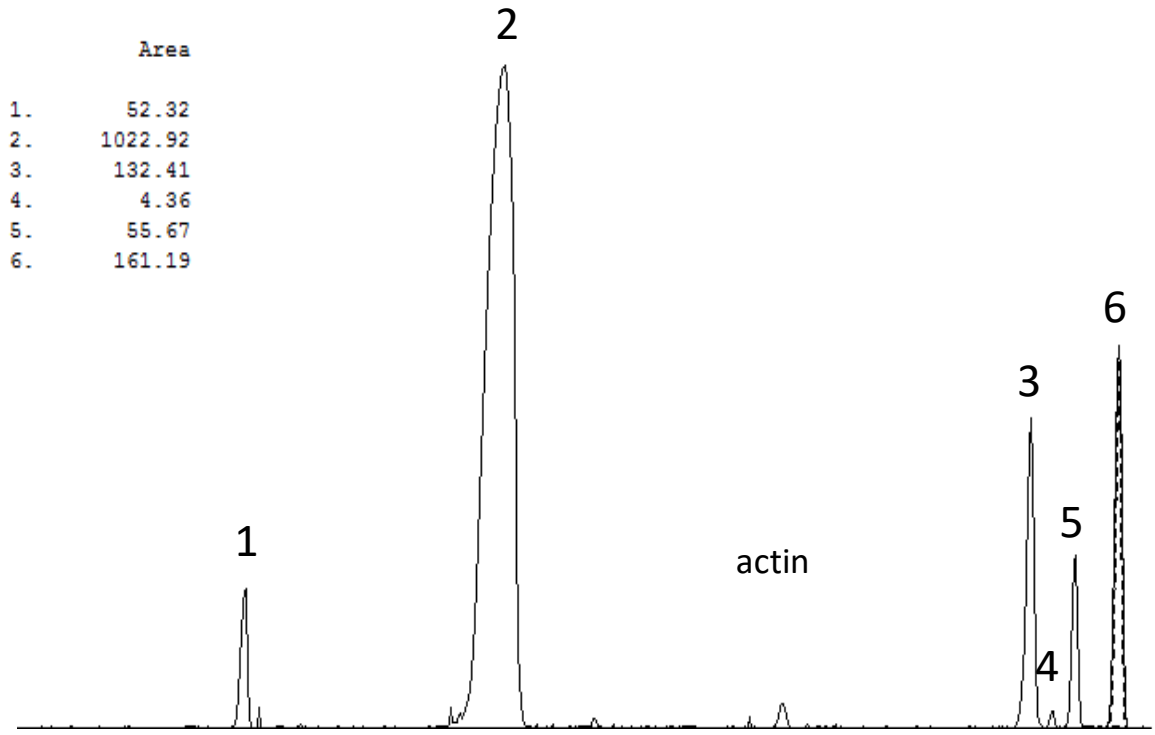

Figure 4.4 – Densitometry analysis of the recombinant MyHC-emb SDS-PAGE. Here the darker or more intense the bands on the gel the bigger the peaks. 1 = endogenous mouse full length myosin, 2 = recombinant MyHC-emb S1, 3 = myosin light chain 1A (*MLC1A*), 4 = myosin light chain 3F (*MLC3F*), 5 = myosin light chain 1F (*MLC1F*), and 6 = myosin light chain 2F (*MLC2F*). The area of each peak (insert) was determined using the densitometry software (Scion Image). The light chains were identified using analysis from Deacon *et al.* (Deacon, Bloemink et al. 2012) and assigned based on their molecular weight. This densitometry analysis was used to estimate the ratio of protein bands on the SDS-PAGE gel from figure 4.3.

The percentage of myosin compared to S1 by mass could be calculated by dividing the area of the myosin peak by the area of the S1 and myosin peaks and multiplying by 100:

$$\frac{52}{1022} \times 100 \ = 5.1\% \text{ by mass}$$

This value could then be used to calculate the percentage of myosin by molecular weight by multiplying the percentage by mass by the molecular weight of the S1 divided by the molecular weight of the myosin (molecular weights estimated from gel, Figure 4.3):

$$5.1 \ \times \ \frac{90}{220} = 2.09\% \text{ by MW}$$

Therefore the amount of endogenous mouse myosin is low and unlikely to appear in the stopped-flow traces since it is <5 % by weight, however caution was taken to be observant of slow secondary transients in the stopped-flow assays that would be indicative of endogenous myosin in the system. The endogenous myosin may be present due to the presence of actin. It is possible that the S1 is still bound to the actin and so is the myosin, therefore they purifying together. For the ATPase assays conducted by Carlos Vera he utilised a second purification step using ion exchange to remove the endogenous myosin. This was necessary for the steady-state ATPase assays as the basal activity was measured and a contaminating myosin could affect the results. However for these stopped-flow assays, the contaminating myosin had no interference than therefore the extra purification step was not needed. Using an extra day to clean the sample and possible purify less protein would have not been an economical use of this precious sample.

One issue of the construct used is that the light chains bound to the S1 are the endogenous mouse light chains from the C2C12 cells. Deacon *et al*. (Deacon, Bloemink et al. 2012) analysed these light chains and found they were *MLC1A*, *MLC3F*, *MLC1F*, and *MLC2F*. The light chains were assigned based on their molecular weights.

A review by Bottinelli and Reggiani (Bottinelli, Reggiani 2000) stated that the myosin light chains (*MLC*) 1A, 1F, and 2F are known to bind to the embryonic myosin. *MLC1A* is also known as the *MLC-1 atrial/foetal* isoform expressed in embryonic skeletal tissue and the heart and in the atria of adults (Whalen, Butler-Browne et al. 1978, Kurabayashi, Komuro et al. 1988). We were therefore encouraged to find that these light chains had a greater density than the *MLC3F*. This also correlates to the level of S1 and endogenous myosin in the sample, suggesting these three light chains are binding to the S1 (MLC1A - essential light chain, and either MLC1A or MLC2F - regulatory light chains) while *MLC3F* which does not bind to the embryonic myosin appears to be associating with the endogenous myosin. Deacon *et al*. (Deacon, Bloemink et al. 2012) used a construct with the recombinant *MYL3* which is a specific cardiac light chain. Since there is a specific embryonic myosin light chain it would be interesting to see if there is a change in the kinetics with the human form present as there is in the cardiac β-S1.

4.2.2 Difference in nucleotide binding to WT embryonic S1 compared to WT β S1

Upon binding of ATP to myosin S1 (in the absence of actin) there is a fluorescence change associated with tryptophan-509 moving on the relay loop.

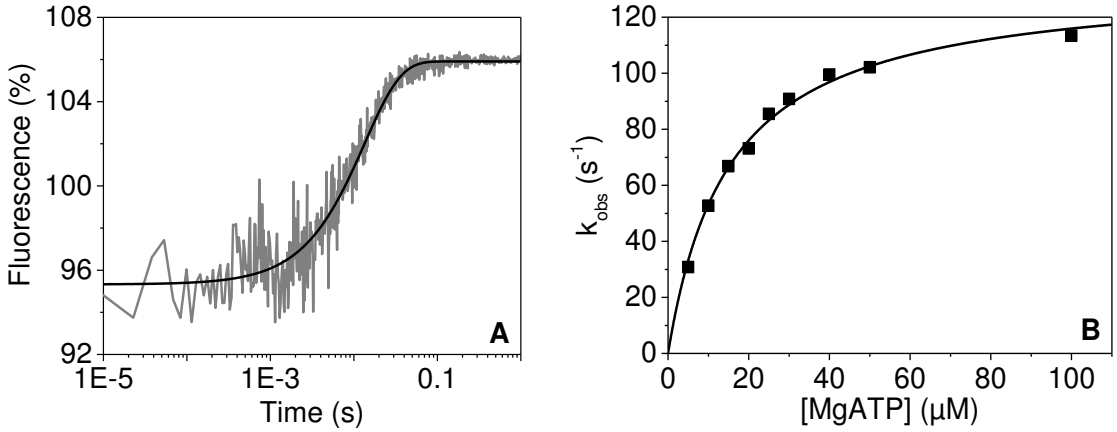

Figure 4.5 – Tryptophan fluorescence of ATP binding to wild type embryonic myosin S1. (A) An example trace of the fluorescence change upon 10 μM ATP binding to 100 nM S1. The k_{obs} = 5.4 s^{-1} with fluorescence increase = 10.6 %. (B) Hyperbolic dependence of k_{obs} from ATP binding on ATP concentration.

ATP of varying concentrations was rapidly mixed with 100 nM wild type embryonic myosin S1. The change in fluorescence was well described by a single exponential (Equation 2.4, Figure 4.5A). The k_{obs} was dependent on ATP concentration such that as the ATP concentration increased so did the k_{obs}. This dependence could be well described by the hyperbolic equation 2.13 (Chapter 2.3.2.1, Figure 4.5B). The percentage fluorescence increase was 10 % and unaffected by the increase in ATP concentration.

One value obtained from the hyperbola is the second order rate constant of ATP binding to S1 (K_1k_{+2}). This is determined from the initial section of the fit at the low concentrations of ATP (<50 μM). The K_1k_{+2} value was nearly 2.5 fold faster for MyHC-emb (12.5 ± 1.9 μM^{-1} s^{-1}) than for MyHC-β (5.8 ± 0.4 μM^{-1} s^{-1}, Table 4.1). Values shown are the average of three biological repeats with the S.E.M.

At higher concentrations of ATP (>50 μM) the ATP becomes saturating and a different step becomes rate limiting. The fit then gives two more values, k_{max} and $K_{50\%}$. The value of k_{max} has been linked to the maximum rate of ATP binding to S1 (k_{+2}) and to the hydrolysis rate constant (k_{+3} + k_{-3}). The $K_{50\%}$ gives the concentration of ATP needed to reach 50 % of

the k_{max} which is termed $1/K_1$. The k_{+2} (or $k_{+3} + k_{-3}$) is 30 % faster for MyHC-emb (130 ± 3.4 s^{-1}) than the MyHC-β (91.2 ± 1.8 s^{-1}, Table 4.1). The value $1/K_1$ is the ATP affinity which appears slightly tighter for the MyHC-emb (10.9 ± 2 μM) than MyHC-β (15.9 ± 1.4 μM); however this is not as there is not a significant difference.

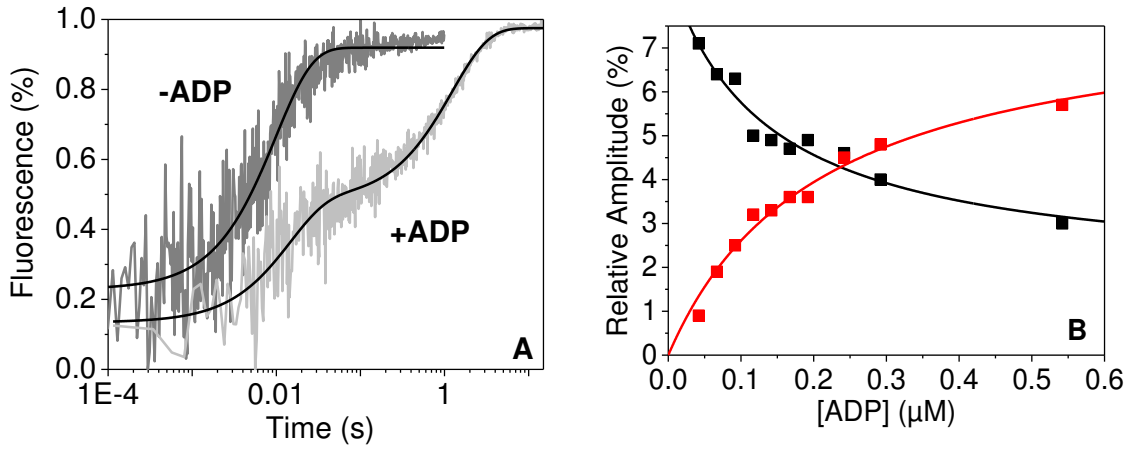

Figure 4.6 – ADP affinity to S1 in the absence of actin. (A) Trace of 100 nM S1 vs 50 μM ATP results in a transient best described by a single exponential. From this fit the value of k_{obs} = 96 s^{-1} and a fluorescence increase of 8 %. 100 nM S1 was pre-incubated with 0.25 μM ADP before being rapidly mixed with 50 μM ATP. The transients were best described by a double exponential. This fit yielded a k_{obs} = 63 s^{-1} and fluorescence increase = 3.2 % for the fast phase while k_{obs} = 0.8 s^{-1} and fluorescence increase = 5.7 % for the slow phase. (B) The relative amplitudes of the fast and slow phases could be plotted against the ADP concentration, which shows a hyperbolic dependence. The ADP affinity (K_6K_7) can be determined form these two fits.

Using a similar assay it is possible to determine the ADP affinity (K_6K_7) and ADP release rate constant (k_{+6}, measureable whereas step 7 is too fast to measure) in the absence of actin.

100 nM S1 was preincubated with varied concentrations of ADP. These mixtures were rapidly mixed with 50 μM ATP. The fluorescence change was well described by a double exponential fit (Figure 4.6). The two phases seen in these transients are descriptive of the S1 complexed with ADP. The fast phase arises from ATP binding to S1 that has no nucleotide bound and is why only this phase is seen in the absence of ADP. The slow phase emerges as ADP concentration increases as it is added to the S1. This is due to ADP occupying the nucleotide pocket preventing ATP binding. Therefore ADP must first dissociate before ATP binding. The slow phase then represents the ADP release rate constant (k_{+6}). For the MyHC-emb the k_{+6} was slightly faster (0.89 ± 0.07 s^{-1}) than the

MyHC-β (0.63 ± 0.03 s^{-1}) which is a statistically significant difference (Table 4.1). The k_{obs} of both phases was unaffected by the increase in ADP concentration.

The ADP affinity can be determined by plotting the amplitudes of the fast and slow phases against the ADP concentration. The fast phase and slow phases can be best described by hyperbolic fits using equations 2.20 and 2.24 respectively (Chapter 2.3.2.1). As the ADP concentration increase so does the amplitude of the slow phase as more S1 is occupied by ADP that must dissociate before ATP can bind. Conversely the fast phase amplitude decreases as less of the S1 is free to bind ATP without an ADP molecule already bound. Both fits will give similar values for ADP affinity (K_6K_7) which can be averaged. For MyHC-emb the K_6K_7 value was over 3.5-fold tighter (0.15 ± 0.018 μM) than MyHC-β (0.53 ± 0.07 μM, Table 4.1).

4.2.3 Differences in nucleotide binding to WT embryonic acto.S1 to WT β acto.S1

The assays above were repeated this time in the presence of actin by monitoring a pyrene label on Cysteine-374 of actin which is quenched when S1 is bound to the actin. The fluorescence can be followed when ATP binds to S1 and leads to a dissociation of S1 from actin.

50 nM pyrene-labelled actin in complex with 50 nM S1 was rapidly mixed with 10 μM ATP (Figure 4.7A) leading to an increase in fluorescence as ATP induces a dissociation of S1 from actin. The increase in fluorescence was best described by a single exponential at all ATP concentrations.

At increasing concentrations of ATP, similar to the ATP binding to S1 assay, the k_{obs} dependence on ATP concentration is hyperbolic (Figure 4.7B), well described by equation 2.13 (Chapter 2.3.2.1). The second order rate constant for ATP binding to acto.S1 ($K'_1k'_{+2}$), is more than twice as fast for the MyHC-emb (9.4 ± 1.0 μM^{-1} s^{-1}) than for MyHC-β (4.4 ± 0.2 μM^{-1} s^{-1}, Table 4.1). The maximum rate of dissociation (k'_{+2}) however is 2 fold slower for MyHC-emb (777 ± 17 s^{-1}) than MyHC-β (1543 ± 100 s^{-1}). The affinity of ATP for acto.S1 ($1/K'_1$) can be determined by the $K_{50\%}$ from the hyperbolic fit. The $1/K'_1$ for MyHC-emb is

almost 4 fold tighter (84.3 ± 9.7 µM) than MyHC-β (327.9 ± 53.3 µM). The percent fluorescence increase was not affected by the increase in the ATP concentration.

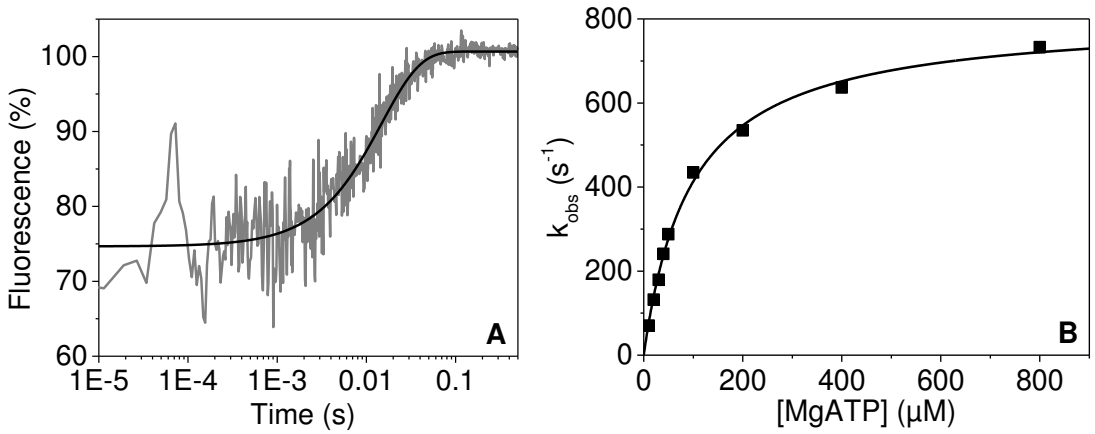

Figure 4.7 – ATP induced dissociation of MyHC-emb from pyrene-labelled actin. (A) An example transient of 50 nM pyrene-actin.S1 rapidly mixed with 10 µM ATP. The increase in fluorescence was best described by a single exponential. The k_{obs} = 70 s^{-1} and the increase in fluorescence = 26.6 %. (B) The hyperbolic dependence of k_{obs} on the ATP concentration.

Repeating this assay in the presence of ADP can be used to define the ADP affinity ($K'_6K'_7$) for acto.S1. ADP affinity could also be determined by mixing ADP with acto,S1 in the absence of ATP, however this was not used in this thesis

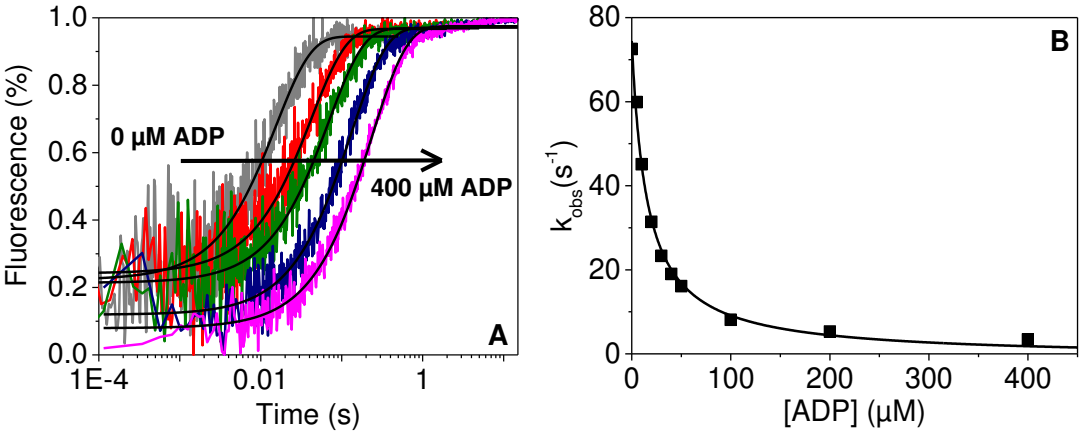

Figure 4.8: ADP affinity in the presence of actin. (A) Transients showing 50 nM acto.S1 rapidly mixed with a combination of 10 µM ATP and 0-400 µM ADP. The increase in fluorescence was best described by a single exponential. As the ADP concentration increased, the k_{obs} decreased from 70 s^{-1} to 4.8 s^{-1} while the fluorescence amplitude stayed stable at 29 %. (B) k_{obs} plotted as a function of ADP concentration can be fit with a hyperbolic equation resulting in a ADP affinity value.

In order to determine the ADP affinity a competition assay was used. A fixed concentration of 10 μM ATP was mixed with varying concentrations of ADP (0-400 μM) outside of the stopped-flow. Using the stopped-flow 100 nM pyrene-labelled acto.S1 was rapidly mixed with the ATP/ADP solutions. This led to a competition in binding between the ATP and ADP. As more ADP is added to the assay more will be available to bind to the S1 preventing it from binding ATP and therefore slowing the dissociation reaction down. This resulted in a slower k_{obs} at higher ADP concentrations than at 0 μM ADP (Figure 4.8A).

The k_{obs} can be plotted as a function of ADP concentration which has a hyperbolic dependence (Figure 4.8B). When fit with equation 2.15 (Chapter 2.3.2.1) this gives the ADP affinity ($K'_6K'_7$). For MyHC-emb the $K'_6K'_7$ is over 2 fold weaker (14.3 ± 1.9 μM) than the MyHC-β (6.1 ± 0.3 μM). The fluorescence amplitude was not affected by the increase in the ADP concentration.

To determine the ADP release rate (k'_{+6}) a displacement reaction is utilised instead of the competition assay. 100 nM pyrene-labelled acto.S1 is incubated with a saturating concentration of ADP (over 20 times the $K'_6K'_7$ value) which for MyHC-emb was 300 μM ADP. The acto.S1.ADP solution was then rapidly mixed in the stopped-flow with varying high concentrations (1-10 mM) of ATP. The k_{obs} should be unaffected by the change in ATP concentration resulting in the ADP release rate (k'_{+6}). For MyHC-emb the k'_{+6} is nearly 3 times slower (22 ± 1.8 s^{-1}) than MyHC-β (58.7 ± 1.7 s^{-1}, Table 4.1).

Using these values it is also possible to calculate the second order rate constant for ADP binding ($K'_7k'_{-6}$). This is achieved by dividing the k'_{+6} value by the $K'_6K'_7$ value. For MyHC-emb again this is much slower (1.5 μM^{-1} s^{-1}) than MyHC-β (9.6 μM^{-1} s^{-1}), over a 6-fold difference.

4.2.4 Differences in actin affinity to WT embryonic S1 compared to WT β S1

The method of determining the actin affinity described by Kurzawa *et al*. (Kurzawa, Geeves 1996) using stopped-flow spectroscopy was used for the MyHC-emb.

30 nM pyrene-labelled actin is incubated with a varied concentration of S1 (0 – 100 nM) and then rapidly mixed with 20 µM ATP (concentrations before mixing). As the S1 concentration is increased, more of it will bind to the actin quenching the pyrene signal. When the acto.S1 is mixed with ATP it will lead to the dissociation step. As more S1 is added to the actin, an increasing amount of the pyrene will be quenched at the beginning of the assay. Therefore when mixed with the ATP the starting fluorescence amplitude will decrease, but at the end of the reaction reach the same maximum fluorescence leading to an overall increase in fluorescence amplitude (Figure 4.9A). Since the ATP concentration is kept constant the k_{obs} remains constant also. To adjust to the fluctuation that may occur in the maximum fluorescence the relative amplitude was calculated ((fluorescence amplitude / maximum fluorescence) x 100) and plotted as a function of S1 concentration (Figure 4.9B). This can be well described by a quadratic equation (equation 2.25, Chapter 2.3.2.1) which gives the actin affinity (K_A) of S1. For MyHC-emb the K_A appears to be nearly 5 times tighter (2.1 ± 0.2 nM) than MyHC-β (10 ± 1.8 nM).

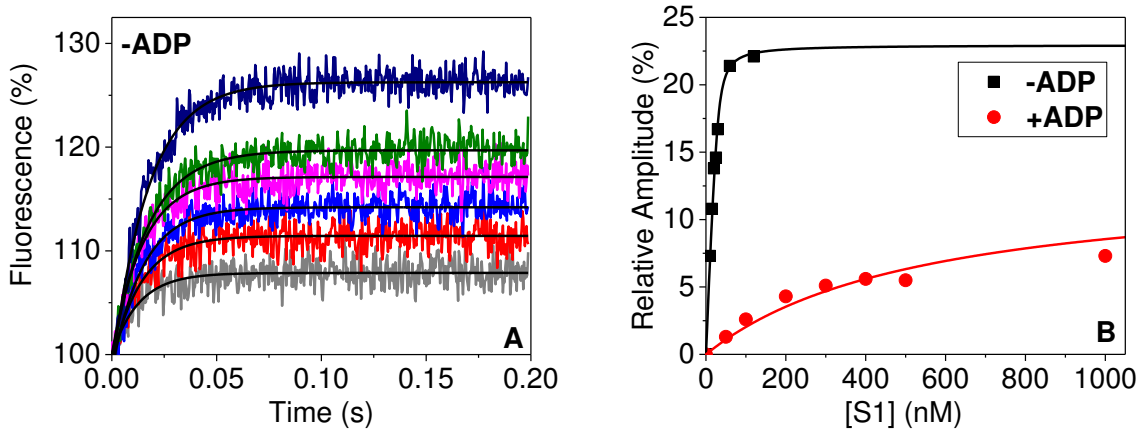

Figure 4.9: Actin affinity of MyHC-emb in the absence and presence of ADP. (A) Transients of 30 nM actin + varied S1 concentrations (0-100 nM) versus a fixed concentration of 10 µM ATP in the absence of ADP. As the concentration of S1 increased so did the fluorescence amplitude. These transients are normalised to the same start point so that the increase in fluorescence can be observed easier. The transients reach the same end point it is the start point that changes, however this is hard to see when plotted on the same graph (B) Fluorescence amplitude plotted as a function of S1 concentration can be described by a quadratic fit which results in the actin affinity in the absence or presence of ADP.

This assay can be repeated in the presence of ADP to give the actin affinity in the presence of ADP (K_{DA}). The same concentration of actin is used and the S1 concentration is varied, however since ADP weakens the S1 actin affinity, higher concentrations are

needed than for the K_A measurement. The same concentration of ADP (300 µM) is used as for the ADP release rate for acto.S1 (20 times the $K'_6K'_7$), this is to ensure that the S1 has a saturating level of ADP. This is incubated with the acto.S1 to allow binding. The acto.S1.ADP complex is then rapidly mixed with 100 µM ATP. This results in a similar effect to the K_A measurements (Figure 4.9A) where the fluorescence amplitude increases with S1 concentration but the k_{obs} remains constant. A plot of the relative amplitudes as a function of S1 concentration again results in an actin affinity (K_{DA}) which should be weaker in the presence of ADP (Figure 4.9B). The K_{DA} value for MyHC-emb is 5-fold weaker (526 ± 60.3 nM) than MyHC-β (109.3 ± 24.1 nM). For an unknown reason the relative amplitude in the presence of ADP does not reach the same level as when ADP is not present which may be indicative of S1.ADP staying bound to actin.

4.2.5 Steady state ATPase data

The steady state ATPase rate was determined using a NADH-coupled assay (Chapter 2.3.3). The S1 binds and hydrolyses ATP to ADP. This is then converted back to ATP by pyruvate kinase as it converts phosphoenolpyruvate (PEP) to pyruvate. The pyruvate can then be converted by lactate dehydrogenase to lactate. In the process NADH is oxidised to NAD^+, which can be monitored via optical spectroscopy. NADH absorbs light at 340 nm and so measuring at this wavelength the absorbance will decrease as the NADH is converted to NAD^+. The gradient of this line can be used to determine the rate of the ATPase cycle. S1 has a very low basal ATPase rate in the absence of actin; however this rate is stimulated by actin and becomes much quicker as more actin is added.

ATPase measurements were carried out by Carlos Vera (University of Colorado, USA).

As the actin concentration increases the ATPase rate also increases, however this relationship is only linear at the lower concentrations of actin and has a hyperbolic dependence over larger actin concentrations (Figure 4.10). This hyperbolic dependence follows a classic Michaelis-Menten equation (equation 2.28, chapter 2.3.3). This results in the maximum ATPase rate (V_{max}) and the half maximum rate concentration (K_M). There was no significant difference in V_{max} between the MyHC-emb (7.0 ± 0.15 s^{-1}) and MyHC-β

(6.0 ± 0.5 s^{-1}). The same was true for the K_M value where the MyHC-emb (38.5 ± 2.4 μM) was very similar to the MyHC-β (40 ± 6 μM).

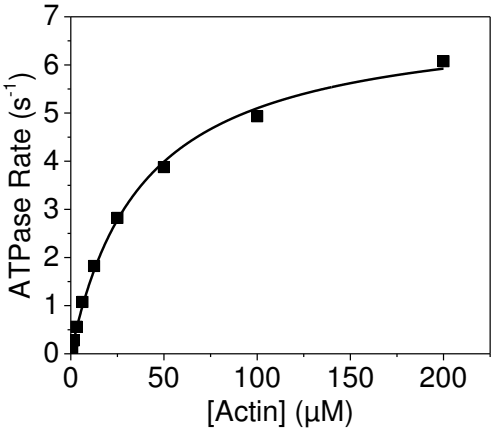

Figure 4.10 – ATPase rate for MyHC-emb. Myosin is an actin activated ATPase so as the actin concentration increases so does the ATPase rate.

To determine the MyHC-emb activity at low actin concentrations (below half V_{max}) it is possible to use the V_{max}/K_M. For both the MyHC-emb (0.18 s^{-1} μM^{-1}) and MyHC-β (0.15 s^{-1} μM^{-1}) this value did not change significantly.

Table 4.1 – Rate and equilibrium constants of the wild type MyHC-emb.S1 compared to the wild type MyHC-β S1. Statistically significant differences (determined by a two-tailed Student's *t* test) have been shaded grey. Values are averages of 3 biological repeats (from three different cell preparations) ± SEM. All assays conducted in 25 mM KCl, 20 mM MOPS, 5 mM $MgCl_2$, 1 mM NaN_3, pH 7.0 unless otherwise stated.

Rate/Equilibrium Constant	Wild Type β [a]	Wild Type Emb
ATP binding to S1		
K_1k_{+2} (μM^{-1} s^{-1})	5.8 ± 0.4	12.5 ± 1.9 [b]
$1/K_1$ (μM)	15.9 ± 1.4	10.9 ± 2.0
k_{max} or $k_{+3} + k_{-3}$ (s^{-1})	91.2 ± 1.8	130 ± 3.4 [d]
ADP binding to S1		
K_6K_7 (μM)	0.53 ± 0.07	0.15 ± 0.018 [c]
k_{+6} (s^{-1})	0.63 ± 0.03	0.89 ± 0.07 [b]
ATP binding to actin.S1		
$K'_1k'_{+2}$ (μM^{-1} s^{-1})	4.4 ± 0.2	9.4 ± 1.0 [c]
$1/K'_1$ (μM)	327.9 ± 53.3	84.3 ± 9.7 [b]
k'_{+2} (s^{-1})	1543 ± 100	777 ± 17 [d]
$K_{\alpha1}$	4.1 ± 1.4	-
$k_{+\alpha1}$ (s^{-1})	153.4 ± 10.6	-
ADP binding to actin.S1		
$K'_6K'_7$ (μM)	6.1 ± 0.3	14.3 ± 1.9 [b]
k'_{+6} (s^{-1})	58.7 ± 1.7	22.0 ± 1.8 [d]
$K'_7k'_{-6}$ (μM^{-1} s^{-1})	9.6	1.5
$K'_6K'_7/K_6K_7$	11.5	95
S1 affinity for actin		
K_A (nM)	10 ± 1.8	2.1 ± 0.2 [b]
K_{DA} (nM)	109.3 ± 24.1	526 ± 60.3 [d]
K_{DA}/K_A	10.9	250
ATPase *		
V_{max} (s^{-1})	6.0 ± 0.5	7.0 ± 0.15
K_M (μM)	40 ± 6	38.5 ± 2.4
V_{max}/K_M (s^{-1} μM^{-1})	0.15	0.18

[a] (Nag, Sommese et al. 2015)

[b] $p < 0.05$ determined by Student's *t* test as compared to wild type MyHC-β S1.

[c] $p < 0.01$ determined by Student's *t* test as compared to wild type MyHC-β S1.

[d] $p < 0.005$ determined by Student's *t* test as compared to wild type MyHC-β S1.

* 0 mM KCl, 20 mM MOPS, 5 mM $MgCl_2$, 1 mM NaN_3, pH 7.0.

4.3 Discussion

4.3.1 Comparison of wild type MyHC-emb to wild type MyHC-β

Much of the previous work carried out on embryonic myosin led to the idea that the isoform was a slow type myosin like the cardiac-β myosin. It appears from this investigation that there are similar characteristics between MyHC-emb and MyHC-β. However there are some key differences between the two isoforms that shall be discussed here. A comparison of the percentage changes between MyHC-emb and MyHC-β is summarised in figure 4.11.

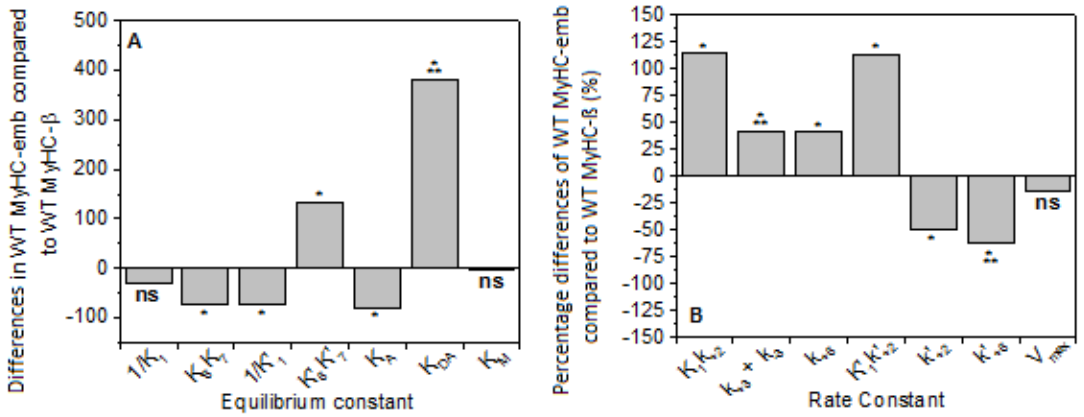

Figure 4.11: Percentage changes between MyHC-emb and MyHC-β. (A) Percentage changes in equilibrium constants between MyHC-emb and MyHC-β. An increase or decrease in equilibrium constant indicates a weakening or tightening of the affinities compared to MyHC-β respectively (B) Percentage changes in rate constants between MyHC-emb and MyHC-β. An increase or decrease in rate constant indicates the step is faster or slower than MyHC-β respectively. * $p < 0.05$, ** $p < 0.01$, *** $p < 0.005$. The increases may appear greater than the decreases but it is worth noting the decreases are as large as the increases.

The hallmark of a slow myosin is a relatively tight ADP affinity (tighter than the fast skeletal myosin isoforms IIa, IIb, and IIx) and a slow ADP release rate in the presence of actin. The study from Nag *et al*. (Nag, Sommese et al. 2015) showed that at the same ionic strength as this study the ADP affinity was very tight at 6.1 ± 0.3 µM for MyHC-β. The embryonic myosin has a 2-fold tighter ADP affinity though this is still very tight at 14 ± 1.9 µM. When the fast skeletal isoforms are compared to MyHC-β at a higher salt (100 mM KCl) this affinity (21 ± 5 µM) is 2.5- to 6-fold weaker than IIa (80 ± 15 µM), IIb (54 ± 11),

and IIx (118 ± 33 μM) isoforms (Deacon *et al.*, 2012; Bloemink *et al.*, 2013). It would seem therefore that the MyHC-emb sits in-between the slow MyHC-β and fast skeletal isoforms in terms of ADP affinity.

The second characteristic of a slow type myosin, the ADP release rate from acto.S1 (k'_{+6}), is also very slow for the MyHC-emb and MyHC-β. Bloemink *et al*. (Bloemink *et al.*, 2013) found the fast isoforms to have a very fast ADP release rate constant (> 1,000 s^{-1}) compared to MyHC-β which had a k'_{+6} of 93 ± 5 s^{-1} in similar conditions (100 mM KCl). Nag *et al*. (Nag *et al.*, 2015) found the k'_{+6} to be slightly slower in the lower salt (25 mM KCl) at 58.7 ± 1.7 s^{-1}, which compared to MyHC-emb, at 22 ± 1.8 s^{-1}, is almost 3 fold faster.

One interesting difference between the MyHC-β and MyHC-emb is the lack of a second slow phase with pyrene fluorescence during the ATP induced dissociation assay. This slow phase in the transients is thought to be caused by a conformational change of the nucleotide binding pocket between an open and closed state. This has become indicative of the slow MyHC-β as it is also not seen for the 'fast adult' skeletal myosin class II isoforms. The lack of this second phase would suggest that the conformation change does not occur in the MyHC-emb, however there may be two other reasons why this may not be the case. Firstly the rate constant for the opening on the nucleotide binding pocket is 153 s^{-1} for the MyHC-β. Given that the maximum rate of dissociation is fairly slow for the MyHC-emb (777 s^{-1}) compared to the MyHC-β (1543 s^{-1}) it is likely that there is insufficient distinction between the fast and slow phase for the MyHC-emb. The second reason could be the salt concentration. Deacon *et al*. found that the $k_{+\alpha1}$ (isomerisation between an open and closed state of the nucleotide pocket on myosin) = 49 s^{-1} at 100 mM KCl (Deacon, Bloemink et al. 2012) while at 25 mM KCl the $k_{+\alpha1}$ = 153 s^{-1} (Nag, Sommese et al. 2015). This 3-fold reduction in the rate of conformation change could potentially allow the two phases to be separated if it is there.

However the embryonic myosin does appear to have some characteristics of a faster myosin. This includes a 30% faster ATP hydrolysis rate constant (k_{+3} + k_{-3}) and a 2-fold faster second order rate constant for ATP induced dissociation ($K'_1k'_{+2}$). Due to the slow ADP release rate constant, tight ADP affinity and slow ATPase rate, this has led us to conclude that the embryonic myosin while a slow isoform is faster than the cardiac β-myosin.

4.3.2 Limitations of assays

One limitation of this investigation is that using a low salt buffer, the actin affinity (K_A) becomes much tighter than if carried out at 100 mM KCl. The salt concentration chosen was 25 mM KCl with our collaborators to allow for easier comparison between stopped-flow data, ATPase data, and *in vitro* motility assays, the latter, require low salt. Stopped-flow spectroscopy instruments have become much more sensitive and the ability to use 30 nM pyrene-actin is a huge achievement. However to have confidence in the value of K_A the measurement would ideally be conducted with an actin concentration ≤ K_A. Therefore the concentration of actin would have to be lower to get a more accurate measurement. One thing we can be sure of is that the K_A for MyHC-emb is very tight similar to MyHC-β. Given more time and protein it would have been useful to repeat this assay at a higher salt such as 100 mM KCl. This would have weakened the K_A possibly to above 30 nM.

A second problem with this assay is that the concentration of active myosin must be correct. To ascertain the concentration of active S1 we do an activity test (Chapter 2.2.1.4). However the K_A measurement was usually the second to last assay carried out. In the time from the activity test to this actin affinity assay the active concentration of S1 may have decreased. Repeating the activity test would have been an option however due to limited amounts of sample this was not viable.

One measure of how accurate the K_A and K_{DA} assays are, is to compare the K_{DA}/K_A to the $K'_6K'_7/K_6K_7$ (Table 4.1). These values should be very similar and a deviation may indicate an error in one of the measurements. Since the measurements of ADP affinity are only dependent on knowing the ADP concentration these are very reliable so the $K'_6K'_7/K_6K_7$ of 95 is very reasonable. Since the K_{DA} value of 526 nM, and is much higher than the actin concentration of 30 nM, this measurement will not be susceptible to the same error as the K_A. Therefore the value of 250 for K_{DA}/K_A is most likely due to the K_A measurement being slightly out due to the affinity being tighter than the actin concentration and some error occurring consequentially. If we assume the value should be 95, then a calculated value of the K_A ($K_{DA}/95 = 526/95 = 5.5$ nM) shows that there is some error but very small, and again shows the affinity is very tight and closer to the value of MyHC-β.

5 Characterisation of Freeman-Sheldon Syndrome causing mutations R672H, R672C, and T178I

5.1 Introduction

Investigations into mutations in genes that may cause FSS found out of 28 FSS cases tested 26 were caused by missense mutations in the MYH3 gene (T178I, E498G, Y582S, R672C, R672H, and V825D, Figure 5.1) which codes for MyHC-emb (Toydemir, Rutherford et al. 2006). The three most common mutations were: Arginine-672 to a histidine (R672H, 12/28), Arginine-672 to a cysteine (R672C, 8/28), and Threonine-178 to an isoleucine (T178I, 3/28). T178I was also linked to the most common DA syndrome Sheldon-Hall Syndrome (SHS) (Toydemir, Rutherford et al. 2006), however this was later found to be a misdiagnosis and both cases of SHS where the T178I mutation was found have been diagnosed as FSS (Beck, McMillin et al. 2014). Beck *et al*. extended the study revealing more mutations and showed R672H (20/46), R672C (11/46), and T178I (8/46) were the three most common *MYH3* mutations causing FSS (Beck, McMillin et al. 2014).

The three mutations R672H, R672C, and T178I accounted for > 90% of all the *MYH3* mutations and T178I had the most severe phenotype. R672H was less severe than T178I and R672C the least severe of the three (Figure 5.2).

Using recombinant myosin S1 produced by the same method as Chapter 4 it should be possible to determine the kinetic parameters defining the ATPase cycle to observe any defects caused by the mutations R672H, R672C, and T178I in MyHC-emb. The aim therefore is to characterise the kinetics of the mutated myosin S1 compared to the wild type and to investigate how the mutations may manifest the differing phenotypes observed. It will also be of interest to investigate the location of the R672 and T178 residues in closer detail to predict which intermolecular interactions are affected when mutated using homology models of the MyHC-emb.

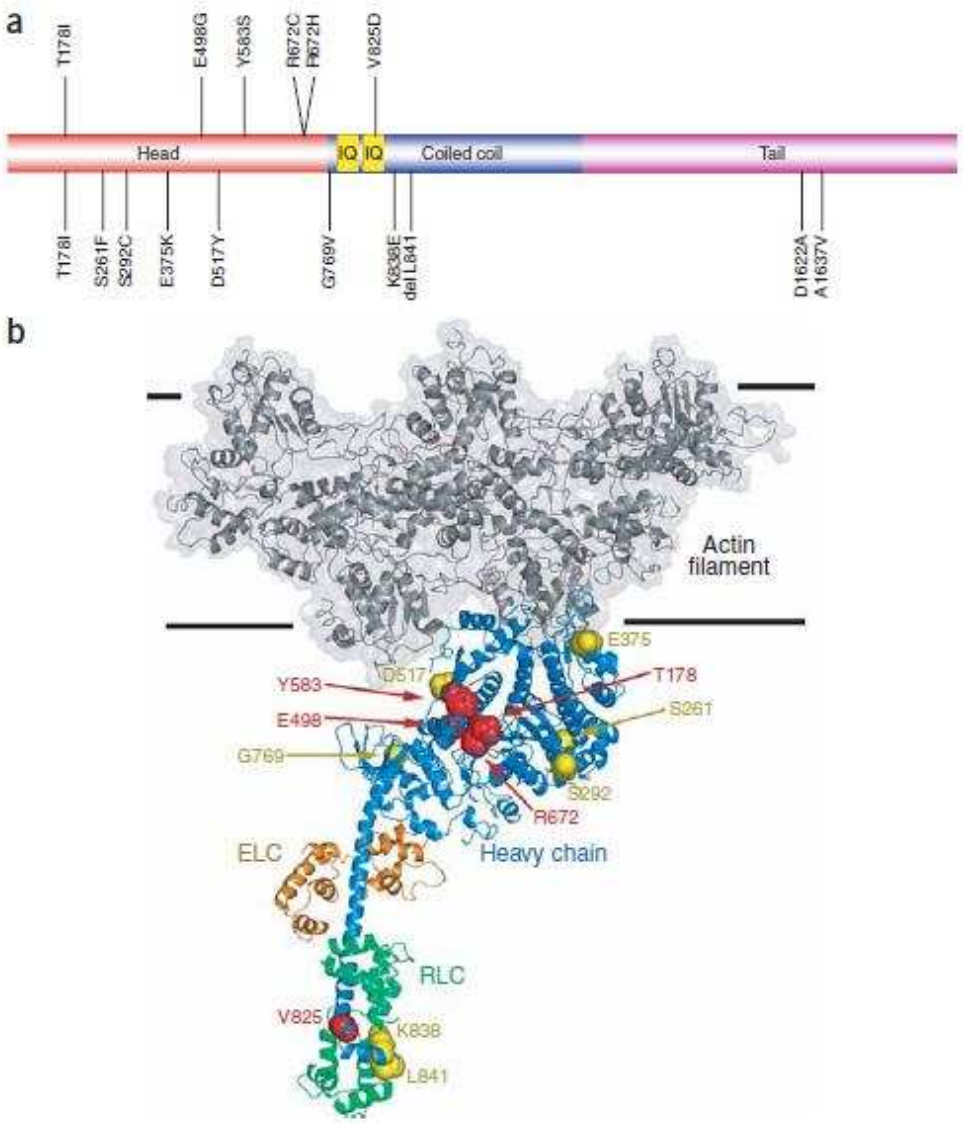

Figure 5.1 – Freeman-Sheldon Syndrome (FSS) and Sheldon-Hall Syndrome (SHS) mutations in the MYH3 gene. (A) Locations of FSS mutations (top) and SHS mutation (bottom). (B) Location of mutations in the myosin motor domain. Residues in red are FSS and yellow are SHS. 5 actin subunits are also shown in grey. Image from (Toydemir *et al.*, 2006).

Figure 5.2 – A comparison of individuals with FSS causing mutations T178I, R672H, and R672C in the *MYH3* gene. Individuals with the T178I mutation had the most severe facial contractures, R672C had relatively mild, while R672H was somewhere in between. Figure from (Beck *et al.*, 2014)

The kinetic data on the FSS MyHC-emb mutations was published along with the wild type data in the Journal of Biological Chemistry in May 2016:

Walklate, J., Vera, C., Bloemink, M. J., Geeves, M. A., Leinwand, L., The most prevalent Freeman-Sheldon syndrome mutations in the embryonic myosin motor share functional defects. The Journal of Biological Chemistry, 2016, **291**, p.10318-10331.

5.2 FSS mutation stopped-flow kinetics

5.2.1 Differences in nucleotide binding to R672H, R672C, and T178I embryonic S1 compared to WT embryonic S1

The preparations of the FSS mutations had similar yields to the wild type MyHC-emb of 1-2 mL 10-20 µM active S1.

The method for determining nucleotide binding rate and equilibrium constants was the same as for the wild type embryonic myosin (Chapter 4.2.1). The results of the ATP binding to S1 assays are shown in figure 5.3.

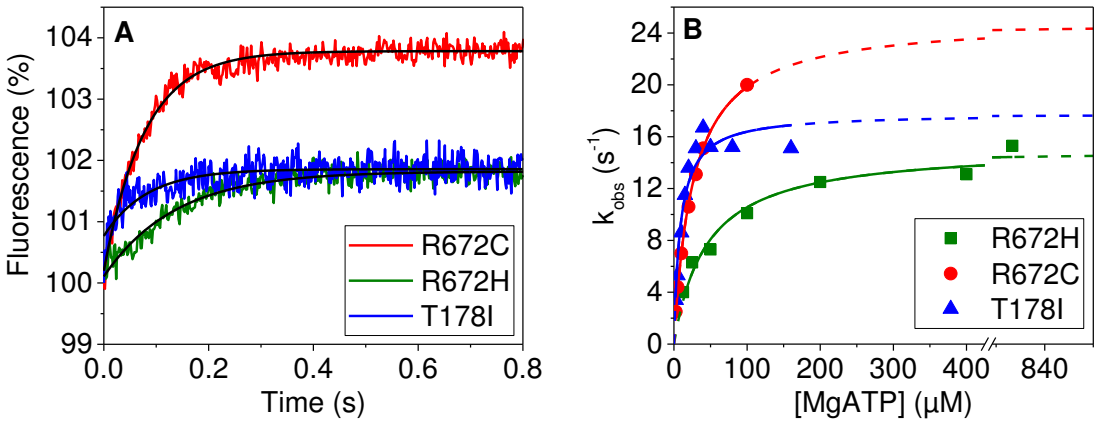

Figure 5.3: Tryptophan fluorescence for the three FSS mutation R672H, R672C, and T178I. (A) Representative transients of 100 nM MyHC-emb R672H (green), R672C (red), and T178I (blue) S1 rapidly mixed with 50 µM ATP. The increase in fluorescence could be best described by a single exponential in all three cases. The k_{obs} and fluorescence amplitudes for the three mutants were: 7.3 s^{-1} and 1.6 % respectively for the R672H, 12 s^{-1} and 3.5 % respectively for R672C, and 18 s^{-1} and 1.4 % for T178I respectively. (B) The hyperbolic dependence of k_{obs} on ATP concentration showing the different ATP affinities and maximum rate constants of ATP binding.

The use of tryptophan fluorescence was more problematic for the three mutants than for the wild type due to the reduced fluorescence amplitude (Figure 5.3A). For wild type the amplitude was around 10 % (Chapter 4.2.1) however for the R672C this was 3-4 % which was harder to measure but still possible. For the R672H and T178I the amplitude was low, around 1-2 % which could be measured due to the sensitivity of the newer stopped-flow spectroscopy instruments and that the k_{obs} were slower. At an ATP concentration of 50 µM the transients were best described by a single exponential however the k_{obs} was

reduced for all three compared to the wild type MyHC-emb. The k_{obs} for the mutants was: 7.3 s^{-1} for R672H, 12 s^{-1} for R672C, and 18 s^{-1} for T178I, while the wild type had a k_{obs} of 102 s^{-1} at the same ATP concentration.

When plotted as a function of ATP the k_{obs} followed a hyperbolic dependence (Equation 2.13) from which the second order rate constant of ATP binding (K_1k_{+2}), ATP affinity ($1/K_1$) and maximum rate of ATP binding/ATP hydrolysis (k_{max} or k_{+3} + k_{-3}) were determined (Chapter 4.2.1, Figure 5.3B).

For R672H, the K_1k_{+2} rate constant was over 30 times slower (0.4 ± 0.04 μM^{-1} s^{-1}) than the wild type MyHC-emb (12.5 ± 1.9 μM^{-1} s^{-1}). The value of $1/K_1$ was again affected this time by a 3-fold weakening in the affinity (34.4 ± 5 µM) compared to the wild type (10.9 ± 2 µM). The k_{+3} + k_{-3} was 9 times slower (14.3 ± 0.5 s^{-1}) for the mutant than the wild type (130 ± 3.4 s^{-1}). All of these changes were statistically significant (Table 5.1).

For R672C, the K_1k_{+2} similar to the R672H was slower (1.1 ± 0.07 μM^{-1} s^{-1}), but not as marked as the R672H as there was only an 11-fold change. Again ATP affinity ($1/K_1$), was 2-fold weaker (23.6 ± 2.6 µM) so not as weak as the R672H. The apparent ATP hydrolysis rate (k_{+3} + k_{-3}) however was 5 times slower than the wild type but 2-fold faster than the R672H. Again all these changes were significantly different than the wild type (Table 5.1).

Finally for the T178I, the K_1k_{+2} is the least affected (2.3 ± 0.1 μM^{-1} s^{-1}) of the three mutations compared to the wild type but is still 5-fold slower. The $1/K_1$ value was 40 % tighter (7.7 ± 0.6 µM) than wild type rather than the weaker affinity seen for the other two mutants. The k_{+3} + k_{-3} was however similar to the other two mutant by having a hydrolysis rate constant 7-fold slower than wild type (17.7 ± 0.6 s^{-1}). The only change not significantly different was the $1/K_1$.

Similar to the wild type MyHC-emb the ADP affinity measurements for the mutant MyHC-emb S1s were attempted. However due to the very low fluorescence amplitude seen for the R672H and T178I this assay proved not possible. The use of fluorescent nucleotides both Mant-ATP and –ADP or Coumarin-ATP and –ADP failed to even yield a fluorescence signal change, let alone one which could be used in this assay. The small fluorescence signal also proved difficult for the R672C mutation. While it was possible to observe the reduction in the fast phase amplitude, a slow second component failed to appear.

However the amplitudes of the fast phase was plotted against the ADP concentration which followed a hyperbolic dependence and could be fit with the same equation (Equation 2.20) as the fast phase of the wild type MyHC-emb (Chapter 4.2.1, Figure 5.4). Similar to the assay for the wild type MyHC-emb the k_{obs} was unaffected by the increase in ADP concentration.

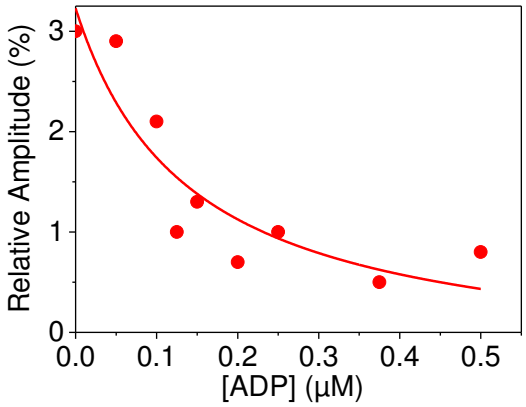

Figure 5.4 - R672C ADP affinity for S1. 100 nM MyHC-emb R672C S1 was preincubated with varied concentrations of ADP (0-0.5 μM) before being rapidly mixed with 50 μM ATP. Only the fast phase of the assay could be measured however the relative amplitude decreased with a hyperbolic dependence.

The ADP affinity in the absence of actin (K_6K_7) appeared to be slightly weaker (0.2 ± 0.04 μM) than the wild type (0.15 ± 0.018 μM) however this difference was not significantly different.

5.2.2 Differences in nucleotide binding to R672H, R672C, and T178I embryonic acto.S1 compared to WT embryonic acto.S1

The nucleotide binding rate and equilibrium constants were determined the same way as for the wild type MyHC-emb (Chapter 4.2.2). The results of the ATP induced dissociation assay are shown in figure 5.5.

Upon ATP binding the dissociation reaction occurs (Figure 5.5A) which followed a single exponential for the R672C at all ATP concentrations and T178I at low concentrations. R672H displayed a double exponential at all ATP concentrations and T178I at high concentrations (above 50 μM). The dependence of fast k_{obs} on ATP concentration

followed a hyperbolic dependence as with the wild type MyHC-emb (Chapter 4.2.2). From this the second order rate constant of ATP binding ($K'_1k'_{+2}$), ATP affinity ($1/K'_1$), and maximum rate of dissociation (k'_{+2}) could all be determined (Figure 5.5B).

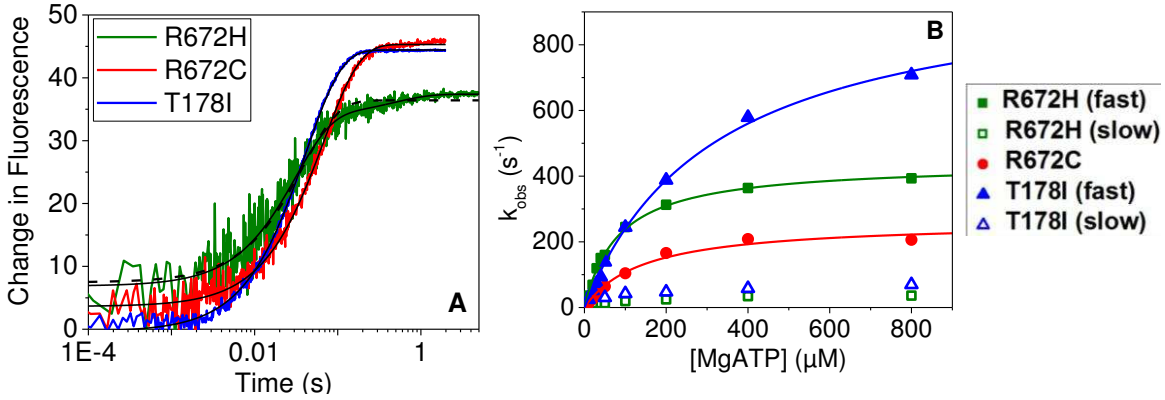

Figure 5.5 – ATP induced dissociation of the three FSS mutants from pyrene labelled actin. (A) Transients of the ATP induced dissociation of the mutant MyHC-emb S1 from pyrene-labelled actin. 10 μM ATP was rapidly mixed with 50 nM pyrene-actin.S1. R672C was described by a single exponential yielding a k_{obs} = 14 s^{-1} and a fluorescence amplitude = 41 %. T178I was also best described by a single exponential at this concentration yielding a k_{obs} = 24.8 s^{-1} and a fluorescence amplitude = 45 %. The transient of the R672H was best described by a double exponential yielding a k_{obs} = 30 s^{-1} and 1.9 s^{-1} for the fast and slow phase respectively, while the fluorescence amplitude = 26.6 % and 3.4 % for the fast and slow phases respectively. (B) The k_{obs} of the R672C, and fast phase k_{obs} of R672H and T178I when plotted against ATP concentration follows a hyperbolic dependence. Neither slow phase was affected by ATP concentration.

For R672H, the k_{obs} from the two phases were plotted against ATP concentration. The fast phase followed the hyperbolic dependence while the slow phase was unaffected by increased ATP. To ensure that there was no contaminating ADP present apyrase was added to convert the ADP to AMP however this had no effect on the presence of the slow component. From the fast phase the parameters could be determined. The $K'_1k'_{+2}$ was more than 2-fold slower (4.5 ± 0.3 μM^{-1} s^{-1}) than the wild type (9.4 ± 1 μM^{-1} s^{-1}). The $1/K'_1$ was 10 % weaker (92.3 ± 9 μM) than the wild type (84.3 ± 9.7 μM) however this difference was not significantly different. The k'_{+2} is almost 2-fold slower (413 ± 32 s^{-1}) than the wild type (777 ± 17 s^{-1}). The slow phase of ATP induced dissociation has previously been described (Deacon, Bloemink et al. 2012) for the MyHC-β, and is thought to be the conformational change between an open and closed state of the nucleotide pocket. The equilibrium constant for this process (K_α) is calculated as the ratio of the fast and slow phase fluorescence amplitude percentage. The rate constant for this pocket opening ($k_{+\alpha}$) is determined by the k_{obs} of the slow phase. Due to the slow phase not being

present for wild type the value of K_{α} (4.4 ± 0.8) and $k_{+\alpha}$ (31.5 ± 2.5 s^{-1}) is a significant difference.

For R672C, there was no slow element to the transients. The $K'_1k'_{+2}$ was however 4-fold slower (2.2 ± 0.5 μM^{-1} s^{-1}) than the wild type and even slower than R672H. The $1/K'_1$ value was 40 % weaker than the wild type however this is not a significant difference. The k'_{+2}value was nearly 3-fold slower (261 ± 8.4 s^{-1}) than the wild type, and is slower than the R672H as well.

For the T178I the $K'_1k'_{+2}$ value sits between the two other mutants with a 3-fold slower rate constant (3.3 ± 0.2 μM^{-1} s^{-1}) than wild type. This was the only mutant to have a significantly weaker ATP affinity (317.7 ± 41.1 µM) than the wild type by nearly 4-fold. This was also the only mutant that showed an increase in the k'_{+2} value (1033 ± 60 s^{-1}) compared to the wild type. Like the R672H there was a slower second phase that occurred, however unlike the R672H this only appeared at ATP concentrations above 50 µM. The K_{α} (6.9 ± 1) was slightly higher than the R672H, and the $k_{+\alpha}$ was 2 times faster (66.1 ± 9.1 s^{-1}) than the R672H. The K_{α} difference between T178I and R672H was not significantly different while the $k_{+\alpha}$ values were.

The ADP affinity was determined the same way as the wild type MyHC-emb (Chapter 4.2). Here acto.S1 was rapidly mixed with a mixture of ATP and ADP. The T178I behaved in the same manner as the wild type, where there is only one phase that gets slower as the ADP concentration increases (Figure 5.6).

For the T178I the k_{obs} decreased as the ADP concentration increased (Figure 5.6). When k_{obs} was plotted as a function of ADP concentration it followed a similar hyperbola as the wild type S1 and resulted in a similar ADP affinity (12.4 ± 2.2 µM) as the wild type (14.3 ± 1.9 µM) with no significant difference between the two.

For the two R672 mutations there was a constant second slow phase at all ADP concentrations. The k_{obs} was not affected by the ADP concentration, but the relative amplitude was. Figure 5.7A shows the transients for R672H as an example of how the fast and slow phases were affected by the increase in ADP concentration. As the ADP concentration increased the amplitude of the fast phase decreased, while the amplitude of the slow phase increased.

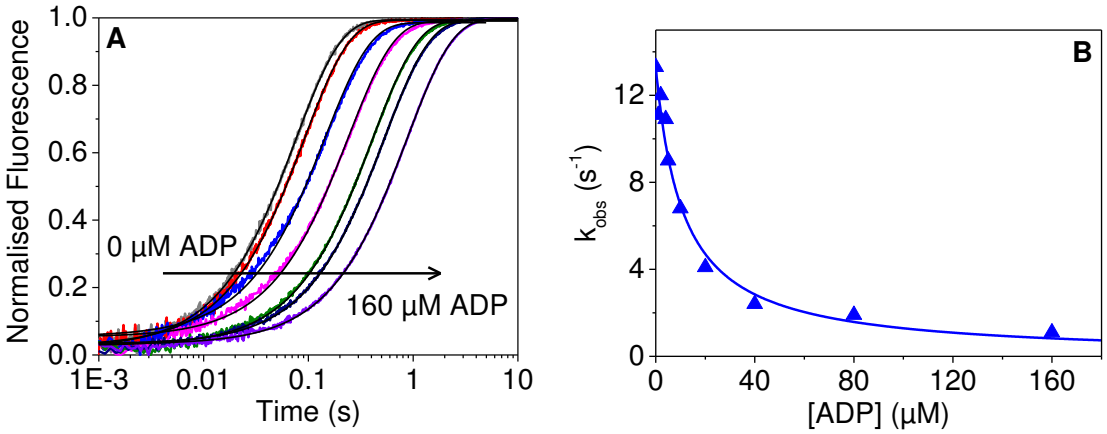

Figure 5.6 - T178I ADP affinity in the presence of actin. (A) Transients of 50 nM acto.S1 versus 0-160 µM ADP and 5 µM ATP. As the ADP concentration increases the k_{obs} decreases. The increase in fluorescence was best described by a single exponential in all cases. (B) Plotting the k_{obs} as a function of ADP concentration follows a hyperbolic dependence which resulted in a value of $K'_6K'_7$.

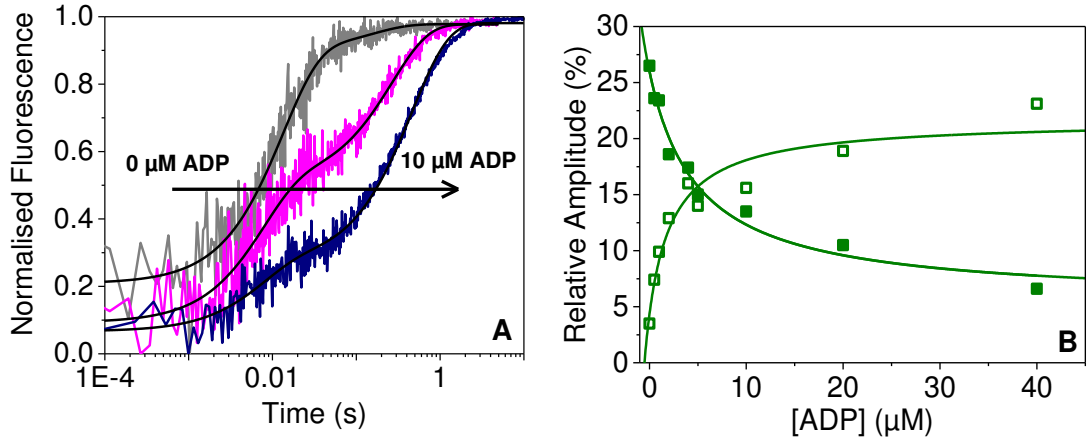

Figure 5.7 - R672H ADP affinity in the presence of ADP. (A) Transients of 50 nM R672H acto.S1 rapidly mixed with 30 µM ATP and 0-10 µM ADP. In all cases the increase in fluorescence was best described by a double exponential. The amplitude of the fast phase decreased while the amplitude of the slow phase increased, the k_{obs} was not affected with the increase in ADP concentration. (B) When the relative amplitude (fluorescence amplitude/end point fluorescence x 100) of the two phases are plotted against the ADP concentration then it follows two hyperbolic fits which can give the ADP affinity ($K'_6K'_7$).

Plotting the relative amplitudes as a function of ADP concentration resulted in two hyperbolic functions (Figure 5.7B) which were best described by equations 2.20 (fast phase) and 2.24 (slow phase, Chapter 2.3.2.1). R672H has been shown as an example of what happened for both the R672 mutants.

The ADP affinity for the R672H mutation was found to be nearly 3-fold tighter (4.8 ± 0.5 μM) than the wild type (14.3 ± 1.9 μM). For the R672C however there was no significant change however the affinity did become weaker (18.1 ± 1.7 μM) than the wild type.

The ADP release rate constant (k'_{+6}) was determined using the same method as wild type MyHC-emb. Acto.S1 was incubated with a saturating concentration of ADP (20 times the $K'_6K'_7$, therefore 100, 360 or 250 μM ADP for R672H, R672C, and T178I respectively) and rapidly mixed with mM concentrations of ATP. Since the acto.S1 is saturated with ADP it will all be in the A.M.D state and the k_{obs} will be unaffected by ATP concentration. Therefore the k_{obs} observed will be the rate of ADP release. For R672H the k'_{+6} was almost 3-fold slower (7.4 ± 0.2 s^{-1}) than the wild type (22 ± 1.8 s^{-1}). However for the other two mutants there was a slight change but this was not found to be significantly different. R672C was 18.6 ± 1.1 s^{-1}, while T178I was 25.7 ± 0.5 s^{-1}.

5.2.3 Differences in actin affinity to R672H, R672C, and T178I embryonic S1 compared to WT embryonic S1

Determining the actin affinity in the absence and presence of ADP was carried out the same way as for the wild type MyHC-emb where a constant actin concentration was pre-incubated with increasing S1 concentrations and rapidly mixed with a constant ATP concentration (Chapter 4.2.3). Similarly to the wild type this assay carries the most error as the exact concentration of active S1 is needed. The method of determining this is the same as for the wild type (Chapter 4.2.3).

For R672H as the S1 concentration was increased the fluorescence amplitude also increases (Figure 5.8A). The relative amplitudes were plotted as a function of S1 concentration and fit using quadratic equation 3.1 (Chapter 3.2.3, Figure 5.8B and C). The actin affinity (K_A) was nearly 20-fold weaker (40.2 ± 2.1 nM) than the wild type (2.1 ± 0.2 nM). While the actin affinity in the presence of ADP (K_{DA}) was 40 % tighter (366.7 ± 31

nM) than the wild type (526 ± 60.3 nM), this was not a statistically significant difference.

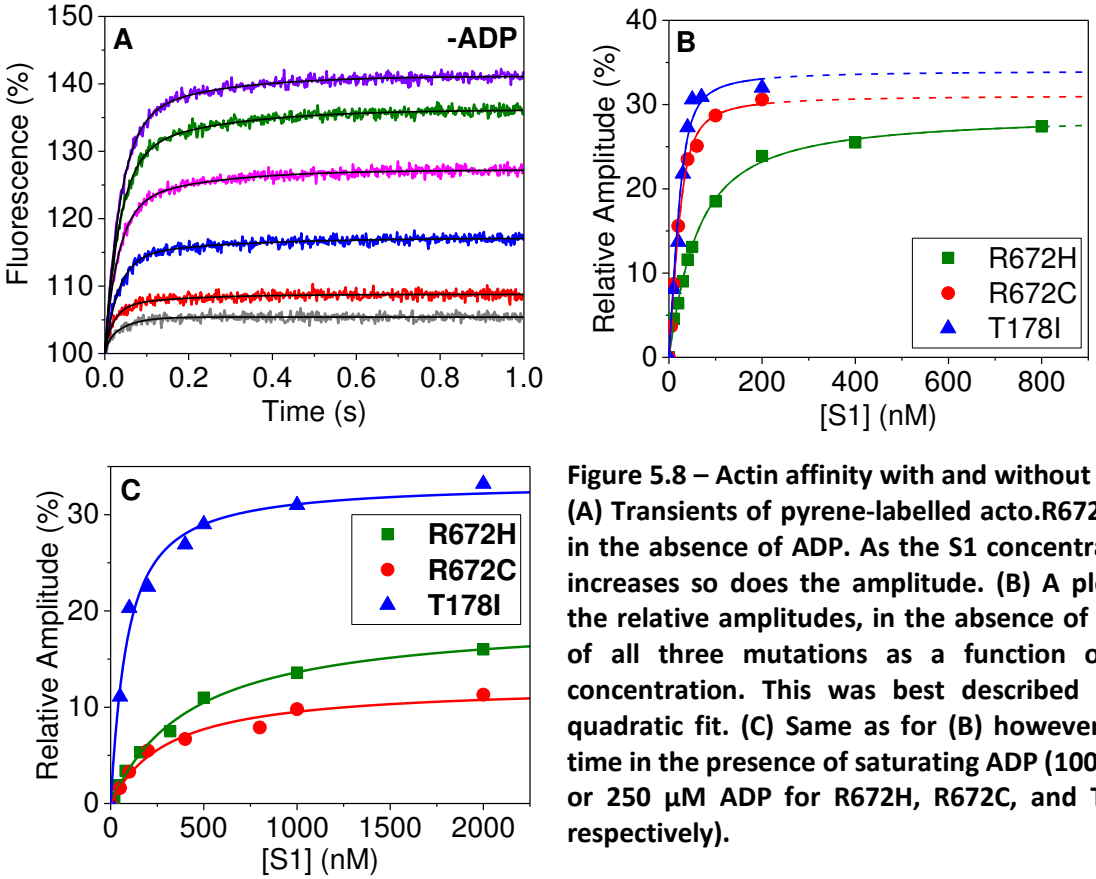

Figure 5.8 – Actin affinity with and without ADP. (A) Transients of pyrene-labelled acto.R672H S1 in the absence of ADP. As the S1 concentration increases so does the amplitude. (B) A plot of the relative amplitudes, in the absence of ADP, of all three mutations as a function of S1 concentration. This was best described by a quadratic fit. (C) Same as for (B) however this time in the presence of saturating ADP (100, 360 or 250 µM ADP for R672H, R672C, and T178I respectively).

For R672C there was also a statistically significant weakening (7.2 ± 1.2 nM) in the K_A compared to the wild type (Figure 5.8B) however given the limitations to this measurement (Chapter 4.3.2) this may not be an actual difference. The K_{DA} similarly to the R672H was found to be tighter (331.3 ± 68.6 nM) than the wild type however this was not statistically significant either (Figure 5.8C).

The T178I had a 2-fold weaker K_A (4.8 ± 0.2 nM) which was found to be a statistically significant change (Figure 5.8B) however like the R672C may not be an actual change. The K_{DA} on the other hand was found to be 4 times tighter (123.5 ± 15.1 nM) than the wild type, which is also a significant change (Figure 5.8C).

The relative fluorescence amplitudes only reached the same maximum level for the T178I in the presence of ADP. This may be indicative of the S1.ADP being less able to quench the signal.

5.2.4 Steady state ATPase data

The steady state ATPase assay was carried out using the same method as for the wild type MyHC-emb (Chapter 4.2.4) by Carlos Vera (University of Colorado, USA). The maximum rate of the cycle (V_{max}) and concentration of actin needed for half the maximum rate (K_M) was determined the same way (Figure 5.9).

For the R672H, the V_{max} was 5-fold slower (1.3 ± 0.05 s^{-1}) compared to the wild type (7.0 ± 0.15 s^{-1}). The K_M was also affected; this was 10 times tighter (3.7 ± 0.7 µM) than the wild type (Figure 5.7A). The V_{max}/K_M was therefore affected, this calculated value was larger (0.35 s^{-1} μM^{-1}) than the wild type (0.18 s^{-1} μM^{-1}, Table 5.1).

The R672C also had a much slower V_{max} (0.35 ± 0.05 s^{-1}) than the wild type and even the R672H; this was 20-fold slower. The K_M was also tighter (4.6 ± 0.3 µM) than the wild type though not as tight as the R672H (Figure 5.9A). The V_{max}/K_M was over 4 time faster (0.76 s^{-1} μM^{-1}) than the wild type and R672H (Table 5.1).

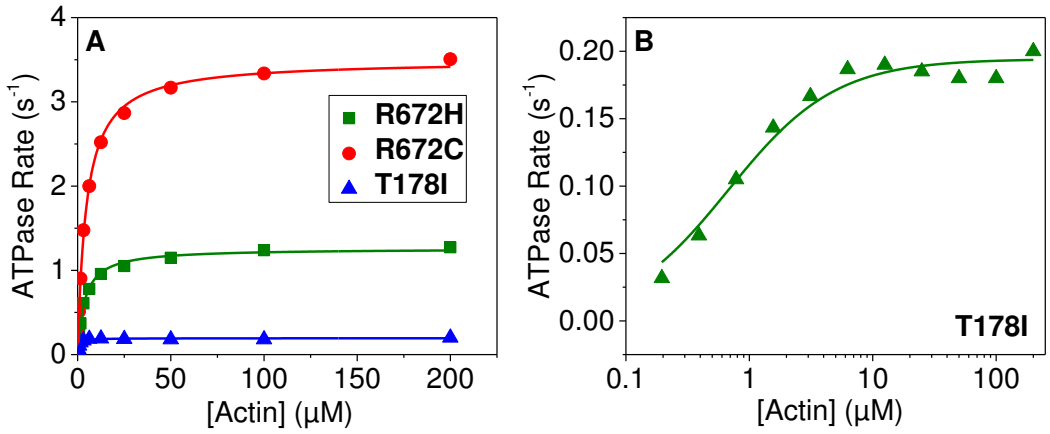

Figure 5.9 – ATPase data for the three FSS mutations. (A) Comparison of all three ATPase curves. (B) ATPase data for the T178I plotted on a logarithmic scale to highlight that the data was not linear.

Finally, for the T178I the V_{max} was significantly slower (0.2 ± 0.008 s^{-1}) than the wild type. This value is 35 times slower, and is considerably slower than the other two mutants as well. The K_M value is also orders of magnitude tighter (0.67 ± 0.16 µM) than the wild type and both R672 mutants (Figure 5.9A). The ATPase activity is so small that on a linear plot of ATPase rate against actin concentration the data looked like a flat line and therefore

that there was no activation upon actin binding. To highlight that there is some activity the data was plot using a logarithmic scale of actin concentration instead (Figure 5.7B). The V_{max}/K_M was very similar to the R672H (0.30 s^{-1} μM^{-1}) and nearly 2-fold faster than the wild type.

Table 5.1 – Rate and equilibrium constants of the wild type MyHC-emb compared to the 3 FSS mutations: R672H, R672C, and T178I. Statistically significant differences compared to wild type MyHC-emb (determined by Student's *t* test) have been shaded grey. Buffer conditions were: 25 mM KCl, 20 mM MOPS, 5 mM $MgCl_2$, 1 mM DTT, pH 7.0 unless stated otherwise.

Rate/Equilibrium Constant	Wild Type Emb [a]	Emb R672H	Emb R672C	Emb T178I
ATP binding to S1				
K_1k_{+2} (μM^{-1} s^{-1})	12.5 ± 1.9	0.4 ± 0.04 [d]	1.1 ± 0.07 [d]	2.3 ± 0.1 [c]
$1/K_1$ (μM)	10.9 ± 2.0	34.4 ± 5.0 [b]	23.6 ± 2.6 [b]	7.7 ± 0.6
k_{max} or $k_{+3} + k_{-3}$ (s^{-1})	130 ± 3.4	14.3 ± 0.5 [d]	25.4 ± 1.3 [d]	17.7 ± 0.6 [d]
ADP binding to S1				
K_6K_7 (μM)	0.15 ± 0.018	-	0.2 ± 0.04	-
k_{+6} (s^{-1})	0.89 ± 0.07	-	-	-
ATP binding to actin.S1				
$K'_1k'_{+2}$ (μM^{-1} s^{-1})	9.4 ± 1.0	4.5 ± 0.3 [c]	2.2 ± 0.5 [d]	3.3 ± 0.2 [d]
$1/K'_1$ (μM)	84.3 ± 9.7	92.3 ± 9	120 ± 19.3	317.7 ± 41.1 [c]
k'_{+2} (s^{-1})	777 ± 17	413 ± 32 [d]	261 ± 8.4 [d]	1033 ± 60 [b]
$K_{\alpha1}$	-	4.4 ± 0.8	-	6.9 ± 1
$k_{+\alpha1}$ (s^{-1})	-	31.5 ± 2.5	-	66.1 ± 9.1
ADP binding to actin.S1				
$K'_6K'_7$ (μM)	14.3 ± 1.9	4.8 ± 0.5 [c]	18.1 ± 1.7	12.4 ± 2.2
k'_{+6} (s^{-1})	22.0 ± 1.8	7.4 ± 0.2 [d]	18.6 ± 1.1	25.7 ± 0.5
$K'_7k'_{-6}$ (μM^{-1} s^{-1})	1.5	1.5	1	2.1
$K'_6K'_7/K_6K_7$	95	-	90.5	-
S1 affinity for actin				
K_A (nM)	2.1 ± 0.2	40.2 ± 2.1 [d]	7.2 ± 1.2 [b]	4.8 ± 0.2 [d]
K_{DA} (nM)	526 ± 60.3	366.7 ± 31	331.3 ± 68.6	123.5 ± 15.1 [d]
K_{DA}/K_A	250	9	46	25.7
ATPase *				
V_{max} (s^{-1})	7.0 ± 0.15	1.3 ± 0.05 [d]	3.5 ± 0.05 [d]	0.2 ± 0.008 [d]
K_M (μM)	38.5 ± 2.4	3.7 ± 0.7 [c]	4.6 ± 0.3 [d]	0.67 ± 0.16 [d]
V_{max}/K_M (s^{-1} μM^{-1})	0.18	0.35	0.76	0.30

[a] Chapter 4

[b] $p < 0.05$ determined by Student's *t* test as compared to wild type MyHC-emb S1.

[c] $p < 0.01$ determined by Student's *t* test as compared to wild type MyHC-emb S1.

[d] $p < 0.005$ determined by Student's *t* test as compared to wild type MyHC-emb S1.

* 0 mM KCl, 20 mM MOPS, 5 mM $MgCl_2$, 1 mM DTT, pH 7.0

5.2.5 Modelling the ATPase cycle

The stopped-flow data reveals the majority of the steps in the cross-bridge cycle while the ATPase data shows how quickly the cycle proceeds. However, the actin rebinding step following the ATP hydrolysis and the phosphate release step are not well defined using either method. Using a more detailed cross-bridge cycle (Scheme 5.1) and modelling software (Berkeley Madonna), it is possible to use the data from the stopped-flow and ATPase assays to estimate these two steps.

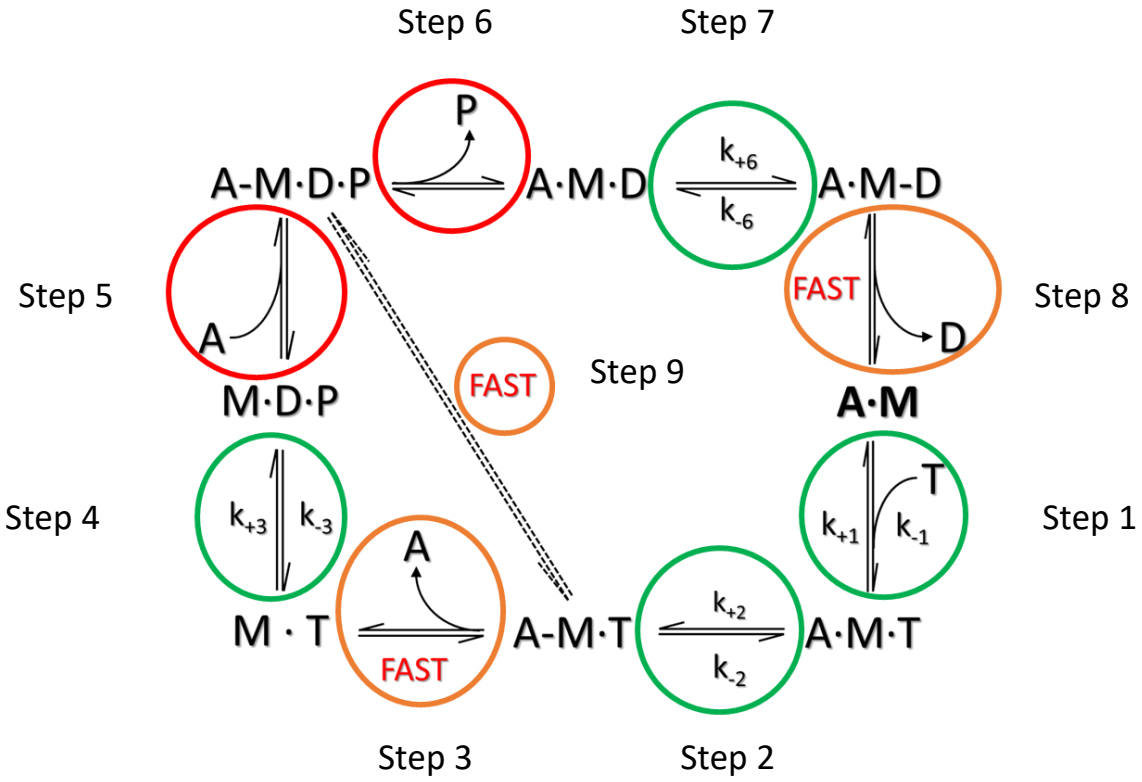

Scheme 5.1 – Scheme used for the modelling on Berkley Madonna. Equilibria circled in green are values that were determined from the stopped-flow measurements. Those circled in orange are either diffusion limited or generally very fast and such were given values to make them fast. Those circled in red were not measured in the stopped-flow assays, however can be estimated by fitting the whole cycle to the V_{max} and K_M values from the ATPase assays. If step 9 were not there then at very high actin concentrations the cycle would be inhibited as step 3 is reversible and the cycle would be stuck in the A-M.T state (Stein *et al*, 1981) The step numbers shown are those used in the modelling, those in the circles correspond to that seen in figure 1.10 and scheme 4.1.

As scheme 5.1 shows four of the rate constants were known from the stopped-flow assays (green circles). Three of the steps are assumed to be fast and therefore given a

forward rate constant of 1,000 (orange circles). These variables have little impact upon the cycling rate and therefore the only two variables that will need to be adjusted are the actin rebinding and phosphate release. Using the ATPase data as a guide it was possible through trial and error to estimate these values to result in modelled ATPase data that matched the measured data.

Step	Equilibrium Constant		Forward rate constant		Reverse rate constant	
	value	units	value	units	value	units
1 – ATP binding	**0.0119**	μM^{-1}	10.0000	$s^{-1}\ \mu M^{-1}$	**843.0000**	s^{-1}
2 – conformational change in AMT	10.0000	-	**777.0000**	s^{-1}	77.7000	s^{-1}
3 – dissociation	100.0000	µM	1000.0000	s^{-1}	10.0000	$s^{-1}\ \mu M^{-1}$
4 – hydrolysis	10.0000	-	**130.0000**	s^{-1}	13.0000	s^{-1}
5 – actin rebinding	**0.0154**	μM^{-1}	**10.0000**	$s^{-1}\ \mu M^{-1}$	**650.0000**	s^{-1}
6 – phosphate release	**135.0000**	µM	**13.5000**	s^{-1}	**0.1000**	$s^{-1}\ \mu M^{-1}$
7 – conformational change in AMD	7.3333	-	**22.0000**	s^{-1}	3.0000	s^{-1}
10 – ADP release	100.0000	µM	1000.0000	s^{-1}	10.0000	$s^{-1}\ \mu M^{-1}$
11 – ATP hydrolysis without detachment	100.0000	-	20.0000	s^{-1}	0.2000	s^{-1}
V_{max}	**7**					
K_M	**38.5**					

Table 5.4A – WT embryonic myosin - Values used to model the cross bridge cycle. Green text indicate values determined from either stopped-flow or ATPase assays, orange indicates values assumed to be very fast or diffusion limited, red text shows values that were estimated to fit the V_{max} and K_M, grey text indicates values from detailed balance ($K_i = k_{+i}/k_{-i}$). The forward and reverse rate constants were used in the Berkley Madonna software.

Step	Equilibrium Constant		Forward rate constant		Reverse rate constant	
	value	units	value	units	value	units
1 – ATP binding	**0.0109**	μM^{-1}	**10.0000**	$s^{-1}\ \mu M^{-1}$	**920.0000**	s^{-1}
2 – conformational change in AMT	**100.0000**		**400.0000**	s^{-1}	**4.0000**	s^{-1}
3 – dissociation	**100.0000**	µM	**1000.0000**	s^{-1}	**10.0000**	$s^{-1}\ \mu M^{-1}$
4 – hydrolysis	**10.2143**		**14.3000**	s^{-1}	**1.4000**	s^{-1}
5 – actin rebinding	**0.2500**	μM^{-1}	**10.0000**	$s^{-1}\ \mu M^{-1}$	**40.0000**	s^{-1}
6 – phosphate release	**17.0000**	µM	**1.7000**	s^{-1}	**0.1000**	$s^{-1}\ \mu M^{-1}$
7 – conformational change in AMD	**18.5000**		**7.4000**	s^{-1}	**0.4000**	s^{-1}
10 – ADP release	**100.0000**	µM	**1000.0000**	s^{-1}	**10.0000**	$s^{-1}\ \mu M^{-1}$
11 – ATP hydrolysis without detachment	**100.0000**		**20.0000**	s^{-1}	**0.2000**	s^{-1}
V_{max}	**1.3**					
K_M	**3.7**					

Table 5.4B – R672H embryonic myosin - Values used to model the cross bridge cycle. Green text indicate values determined from either stopped-flow or ATPase assays, orange indicates values assumed to be very fast or diffusion limited, red text shows values that were estimated to fit the V_{max} and K_M, grey text indicates values from detailed balance ($K_i = k_{+i}/k_{-i}$). The forward and reverse rate constants were used in the Berkley Madonna software.

Step	Equilibrium Constant		Forward rate constant		Reverse rate constant	
	value	units	value	units	value	units
1 – ATP binding	**0.0083**	μM^{-1}	**10.0000**	$s^{-1}\ \mu M^{-1}$	**1200.0000**	s^{-1}
2 – conformational change in AMT	**100.0000**		**261.0000**	s^{-1}	**2.6100**	s^{-1}
3 – dissociation	**100.0000**	μM	**1000.0000**	s^{-1}	**10.0000**	$s^{-1}\ \mu M^{-1}$
4 – hydrolysis	**10.0000**		**25.4000**	s^{-1}	2.5400	s^{-1}
5 – actin rebinding	**0.1667**	μM^{-1}	**10.0000**	$s^{-1}\ \mu M^{-1}$	**60.0000**	s^{-1}
6 – phosphate release	**60.0000**	μM	**6.0000**	s^{-1}	**0.1000**	$s^{-1}\ \mu M^{-1}$
7 – conformational change in AMD	**5.4706**		**18.6000**	s^{-1}	**3.4000**	s^{-1}
10 – ADP release	**100.0000**	μM	**1000.0000**	s^{-1}	**10.0000**	$s^{-1}\ \mu M^{-1}$
11 – ATP hydrolysis without detachment	**100.0000**		**20.0000**	s^{-1}	**0.2000**	s^{-1}
V_{max}	**3.5**					
K_M	**4.6**					

Table 5.4C – R672C embryonic myosin - Values used to model the cross bridge cycle. Green text indicate values determined from either stopped-flow or ATPase assays, orange indicates values assumed to be very fast or diffusion limited, red text shows values that were estimated to fit the V_{max} and K_M, grey text indicates values from detailed balance ($K_i = k_{+i}/k_{-i}$). The forward and reverse rate constants were used in the Berkley Madonna software.

Step	Equilibrium Constant		Forward rate constant		Reverse rate constant	
	value	units	value	units	value	units
1 – ATP binding	**0.0031**	μM^{-1}	**10.0000**	$s^{-1} \mu M^{-1}$	**3177.0000**	s^{-1}
2 – conformational change in AMT	**10.0000**		**1033.2000**	s^{-1}	**10.3320**	s^{-1}
3 – dissociation	**100.0000**	µM	**1000.0000**	s^{-1}	**10.0000**	$s^{-1} \mu M^{-1}$
4 – hydrolysis	**10.0000**		**17.7000**	s^{-1}	**1.7700**	s^{-1}
5 – actin rebinding	**1.6667**	μM^{-1}	**10.0000**	$s^{-1} \mu M^{-1}$	**6.0000**	s^{-1}
6 – phosphate release	**2.0000**	µM	**0.2000**	s^{-1}	**0.1000**	$s^{-1} \mu M^{-1}$
7 – conformational change in AMD	**8.0313**		**25.7000**	s^{-1}	**3.2000**	s^{-1}
10 – ADP release	**100.0000**	µM	**1000.0000**	s^{-1}	**10.0000**	$s^{-1} \mu M^{-1}$
11 – ATP hydrolysis without detachment	**100.0000**		**20.0000**	s^{-1}	**0.2000**	s^{-1}
V_{max}	**0.2**					
K_M	**0.67**					

T178I embryonic myosin

Table 5.4D – Values used to model the cross bridge cycle. Green text indicate values determined from either stopped-flow or ATPase assays, orange indicates values assumed to be very fast or diffusion limited, red text shows values that were estimated to fit the V_{max} and K_M, grey text indicates values from detailed balance ($K_i = k_{+i}/k_{-i}$). The forward and reverse rate constants were used in the Berkley Madonna software.

To conduct the modelling a concentration of 0.1 µM S1 was set, along with 5 mM ATP. The program has an option to perform a batch run where the parameter changing (actin

concentration) could be set, the number of runs that would be performed (11 actin concentrations), and the initial (0 µM) and final (100 µM) actin concentrations.

Myosin has a very low basal ATPase rate, hydrolysing ATP very slowly while actin works to enhance the ATPase activity by rebinding to S1 and forcing phosphate and ultimately ADP off the S1. Therefore to determine the ATPase rate at each actin concentration the free ADP concentration was monitored (Figure 5.10). The gradients from the increases in ADP concentration were then used to determine the ATPase rate (Equation 5.1).

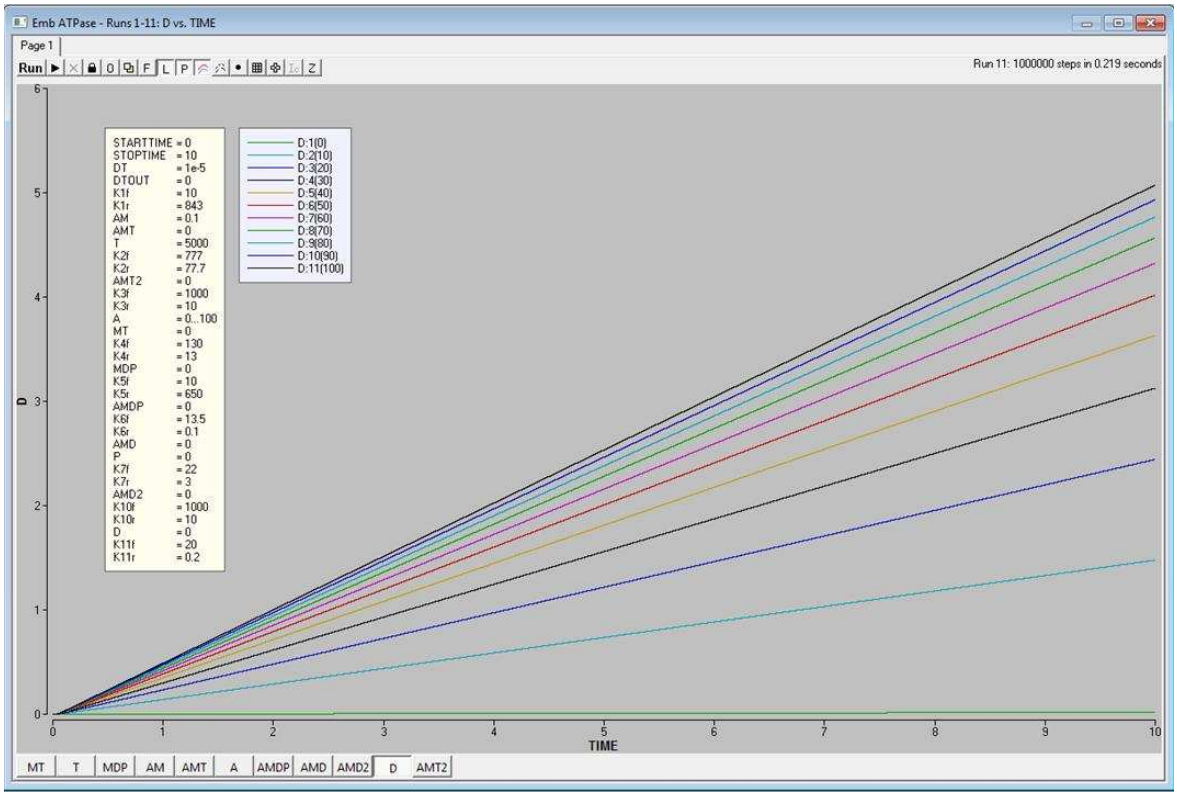

Figure 5.10 – An example batch run for WT MyHC-emb. The initial actin concentration was set at 0 µM increasing by 10 µM to a maximum concentration of 100 µM. The initial concentration of ATP was set at 5 mM and the concentration of ADP monitored. The units for the y-axis is µM and the x-axis is seconds.

$$ATPase\ rate = \frac{gradient}{[S1]} \qquad \text{Equation 5.1}$$

These ATPase rates were then plotted as a function of actin concentration (Figure 5.11) and fit with the classic Michaelis-Menten equation (Equation 5.2) to determine the V_{max} and the K_M.

$$v = \frac{V_{max}[S]}{K_M + [S]} \qquad \text{Equation 5.2}$$

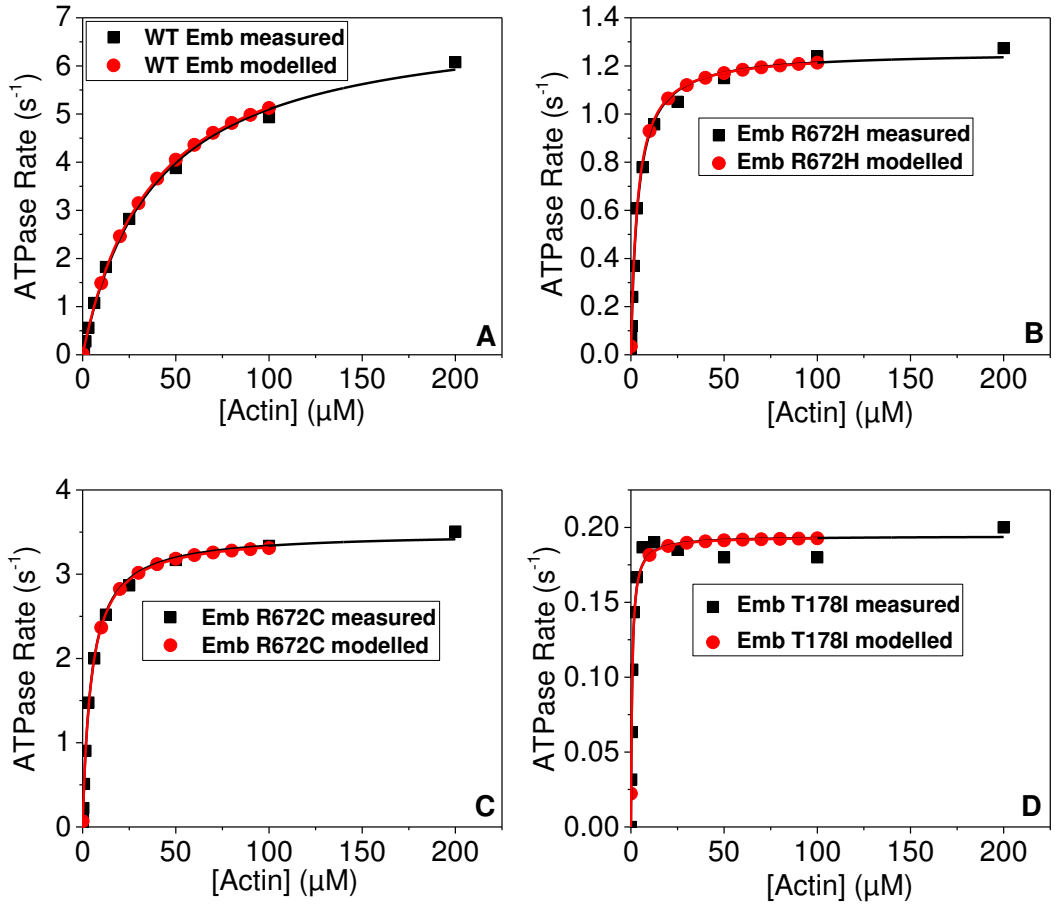

Figure 5.11 – Modelled ATPase data compared to ATPase measurements from figures 4.10 and 5.9. (A) Modelled ATPase data versus the measured ATPase data of the wild type MyHC-emb. The V_{max} of the measured and modelled are 7.06 s^{-1} and 7.04 s^{-1} respectively, while the K_M for the measured and modelled are 38.5 µM and 37.1 µM respectively. (B) Modelled ATPase data versus the measured ATPase data of the R672H MyHC-emb. The V_{max} of the measured and modelled are 1.26 s^{-1} and 1.25 s^{-1} respectively, while the K_M for the measured and modelled are 3.7 µM and 3.5 µM respectively. (C) Modelled ATPase data versus measured ATPase data of the R672C MyHC-emb. The V_{max} of the measured and modelled are 3.5 s^{-1} and 3.47 s^{-1} respectively, while the K_M for the measured and modelled are 4.6 µM and 4.62 µM respectively. (D) Modelled ATPase data versus the measured ATPase data of the T178I MyHC-emb. The V_{max} of the measured and modelled are both 0.19 s^{-1}, while the K_M for the measured and modelled are 0.67 µM and 0.68 µM respectively.

It was found that the actin rebinding step strongly influenced the K_M value while the phosphate release step influenced the V_{max}. As figure 5.10 shows the modelled data matches the measured ATPase data very well with K_M and V_{max} values very similar. This increased the confidence in our models since the model and measured data matched.

Using the measured and estimated values it was then possible to run the assay until it reached a steady state and determine what proportion of the cycle is occupied by each step. The cycle at V_{max} was simulated by setting the actin concentration to 3 times the K_M

value for the wild type and three mutants individually (Figure 5.12). Since the actin concentration can vary significantly in a functioning muscle due to the proximity of a myosin to actin. Therefore a high concentration of actin was simulated. An actin concentration equal to 3 x K_M was used which should give a V_{max} of 75%. These models were under unloaded conditions. To model loaded conditions the phosphate release step and ADP release step are thought to be reduced. However when modelling a loaded system the occupancy of the cycle was relatively unchanged due to already slow phosphate and ADP release steps, slowing these steps further had little effect.

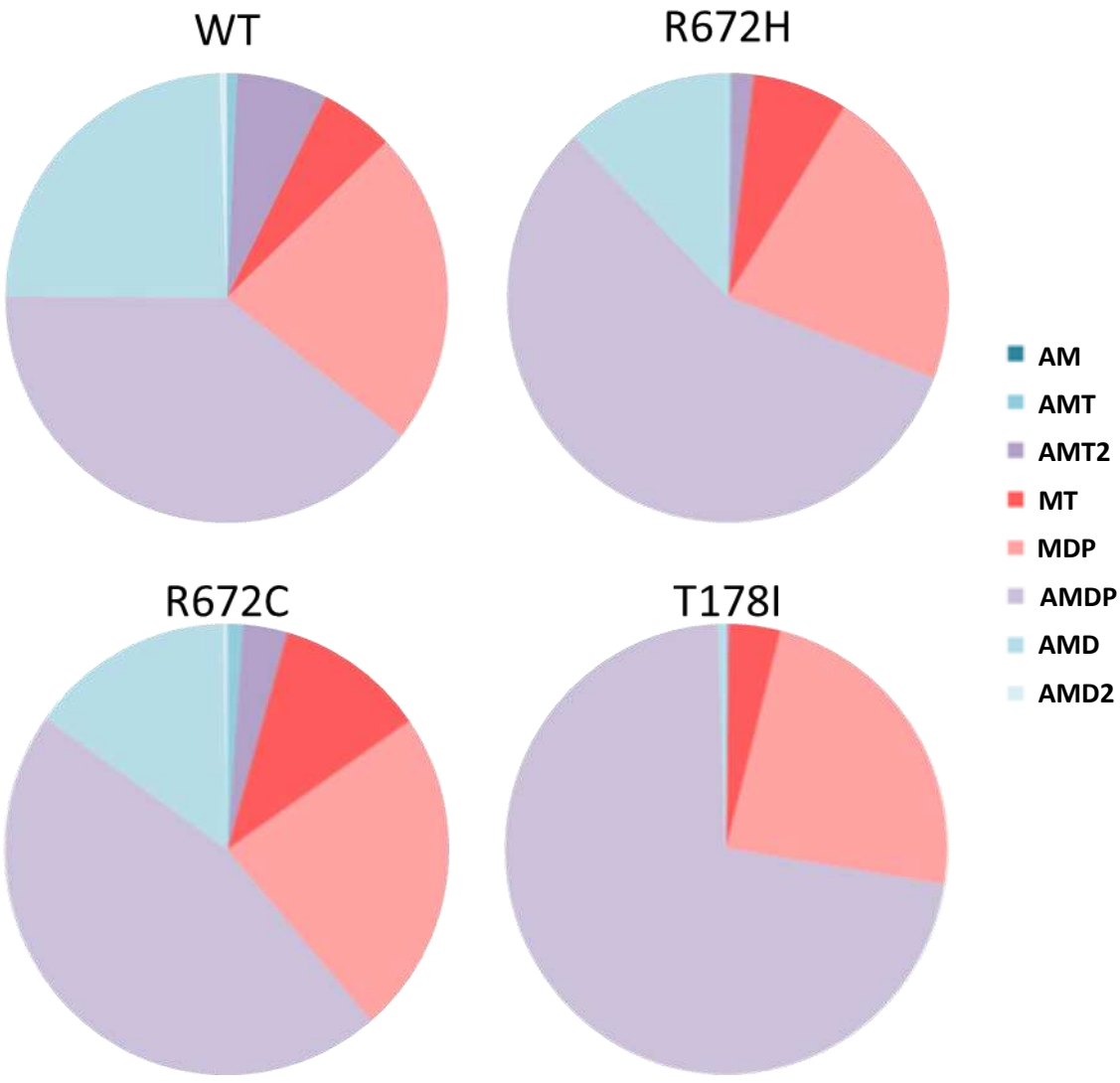

Figure 5.12 – Myosin head domain occupancy of unloaded S1 at 75% V_{max} with an actin concentration 3 x K_M. After 1 second the reaction was at steady state for all four myosins when modelled. The occupancy of the cross bridge is displayed as a pie chart and colour coded based on the strength of binding. Blue indicates strong binding between myosin and actin, purple is weak binding between actin and myosin, and pink is detachment of myosin from actin.

As figure 5.12 shows approximately 75 % of the time the WT MyHC-emb is in the weakly bound (AMT2 and AMDP) or detached state (MT and MDP). AMDP is the largest section indicating that the phosphate release step is limiting the cycle somewhat as it is slow enough to accumulate more of the S1. The AMD state is also large due to the slow ADP release rate constant (k'_{+6}). The AMDP state increases dramatically for the three mutants most notably for the T178I. Therefore once activated the mutants will spend a longer time in the AMDP state due to a slower phopshate release step.

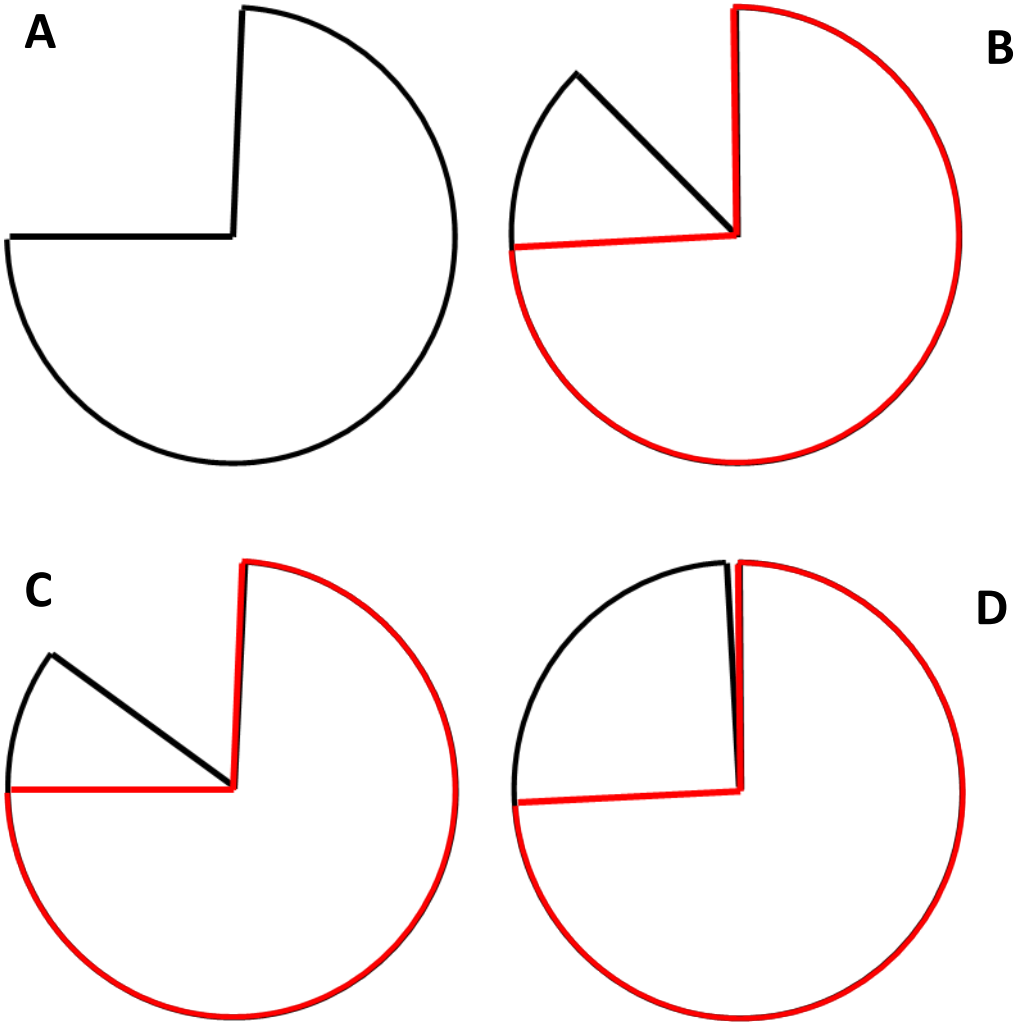

Figure 5.13 – Comparison of the weakly and unbound myosin from actin. (A) Approximately 75 % of the WT MyHC-emb is in the weak binding or detached state. (B) The overlay of WT MyHC-emb (red) shows that there is an increase in the detached and weakly bound states for R672H MyHC-emb (black). (C) The overlay of WT MyHC-emb (red) shows that there is an increase in the detached and weakly bound states for R672C (black), however this is smaller than the R672H. (D) The overlay of WT MyHC-emb (red) shows there is a huge increase in the detached and weakly bound states for T178I (black). This is the largest increase seen with almost all of the myosin either detached or weakly bound.

Figure 5.13 shows a comparison of the weakly bound and detached states of the WT MyHC-emb and the three mutants by overlaying the WT MyHC-emb (red) on top of the mutants (black). The R672C (Figure 5.13C) has the smallest increase in this weak attachment, R672H has a bigger increase (Figure 5.13B) and T178I is almost entirely weakly attached (Figure 5.13D).

5.2.6 Interaction changes between surrounding residues in mutants and WT MyHC-emb

R672 and T178 are both found within the centre of the myosin motor domain (Figure 5.10A). They are also very far apart in the myosin sequence but are very close to each other in the structure which will have some significance in their importance to each other.

R672 is located on the third strand of the central 7-stranded β-sheet that runs through the motor domain. The T178 is found at the C-terminal end of the fourth β strand of the central β-sheet at the start of the P-loop of the nucleotide binding pocket. Preliminary observations have highlighted potential residues for interaction (Figure 5.10B).

Due to no MyHC-emb X-ray crystallography structure yet being available, homology models were built using 6 structures of the scallop myosin S1. These represent the motor domain during various steps of the cross-bridge cycle and will help provide information into how these interactions change throughout the ATPase cycle. To build the homology models the sequence of the scallop structures were pairwise aligned with the sequence of the MyHC-emb. This was then uploaded to SWISS-MODEL (Biasini, Bienert et al. 2014, Arnold, Bordoli et al. 2006, Guex, Peitsch et al. 2009, Kiefer, Arnold et al. 2009) which was used to build the models.

The interactions present in the wild type and two R672 mutants are summarised in Table 5.2.

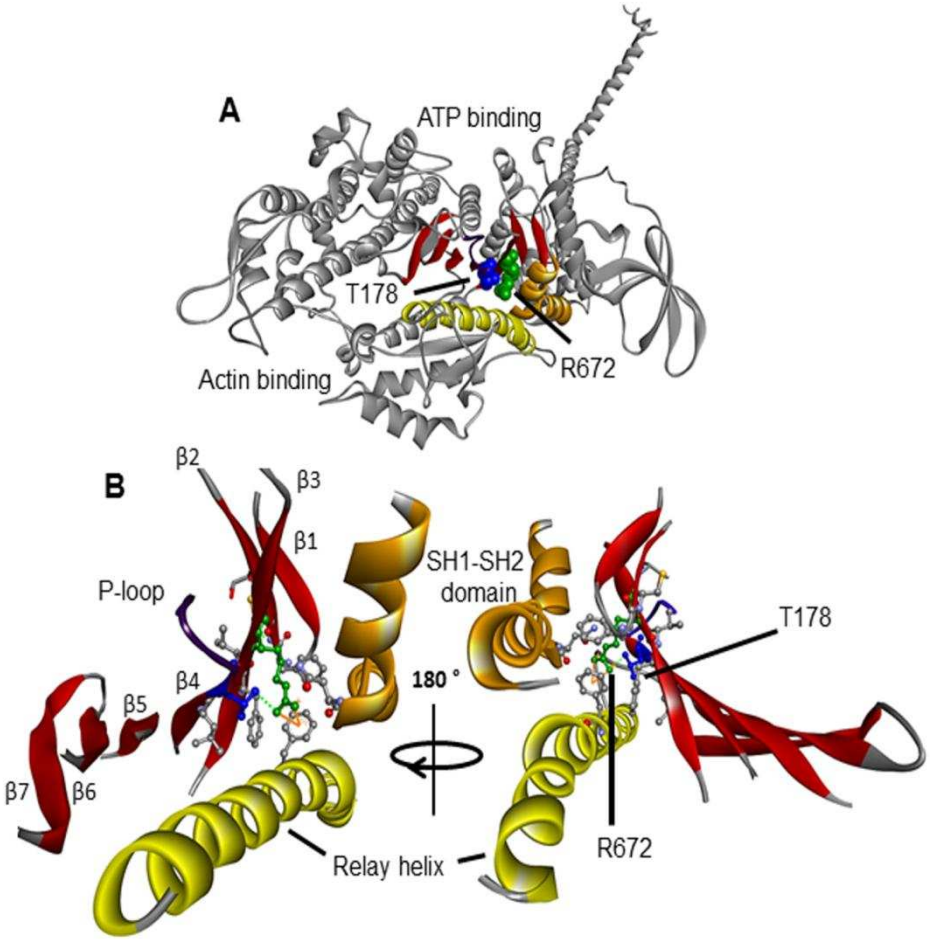

Figure 5.10 – Ribbon diagram of the homology MyHC-emb structure in the pre-power stroke state (1QVI). (A) Shows the whole molecule with the relay helix (yellow), central β sheet (red), and SH1-SH2 domain (orange). R672 (green) and T178 (blue) are shown as space filling. (B) An enhanced image of the R672 and T178 and the residues in possible contact with the two residues.

The two key interactions found to be partially or completely lost in the two mutants are a hydrogen bond between R672 and T178, and a π-cation bond between R672 and F490. A hydrogen bond is a fairly weak intermolecular bond between a hydrogen and either an oxygen, nitrogen or fluorine. A π-cation bond however is much stronger, similar to an ionic bond (Dougherty 1996). These occur between positive ions (in this case the R group of the R672) and the negative delocalised electrons of a benzene ring structure (the R group of the F490). A loss of such a bond could have serious and significant implications for the molecule.

For the R672H, there is a partial loss of the hydrogen bond between T178 which is present in all structures of the ATPase cycle. However the π-cation to F490 is completely lost in all cases. The R672C on the other hand has a complete loss of the hydrogen bond to T178 in all the structures as well as complete loss of the π-cation bond to F490.

The interactions for T178 are summarised in Table 5.3. There are fewer potential interactions compared to the R672 and only the hydrogen bond between T178 and R672 appears to be affected by the mutation to isoleucine. This is completely lost in all 6 models. Figure 5.11 show the conservation of T178 and R672 across different myosins in humans. T178 is highly conserved among the skeletal myosins and is replaced by a serine in the other myosin molecules. The R672 however is highly conserved across all myosins apart from myosin 9 which has a lysine instead. In both cases the residues may have changed but the type of amino acid stays the same.

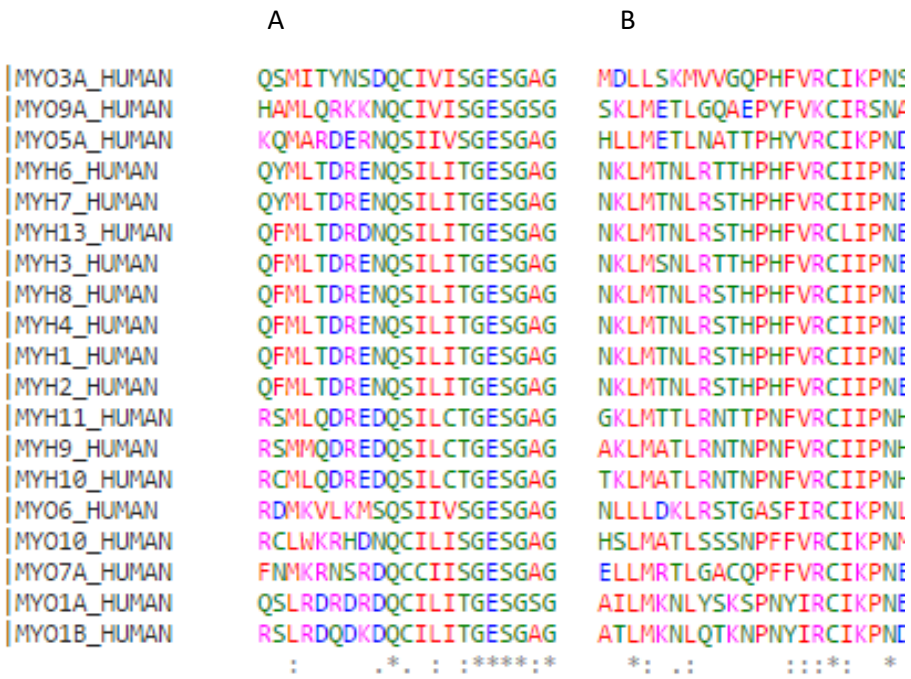

Figure 5.11 - Sequence alignment of multiple human myosin heavy chains. (A) The conservation of threonine 178 from MyHC-emb across different myosins. The threonine is either conserved or replaced by a serine. (B) The conservation of arginine 672 from MyHC-emb across different myosins. The arginine is highly conserved apart from a lysine in myosin 9.

R672 interactions	PDB		2OTG	2OS8	1SR6	1QVI	1KK8	1S5G
Residue (Scallop/Homology)	Location	Interaction	post-rigor (ADP)	rigor	post-rigor	pre-power	detached	near rigor ADP-
F119/F122	β2	π-cation/π-π bond						
C120/C123	β2	H-bond (main chain)						
A122/T125	β2	H-bond (main chain)						
L173/L176	β4	H-bond (side chain)						
T175/T178	β4	H-bond (side chain)						
F488/F490	Relay helix	π-cation bond						
F667/F670	β3	π-cation/π-π bond						
V668/V671	β3	H-bond (side chain)						
N694/N697	SH1-SH2	H-bond (side chain)						

	Interaction present in wt
	Interaction present in R672H
	Interaction present in R672C
	No interaction

Table 5.2 – Summary of R672 interactions. The interactions to T178 and F490 are explained in the text. The π-cation bond to F122 is lost in the R672C, while a π-π bond is formed in the 672H through benzene rings stacking. The hydrogen bonds to C123 and T125 are maintained in both mutants since they are on strands in the β-sheet. The hydrogen bond to L176 is lost in both mutations. Another π-π bond forms in the R672H to F670 in the pre-power orientation. While the hydrogen bond here in the detached state is lost. There is complete loss of the hydrogen bond between R672 and V671 for both mutations. An interesting occurrence is the formation of hydrogen bonds between R672 and N697 in both mutations.

T178I	PDB		2OTG	2OS8	1SR6	1QVI	1KK8	1SSG
Residue (Scallop/Homology)	Location	Interaction	post-rigor (ADP)	rigor	post-rigor	pre-power	detached	near rigor ADP-bound
V668/V671	β3	H-bond (main chain)		X	X	X	X	X
R669/R672	β3	H-bond (side chain)						
C670/C673	β3	H-bond (main chain)	X	X	X	X	X	X

	Interaction present in wt
X	Interaction present in T178I
	No interaction

Table 5.3 – Summary interaction of T178. The hydrogen bond between R672 and T178 is explained in the text. The hydrogen bonds between V671 and C673 are maintained in both mutations, due to the interactions occurring within the β-sheet.

5.3 Discussion

5.3.1 Kinetic differences between FSS mutants and wild type MyHC-emb

It is apparent from Table 5.1 that the kinetic changes between wild type MyHC-emb and the other three mutants are very significant. These differences have been summarised in figure 5.12 which clearly shows where there is an increase or decrease in affinity (Figure 5.12A) or rate constant (Figure 5.12B).

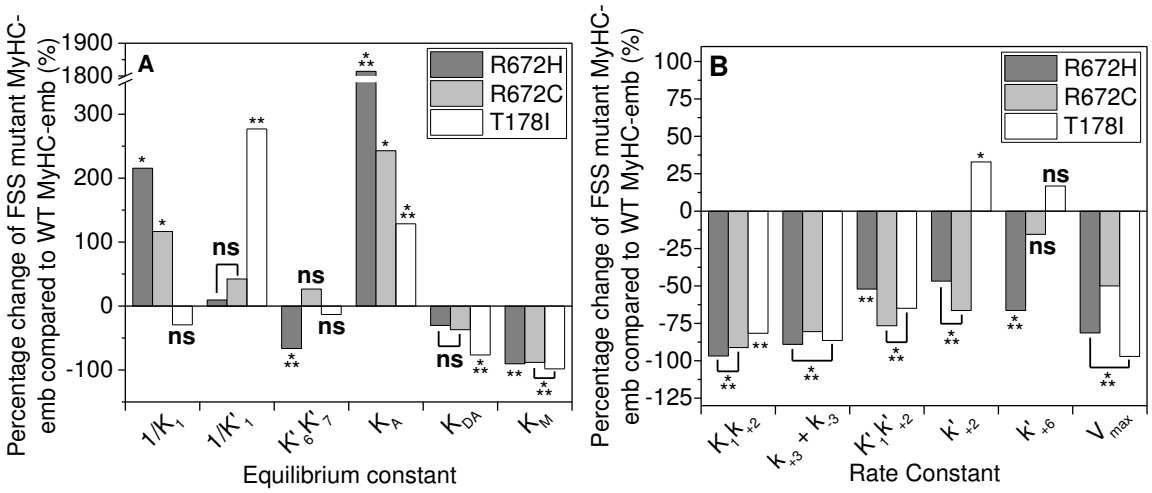

Figure 5.12 – Percentage changes between FSS mutants and WT MyHC-emb. (A) Percentage changes in the equilibrium constants of the three FSS mutants compared to wild type MyHC-emb. An increase or decrease in equilibrium constant indicates a weakening or tightening of the affinities compared to wild type respectively. (B) Percentage changes in rate constants of the three FSS mutants compared to wild type MyHC-emb. An increase or decrease in rate constant indicates the step is faster or slower than wild type respectively. * $p < 0.05$, ** $p < 0.01$, *** $p < 0.005$.

One of the common significant changes that was seen between the wild type MyHC-emb and the three mutants is the reduction in ATP hydrolysis rate constant ($k_{+3} + k_{-3}$). The slowing of this rate constant may even become the rate limiting step of the ATPase cycle. This could therefore be the cause of the reduction in maximum ATPase rate (V_{max}). However as the Berkeley Madonna modelling shows the rate limiting step is the phosphate release.

The slowing of the cycle also appears to be a common significant change for all three mutants. The slowing of the ATPase cycle will lead to a non-functioning motor which will inhibit the muscle. The reduction in the V_{max} may also contribute to the phenotype seen

for the T178I. Beck *et al*. (Beck, McMillin et al. 2014) showed that the phenotype of T178I was the most severe of the three mutations, followed by R672H, and R672C as the least severe. Taking into account the ATPase assay the kinetics begin to mirror the phenotypes somewhat. R672H has more differences compared to the wild type, T178I has some of the most significant differences and R672C while still having big changes may not be as severe as the other two.

5.3.2 Berkeley Madonna modelling

The modelling data gives a clear impression of how the ATPase cycle is behaving in the WT MyHC-emb and the three mutants. It also shows how the duty ratio will be affected in each case. For the WT MyHC-emb ≈75 % of the S1 was in the weakly bound and detached state. For the two R672 mutations the detached state increases to around 80 – 85 % of the cycle, while for the T178I almost all of the S1 is in either the detached or weakly bond state (Figure 5.13). This decreased attachment will reduce the force producing capabilities of the mutants, potentially causing them to be redundant motors. This would result in a net loss of energy as the ATP can still be hydrolysed but at a slower rate. The modelling data also estimates that the phosphate release step becomes the rate limiting step in the cycle, particularly in the T178I where the V_{max} is significantly limited by the phosphate release. Given that T178 is located in the P-loop which is responsible for binding to the γ-phosphate of ATP it is unsurprising that the release of this γ-phosphate is affected. However a prediction of how the mutation could affect the phosphate release step could not be made based on the structure.

5.3.3 Significance of interaction losses in the mutated myosin motor

Some clues as to the stopped-flow kinetic changes can be found in the homology models that were built. Both residues are located near to or adjacent to the nucleotide binding pocket. The loss of the hydrogen bond between the R672 and T178 may explain why the ATP binding ($K'_1k'_{+2}$) is reduced for all three mutations. This may also explain why the R672H mutation is the least effected since the hydrogen bond is maintained in some of

the structures. This would indicate that the bond is stabilising the nucleotide pocket, and losing it significantly affects the ability for ATP to bind. The effect of the two R672 mutations on the γ-phosphate release could be caused by one of two things or both: Firstly the loss of the H-bond between R672 and T178 disrupts the P-loop. Secondly the loss of the interaction with the relay helix limits the power stroke which is linked to the phosphate release.

Another observation from the structures is the cause for the reduced tryptophan fluorescence in all mutants most notably in the R672H and T178I. The loss of the π-cation bond between R672 and F490 on the relay helix may be a cause for this observation. Upon investigation in two structures: one in the rigor conformation (PDB 2OS8) where the relay helix is straight, and the other in the pre-power stroke (1QVI) where the relay helix is bent (Figure 5.13A). When the relay helix bends during ATP binding, the loop at the N-terminus of the helix moves in relation to the rest of the molecule. This results in the fluorescence signal seen. The F490 is located on the relay helix just before the helix bend and may contribute to holding the relay helix in place. Considering that the two R672 mutations lose tryptophan fluorescence and F490 interaction, this is a possible cause. F490 has also been identified as one of three phenylalanines (Fischer *et al.*, 2005) (Figure 5.13B) that lock together to form a fulcrum for the relay helix to bend around and generate the force of the power stroke.

The reduction in tryptophan fluorescence for the T178I however is less obvious. It may be a disruption in the nucleotide pocket or the hydrogen bond to R672, which may in turn relay the signal. F490 also has been identified as one of three phenyalanines that may play a part in creating a hinge around which the relay helix bends. Therefore the loss of the π-cation bond may reduce the stability of this region.

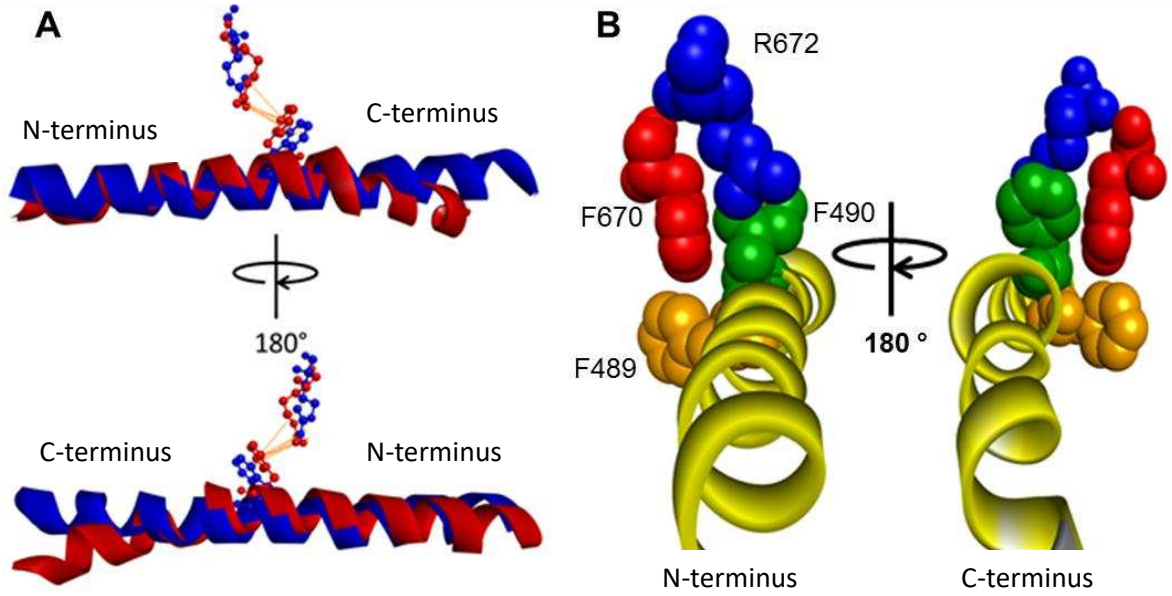

Figure 5.13 – Interaction between R672 and F490 in the rigor and pre-power stroke. (A) The relay helix in the rigor structure (blue) and in the pre-power stroke (red) are superimposed to display that the helix bends just after the F490. (B) Two other phenylalanines (F489 and F670) have been postulates to be involved in a hinge point around which the relay helix bends (Fischer *et al.*, 2005).

6 Characterisation of Juvenile Hypertrophic Cardiomyopathy mutation H251N

6.1 Introduction

6.1.1 Background

Hypertrophic cardiomyopathy (HCM) is an autosomal dominant disease with a variable clinical expression (Spirito, Seidman et al. 1997). The clinical symptom of HCM is enlarged hypertrophic ventricle walls and a reduced intra-ventricular volume (Colan, Lipshultz et al. 2007). While adult cardiomyopathy is a fairly common disease (rate of incidence is 1 in 500 in the US, (Maron, Gardin et al. 1995, Harvey, Leinwand 2011, Semsarian, Ingles et al. 2015)) the juvenile form of the disease is rarer (estimated 1.13 in 100,000 children for all juvenile cardiomyopathies, (Bublik, Alvarez et al. 2008)).

There is however debate as to the underlying cause of HCM in both adults and children with sarcomeric mutations only accounting for between 40-60 % of cases (Richard, Charron et al. 2003, Van Driest, Vasile et al. 2004, Van Driest, Ommen et al. 2005). Non-sarcomeric disorders have also being linked to causes of HCM, such as: Glycogen storage disease (Arad, Maron et al. 2005), 5' adenosine monophosphate-activated protein kinase (Murphy, Mogensen et al. 2005), and lysosomal storage disease (Sachdev, Takenaka et al. 2002). However recent studies claim that these conditions may account for less than 10 % of HCM cases (Colan, Lipshultz et al. 2007, Nugent, Daubeney et al. 2005) and therefore mutations in sarcomeric proteins may account for more HCM cases that currently believed.

A study from 2009 (Kaski, Syrris et al. 2009) investigated causes of HCM in 140 patients diagnosed before or at the age of 13. Of these 25 had a syndrome or metabolic disorder and 36 other patients refused to take part in the study. In the end 79 patients took part of which 42 were found to be mutation positive. Many of these mutations were known mutations in actin, myosin binding protein-C (MyBP-C), β cardiac myosin (MyHC-β),

myosin light chain, troponin I and troponin T. However several novel mutations were also identified, among these was H251N in the MyHC-β. This was a novel mutation found in one of the 42 preadolescents investigated in that study. Little is known about the causes of HCM in children due to observational studies reporting a lower frequency of the disease in children (Colan, Lipshultz et al. 2007, Nugent, Daubeney et al. 2005) and that left ventricle hypertrophy usually develops during the adolescent growth spurt (Maron, Spirito et al. 1986). This has meant the cases are overlooked and we are only just starting to investigate the diseases in children. A recent study reported that in patients diagnosed with HCM under the age of 15, 55% had a mutation in a sarcomeric protein (Morita, Rehm et al. 2008). These studies have helped to highlight the growing evidence that sarcomeric gene mutations causing HCM are as common in children as in adults.

6.1.2 Aim

In order to investigate the effects of this mutation on the function of MyHC-β, we used the same recombinant expression system (Chapter 2.2) as the WT embryonic myosin (Chapter 4), and the 3 Freeman-Sheldon Syndrome mutations (Chapter 5). The purified H251N was then used in a number of kinetic stopped-flow spectroscopy assays to assess how the ATPase cycle is affected in the mutation.

The aim of this investigation then is to assess whether or not there is a significant change in one or all of the kinetic parameters of the ATPase cycle. Two ‘adult’ mutations R403Q (Nag, Sommese et al. 2015) and R453C (Bloemink, Deacon et al. 2014) have already been characterised; however the unloaded kinetic parameters changed very little suggesting these severe mutations alter the myosin only very slightly. It is thought that this novel ‘juvenile HCM’ mutation may have a more significant effect on the myosin leading to the phenotypic HCM heart to present itself in infants and children.

6.2 MyHC-β H251N kinetics

6.2.1 Changes in nucleotide binding to H251N β-S1 compared to WT MyHC-β-S1

The H251N MyHC-β was expressed using the same method (Chapter 2.2.1.3) as the wild type (Chapter 4) and FSS mutants (Chapter 5).Here however the his- tag was located on the human essential light chain (MYL3). This meant that only the S1 was purified along with one light chain. The yields were similar as well at 1-2 mL 10-20 µM active S1 which is similar to the yields obtained for the wild type MyHC-β S1 (Nag, Sommese et al. 2015). The data presented here for the H251N mutation was compared to wild type MyHC-β S1 obtained by Nag *et al*. The buffer conditions used here are the same as those used in the wild type S1 stopped-flow assays.

It is possible to follow the ATP binding to myosin S1 through the exploitation of the tryptophan at the end of the relay helix (Trp508). Upon binding the conformational change associated with the recovery stroke causes the tryptophan to move relative to the rest of the motor domain. Mixing S1 (100 nM after mixing) with MgATP (10 µM after mixing) leads to a change in fluorescence that can be measured (Figure 6.1A). By increasing the MgATP concentration the k_{obs} increases in a hyperbolic manner (Figure 6.1B) which can be described by equation 2.3 (Chapter 2.3.2.1).

The second order rate constant for ATP binding (K_1k_{+2}) to H251N β-S1 is 6.4 ± 0.6 $\mu M^{-1}\ s^{-1}$ which is slightly faster than wild type (5.8 ± 0.4 $\mu M^{-1}\ s^{-1}$) but this was not significant different. The ATP binding affinity for S1 ($1/K_1$) for the mutant is 20.3 ± 3.4 µM. This is weaker than the wild type (15.9 ± 1.4 µM) but again not significantly different. The most drastic change determined from this assay is the k_{max} which is associated with the hydrolysis rate constant (k_{+3} + k_{-3}). For the mutant, this hydrolysis rate constant value (125.7 ± 9.3 s^{-1}) was significantly 38 % faster (91.2 ± 1.8 s^{-1}) than the wild type.

Tryptophan fluorescence can also be used to measure the ADP affinity for S1 (K_6K_7) as well as the ADP release rate constant (k_{+6}, Figure 6.2). S1 was incubated with varying concentrations of ADP and rapidly mixed with a fixed concentration of ATP.

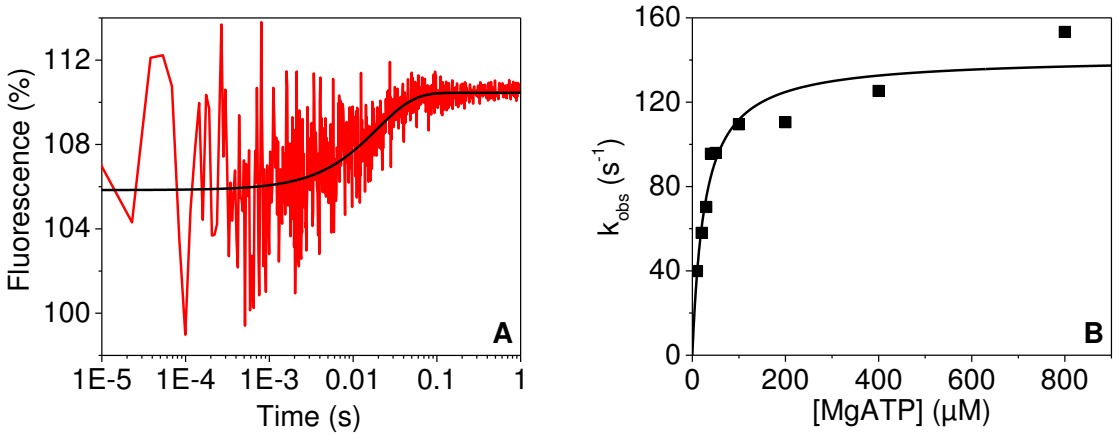

Figure 6.1 – Tryptophan fluorescence of MgATP binding to H251N β-S1. (A) A trace of 100 nM H251N β-S1 rapidly mixed with 10 μM MgATP. As MgATP bound to the S1 it caused a conformational change in the relay helix of the S1, which led to a change in fluorescence. This could be well described by a single exponential fit (black line). This yielded a k_{obs} = 55.2 s^{-1} and an increase in fluorescence amplitude = 4.8 %. (B) As the MgATP concentration increased so did the k_{obs}. This was plotted against MgATP concentration and follows a hyperbolic dependence.

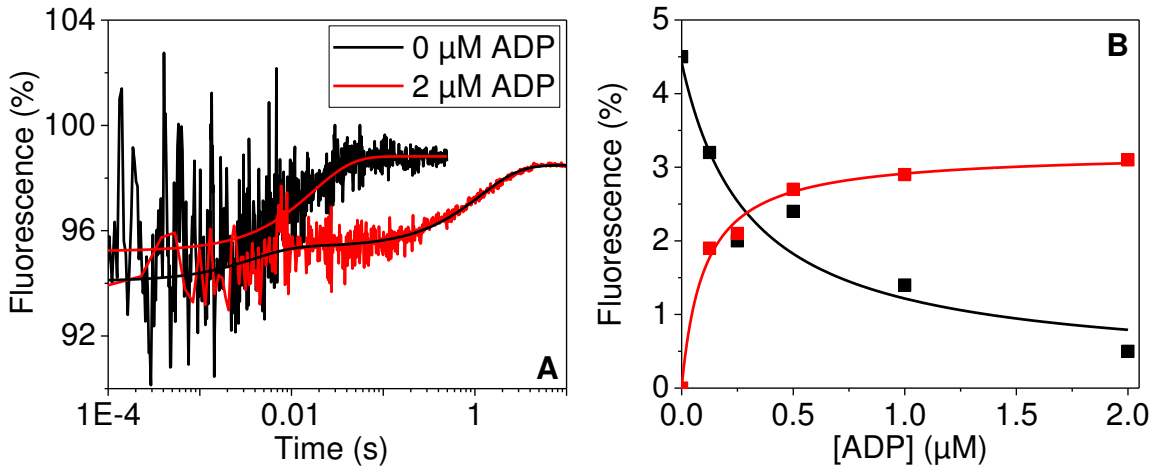

Figure 6.2 – H251N β-S1 ADP affinity. (A) The black trace shows 100 nM H251N β-S1 rapidly mixed with 20 μM MgATP. This was best described by a single exponential (red fit line). This resulted in a k_{obs} = 58 s^{-1} and an increase in fluorescence amplitude = 4.5 %. The red trace shows 100 nM H251N β-S1 preincubated with 2 μM ADP rapidly mixed with 20 μM MgATP. This was best described by a double exponential (black fit line). This yielded a k_{obs} = 90 s^{-1} for the fast phase and 0.8 s^{-1} for the slow phase. The increase in fluorescence amplitude = 0.5 % for the fast phase and 3.1 % for the slow phase. (B) The hyperbolic dependence of the amplitude of the fast (black) and slow (red) phases on ADP concentration.

H251N β-S1 (100 nM after mixing) was preincubated with increasing concentrations of ADP to allow ADP to bind to the nucleotide pocket of the motor. It was then rapidly mixed with a fixed concentration of MgATP (20 μM after mixing) which displaced the ADP and

bound to the S1. The fast phase in figure 6.2A represents the MgATP binding to S1 with no ADP already bound. The slow phase is indicative of ADP being released from the nucleotide binding pocket and ATP binding resulting in the fluorescence change.

Given that the fluorescence amplitude is associated with the tryptophan fluorescence upon ATP binding, as the ADP concentration increases the amplitude of the fast phase decreases. This is due to the pool of 'free' S1 being reduced as it is already occupied with ADP. Therefore the amount of S1 that ATP can bind to will decrease, leading to the reduced amplitude observed. Similarly for the slow phase more S1 has an ADP bound which has to be released before ATP can bind and so the amplitude increases. The k_{obs} should be unaffected by the ADP concentration. However at the higher ADP concentration the k_{obs} increased from 58 s^{-1} to 90 s^{-1}. This was most likely caused by the amplitude of the fast phase becoming too small and measuring the k_{obs} accurately became harder.

The k_{obs} of the slow phase is also very important since this represents the ADP being displaced from the S1 before ATP binding. The average of the slow phase k_{obs} therefore yields the ADP release rate constant (k_{+6}). For the mutant H251N β-S1 the k_{+6} (1.0 ± 0.2 s^{-1}) is not significantly faster than the wild type (0.63 ± 0.03 s^{-1}, Table 6.1).

Finally the amplitudes of the fast and slow phases can be plotted against the ADP concentrations. This yields two hyperbolic curves, with the fast phase decreasing and the slow phase increasing. The plot of the fast phase is well described by equation 2.20 (Chapter 2.3.2.1) and the slow phase by equation 2.24 (Chapter 2.3.2.1). Both fits result in a $K_{50\%}$ value equal to the ADP affinity (K_6K_7). The value for the mutant H251N β-S1 (0.19 ± 0.01 μM) is significantly tighter than the wild type (0.53 ± 0.07 μM).

6.2.2 Changes in nucleotide binding to H251N β acto.S1 compared to WT MyHC-β acto.S1

Myosin S1 when bound to pyrene-actin (pA) quenches the fluorescence signal. When ATP is mixed with the pyrene-actin.S1 (pA.S1) it rapidly dissociates the S1 from actin. This leads to an increase in fluorescence (Figure 6.3A).

50 nM pA.S1 (concentration after mixing) was rapidly mixed with increasing concentrations of MgATP. At MgATP concentrations lower than 40 μM the transient was best described by a single exponential (Figure 6.3A). At 40 μM MgATP and above a slow phase emerged (Figures 6.3A and B) which is thought to be associated with an opening of the nucleotide pocket (Deacon, Bloemink et al. 2012). The equilibrium constant for the opening of the pocket ($K_{\alpha 1}$) is determined by the ratio of fast phase amplitude to slow phase amplitude (Figure 6.3B). The ratio was calculated for each trace best described by a double exponential then averaged per biological replicate. The rate of the fast phase becomes so fast at the higher ATP concentrations that the amplitude becomes lost in the dead time of the instrument. Therefore the value calculated for figure 6.3B is lower than the average value of $K_{\alpha 1}$. The $K_{\alpha 1}$ for the mutant is 6.7 ± 1.1 compared to the wild type 4.1 ± 1.4; however this is not a statistically significant difference.

The rate constant for the pocket opening ($k_{+\alpha 1}$) can also be determined from the traces in figure 6.3A. ATP cannot bind to the S1 while it is in the closed state. Since the fluorescence change can only occur once ATP binds to S1 causing it to dissociate and stop quenching the pyrene, the slow phase must be the rate of the conformation change from closed to open. Also the k_{obs} did not increase with ATP concentration consistent with it not being ATP dependent. The average of the slow phase for the mutant H251N β-S1 gave a $k_{+\alpha 1}$ (39.7 ± 5.9 s^{-1}) significantly slower than the wild type (153.4 ± 10.6 s^{-1}, Table 6.1).

Plotting the fast phase k_{obs} as a function of MgATP concentration (Figure 6.3B) the k_{obs} can be best described by a hyperbolic dependence using equation 2.3 (Chapter 2.3.2.1). At low MgATP concentration the dependence is linear resulting in the second order rate constant ($K'_1k'_{+2}$). The $K'_1k'_{+2}$ value for H251N β-S1 is 5.1 ± 0.4 μM^{-1} s^{-1} compared to the wild type value of 4.4 ± 0.2 μM^{-1} s^{-1}; however this is not a significant difference. The S1 ATP affinity ($1/K'_1$), as determined by the $K_{50\%}$ of the hyperbola, is almost 3 fold tighter for the H251N β-S1 (131 ± 19 μM) compared to the wild type (327.9 ± 53.3 μM). The final rate constant that can be determined from this assay is the maximum rate of ATP induced dissociation (k'_{+2}). This is over 2 fold slower for the H251N (666 ± 58 s^{-1}) when compared to the wild type (1543 ± 100 s^{-1}).

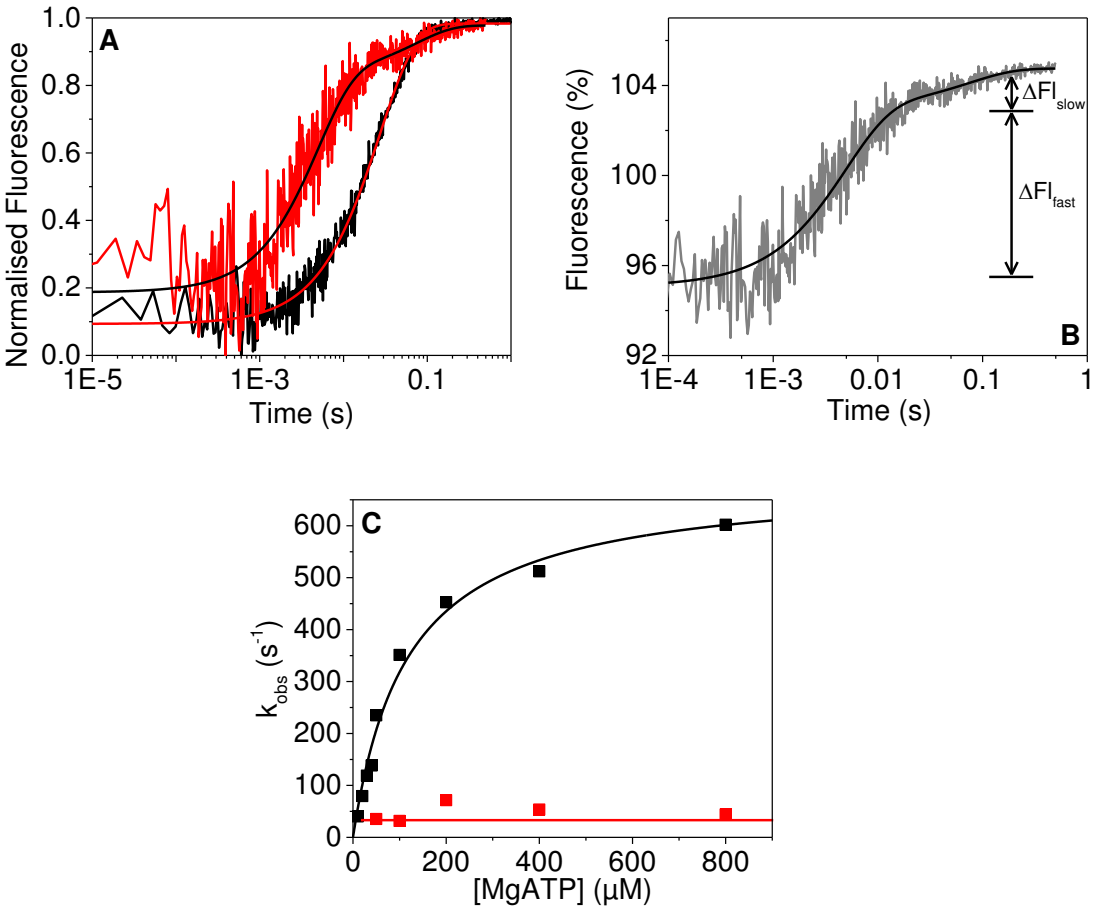

Figure 6.3 – ATP induced dissociation of H251N β-S1 from pyrene labelled actin. (A) The black trace shows 50 nM pyrene-actin.S1 (pA.S1) vs 10 µM MgATP (concentrations after mixing). This is best described by a single exponential (red fit line). This resulted in a k_{obs} = 36.8 s^{-1} and an increase in fluorescence amplitude = 17.6 %. At the highest MgATP concentration (800 µM after mixing, red trace) the transient was described by a double exponential (black fit line), which can be seen more clearly in (B). Graph has been normalised between 0 and 1. (B) 50 nM pyrene-actin H251N β-S1 rapidly mixed with 800 µM MgATP resulted in a k_{obs} = 369 s^{-1} and 33.1 s^{-1} for the fast and slow phase respectively, while the increase in fluorescence amplitude = 8.6 % and 3.1 % for the fast and slow phase respectively. The $K_{\alpha 1}$ can be calculated from the ratio of these amplitudes, for the H251N mutation $K_{\alpha 1}$ = 2.8. (C) The k_{obs} of the fast phase when plotted against MgATP concentration had a hyperbolic dependence on MgATP concentration whereas the slow phase did not.

In order to determine the H251N β-S1 ADP affinity in the pA.S1 complex a competition assay is used where pA.S1 is pushed against a mixture of a constant ATP concentration and an increasing ADP concentration. As more ADP is added it will compete with the ATP

for binding, occupying the nucleotide binding pocket, and therefore slowing the rate of ATP binding and dissociation.

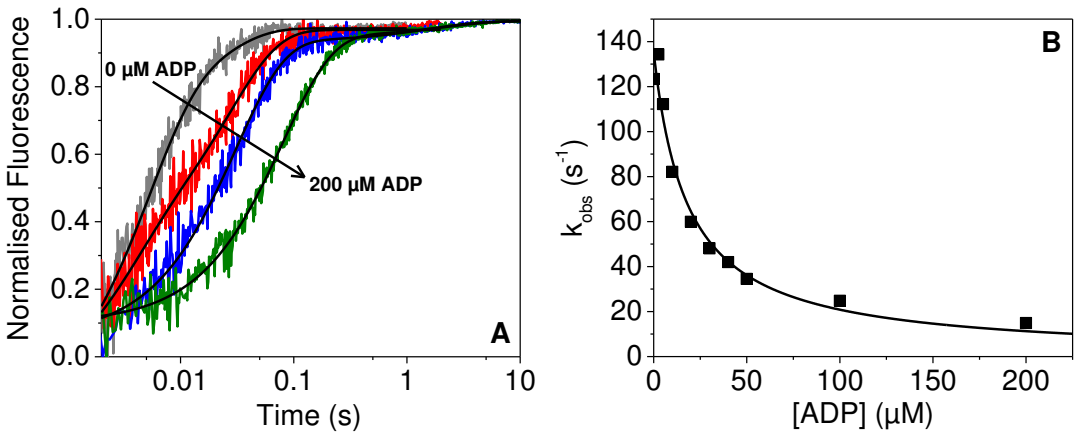

Figure 6.4 – Acto-251N β-S1 affinity for ADP using the ATP competition assay. (A) Transients of 50 nM pA.S1 rapidly mixed with a constant 50 µM MgATP and increasing ADP concentrations (0 – 200 µM). Either ADP or ATP binds to the acto.S1 with the dissociation event occurring after ATP binding. If ADP binds then this needs to dissociate before an ATP can bind. For a fast type myosin the ADP dissociation is very fast and no slow phase would be seen. However for slow type myosins such as MyHC-β the dissociation is slow and a slow phase appears in the transients. All were fit with a double exponential with the fast phase k_{obs} slowing as ADP concentration increased, except for the 0 µM ADP trace which was a single exponential. The slow phase k_{obs} is indicative of the nucleotide pocket opening/closing and averaged to 39.7 s^{-1}. (B) The fast phase k_{obs} plotted against ADP concentration. The k_{obs} has a hyperbolic dependence upon ADP concentration.

Figure 6.4A shows the transients of the ADP competition assay. 50 nM pA.S1 (concentration after mixing) was rapidly mixed with 50 µM MgATP and 0 to 200 µM ADP (concentrations after mixing). The trace obtained at 0 µM ADP was best described by a single exponential while the traces at all other ADP concentrations were double exponentials. This can be caused by the ADP binding to the acto.S1 preventing an ATP from binding. The slow phase emerges as ADP dissociates at a slow rate before either a new ADP or an ATP can bind. A second cause of the slow phase observed is thought to be associated to the open and closed state of the nucleotide pocket as seen with the ATP induced dissociation (Deacon, Bloemink et al. 2012). ADP can bind to pA.S1 in the open state and the pocket closes. Therefore the conformational change from closed to open

must occur before ADP can be released and before ATP can bind and lead to the dissociation step. The equilibrium constant for the close to open step ($K_{\alpha D}$) is 5.5 ± 1.1 for the H251N β-S1 (Table 6.1). This step was not observed for the wild type under the same conditions (25 mM KCl) however it was seen at higher salt (100 mM KCl, (Deacon, Bloemink et al. 2012)) suggesting some salt dependence. The rate constant for the conformational change from closed to open ($k_{+\alpha D}$) was determined from the k_{obs} of the slow phase. Again this was not observed for the wild type under the same conditions but was at the higher salt (Deacon, Bloemink et al. 2012). The value for H251N β-S1 is 5.4 ± 2.7 s^{-1} (Table 6.1). This value is an average of the slow phases observed. The k_{obs} and fluorescence amplitude were unaffected by the increase in ADP.

The ADP affinity for acto.S1 ($K'_6K'_7$) could be determined by plotting the k_{obs} of the fast phase against the ADP concentration (Figure 6.4B). As the concentration of ADP increases more will be available to bind to the acto.S1 complex therefore outcompeting the MgATP slowing the dissociation reaction. This leads to the curve seen in figure 6.4B which has a hyperbolic dependence best described by equation 2.16 (Chapter 2.3.2.1) which gives the $K'_6K'_7$ value. The mutant H251N β-S1 was found to have a significantly weaker ADP affinity (20.8 ± 3.6 μM) compared to wild type (6.1 ± 0.3 μM) in the presence of actin.

In a separate assay to measure the ADP release rate constant (k'_{+6}), 50 nM pA.S1 was preincubated with a saturating ADP concentration (0.5 mM) and rapidly mixed with high concentrations of MgATP (0.5-4 mM). The ADP was pre-treated with hexokinase and glucose to ensure any ATP contamination was converted to ADP and would not affect the assay. P1, P5-Di(adenosine-5') pentaphosphate (Ap5A) was also added to inhibit any adenylate cyclase activity, which would phosphorylate ADP back to ATP. An average of the k_{obs} was calculated and summarised in table 6.1. The ADP release rate constant is not significantly different for the mutant (56.7 ± 2.9 s^{-1}) and the wild type (58.7 ± 1.7 s^{-1}).

Using the ADP affinity ($K'_6K'_7$) and the ADP release rate constants it is possible to calculate the second order ADP binding rate constant ($K'_7k'_{-6}$) by dividing the k'_{+6} value by the $K'_6K'_7$. This rate of ADP binding is over three fold slower for the mutant (27 μM^{-1} s^{-1}) compared to the wild type (9.6 μM^{-1} s^{-1}).

6.2.3 Changes in actin affinity to H251N MyHC-β S1 compared to WT MyHC-β S1

The affinity of S1 for actin was determined by the method previously described in Chapter 3. A fixed concentration of pyrene-actin is incubate with varied S1 concentrations and rapidly mixed with a constant concentration of MgATP. As the S1 concentration increases the start point of the dissociation trace decreases, resulting in increasing fluorescence

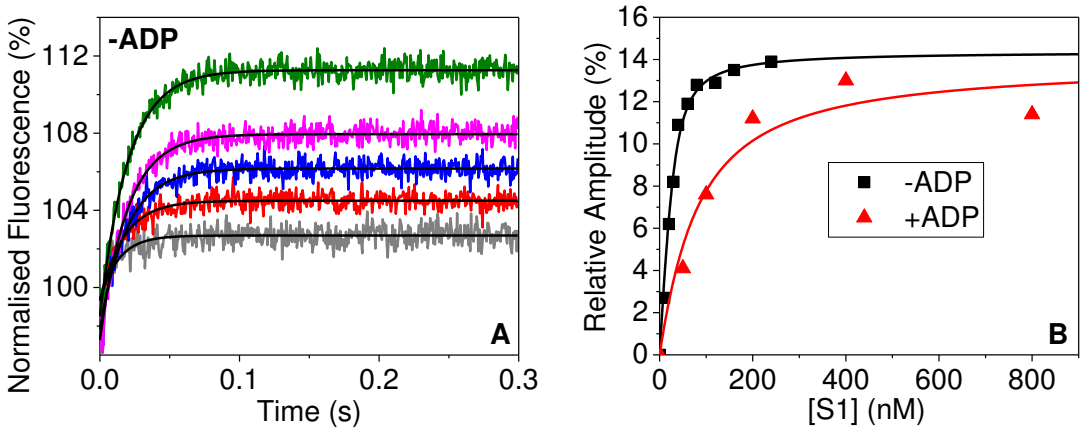

Figure 6.5 – Actin affinity of H251N β-S1 in the absence and presence of ADP. (A) Transients of increasing concentrations of S1 (0 – 200 nM) incubated with a fixed concentration of 30 nM pA rapidly mixed with a fixed MgATP concentration (20 µM). Since the ATP concentration was fixed the k_{obs} remained constant throughout. The transients have been normalised to the same start point to highlight that the fluorescence increases, in reality they would all have the same end point. (B) The relative amplitudes plotted as a function of the S1 concentration. The black squares indicate the assay without ADP present, while the red triangles represent the assay with (500 µM) ADP present.

amplitudes. This can be carried out in the absence (K_A) or presence (K_{DA}) of ADP.

For the actin affinity in the absence of ADP (K_A) assay, 30 nM pA was incubated with varying S1 concentrations (0-240 nM) which was rapidly mixed with 20 µM MgATP (Figure 6.5A, concentrations before mixing). As the S1 concentration increased so did the relative amplitude ((fluorescence amplitude/end point fluorescence) x 100) which was plotted as a function of S1 concentration (figure 6.5B). The data was then fit with the quadratic equation 3.1 (Chapter 3.2.3). The actin affinity in the absence of ADP was slightly tighter for the mutant (8.7 ± 1.5 nM) but not significantly different to the wild type (10 ± 1.8 nM).

The assay could be repeated this time in the presence of ADP to determine the actin affinity with ADP (K_{DA}). 30 nM pA was incubated with varied S1 concentrations and 500 µM ADP (treated with hexokinase and glucose, see above) and Ap5A and was rapidly mixed with 500 µM MgATP (concentrations before mixing). ADP weakens S1 affinity for actin so a higher concentration was required to determine the K_{DA}. The relative amplitude increased with S1 concentration as in the absence of ADP and again is best described by a quadratic equation (Figure 6.5B).The mutant H251N β-S1 has an almost 2 fold tighter affinity for actin in the presence of ADP (56.3 ± 9.3 nM) compared to the wild type (109.3 ± 24.1 nM). The number of repeats for the mutant was only 2 for this measurement.

Table 6.1 – Rate and equilibrium constants of the H251N β-S1 compared to the wild type β-S1. Statistically significant differences (determined by Student's t test) have been shaded grey.

Rate/Equilibrium Constant	Wild Type β [a]	β H251N
ATP binding to S1		
K_1k_{+2} (μM^{-1} s^{-1})	5.8 ± 0.4	6.4 ± 0.6
$1/K_1$ (μM)	15.9 ± 1.4	20.3 ± 3.4
k_{max} or $k_{+3} + k_{-3}$ (s^{-1})	91.2 ± 1.8	125.7 ± 9.3 [b]
ADP binding to S1		
K_6K_7 (μM)	0.53 ± 0.07	0.19 ± 0.01 [c]
k_{+6} (s^{-1})	0.63 ± 0.03	1.0 ± 0.2
ATP binding to actin.S1		
$K'_1k'_{+2}$ (μM^{-1} s^{-1})	4.4 ± 0.2	5.1 ± 0.4
$1/K'_1$ (μM)	327.9 ± 53.3	131 ± 19 [b]
k'_{+2} (s^{-1})	1543 ± 100	666 ± 58 [d]
$K_{\alpha1}$	4.1 ± 1.4	6.7 ± 1.1
$k_{+\alpha1}$ (s^{-1})	153.4 ± 10.6	39.7 ± 5.9 [d]
ADP binding to actin.S1		
$K'_6K'_7$ (μM)	6.1 ± 0.3	20.8 ± 3.6 [b]
k'_{+6} (s^{-1})	58.7 ± 1.7	56.7 ± 2.9
$K'_7k'_{-6}$ (μM^{-1} s^{-1})	9.6	2.7
$K_{\alpha D}$	No second phase	5.5 ± 1.1
$k_{+\alpha D}$ (s^{-1})	No second phase	5.4 ± 2.7
$K'_6K'_7/K_6K_7$	11.5	109.5
S1 affinity for actin		
K_A (nM)	10 ± 1.8	8.7 ± 1.5
K_{DA} (nM)	109.3 ± 24.1	56.3 ± 9.3
K_{DA}/K_A	10.9	6.5

[a] (Nag, Sommese et al. 2015)

[b] $p < 0.05$ determined by Student's *t* test as compared to wild type β-S1.

[c] $p < 0.01$ determined by Student's *t* test as compared to wild type β-S1.

[d] $p < 0.005$ determined by Student's *t* test as compared to wild type β-S1.

6.2.4 Structure analysis

In an attempt to understand the cause of the changes in the H251N β-S1, structural analysis was carried out. H251 is located on the 6th β-strand on the central 7 stranded β-sheet than runs through the middle of the myosin motor domain separating the upper and lower 50 K domains (Figure 6.6).

The location of H251 is very close to the HO-linker previously described for the Arginine 453 Cysteine (R453C) mutation in MyHC-β also associated with HCM (Bloemink, Deacon et al. 2014). In fact Bloemink *et al*. identified H251 as a residue that interacts with the R453 residue throughout the myosin cross-bridge cycle.

To investigate this further, 6 homology models were made using SWISS-MODEL (Biasini, Bienert et al. 2014, Arnold, Bordoli et al. 2006, Guex, Peitsch et al. 2009, Kiefer, Arnold et al. 2009). The 6 scallop structures (PDB: 2OTG, 2OS8, 1SR6, 1QVI, 1KK8, and 1S5G) were used as a template to which the MyHC-β sequence was mapped. To do this the sequence for MyHC-β was pairwise aligned to the sequence of the PDB structures, and then SWISS-MODEL was used to create the homology models. These scallop structures represent nearly all the states of the cross-bridge cycle so give us an indication of how the molecule structure changes as well as the intramolecular bonds. The structures were visualised using Visual Molecular Dynamics (VMD) software (Humphrey, Dalke et al. 1996). The interactions of H251 are summarised in table 6.2 along with the interactions lost in the mutant H251N. The structure of the recombinant human β-cardiac GFP chimera (PDB 4P7H) was also visualised to verify the interactions seen in the homology models were consistent and accurate.

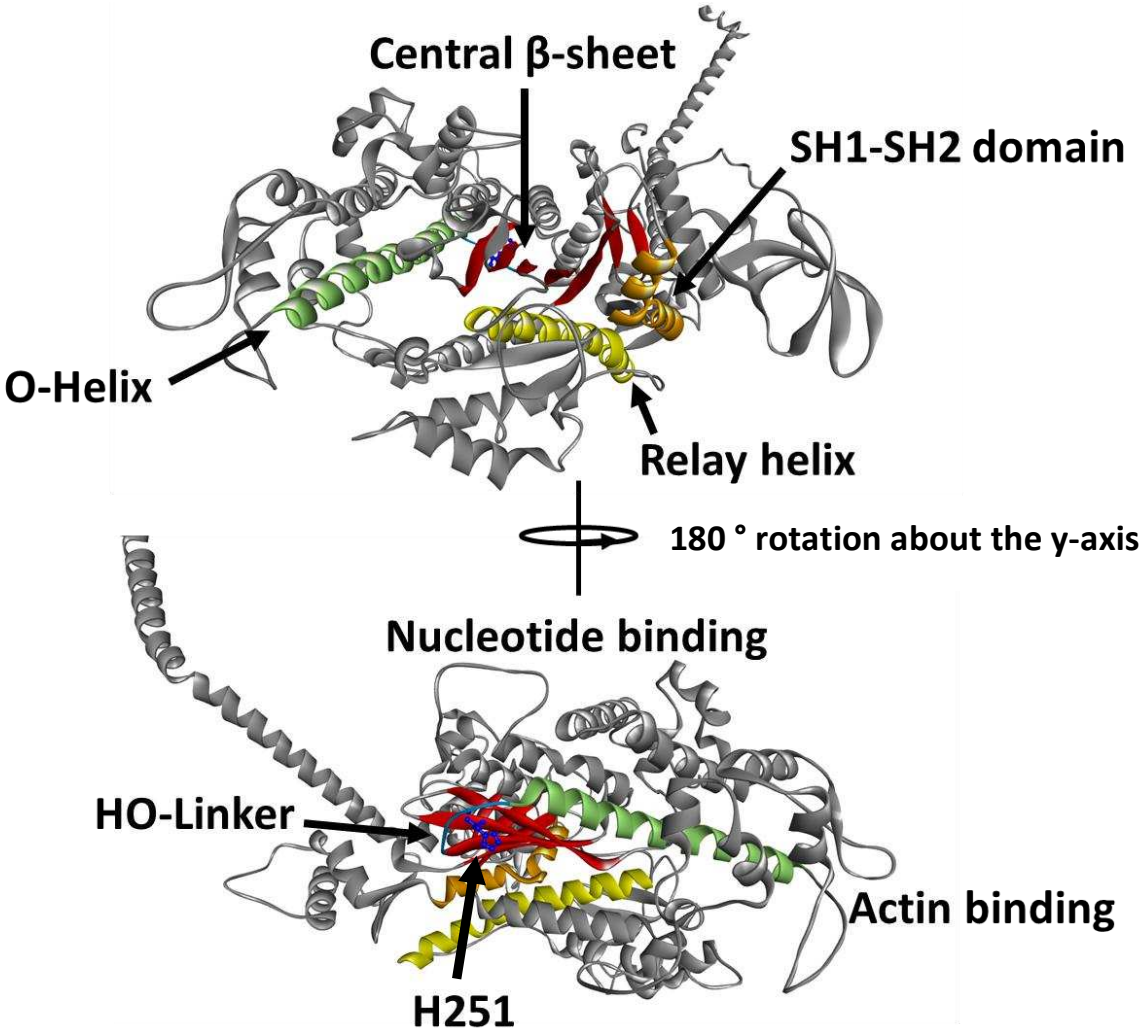

Figure 6.6 – A homology model of the MyHC-β showing the location of H251 built using PDB 1QVI. (A) The overall structure of the motor domain showing the relay helix (yellow), SH1-SH2 (orange), O-helix (pale green), HO-linker (pale blue) and central β-sheet (red). (B) A 180 ° rotation of (A) showing the location of H251 (blue). H251 is on the 6th strand of the central β-sheet facing towards the HO-linker.

H251 interacts with 3 residues (Figure 6.7); Alanine 259 (A259), Serine 260 (S260), and Arginine 453 (R453). A259 and S260 are found on β-strand 6 opposite H251 and form a hydrogen bond (H bond) to the histidine backbone rather than the R group. This interaction was found to persist in all but one of the homology models (PDB 2OS8). The interaction was also unaffected by the mutation of the histidine to asparagine so is unlikely to affect the structure of the β-sheet. The third interaction between H251 and R453 as mentioned has already been identified in Bloemink *et al*. (Bloemink, Deacon et al. 2014). This is a π-cation bond which forms between the positive charge of certain residues (arginine, lysine, or histidine) and the delocalised electrons of benzene like ring

structures (phenylalanine, tryptophan, tyrosine, and histidine). These interactions can be as strong, or stronger, than salt bridges (Dougherty 1996). In this case R453 is the positive residue binding to the ring of histidine. This interaction persists through all the structures; however it is lost when the histidine is mutated to asparagine, which is unsurprising since asparagine is a non-charged polar residue.

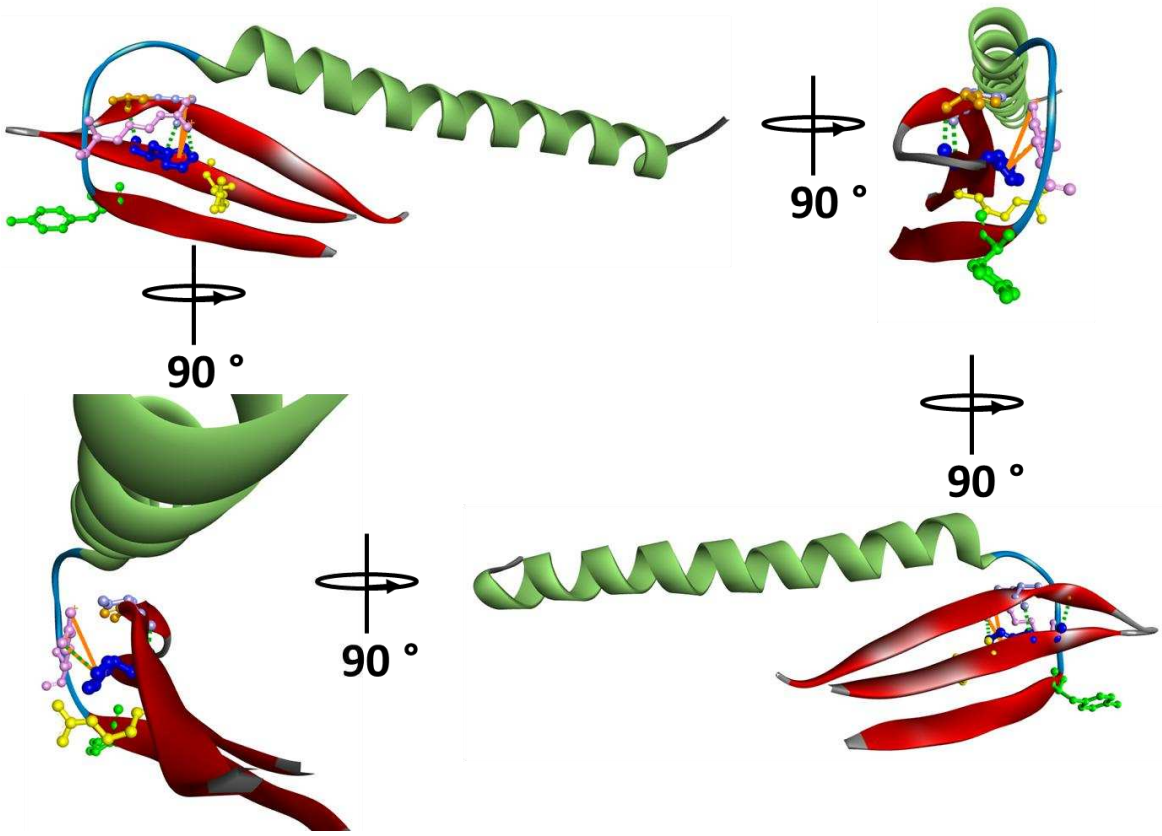

Figure 6.7 – Interactions between H251 and surrounding residues. H251 (dark blue) can form multiple intermolecular bonds with its neighbours: R249 (yellow), A259 (orange), S260 (purple), R453 (pink), and Y455 (green). Dark green dashed lines indicate hydrogen bonds while solid orange lines π-cation bonds. Colours of the structures are the same as in figure 6.6.

Two other interactions identified are an H bond to R249 (PDB 2OS8 and 1S5G) and an H bond to Y455 (PDB 2OS8), both of which are lost in the mutant.

H251N	PDB		4P7H	2OTG	2OS8	1SR6	1QVI	1KK8	1S5G
Residue	Location	Interaction	β-cardiac GFP chimera	post-rigor (ADP)	rigor	post-rigor	pre-power	detached	near rigor ADP-bound
R249	β6	H-bond							
A259	β7	H-bond							
S260	β7	H-bond							
R453	HO-linker	π-cation (+ H bond for 1QVI)							
Y455	HO-linker	H-bond							

	Interaction present in wild type not in H251N
	Interaction present in wild type and H251N
	Interaction not present in either structure

Table 6.2 – Interactions present between H251 in wild type, and N251 in the H251N mutation. PDB 4P7H is one of two structures of the human MyHC-β, while 2OTG, 2OS8, 1SR6, 1QVI, 1KK8, and 1S5G are homology models built using scallop structures as a template and the MyHC-β sequence as a target in SWISS-MODEL.

6.3 Discussion

6.3.1 Kinetics

It is clear from the stopped-flow spectroscopy kinetics that there are few but significant differences between the mutant H251N β-S1 and the wild type. These have been summarised in figure 6.8 which clearly shows where there is an increase or decrease in affinity (Figure 6.8A) or rate constant (Figure 6.8B).

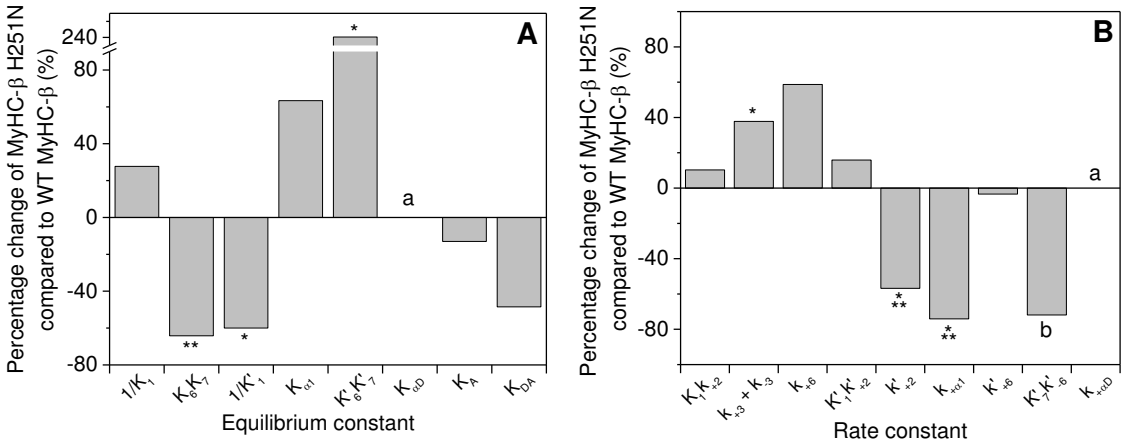

Figure 6.8 – Percentage changes between MyHC-β H251N and WT MyHC-β. (A) Percentage changes in the equilibrium constants of MyHC-β H251N compared to wild type. The increases and decreases in equilibrium constant indicate a weakening or tightening of the affinities respectively compared to wild type. (B) Percentage changes in the rate constants of MyHC-β H251N compared to wild type. The increases and decreases in rate constant indicate a faster or slower rate constant respectively compared to wild type. * $p < 0.05$, ** $p < 0.01$, *** $p < 0.005$, *a* = comparison not possible due to lack of data, *b* = calculated value therefore no error.

There was no significant difference in the second order rate constant of ATP binding ($K'_1k'_{+2}$) but the ATP affinity for acto.S1 ($1/K'_1$) 3 fold tighter. This is offset by the maximum rate constant of dissociation (k'_{+2}) slowing by just over 2 times. To add to this, the rate constant for the pocket conformational change is nearly 4 times slower. The cumulative effect of these changes in the dissociation step of the cross-bridge cycle would lead to the myosin being bound to actin longer and detaching slower. This step depends upon the ATP concentration but it would not be wrong to assume that the concentration of ATP in the heart will be relatively constant and high.

Once the myosin has detached from actin however the rate constant for ATP hydrolysis (k_{+3} + k_{-3}) is around 30 % faster for H251N. Once S1 hydrolyses ATP to ADP it forms an S1.ADP.P_i complex which has a low affinity for actin. Once bound to the actin phosphate is released and the power stroke occurs. This newly formed actin.S1.ADP complex will be stronger for the H251N mutation given that the actin affinity in the presence of ADP equilibrium constant (K_{DA}) is almost 2 fold tighter than wild type. The lack of a significant difference for the K_{DA} value could simply be due to the lack of technical repeats for the mutant (n=2 rather than n=3). This would potentially make the detached state shorter as the affinity for actin increases after hydrolysis. It is unlikely but possible that the myosin will not detach from the actin and actually just hydrolyse the ATP while still bound to actin and therefore not go through the recovery stroke.

The ADP has to be released from the myosin before ATP can bind and repeat the cycle. The ADP affinity for acto.S1 ($K'_6K'_7$) is over 3 times weaker than the wild type suggesting once ADP is displaced from the myosin it is unlikely to rebind over ATP. However the ADP release rate (k'_{+6}) is very similar to the wild type.

With the reduced maximum rate of detachment and stronger actin affinity in the presence of ADP it could be possible that the H251N mutant has a higher duty ratio. This prolonged attachment may have a negative consequence of providing a 'drag' on the system. Therefore the fibres will not be able to shorten as quickly as if the fibre just contained wild type protein. A second effect of this prolonged attachment could be an increase force production however this would need to be investigated using force measurements.

6.3.2 Structure

The major change in the structure for this mutation was the π-cation bond between H251 and R453 being completely lost when the histidine is mutated to an asparagine. R453 is also the location of a mutation (R453C) that leads to HCM. The mutation R453C has been associated with a severe form of HCM in adults but has also been identified in children (Kaski, Syrris et al. 2009). It seems wise then to compare the two mutations given their proximity and phenotype.

R453 is located on a surface loop of the upper 50-kDa domain in a linker region. At the C-terminal end is Switch-2 which is part of the nucleotide binding pocket, which binds ATP via β5 of the central β-sheet. The N terminal end connects to the actin binding site (cardiomyopathy loop) via a long α-helix (helix O). This HO-linker is in an ideal location to sense changes in both the actin binding site and nucleotide binding pocket. Meanwhile H251 is located on β6 of the central β sheet. The N terminal end of this strand is directly linked to Switch-1 of the nucleotide pocket (Geeves, Fedorov et al. 2005). This bond between H251 and R453 could give the linker even more sensitivity to nucleotide binding through both Switch-1 and Switch-2.

For both mutants the rate constant for ATP hydrolysis is significantly affected (Figure 6.8, (Bloemink, Deacon et al. 2014)) which may be due to the proximity of the residues to the nucleotide binding pocket. However there is an increase in the hydrolysis step for H251N (125.7 ± 9.3 s^{-1}) compared to the wild type (91.2 ± 1.8 s^{-1}) in the 25 mM KCl buffer, while for the R453C, the hydrolysis step (102 ± 14 s^{-1}) is slower than the wild type (160 ± 23 s^{-1}) in a 100 mM KCl buffer. It seems that destabilisation of this HO-linker can have a downstream effect on the nucleotide pocket and its ability to hydrolyse ATP. This is also apparent in the values for k'_{+2} which is decreased in both the H251N and R453C. This rate constant estimates the maximum rate of ATP induced dissociation. The k'_{+2} value then links the rate of ATP binding and actin dissociation, and a reduction in this value for both mutants adds to the theory that the HO-linker is relaying changes in both domains (Bloemink, Deacon et al. 2014).

7 General Discussion and Conclusions

7.1 General discussion

7.1.1 Stopped-flow modifications

Stopped-flow is a powerful tool for studying the rapid kinetics biological systems that would not be measurable otherwise. However, as discussed in chapter 1.4.3 there are a few limitations to using this method.

7.1.1.1 Temperature manifold

The temperature manifold was designed to be a simple solution for laboratories that do not have access to the more specialised equipment for using temperature to affect rapid kinetics. This method differs from temperature jump or joule heating assays where a temperature change is used to perturb the system. Instead the sample, which may be labile at high temperatures such as delicate proteins can be kept at a tolerable temperature then rapidly heated or cooled just prior to mixing. Therefore the mixture would be at the desired temperature upon measurement without risking damaging the proteins by holding them at a high temperature for a prolonged amount of time.

The design of the manifold is very simple with a machined block that allows water or other coolant from a water bath to heat up or cool down the aluminium block. It was then a simple case of insulating the block from the rest of the stopped-flow to minimize any thermal diffusion. By placing insulation and the manifold between the drive syringes and observation cell the distance the samples have to move also increases. This was a problem since the tubes that carry the samples rely on the stopped-flow being attached directly to the observation cell. We therefore filled this gap with an extender which contained two tubes for sample to flow into the cell and a waste tube for samples to exit the cell. This had to be a smooth surface to prevent perturbation of the sample which

would result in undesirable mixing artefacts in the transients. They also had to be the same diameter as the tubes from the stopped-flow and the cell again to prevent any turbulence of the samples. The material also had to be inert to prevent any unexpected reactions before mixing and measurement. Also the material had to be a thermal conductor in order for the sample to reach the desired temperature before mixing.

To determine the temperature of the samples when they reached the observation cell fluorescein in a temperature sensitive buffer was used. As the temperature changed so did the pH, which in turn changed the fluorescence of the fluorescein. The initial amplitude for differing shot volumes gave information on how far from the desired temperature the sample was. The minimum shot volume that would be used for a 22.5 µL observation cell, 60 µL, was at most 3 °C away for the biggest temperature differences from the desired temperature in an aqueous solution. When ethylene glycol was added to allow temperatures below 0 °C it was > 5 °C away this is most likely a result of the large temperature difference (ΔT = 30 °C). Once in the observation cell the temperature of the sample continued to adjust to the desired slowly over 20 seconds and may have had some undesired effects on the transients. However this should not be a problem on reactions that are complete within 1 second. Therefore we investigated a well-established system, ATP-induced dissociation of myosin S1 from actin. Acto.S1 was rapidly mixed with a fixed ATP concentration in in the stopped-flow using the temperature manifold, which was set at different temperatures to the stopped-flow. The transients were all best described by a single exponential fit which is expected and seen using the conventional set up. If there was an artefact caused by the gradual temperature change seen with the fluorescein then it would have presented as a second phase.

Previous work (Iorga, Adamek et al. 2007) had shown that as temperature increase the second order rate constant for ATP induced dissociation ($K'_1k'_{+2}$) also increases. Upon separating the two constants ($1/K'_1$ – the reciprocal of the K'_1 term, and k'_{+2}) it was shown that $1/K'_1$ is not effected by temperature, while k'_{+2} is and therefore it is the change in the k'_{+2} value that effects the value of $K'_1k'_{+2}$. In this investigation the whole system was set to the same temperature. This therefore gave a control with which to test the efficiency of the temperature manifold. An earlier investigation (Millar, Geeves 1983) also looked at

the ATP induced dissociation at sub-zero temperatures which also acted as a control for those assays.

For the aqueous solutions the Van't Hoff plot of $1/K'_1$ gave a similar ΔH^0 and ΔS^0 as that already published. The ΔH^0 is the most significant here in that it is very close to 0 and therefore unaffected by the change in temperature. The Arrhenius plot of the k'_{+2} showed the same trend as Iorga *et al*., where the $\Delta H^{\ddagger}$ is positive (23.9-35.7 $kJ.mol^{-1}$) and the $\Delta S^{\ddagger}$ is larger (140-180 $J.K.mol^{-1}$) however the values found here were slightly lower than that seen previously (Iorga, Adamek et al. 2007). One cause of this is most likely due to a more pronounced 'break point' that was initially seen in (Millar, Geeves 1983) where there are two linear lines for the Arrhenius plot. One linear relationship exists below 12 °C and the other above this point. Therefore to fit a linear line is strictly not true but given the small temperature window explored they only affected the results slightly. Regardless the trend was the more important result and helped to show that the temperature manifold worked over this temperature range.

The temperature manifold therefore is a simple addition to the stopped-flow that could facilitate non-specialist labs to conduct assays at temperatures that would otherwise damage the machinery. It will also allow these laboratories to study chemical and biochemical intermediates.

One limitation of the temperature manifold is the lack of insulation around the aluminium block and the pipes supplying the manifold from the water bath. These are both areas in which the coolant loses or gains thermal energy. As such the water bath would have to be set higher or lower so that the manifold was at the correct temperature. To monitor the temperature of the manifold a digital thermometer was inserted into a screw hole of the observation block close to the back of the cell close to where the reaction is measured. This gave some indication of the temperature within the cell and could adjust the water bath accordingly. Foam tubes and tissue paper were used as a makeshift insulator for the purposes of this investigation, however a more appropriate solution to this should be found if turned into a commercial product. One solution would be to cover the aluminium block in acetate which was used for the insulation plate.

7.1.1.2 Micro-volume manifold

One of the major limitations when considering stopped-flow is the need for large volumes and high concentrations when working with a 'weak' fluorophore. If working with an expression system that does not yield a large amount of protein, or unstable protein this can become a real issue and prevent experiments from being conducted. Reducing the volumes needed therefore seemed like an issue that could be tackled. To do this a new manifold was designed that is positioned between the stopped-flow and observation cell like the temperature manifold. Moving the sample loading closer to the observation cell would reduce the volume of sample needed since 90-120 µL of each sample are wasted in order to clear the system of buffer/previous sample.

The manifold was designed to have two inputs at the top for reagents, one for each drive syringe. These were cone shaped in order to reduce the chance of developing an air bubble which could ruin a measurement. Each had a valve that could be independently opened and closed to allow sample into the loading loop. The volume in the loops contain approximately 150 µL. To investigate whether this volume was adequate to be loaded into the system, different load volumes were used and the k_{obs}, amplitude, end point, and relative amplitude were monitored with different shot volumes. A 5 µL cell was used since the shot volume could be reduced while clearing the cell of the previous sample. Therefore a shot volume of 20 µL (10 µL from each side) could be used. ATP was loaded using the normal method, while S1 or acto.S1 were added through one of the inputs and then pushed using buffer in the drive syringe. Using a load volume of 80, 100, and 120 µL it was apparent that a load volume of 120 µL gave the most stable amplitude and endpoint which are both important measures of the fluorescence and therefore protein concentration in the observation cell.

Actin affinity of myosin S1 in the absence and presence of ADP can be very demanding on protein since high concentrations of S1 are needed. As such this method could lend itself to reducing the overall protein needed to determining these variables. Using a method of determining the actin affinity on the stopped-flow (Kurzawa, Geeves 1996) where the acto.S1 complex is made then rapidly mixed with ATP. The fluorescence amplitude of the dissociation event increases as the S1 concentration is increased. When fitted with a

quadratic function (equation 3.1) results in the actin affinity. The values obtained were compared to the value observed originally (Kurzawa, Geeves 1996) at both 50 and 30 nM pyrene actin with both giving similar results to the Kurzawa and Geeves findings.

It therefore seems that the micro-volume manifold is a useful addition to the stopped-flow set-up for reducing volumes of proteins needed. A user could conduct a stopped-flow assay with 300 µL of their protein so even halving this volume needed would be beneficial for those with low yields of samples.

There are three design issues that need to be addressed before this could become a commercial product.

1. There was no thermostat since there are no coolant channels within the manifold. This meant that the manifold is at room temperature. This is a major issue that will need to be addressed due to temperature playing such a large role in kinetics.
2. When the valve on the manifold is in the position to load the sample, if the waste valve is in the flush position the sample will leak straight through the system into the waste. It is unlikely that there is a solution to this other than making the user aware that when loading the sample the waste valve must be on either drive or waste.
3. Due to the complex plumbing within the manifold the lines for syringe A and B swap over (Figure 7.1). This is very important to know if the user is using just one reagent in the manifold since both reagents could be mixed before they should be. However this is an early prototype and the design can be addressed in later iterations of the manifold.

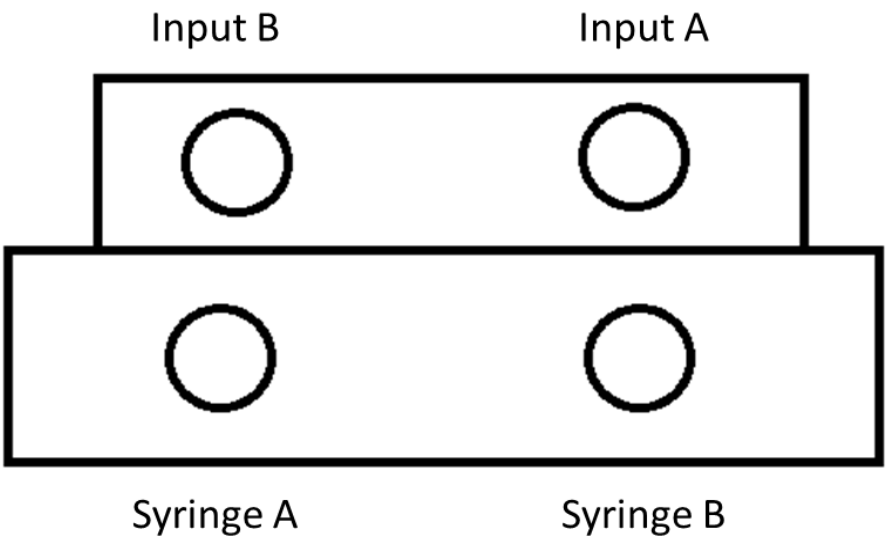

Figure 7.1 – Schematic to show how the inputs on the manifold match up to the drive syringes.

7.1.1.3 Wild type MyHC-emb

Previous work has shown that the embryonic myosin is a slow type myosin similar to the β-myosin. One of the characteristic features of a slow type myosin is a tight ADP affinity and a slow ADP release rate as well as a slower ATPase rate which is indicative of the overall cross-bridge cycle.

The ADP affinity of the MyHC-emb was over two fold weaker than the MyHC-β, however this was still tighter than comparisons with the other adult isoforms expressed in humans. The issue of comparing the rates between the MyHC-emb in this study and the adult isoforms (Bloemink, Deacon et al. 2013) is that the studies are at different salt concentrations. However the MyHC-β has been characterised at both 100 mM KCl (Deacon, Bloemink et al. 2012) and 25 mM KCl (Nag, Sommese et al. 2015), which allowed the direct comparison of MyHC-emb to MyHC-β, then comparison of MyHC-β to the adult muscle isoforms. The differences between the two salt concentrations for the wild type MyHC-β are mainly increases in the affinities for nucleotide and actin at the lower salt concentration. Some of the rate constants are also increased, likely due to the reduced ionic concentration which may reduce the rates of association. At the higher salt, the ADP affinity of the MyHC-β was around 3.5-fold weaker than at the lower salt. If the trend

holds true for the MyHC-emb then the ADP affinity at higher salt would be around 50 μM. This is similar to the MyHC-IIb value (which is not expressed in humans), but much weaker than the MyHC-IIa, MyHC-IIx, MyHC-extraocular, and MyHC-α.

The ADP release rate for MyHC-emb is over two-fold slower than the MyHC-β. Comparing the salt differences both MyHC-emb and MyHC-β are significantly slower than the adult isoforms as these rate constants are >1,000 s^{-1}. This step is also thought to be the rate limiting step for slow myosin velocity and is the main characteristic of a slow type myosin. The maximum cycling time (V_{max}) however showed that there is only a slight difference between the MyHC-emb and MyHC-β, with the embryonic isoform having a faster V_{max}.

The data presented supports the hypothesis that the MyHC-emb is a slow type myosin due to the slow ADP release rate constant. One observation is a second slow phase during the ATP induced dissociation of acto.S1 was not seen for the wild type MyHC-emb. This step has been suggested to be caused by a conformational change from a closed to open state in the nucleotide binding pocket. This is only seen in the MyHC-β and could be a characteristic of slow type myosins (myosin I, V, VI etc.) or just the beta isoform. One explanation why this was not seen in the MyHC-emb is that the maximum rate of dissociation (k'_{+2}) is relatively slow, over half the rate as seen for MyHC-β. This would make it difficult to isolate the two phases in the transients and may result in it being missed. It is also unlikely that an increase in ionic strength would increase the dissociation rate as it has no effect for MyHC-β. The ATPase V_{max} was also slightly faster than the MyHC-β (7 s^{-1} rather than 6 s^{-1}) which are both slower than the adult isoforms (V_{max} for MyHC-IIa is >16 s^{-1}, (Swenson, Trivedi et al. 2014)).

One limitation of this investigation is that using a low salt buffer, the actin affinity (K_A) becomes much tighter than if carried out at 100 mM KCl. Stopped-flow spectroscopy instruments have become much more sensitive and the ability to use 30 nM pyrene-actin is a huge achievement. However to have confidence in the value of K_A the measurement would ideally be conducted with an actin concentration ≤ K_A. So when we get an affinity of 2.1 nM for the MyHC-emb some doubt occurs to the accuracy of the measurement. One thing we can be sure of it that the K_A for MyHC-emb is very tight similar to MyHC-β. Given more time and protein it would have been useful to repeat this assay at a higher salt such as 100 mM KCl where the K_A for MyHC-β is 17 nM.

A second problem with this K_A assay is that the concentration of active myosin must be correct. To ascertain the concentration of active S1 we do an activity test. This is a similar and simpler assay to the K_A measurement where equimolar acto.S1 is rapidly mixed with ATP. The S1 concentration is then doubled to observe if the relative amplitude also doubles or increases. This is repeated until the relative amplitude remains the same. The active S1 concentration can then be estimated more accurately than using UV spectroscopy. However the K_A measurement was usually the second to last assay carried out and as such the active concentration of S1 may have decreased. Ideally this activity test would have been repeated before the actin affinity measurements; however these assays use large quantities of protein which could not be used on a second activity test. The length of time between purification and the K_A assay was also within 3-4 days which will have limited the deterioration of S1.

One issue of the construct used is that the light chains bound to the S1 are the endogenous mouse light chains from the C2C12 cells. Deacon *et al*. (Deacon, Bloemink et al. 2012) analysed these light chains and found they were MLC1A, MLC3F, MLC1F, and MLC2F.

A review by Bottinelli and Reggiani (Bottinelli, Reggiani 2000) stated the myosin light chains (MLC) 1A, 1F, and 2F are known to bind to the embryonic myosin. MLC1A is also known as the MLC-1 atrial/foetal isoform expressed in embryonic tissue and heart and in the atria of adults (Whalen, Butler-Browne et al. 1978, Kurabayashi, Komuro et al. 1988). We were therefore encouraged to find that these light chains had a greater density than the MLC3F. This also correlates to the level of S1 and endogenous myosin in the sample, suggesting these three light chains are binding correctly to the S1 while MLC3F which does not bind to the embryonic myosin appears to be associating with the endogenous myosin. Deacon *et al*. (Deacon, Bloemink et al. 2012) used a construct with the recombinant MYL3 which is known to be associated with a specific cardiac light chain. Since there is a specific embryonic myosin light chain it would be interesting to see if there is a change in the kinetics with the human form present as there is in the cardiac β-S1.

7.1.2 FSS mutations

T178I, R672H, and R672C are the three most common mutations in embryonic myosin that cause Freeman-Sheldon syndrome. Given the location of the residues it is unsurprising that they have such dramatic effects on the patients. It is also unsurprising that since the residues are close to the nucleotide binding pocket (at the γ-phosphate binding site) that ATP hydrolysis is so significantly affected. The slowing of the ATP hydrolysis may be one cause of the decrease in the V_{max} of the ATPase assay. The changes in the ATPase assays compared to the wild type correlate with the severity of the phenotypes observed with these mutations. T178I has the most severe phenotype, slowest V_{max}, and tightest K_M. On the other hand the R672C has the least severe phenotype, fastest V_{max}, and weakest K_M, which is closest to the wild type.

Using Berkley Madonna, the ATPase cycle was modelled using the values from the stopped-flow kinetics and the ATPase assays. The rate constants for actin rebinding after the ATP hydrolysis step and the phosphate release step were then estimated. As can be seen in chapter 5 the A.M.D.P state is the highest occupied state in the wild type MyHC-emb, caused by a slow phosphate release step. This state becomes greater still for the mutations with T178I having the largest portion of the cycle in this stage. Therefore although not measured directly, the data from the modelling indicates that the phosphate release is affected in the three mutations and again correlates with the clinical findings of phenotype severity. It could therefore be possible the myopathy is caused by a reduced hydrolysis step and phosphate release step leading to the myosin occupying a non/weakly bound state for longer. It is possible to estimate the velocity of each motor and whether the S1 could produce force (Table 7.1).

Isoform	V_{max} (s^{-1})	strongly attached	τ_{total} (s)	$\tau_{strong\ att.}$ (s)	V_0 (nm/s)
WT MyHC-emb	7.0000	0.2500	0.1429	0.0357	140-280
MyHC- emb R672H	1.3000	0.1300	0.7692	0.1000	50-100
MyHC- emb R672C	3.5000	0.1600	0.2857	0.0457	109-218
MyHC-emb T178I	0.2000	0.0060	5.0000	0.0300	166-333

Table 7.1 - Estimates of velocity determined from the Berkley Madonna modelling. τ_{total} = total cycling time, $\tau_{storng\ att.}$ = strongly attached time, V_0 = velocity

The proportion of strongly attached states was determined from the occupancy of the strongly bound states (AM, AMT, AMD, and AMD2). The total cycling time (τ_{total}) was calculated from $1/V_{max}$. By multiplying the τ_{total} by the proportion of strongly attached states, how long this event lasted could be calculated. Finally a step size of 5-10 nm was used to estimate the velocity of each S1. From this the velocity of wild type MyHC-emb is estimated to be 140-280 nm/s, and is reduced for the two R672 mutations. However this method is less suited to the T178I mutation. Due to the low V_{max} the total cycling time would be around 5 seconds. Combined with the very low proportion of strongly attached states this resulted in a strongly attached time similar to the wild type. This is therefore not a very good method for modelling the T178I velocity. The proportion of strongly attached states is also useful in determining how much force each motor could produce. Force will be proportional to the strongly attached state as this is where the power stoke occurs and tension can be held. Therefore the larger the occupancy of these strongly attached states the more force they can produce. The wild type MyHC-emb could produce the most force, with the two R672 producing less (R672H slightly less than R672C), and T178I not being attached for long enough to produce significant force.

Observations of the structure found there appears to be two key interactions involving T178 and R672. The first of these interactions is a hydrogen bond between the two residues which is lost entirely for the T178I and R672C and partially for the R672H. The loss of this bond may explain the ≈4-fold weakening of ATP affinity in the presence of actin for T178I, and slight weakening in the two R672 mutants. The bond may help to stabilise the nucleotide binding pocket since T178 is located adjacent to the P-loop which plays a major role in ATP binding through the gamma phosphate. If the ATP is not binding as tightly or properly this may explain why the tryptophan fluorescence signal was so weak in the mutants. The second interaction is a π-cation bond between the R672 and F490 on the relay helix. This is lost entirely for the two mutants. F490 is located prior to where the relay helix 'kinks' during the ATPase cycle. This kink forces the relay loop at the C-terminus to move relative to the rest of the molecule. This loop, as well as containing the tryptophan that leads to the fluorescence change observed upon ATP binding, also interacts with the converter domain. The converter domain leads into the lever arm and it is thought this area is the fulcrum point in myosin where force is generated. It is

interesting then to observe that F490 is located just before the kink and appears to be anchoring the helix in place to allow the kink to happen. With the π-cation bond broken in the two mutations it is possible that the helix is more flexible at the N-terminal end. This may prevent the kink occurring or reduce it and therefore reduce the force produced by the mutant myosin. This correlates to the reduction in specific force observed in myofibrils obtained from FSS patients (Racca, Beck et al. 2015), however it is unclear if this was due to the mutant protein or the hypertrophied nature of the muscle. It is also unclear if compensation from upregulating other myosin isoforms could be a cause for the myopathy. Perinatal myosin has been found to be expressed in a FSS patient longer into postnatal development than in normal muscle tissue (Tajsharghi, Kimber et al. 2007).

It would be interesting to see if the force produced by wild type MyHC-emb and MyHC-peri are comparable, and then to compare them to the FSS causing mutants. If the force is reduced in the mutants then it would add to the R672-T178 interaction playing a role in force production and give a molecular reason why the myopathy manifests in these mutations. The causes for the T178I seem clear that it is the nucleotide pocket that is being disrupted causing the motor to hold on to phosphate for longer. However any downstream effects caused by the loss of the T178-R672 H-bond should not be ruled out.

7.1.3 MyHC-β H251N mutations

Given that this H251N mutation has only been discovered in children suffering from the juvenile form of HCM (Kaski, Syrris et al. 2009) it would seem logical that the mutation is more severe than mutations in the adult form. However the paper which first identified the H251N mutation also showed two adult HCM mutations, R403Q and R453C, in children (Kaski, Syrris et al. 2009). This would suggest that the two ‘adult’ mutations are as severe as the H251N mutation.

This then raises the question, why were the R403Q and R453C mutations identified in children with HCM when these mutations usually take 20-30 years to manifest which can lead to death, starting at 20 years.

The paper states that 29 of their 79 patients were diagnosed as a result of clinical screening for a family history of HCM. They do not state whether these were the patients where the R403Q and R453C mutations were identified but it is probable. A study into familial and sporadic disease in Austrian children (Greber-Platzer, Marx et al. 2001) found those with the R453C mutation had little to no clinical symptoms of HCM. However the non-familial mutations had left ventricle hypertrophy and other clinical symptoms. Secondary causes may also contribute to these mutations increasing in severity. These include inborn errors of metabolism, mitochondrial dysfunction and neuromuscular conditions.

Compared with the R403Q and R453C mutation's differences to wild type the H251N mutation has more significant differences in stopped-flow kinetics. The only significant change in the R403Q was a weakening in the actin affinity (Nag, Sommese et al. 2015). The R453C again only showed small changes most notably weakening of the K_{DA} value, and slowing of the $K'_1k'_{+2}$ and k'_{+2} values (Bloemink, Deacon et al. 2014). By contrast the changes seen in the H251N mutant are far more significant and numerous. These dramatic changes are a likely explanation to why the disease progresses much faster with this mutation than the other two stated.

One interesting finding is the comparison between the FSS mutations and the H251N mutation. Simply comparing the percentage changes of the equilibrium and rate constants (Figures 5.11 and 6.8) it is clear to see that the FSS have more significant differences than the wild types. Of the HCM mutations so far investigated there appears to be limited differences between the wild type MyHC-β and mutants. Since MyHC-β is essential for correct function of the heart this maybe the why the HCM mutations do not show such severe changes as this would lead to non-viable embryos. Therefore these mutations may exist in the MyHC-β but may not have been identified.

7.2 Limitations

One limitation of the assays conducted with the recombinant S1's was the use of a 25 mM KCl buffer. The standard salt concentration used by our lab for stopped-flow assays is 100 mM KCl, while physiological salt concentrations are around 150 mM (Lodish, Berk et al. 2000). While magnesium, chloride, and other ions were present the salt concentrations used here were much lower than physiological. The reasoning behind the choice of salt concentration was to achieve comparable environments between the stopped-flow and ATPase assays, which are usually done at low to zero salt. As part of the wider collaboration there is also the scope to perform *in vitro* motility assays on these recombinant S1's which again requires a low ionic strength.

The rate constants of myosin kinetics are incredibly fast which is why stopped-flow lends itself well to the study of these parameters. However when measured at human body temperature (37.5 °C) the rate constants can become too fast for current machines to measure reliably. As such the assays were carried out at 20 °C which gave measureable data as close to physiological temperatures as possible.

The use of the temperature manifold would have been ideal to determine some of the kinetic parameters (e.g. $1/K'_1$ and $K'_1k'_{+2}$) which would have allowed the calculation of other values (k'_{+2}) at 37 °C. However due to the low yields of protein, using the temperature manifold for this was not possible while also completing the other kinetic parameters shown in Chapters 4, 5, and 6.

This leads to another limitation of the study, being the cost and low yields of protein produced using this method. From a 3L cell culture only 1-2 mg of protein could be purified which was just enough in some cases to do a full series of assays. The cost of this process was probably one of the most significant limitations as cell culturing involved not just the C2C12 cells, but also HEK293 cells were used to amplify the viruses. However careful use of protein or the micro-volume manifold allowed the full analysis of recombinant S1s.

7.3 Future work

Myopathies are very complex diseases and a better understanding of the progression is needed.

The role that embryonic myosin plays during muscle development is also very poorly understood. Since it is expressed during embryo development and muscle regeneration it is not unreasonable to assume it is helping to build new sarcomeres within fibres.

One potential therapeutic proposed is dATP (Racca, Beck et al. 2013). They showed that the use of dATP can increase the V_{max} of the ATPase rate, which would be beneficial for the three FSS mutations investigated here (Chapter 5) since the V_{max} is reduced in all cases. Given more time and available samples, the stopped-flow kinetics could be examined again this time with dATP present in place of MgATP. Although it is unlikely that a treatment that encourages dATP production in the developing embryo would ever be accepted, it would be interesting to observe whether dATP could rectify the changes seen in the mutants. Using stopped-flow it would then be possible to determine which parts of the cross-bridge cycle are restored.

The emergence of juvenile HCM makes the disease more complex in that some mutations in the sarcomeric proteins can be tolerated into adulthood before symptoms present, while others lead to a disease state in infancy. More information therefore needs to be collected on potential causes on juvenile HCM and any potential risk factors that may contribute to the disease progressing earlier. Collecting data on more HCM mutations may provide a common effect between them all that could explain the phenotype seen. It would then be interesting to see if the juvenile HCM mutations share the same common dysfunction.

Ionic interactions play a big role in the cross-bridge cycle. As such existing data on other myosin isoforms have been conducted at 100 mM KCl, close to physiological concentrations. In these studies to compare the stopped-flow data to the ATPase and *in vitro* measurements the KCl concentration was 25 mM. To help make the comparison between the embryonic myosin and the other characterised myosins easier it would be beneficial to repeat the assays in higher salt buffers.

Given that the temperature manifold works nicely at allowing measurements at human physiological body temperature, it would be good to investigate which constants within the cross-bridge cycle are affected by temperature. It may be the case that the larger differences seen between wild type and mutant are not so significant at 37 °C, or the opposite maybe true that the mutations are in fact much worse.

8 References

AGBULUT, O., NOIREZ, P., BEAUMONT, F. and BULTER-BROWNE, C., 2003. Myosin heavy chain isoforms in postnatal muscle development of mice. *Biology of the Cell,* **95**, pp. 399-406.

ALLEN, D.L., HARRISON, B.C. and LEINWAND, L.A., 2001. Inactivation of Myosin Heavy Chain Genes in the Mouse: Diverse and Unexpected Phenotypes. *Microscopy Research and Technique,* **50**, pp. 492-499.

ALMAAS, V.M. and AMLIE, J.P., 2010. Histopathological changes and clinical implications in patients with hypertrophic cardiomyopathy. *European Cardiology,* **6**(2), pp. 88-90.

ANAN, R., SHONO, H., KISANUKI, A., ARIMA, S., NAKAO, S. and TANAKA, H., 1998. Patients with familial hypertrophic cardiomyopathy caused by a Phe110Ile missense mutation in the cardiac troponin T gene have variable cardiac morphologies and a favorable prognosis. *Circulation,* **98**(5), pp. 391-397.

ANDERSON, K.R., SUTTON, M.G. and LIE, J.T., 1979. Histopathological types of cardiac fibrosis in myocardial disease. *The Journal of Pathology,* **128**(2), pp. 79-85.

ANSON, M., 1992. Temperature dependence and Arrhenius activation energy of F-actin velocity generated *in vitro* by skeletal myosin. *Journal of Molecular Biology,* **224**(4), pp. 1029-1038.

ARAD, M., MARON, B.J., GORHAM, J.M., JOHNSON, W.H., SAUL, J.P., PEREZ-ATAYDE, A.R., SPIRITO, P., WRIGHT, G.B., KANTER, R.J., SEIDMAN, C.E. and SEIDMAN, J.G., 2005. Glycogen storage disease presenting as hypertrophic cardiomyopathy. *New England Journal of Medicine,* **352**(4), pp. 362-372.

ARNOLD, K., BORDOLI, L., KOPP, J. and SCHWEDE, T., 2006. The SWISS-MODEL Workspace: A web-based environment for protein structure homology modelling. *Bioinformatics,* **22**(2), pp. 195-201.

BAJONA, P. and TURER, A., July 20, 2015, 2015-last update, Hypertrophic cardiomyopathy affects young and old [Homepage of UT Southwestern Medical Center], [Online]. Available: http://www.utswmedicine.org/stories/articles/year-2015/hypertrophic-cardiomyopathy.html [March 23, 2016].

BAMSHAD, M., BOHNSACK, J.F., JORDE, L.B. and CAREY, J.C., 1996. Distal arthrogryposis type 1: clinical analysis of a large kindred. *American Journal of Medical Genetics,* **65**(4), pp. 282-285.

BAMSHAD, M., JORDE, L.B. and CAREY, J.C., 1996. A revised and extended classification of the distal arthrogryposes. *American Journal of Medical Genetics,* **65**(4), pp. 277-281.

BARBET, J.P., THORNELL, L.E. and BUTLER-BROWNE, G.S., 1991. Immunocytochemical characterisation of two generations of fibers during the development of the human quadriceps muscle. *Mechanisms of development,* **35**(1), pp. 3-11.

BASSO, C., THIENE, G., CORRADO, D., BUJA, G., MELACINI, P. and NAVA, A., 2000. Hypertrophic cardiomyopathy and sudden death in the young: pathological evidence of myocardial ischemia. *Human Pathology,* **31**(8), pp. 988-998.

BEALS, R.K., 2005. The distal arthrogryposes: a new classification of peripheral contractures. *Clinical Orthopaedics and Related Research,* (435), pp. 203-210.

BECK, A.E., MCMILLIN, M.J., GILDERSLEEVE, H.I.S., SHIVELY, K.M.B., TANG, A. and BAMSHAD, M.J., 2014. Genotype-phenotype relationships in Freeman-Sheldon syndrome. *American Journal of Medical Genetics Part A,* **164**(11), pp. 2808-2813.

BEYLKIN, D.H., ALLEN, D.L. and LEINWAND, L.A., 2006. MyoD, Myf5, and calcineurin pathway activate the developmental myosin heavy chain genes. *Developmental Biology,* **294**(2), pp. 541-553.

BIASINI, M., BIENERT, S., WATERHOUSE, A., ARNOLD, K., STRUDER, G., SCHMIDT, T., KIEFER, F., CASSARINO, T.G., BERTONI, M., BORDOLI, L. and SCHWEDE, T., 2014. SWISS-MODEL: modelling protein tertiary and quaternary structure using evolutionary information. *Nucleic Acids Research,* **42**(W1), pp. 252-258.

BIOSCA, J.A., TRAVERS, F. and BARMAN, T., 1983. A jump in an Arrhenius plot can be the consequence of a phase transition. The binding of ATP to myosin subfragment 1. *FEBS Letters,* **153**(1), pp. 217-220.

BLANCHARD, A., OHANIAN, V. and CRITCHLEY, D., 1989. The Structure and function of α-actinin. *Journal of Muscle Research and Cell Motility,* **10**(4), pp. 280-289.

BLOEMINK, M.J., DEACON, J.C., LANGER, S., VERA, C., COMBS, A., LEINWAND, L.A. and GEEVES, M.A., 2014. The Hypertrophic Cardiomyopathy Myosin Mutation R453C alters ATP-binding and hydrolysis of human cardiac β-myosin . *The Journal of Biological Chemistry,* **289**(8), pp. 5158-5167.

BLOEMINK, M.J., DEACON, J.C., RESNICOW, D.I., LEINWAND, L.A. and GEEVES, M.A., 2013. The Superfast Human Extraocular Myosin Is Kinetically Distinct from the Fast Skeletal IIa, IIb, and IId Isoforms. *The Journal of Biological Chemistry,* **288**(38), pp. 27469-27479.

BONNE, G., CARRIER, L., BERCOVICI, J., CRUAUD, C., RICHARD, P., HAINQUE, B., GAUTEL, M., LABEIT, S., JAMES, M., BECKMANN, J., WEISSENBACH, J., VOSBERG, H.P., FISZMAN, M., KOMAJDA, M. and SCHWARTZ, K., 1995. Cardiac myosin binding protein C splice acceptor site mutation is associated with familial hypertrophic cardiomyopathy. *Nature Genetics,* **11**(4), pp. 438-440.

BOTTINELLI, R. and REGGIANI, C., 2000. Human skeletal muscle fibres: molecular and functional diversity. *Progress in Biophysics & Molecular Biology,* **73**, pp. 195-262.

BOUSSOUF, S. E., AGIANIAN, B., BULLARD, B. and GEEVES, M. A., 2007. The regulation of myosin binding to actin filaments by *Lethocerus* troponin. *Journal of Molecular Biology*, **373**(3), pp. 587-598.

BREITBART, R.E., NGUYEN, H.T., MEDFORD, R.M., DESTREE, A.T., MAHDAVI, V. and NADALGINARD, B., 1985. Intricate combinatorial patterns of exon splicing generate multiple regulation troponin-T isoforms from a single gene. *Cell,* **41**(1), pp. 67-82.

BRITISH HEART FOUNDATION, 2016-last update, Dilated cardiomyopathy [Homepage of British Heart Foundation], [Online]. Available: https://www.bhf.org.uk/heart-health/conditions/cardiomyopathy/dilated-cardiomyopathy [March 31, 2016].

BRUECKNER, J.K., ITKIS, O. and PORTER, J.D., 1996. Spatial and temporal patterns of myosin heavy chain expression in developing rat extraocular muscle. *Journal of Muscle Research and Cell Motility,* **17**(3), pp. 297-312.

BUBLIK, N., ALVAREZ, J.A. and LIPSHULTZ, S.E., 2008. Pediatric cardiomyopathy as a chronic disease: A perspective on comprehensive care programs. *Progress in Pediatric Cardiology,* **25**(1), pp. 103-111.

BURIAN, F., 1962. The "Whistling face" symptom in the polyvalent syndrome. *Acta Chirurgiae Orthopaedicae et Traumatologiae Chechoslovaca,* **29**, pp. 481-483.

BURTON, R.F., 2002. Temperature and acid-base balance in ectothermic vertebrates: The imidazole alphastat hypotheses and beyond. *Journal of Experimental Biology,* **205**(Pt 23), pp. 3587-3600.

BUTLER-BROWNE, G.S., BUGAISKY, L.B., CUÉNOUD, S., SCHWARTZ, K. and WHALEN, R.G., 1982. Denervation of newborn rat muscle does not block the appearance of adult fast myosin heavy chain. *Nature,* **299**(5886), pp. 830-833.

BUTLER-BROWNE, G.S., HERLICOVIEZ, D. and WHALEN, R.G., 1984. Effects of hypothyroidism on myosin isozyme transitions in developing rat muscle. *FEBS Letters,* **166**(1), pp. 71-75.

BUVOLI, M., HAMADY, M., LEINWAND, L.A. and KNIGHT, R., 2008. Bioinformatics assessment of beta-myosin mutations reveals myosin's high sensitivity to mutations. *Trends in Cardiovascular Medicine,* **18**(4), pp. 141-149.

CASSELL, M. and TOBACMAN, L.S., 1996. Opposite effects of myosin subfragment 1 on binding of cardiac troponin and tropomyosin to the thin filament. *The Journal of Biological Chemistry,* **271**(22), pp. 12867-12872.

CHANDY, I.K., LO, J.C. and LUDESCHER, R.D., 1999. Differential mobility of skeletal and cardiac tropomyosin on the surface of F-actin. *Biochemistry,* **38**(29), pp. 9286-9294.

CHEN, A.K., CHENG, Z. and TSOURKAS, A., 2008. Assessing the sensitivity of commercially available fluorophores to the intracellular environment. *Analytical Chemistry,* **80**(19), pp. 7437-7444.

CHENEY, R.E. and MOOSEKER, M.S., 1992. Unconventional myosins. *Current Opinion in Cell Biology,* **4**(1), pp. 27-35.

CHO, M., WEBSTER, S.G. and BLAU, H.M., 1993. Evidence for myoblast-extrinsic regulation of slow myosin heavy chain expression during muscle fiber formation in embryonic development. *The Journal of Cell Biology,* **121**(4), pp. 795-810.

CLARK, K.A., MCELHINNY, A.S., BECKERLE, M.C. and GREGORIO, C.C., 2002. Striated muscle cytoarchitecture: an intricate web of form and function. *Annual Reviews of Cell and Developmental Biology,* **18**, pp. 637-706.

Clinicalgate. 2015. Actin Binding Proteins. [ONLINE] Available at: http://clinicalgate.com/actin-and-actin-binding-proteins/. [Accessed 2 October 2016].

COLAN, S.D., LIPSHULTZ, S.E., LOWE, A.M., SLEEPER, L.A., MESSERE, J., COX, G.F., LURIE, P.R., ORAV, E.J. and TOWBIN, J.A., 2007. Epidemiology and cause-specific outcome of hypertrophic cardiomyopathy in children. *Pediatric Cardiology,* **115**(6), pp. 773-781.

COLEGRAVE, M. and PECKHAM, M., 2014. Structural Implications of β-Cardiac Myosin Heavy Chain Mutations in Human Disease. *The Anatomical Record,* **297**(9), pp. 160-1680.

COLUCCIO, L.M., ed, 2008. *Myosins. A superfamily of molecular motors.* USA: Springer.

CONDON, K., SILBERSTEIN, L., BLAU, H.M. and THOMPSON, W.J., 1990. Development of muscle fiber types in the prenatal rat hindlimb. *Developmental Biology,* **138**(2), pp. 256-274.

CRIDDLE, A.H., GEEVES, M.A. and JEFFRIES, T., 1985. The use of actin labelled with N-(1-pyrenyl)iodoacetamide to study the interaction of actin with myosin subfragments and troponin/tropomyosin. *The Biochemical Journal,* **232**, pp. 343-349.

CUDA, G., FANANAPAZIR, L., ZHU, W.S., SELLERS, J.R. and EPSTEIN, N.D., 1993. Skeletal muscle expression and abnormal function of beta-myosin in hypertrophic cardiomyopathy. *The Journal of Clinical Investigation,* **91**(6), pp. 2861-2865.

DARIN, N., KYLLERMAN, M., WAHLSTROM, J., MARTINSSON, T. and OLDFORS, A., 1998. Autosomal dominant myopathy with congenital joint contractures, ophthalmoplegia, and rimmed vacuoles. *Annals of Neurology,* **44**(2), pp. 242-248.

DAVIES, M.J., 1984. The current status of myocardial disarray in hypertrophic cardiomyopathy. *British Heart Journal,* **51**(4), pp. 361-363.

DAVIS, J.S., 1988. Interaction of C-protein with pH 8.0 synthetic thick filaments prepared from the myosin of vertebrate skeletal muscle. *Journal of Muscle Research and Cell Motility,* **9**(2), pp. 174-183.

DE LA CRUZ, E. M. and OSTAP, E.M., 2009. Kinetic and equilibrium analysis of the myosin ATPase. In: M.L. JOHNSON, J.M. HOLT and G.K. ACKERS, eds, *Methods in enzymology: Biothermodynamics, Part A.* 2009 edn. USA: Elsevier, pp. 158-190.

DE LANEROLLE, P. and SEREBRYANNYY, L., 2011. Nuclear actin and myosins: Life without filaments. *Nature Cell Biology,* **13**(11), pp. 1282-1288.

DEACON, J.C., BLOEMINK, M.J., REZAVANDI, H., GEEVES, M.A. and LEINWAND, L.A., 2012. Erratum to: Identification of functional differences between recombinant human α and β cardiac myosin motors. *Cellular and Molecular Life Sciences,* **69**(24), pp. 4239-4255.

DENARDI, C., AUSONI, S., MORETTI, P., GORZA, L., VELLECA, M., BUCKINGHAM, M. and SCHIAFFINO, S., 1993. Type 2X-myosin heavy chain is coded by a muscle fiber type-specific and developmentally regulated gene. *The Journal of Biological Chemistry,* **123**(4), pp. 823-835.

DOMINQUEZ, R., FREYZON, Y., TRYBUS, K.M. and COHEN, C., 1998. Crystal structure of a vertebrate smooth muscle myosin motor domain and its complex with the essential light chain: visualization of the pre-power stroke state. *Cell,* **94**(5), pp. 559-571.

DOUGHERTY, D.A., 1996. Cation-π Interaction in Chemistry and Biology: A New View of Benzene, Phe, Tyr, and Trp. *Science,* **271**(5246), pp. 163-168.

DRACHMAN, D.B. and JOHNSTON, D.M., 1973. Development of a mammalian muscle: dynamic and biochemical properties correlated. *The Journal of Physiology,* **234**(1), pp. 29-42.

DRAEGER, A., WEEDS, A.G. and FITZSIMONS, R.B., 1987. Primary, secondary and tertiary myotubes in developing skeletal muscle: A new approach to the analysis of human myogenesis. *Journal of the Neurological Sciences,* **81**(1), pp. 19-43.

EATON, B.L., 1976. Tropomyosin binding to F-actin induced by myosin heads. *Science,* **192**(4246), pp. 1337-1339.

ELLIOTT, P.M., ANASTASAKIS, A., BORGER, M.A., BORGGREFE, M., CECCHI, F., CHARRON, P., HAGEGE, A., LAFONT, A., LIMONGELLI, G., MAHRHOLDT, H., MCKENNA, W.J., MOGENSEN, J., NIHOYANNOPOULOS, P., NISTRI, S., PIEPER, P.G., PIESKE, B., RAPEZZI, C., RUTTEN, F.H., TILLMANNS, C. and WATKINS, H., 2014. 2014 ESC guidelines on diagnosis and management of hypertrophic cardiomyopathy: the task force fo the diagnosis and management of hypertrophic cardiomyopathy of the European Society of Cardiology (ESC). *European Heart Journal,* **35**(39), pp. 2733-2779.

ENNION, S., SANT'ANA PEREIRA, J., SARGEANT, A.J., YOUNG, A. and GOLDSPINK, G., 1995. Characterization of human skeletal muscle fibres according to the myosin heavy chains they express. *Journal of Muscle Research and Cell Motility,* **16**(1), pp. 35-43.

FATKIN, D. and GRAHAM, R.M., 2002. Molecular mechanisms of inherited cardiomyopathies. *Physiological Reviews,* **82**(4), pp. 945-980.

FERRARI, D., BETTUZZI, C. and DONZELLI, O., 2008. Freeman-Sheldon syndrome. A case report and review of the literature. *La Chirurgia Degli Organi di Movimento,* **92**(2), pp. 127-131.

FIDZIANSKA, A., 1980. Human ontogenesis. I. Ultrastructural characteristics of developing human muscle. *Journal of Neuropathology and experimental Neurology,* **39**(4), pp. 476-486.

FREEMAN, E.A. and SHELDON, J.H., 1938. Cranio-carpotarsal dystrophy: Undescribed congenital malformation. *Archives of Disease in Children,* **13**(75), pp. 277-283.

FURCH, M., GEEVES, M.A. and MANSTEIN, D.J., 1998. Modulation of actin affinity and actomyosin adenosine triphosphatase by charge changes in the myosin motor domain. *Biochemistry,* **37**(18), pp. 6317-6326.

GAMBKE, B., LYONS, G.E., HASELGROVE, J., KELLY, A.M. and RUBINSTEIN, N.A., 1983. Thyroidal and neural control of myosin transitions during development of rat fast and slow muscles. *FEBS Letters,* **156**(2), pp. 335-339.

GEEVES, M.A., FEDOROV, R. and MANSTEIN, D.J., 2005. Molecular mechanism of actomyosin-based motility. *Cellular and Molecular Life Sciences,* **62**, pp. 1462-1477.

GEEVES, M.A. and HOLMES, K.C., 2005. The Molecular Mechanism of Muscle Contraction. *Advances in Protein Chemistry,* **71**, pp. 161-193.

GEISTERFER-LOWRANCE, A.A.T., KASS, S., TANIGAWA, G., VOSBERG, H.P., MCKENNA, W., SEIDMAN, C.E. and SEIDMAN, J.G., 1990. A molecular basis for familial hypertrophic cardiomyopathy: A ß cardiac myosin heavy chain gene missense mutation. *Cell,* **62**(5), pp. 999-1006.

GIROLAMI, F., HO, Y., SEMSARIAN, C., BALDI, M., WILL, M.L., BALDINI, K., TORRICELLI, F., YEATES, L., CECCHI, F., ACKERMAN, M.J. and OLIVOTTO, I., 2010. Clinical features and outcomes of hypertrophic cardiomyopathy associated with triple sarcomere protein gene mutations. *Journal of the American College of Cardiology,* **55**(14), pp. 1444-1453.

GORDON, A.M., HOMSHER, E. and REGNIER, M., 2000. Regulation of contraction in striated muscle. *Physiological Reviews,* **80**(2), pp. 853-924.

GREASER, M.L. and GERGELY, J., 1973. Purification and properties of the components from troponin. *The Journal of Biological Chemistry,* **248**(6), pp. 2125-2133.

GREBER-PLATZER, S., MARX, M., FLEISCHMANN, C., SUPPAN, C., DOBNER, M. and WIMMER, M., 2001. Beta-myosin heavy chain gene mutation and hypertrophic cardiomyopathy in Austrian children. *Journal of Molecular and Cellular Cardiology,* **33**(1), pp. 141-148.

GROSS-KIESELSTEIN, E., ABRAHAMOV, A. and BEN-HUR, N., 1971. Familial occurrence of the Freeman-Sheldon syndrome: cranio-carpotarsal dysplasia. *Pediatrics,* **47**(6), pp. 1064-1067.

GUEX, N., PEITSCH, M.C. and SCHWEDE, T., 2009. Automated comparative protein structure modelling with SWISS-MODEL and Swiss-PdbViewer: A historical perspective. *Electrophoresis,* **30**(S1), pp. 162-173.

HALL, J.G., 2014. Arthrogryposis (multiple congenital contractures): diagnostic approach to eitology, classification, genetics, and general principles. *European Journal of Medical Genetics,* **57**(8), pp. 464-472.

HALL, J.G., REED, S.D. and GREENE, G., 1982. The distal arthrogryposes: delineation of new entities - review and noslogic discussion. *American Journal of Medical Genetics,* **11**(2), pp. 185-239.

HARVEY, P.A. and LEINWAND, L.A., 2011. Cellular mechanisms of cardiomyopathy. *Journal of Cellular Biology,* **194**(3), pp. 355-365.

HEDERA, P., PETTY, E.M., BUI, M.R., BLAIVAS, M. and FINK, J.K., 2003. The second kindred with autosomal dominant distal myopathy linked to chromosome 14q: genetic and clinical analysis. *Archives of Neurology,* **60**(9), pp. 1321-1325.

HITCHCOCK-DEGREGORI, S.E. and AN, Y., 1996. Integral repeats and a continuous coiled coil are required for binding of striated muscle tropomyosin to the regulated actin filament. *The Journal of Biological Chemistry,* **271**(7), pp. 3600-3603.

HOFFMAN, B., SCHMIDT-TRAUB, H., PERROT, A., OSTERZIEL, K.J. and GESSNER, R., 2001. First mutation in cardiac troponin C, L29Q, in a patient with hypertrophic cardiomyopathy. *Human Mutation,* **17**(6), pp. 524-524.

HOOPER, S.L. and THUMA, J.B., 2005. Invertibrate muscles: Muscle specific genes and proteins. *Physiological Reviews,* **85**(3), pp. 1001-1060.

HORTON, M.J., BRANDON, C.A., MORRIS, T.J., BRAUN, T.W., YAW, K.M. and SCIOTE, J.J., 2001. Abundant expression of myosin heavy-chain IIB RNA in a subset of human masseter muscle fibres. *Archives of Oral Biology,* **46**, pp. 1039-1050.

HUGHES, S.M., CHO, M., KARSCH-MIZRACHI, I., TRAVIS, M., SILBERSTEIN, L., LEINWAND, L.A. and BLAU, H.M., 1993. Three slow myosin heavy chains sequentially expressed in developing mammalian skeletal muscle. *Developmental Biology,* **158**(1), pp. 183-199.

HUMPHREY, W., DALKE, A. and SCHULTEN, K., 1996. VMD: visual molecular dynamics. *Journal of Molecular Graphics,* **14**(1), pp. 33-38.

INGLES, J., DOOLAN, A., CHIU, C., SEIDMAN, J.G., SEIDMAN, C.E. and SEMSARIAN, C., 2005. Compound and double mutations in patients with hypertrophic cardiomyopathy: implications for genetic testing and counselling. *Journal of Medical Genetics,* **42**(10), pp. e59.

INGRAHAM, R.H. and SWENSON, C.A., 1984. Binary interactions of troponin subunits. *The Journal of Biological Chemistry,* **259**(15), pp. 9544-9548.

IORGA, B., ADAMEK, N. and GEEVES, M.A., 2007. The Slow Skeletal Muscle Isoform of Myosin Shows Kinetic Features Common to Smooth and Non-muscle Myosins. *The Journal of Biological Chemistry,* **282**(6), pp. 3559-3570.

KASKI, J.P., SYRRIS, P., ESTEBAN, M.T., JENKINS, S., PANTAZIS, A., DEANFIELD, J.E., MCKENNA, W.J. and ELLIOT, P.M., 2009. Prevalence of sarcomere protein gene mutations in preadolescent children with hypertrophic cardiomyopathy. *Circulation. Cardiovascular genetics,* **2**(5), pp. 436-441.

KIEFER, F., ARNOLD, K., KÜNZIL, M., BORDOLI, L. and SCHWEDE, T., 2009. The SWISS-MODEL Repository and associated resources. *Nucleic Acids Research,* **37**, pp. 387-382.

KIMURA, A., HARADA, H., PARK, J.E., NISHI, H., SATOH, M., TAKAHASHI, M., HIROI, S., SASAOKA, T., OHBUCHI, N., NAKAMURA, T., KOYANAGI, T., HWANG, T.H., CHOO, T.A., CHUNG, K.S., HASEGAWA, A., NAGAI, R., OKAZAKI, O., NAKAMURA, H., MATSUZAKI, M., SAKAMOTO, T., TOSHIMA, H., KOGO, Y., IMAIZUMI, T. and SASAZUKI, T., 1997. Mutations in the cardiac troponin I gene associated with hypertrophic cardiomyopathy. *Nature Genetics,* **16**(4), pp. 379-382.

KLICHE, W., FUJITA-BECKER, S., KOLLMAR, M., MANSTEIN, D.J. and KULL, F.J., 2001. Structure of a genetically engineered molecular motor. *The EMBO Journal,* **20**(1-2), pp. 40-46.

KONIG, S., BURKMAN, J., FITZGERALD, J., MITCHELL, M., SU, L. and STEDMAN, H.H., 2002. Modular organisation of phylogenetically conserved domains controlling developmental regulation of the human skeletal myosin heavy chain gene family. *The Journal of Biological Chemistry,* **277**(31), pp. 27593-27605.

KORETZ, J.F., 1979. Effects of C-protein on synthetic myosin filament structure. *Biophysical Journal,* **27**(3), pp. 433-446.

KRAKOWIAK, P.A., O'QUINN, J.R., BOHNSACK, J.F., WATKINS, W.S., CAREY, J.C., JORDE, L.B. and BAMSHAD, M., 1997. A variant of Freeman-Sheldon syndrome maps to 11p15.5-pter. *American Journal of Medical Genetics,* **60**(2), pp. 426-432.

KURABAYASHI, M., KOMURO, I., TSUCHIMOCHI, H., TAKAKU, F. and YAZAKI, Y., 1988. Molecular cloning and characterisation of human atrial and ventricular myosin alkali light chain cDNA clones. *The Journal of Biological Chemistry,* **263**(27), pp. 13930-13936.

KURZAWA, S.E. and GEEVES, M.A., 1996. A novel stopped-flow method for measuring the affinity of actin for myosin head fragment using microgram quantities of protein. *Journal of Muscle Research and Cell Motility,* **17**(6), pp. 669-676.

LABEIT, S. and KOLMERER, B., 1995. Titins: giant proteins in charge of muscle ultrastructure and elasticity. *Science,* **270**(5234), pp. 293-296.

LAING, N.G., LAING, B.A., MEREDITH, C., WILTON, S.D., ROBBINS, R., HOENYMAN, K., DOROSZ, S., KOZMAN, H., MASTAGLIA, F.L. and KAKULAS, B.A., 1995. Autosomal dominant distal myopathy: linkage to chromosome 14. *American Journal of Human Genetics,* **56**(2), pp. 422-427.

LANDIS, C.A., BOBKOVA, A., HOMSHER, E. and TOBACMAN, L.S., 1997. The active state of the thin filament is destabilised by an internal deletion in tropomyosin. *The Journal of Biological Chemistry,* **272**(22), pp. 14051-14056.

LEHRER, S.S. and KERWAR, G., 1972. Intrinsic fluorescence of actin. *Biochemistry,* **11**(7), pp. 1211-1217.

LEINWAND, L.A., SAEZ, L., MCNALLY, E. and NADAL-GINARD, B., 1983. Isolation and characterisation of human myosin heavy chain genes. *Proceedings of the National Academy of Sciences of the United States of America,* **80**(12), pp. 3716-3720.

LODISH, H., BERK, A., ZIPURSKY, S.L., MATSUDAIRA, P., BALTIMORE, D. and DARNELL, J., 2000. *Molecular cell biology.* 4th edn. New York: W. H. Freeman and Company.

LOMPRÉ, A.M., NADAL-GINARD, B. and MAHDAVI, V., 1984. Expression of the cardiac ventricular alpha- and beta-myosin heavy chain genes is developmentally and hormonally regulated. *The Journal of Biological Chemistry,* **259**(10), pp. 6437-6446.

LOPES, L.R., RAHMAN, M.S. and ELLIOTT, P.M., 2013. A systematic review and meta-analysis of genotype-phenotype associations in patients with hypertrophic cardiomyopathy caused by sarcomeric protein mutations. *Heart (British Cardiac Society),* **99**(24), pp. 1800-1811.

LOPES, L.R., ZEKAVATI, A., SYRRIS, P., HUBANK, M., GIAMBARTOLOMEI, C., DALAGEORGOU, C., JENKINS, S., MCKENNA, W., UK10K CONSORTIUM, PLAGNOL, V. and ELLIOTT, P.M., 2013. Genetic complexity in hypertrophic cardiomyopathy revealed by high-throughput sequencing. *Journal of Medical Genetics,* **50**(4), pp. 228-239.

LOWEY, S., LESKO, L.M., ROVNER, A.S., HODGES, A.R., WHITE, S.L., LOW, R.B., RINCON, M., GULICK, J. and ROBBINS, J., 2008. Functional effects of the hypertrophic cardiomyopathy R403Q mutation are different in an α- or ß-myosin heavy chain backbone. *The Journal of Biological Chemistry,* **283**, pp. 20579-20589.

LOWEY, S., WALLER, G.S. and TRYBUS, K.M., 1993. Function of skeletal muscle myosin heavy and light chain isoforms by an in vitro motility assay. *The Journal of Biological Chemistry,* **268**(27), pp. 20414-20418.

LU, B.D., ALLEN, D.L., LEINWAND, L.A. and LYONS, G.E., 1999. Spatial and temporal changes in myosin heavy chain gene expression in skeletal muscle development. *Developmental Biology,* **216**(1), pp. 312-326.

LUCAS, C.A., RUGHANI, A. and HOH, J.F., 1995. Expression of extraocular myosin heavy chain in rabbit laryngeal muscle. *Journal of Muscle Research and Cell Motility,* **16**(4), pp. 368-378.

LYMM, R.W. and TAYLOR, E.W., 1971. Mechanism of adenosine triphosphate hydrolysis by actomyosin. *Biochemistry,* **10**(25), pp. 4617-4624.

LYNCH, T.L., SADAYAPPAN, S., 2014. Surviving the infarct: A profile of cardiac myosin binding protein-C pathogenicity, diagnostic utility, and proteomics in the ischemic myocardium. *Proteomics. Clinical Applications,* **8**(7-8), pp. 569-577.

LYONS, G.E., ONTELL, M., COX, R., SASSOON, D. and BUCKINGHAM, M., 1990. The Expression of Myosin Genes in Developing Skeletal Muscle in the Mouse Embryo. *The Journal of Cell Biology,* **111**, pp. 1465-1476.

LYONS, G.E., SCHIAFFINO, S., SASSOON, D., BARTON, P. and BUCKINGHAM, M., 1990. Developmental regulation of myosin gene expression in mouse cardiac muscle. *The Journal of Cell Biology,* **111**(6), pp. 2427-2436.

MAK, A.S. and SMILLIE, L.B., 1981. Non-polymerisable tropomyosin - preparation, some properties and F-actin binding. *Biochemical and Biophysical Research Communications,* **101**(1), pp. 208-214.

MALKAWI, H. and TARAWNEH, M., 1983. The whistling face syndrome, or craniocarpotarsal dysplasia. Report of two cases in a father and son and review of the literature. *Journal of Pediatric Orthopaedics,* **3**(3), pp. 364-369.

MARGOSSIAN, S.S. and LOWEY, S., 1982. Preparation of myosin and its subfragments from rabbit skeletal muscle. *Methods in Enzymology,* **85**, pp. 55-71.

MARON, B.J., GARDIN, J.M., FLACK, J.M., GIDDING, S.S., KUROSAKI, T.T. and BILD, D.E., 1995. Prevalence of hypertrophic cardiomyopathy in a general population of young adults. *Circulation,* **92**(4), pp. 785-789.

MARON, B.J., SPIRITO, P., WESLEY, Y. and ARCE, J., 1986. Development and progression of left ventricular hypertrophy in children with hypertrophic cardiomyopathy. *The New England Journal of Medicine,* **315**(10), pp. 610-614.

MARON, B.J., WOLFSON, J.K., EPSTEIN, S.E. and ROBERTS, W.C., 1986. Intramural ("small vessel") coronary artery disease in hypertrophic cardiomyopathy. *Journal of the American College of Cardiology,* **8**(3), pp. 545-557.

MARTINSSON, T., OLDFORS, A., DARIN, N., BERG, K., TAJSHARGHI, H., KYLLERMAN, M. and WAHLSTROM, J., 2000. Autosomal dominant myopathy: missense mutation (Glu-706-Lys) in the myosin heavy chain IIa gene. *Proceedings of the National Academy of Sciences of the United States of America,* **97**(26), pp. 1461-1419.

MARUYAMA, K. and EBASHI, S., 1965. Alpha-actinin, a new structural protein from striated muscle. II. Action on actin. *Journal of Biochemistry,* **58**(1), pp. 13-19.

MILLAR, N.C. and GEEVES, M.A., 1983. The limiting rate of the ATP-mediated dissociation of actin from rabbit skeletal muscle myosin subfragment 1. *FEBS Letters,* **160**(1), pp. 141-148.

MILLIGAN, R.A., 1996. Protein-protein interactions in the rigor actomyosin complex. *Proceedings of the National Academy of Sciences,* **93**(1), pp. 21-26.

MITTEREDER, N., MARCH, K.L. and TRAPNELL, B.C., 1996. Evaluation of the concentration and bioactivity of adenovirus vectors for gene therapy. *Journal of Virology,* **70**(11), pp. 7498-7509.

MOOLMAN, J.C., CORFIELD, V.A., POSEN, B., NGUMBELA, K., SEIDMAN, C., BRINK, P.A. and WATKINS, H., 1997. Sudden death due to tropinin T mutations. *Journal of the American College of Cardiology,* **29**(3), pp. 549-555.

MOORE, L.A., TIDYMAN, W.E., ARRIZUBIETA, M.J. and BANDMAN, E., 1993. The evolutionary relationship of avian and mammalian heavy-chain genes. *Journal of Molecular Evolution,* **36**(1), pp. 21-30.

MORIMOTO, S., 2007. Sarcomeric proteins and inherited cardiomyopathies. *Cardiovascular Research,* **77**(4), pp. 659-666.

MORITA, H., REHM, H.L., MENESSES, A., MCDONOUGH, B., ROBERTS, A.E., KUCHERLAPATI, R., TOWBIN, J.A., SEIDMAN, J.G. and SEIDMAN, C., 2008. Shared genetics causes of cardiac hypertrophy in children and adults. *The New England Journal of Medicine,* **358**(18), pp. 1899-1908.

MOSS, R.L., GIULIAN, G.G. and GREASER, M.L., 1985. The effects of partial extraction of TnC upon the tension-pCa relationship in rabbit skinned skeletal muscle fibers. *The Journal of General Physiology,* **86**(4), pp. 585-600.

MULVIHILL, D.P. and HYAMS, J.S., 2001. Shedding a little light on light chains. *Nature Cell Biology,* **3**(1), pp. E10-E12.

MURPHY, R.T., MOGENSEN, J., MCGARRY, K., BAHL, A., EVANS, A., OSMAN, E., SYRRIS, P., GORMAN, G., FARRELL, M., HOLTON, J.L., HANNA, M.G., HUGHES, S., ELLIOTT, P.M.,

MACRAE, C.A. and MCKENNA, W.J., 2005. Adenosine monophosphate-activated protein kinase disease mimics hypertrophic cardiomyopathy and Wolff-Parkinson-White syndrome: natural history. *Journal of the American College of Cardiology,* **45**(6), pp. 992-930.

NAG, S., SOMMESE, R.F., UJFALUSI, Z., COMBS, A., LANGER, S., SUTTON, S., LEINWAND, L.A., GEEVES, M.A., RUPPEL, K. and SPUDICH, J.A., 2015. Contractility parameters of human ß-cardiac myosin with the hypertrophic cardiomyopathy mutation R403Q show loss of motor function. *Science Advances,* **1**(9), pp. e1500511.

NAKAJIMA-TANIGUCHI, C., MATSUI, H., FUJIO, Y., NAGATA, S., KISHIMOTO, T. and YAMAUCHI-TAKIHARA, K., 1997. Novel missense mutation in cardiac troponin T gene found in Japanese patient with hypertrophic cardiomyopathy. *Journal of Molecular and Cellular Cardiology,* **29**(2), pp. 839-843.

NARUSAWA, M., FITZSIMONS, R.B., IZUMO, S., NADAL-GINARD, B., RUBINSTEIN, N.A. and KELLY, A.M., 1987. Slow myosin in developing rat skeletal muscle. *The Journal of Biological Chemistry,* **104**(3), pp. 447-459.

NATIONAL INSTITUTES OF HEALTH, 22nd December 2015, 2015-last update, NINDS Myopathy Information Page [Homepage of National Institutes of Health], [Online]. Available: http://www.ninds.nih.gov/disorders/myopathy/myopathy.htm [March/23, 2016].

NUGENT, A.W., DAUBENEY, P.E., CHRONDROS, P., CARLIN, J.B., COLAN, S.D., CHEUNG, M., DAVIS, A.M., CHOW, C.W. and WEINTRAUB, R.G., 2005. Clinical feature and outcomes of childhood hypertrophic cardiomyopathy: results from a national population-based study. *Circulation,* **112**(9), pp. 1332-1338.

ODRONITZ, F. and KOLLMAR, M., 2007. Drawing the tree of eukaryotic life based on the analysis of 2,269 manually annotated myosins from 328 species. *Genome Biology,* **8**(9), pp. R196.

OLDFORS, A., 2007. Hereditary myosin myopathies. *Neuromusclar Disorders,* **17**, pp. 355-367.

OLIVOTTO, I., GIROLAMI, F., ACKERMAN, M.J., NISTRI, S., BOS, J.M., ZACHARA, E., OMMEN, S.R., THEIS, J.L., VAUBEL, R.A., RE, F., ARMENTANO, C., POGGESI, C., TORRICELLI, F. and CECCHI, F., 2008. Myofilament protein gene mutation screening and outcome of patients with hypertrophic cardiomyopathy. *Mayo Clinic proceedings,* **83**(6), pp. 630-638.

OLIVOTTO, I., GIROLAMI, F., SCIAGRÀ, R., ACKERMAN, M.J., SOTGIA, J.M., NISTRI, S., SGALAMBRO, A., GRIFONI, C., TORRICELLI, F., CAMICI, P.G. and CECCHI, F., 2011. Microvascular function is selectively impaired in patients with hypertrophic cardiomyopathy and sarcomere myofilament gene mutations. *Journal of the American College of Cardiology,* **58**(8), pp. 839-848.

OLSON, T.M., DOAN, T.P., KISHIMOTO, N.Y., WHITBY, F.G., ACKERMAN, M.J. and FANANAPAZIR, L., 2000. Inherited and de novo mutations in the cardiac actin gene cause hypertrophic cardiomyopathy. *Journal of Molecular and Cellular Cardiology,* **32**(9), pp. 1687-1694.

PANDORF, C.E., JIANG, W., QIN, A.X., BODELL, P.W., BALDWIN, K.M. and HADDAD, F., 2012. Regulation of an antisense RNA with the transition of neonatal to IIb myosin heavy chain during postnatal development and hypothyroidism in rat skeletal muscle. *American Journal of Physiology. Regulatory, Intergrative and Comparative Physiology,* **302**(7), pp. R854-R867.

PASGUALE, F., SYRRIS, P., KASKI, J.P., MOGENSEN, J., MCKENNA, W.J. and ELLIOTT, P.M., 2012. Long-term outcomes in hypertrophic cardiomyopathy caused by mutations in the cardiac troponin T gene. *Circulation. Cardiovascular genetics,* **5**(1), pp. 10-17.

PERIASAMY, M., WIECZOREK, D.F. and NADAL-GINARD, B., 1984. Characterization of a developmentally regulated perinatal myosin heavy chain gene expressed in skeletal muscle. *The Journal of Biological Chemistry,* **259**(21), pp. 13573-13578.

PETSKO, G.A., 2009. Crystallographic cryoenzymology and the legacy of Tony Fink. *Current Protein and Peptide Science,* **10**(5), pp. 416-423.

POETTER, K., JIANG, H., HASSANZADEH, S., MASTER, S.R., CHANG, A., DALAKAS, M.C., RAYMENT, I., SELLERS, J.R., FANANAPAZIR, L. and EPSTEIN, N.D., 1996. Mutations in either the essential or regulatory light chains of myosin are associated with a rare myopathy in human heart and skeletal muscle. *Nature Genetics,* **13**(1), pp. 63-69.

PONOMAREV, M.A., FURCH, M., LEVITSKY, D.I. and MANSTEIN, D.J., 2000. Charge changes in loop 2 affect the thermal unfolding of the myosin motor domain bound to F-actin. *Biochemistry,* **39**(15), pp. 4527-4532.

POTTER, J.D. and GERGELY, J., 1974. Troponin, tropomyosin, and actin interactions in the Ca2+ regulation of muscle contraction. *Biochemistry,* **13**(13), pp. 2697-2703.

RACCA, A.W., BECK, A.E., RAO, V.S., FLINT, G.V., LUNDY, S.D., BORN, D.E., BAMSHAD, M. and REGNIER, M., 2013. Contractility of kinetics of human fetal and human adult skeletal muscle. *The Journal of Physiology,* **591**(12), pp. 3049-3061.

RACCA, A.W., BECK, A.E., MCMILLIN, M.J., KORTE, F.S., BAMSHAD, M.J. and REGNIER, M., 2015. The embryonic myosin R672C mutation that underlies Freeman-Sheldon syndrome impairs cross-bridge detachment and cycling in adult skeletal muscle. *Human molecular genetics,* **24**(12), pp. 3348-3358.

RAYMENT, I., RYPNIEWSKI, W.R., SCHMIDT-BÄSE, K., SMITH, R., TOMCHICK, D.R., BENNING, M.M., WINKELMANN, D.A. and WESENBERG, G., 1993. Three-dimensional structure of myosin subfragment-1: a molecular motor. *Science,* **261**(5117), pp. 50-58.

RESNICOW, D.I., DEACON, J.C., WARRICK, H.M., SPUDICH, J.A. and LEINWAND, L.A., 2010. Functional diversity among a family of human skeletal muscle myosin motors. *Proceedings of the National Academy of Sciences of the United States of America,* **107**(3), pp. 1053-1058.

RICHARD, P., CHARRON, P., CARRIER, L., LEDEUIL, C., CHEAV, T., PICHEREAU, C., BENAICHE, A., ISNARD, R., DUBOURG, O., BURBAN, M., GUEFFET, J.P., MILLAIRE, A., DESNOS, M., SCHWARTZ, K., HAINQUE, B., KOMAJDA, M. and EUROGENE HEART FAILURE PROJECT, 2003. Hypertrophic cardiomyopathy: distribution of disease genes, spectrum of mutations, implications for a molecular diagnosis strategy. *Circulation,* **107**(17), pp. 2227-2232.

ROSSI, A.C., MAMMUCARI, C., ARGENTINI, C., REGGIANI, C. and SCHIAFFINO, S., 2010. Two novel/ancient myosins in mammalian skeletal muscles: MYH14/7b and MYH15 are expressed in extraocular muscles and muscle spindles. *Journal of Physiology,* **588**(2), pp. 353-364.

ROVNER, A.S., FREYZON, Y. and TRYBUS, K.M., 1995. Chimeric substitutions of the actin-binding loop activate dephosphorylated but not phosphorylated smooth muscle heavy meromyosin. *The Journal of Biological Chemistry,* **270**(51), pp. 30260-30263.

RUBINSTEIN, N.A. and KELLY, A.M., 1981. Development of muscle fibre specialization in the rat hindlimb. *The Journal of Biological Chemistry,* **90**(1), pp. 128-144.

RUSSELL, S.D., CAMBON, N., NADAL-GINARD, B. and WHALEN, R.G., 1988. Thyroid hormone induced a nerve-independent precocious expression of fast myosin heavy chain mRNA in rat hindlimb skeletal muscle. *The Journal of Biological Chemistry,* **263**(13), pp. 6370-6374.

SACHDEV, B., TAKENAKA, T., TERAGUCHI, H., TEI, C., LEE, P., MCKENNA, W.J. and ELLIOTT, P.M., 2002. Prevalence of Anderson-Fabry disease in make patients with late onset hypertrophic cardiomyopathy. *Circulation,* **105**(12), pp. 1407-1411.

SAEZ, L. and LEINWAND, L.A., 1986. Characterization of diverse forms of myosin heavy chain expressed in adult human skeletal muscle. *Nucleic Acids Research,* **14**(7), pp. 2951-2969.

SAKAKIBARA, I., SANTOLINI, M., FERRY, A., HAKIM, V. and MAIRE, P., 2014. Six homeoproteins and a linc-RNA at the fast MYH locus lock fast myofiber terminal phenotype. *PLoS Genetics,* **10**(5), pp. e1004386.

SANT'ANA PEREIRA, J., ENNION, S., SARGEANT, A.J., MOORMAN, A.F. and GOLDSPINK, G., 1997. Comparison of the molecular, antigenic and ATPase determinants of fast myosin heavy chains in rat and human: a single-fibre study. *Pflügers Archiv: European Journal of Physiology,* **435**(1), pp. 151-163.

SARTORE, S., MASCARELLO, F., ROWLERSON, A., GORZA, L., AUSONI, S., VIANELLO, M. and SCHIAFFINO, S., 1987. Fibre types in extraocular muscles: a new myosin isoform in the fast fibres. *Journal of Muscle Research and Cell Motility,* **8**(2), pp. 161-172.

SATOH, M., TAKAHASHI, M., SAKAMOTO, T., HIROE, M., MARUMO, F. and KIMURA, A., 1999. Structural analysis of the titin gene in hypertrophic cardiomyopathy: Identification of a novel disease gene. *Biochemical and Biophysical Research Communications,* **262**(2), pp. 411-417.

SCHIAFFINO, S., ROSSI, A.C., SMERDU, V., LEINWAND, L.A. and REGGIANI, C., 2015. Developmental myosins: expression patterns and functional significance. *Skeletal Muscle,* **5**(1), pp. 1-14.

SCHMIDT, W.M., LEHMAN, W. and MOORE, J.R., 2015. Direct observation of tropomyosin binding to actin filaments. *Cytoskeleton,* **72**(6), pp. 292-303.

SEIDMAN, J.G. and SEIDMAN, C.E., 2001. The genetic basis for cardiomyopathy: from mutation identification to mechanistic paradigms. *Cell,* **104**(4), pp. 557-567.

SEMSARIAN, C., INGLES, J., MARON, M.S. and MARON, B.J., 2015. New perspectives on the prevalence of hypertrophic cardiomyopathy. *Journal of the American College of Cardiology,* **65**(12), pp. 1249-1254.

SHENG, Z., STRAUSS, W.L., FRANCOIS, J.M. and POTTER, J.D., 1990. Evidence that both Ca(2+)-specific sites of skeletal muscle TnC are required for full activity. *The Journal of Biological Chemistry,* **265**(35), pp. 21554-21560.

SMERDU, V., KARSCH-MIZRACHI, I., CAMPIONE, M., LEINWAND, L.A. and SCHIAFFINO, S., 1994. Type IIx myosin heavy chain transcripts are expressed in type IIb fibers of human skeletal muscle. *The American Journal of Physiology,* **267**(6 Pt 1), pp. C1723-1728.

SMILLIE, L.B., GOLOSINSKA, K. and REINACH, F.C., 1988. Sequences of complete cDNAs encoding four variants of chicken skeletal muscle troponin T. *The Journal of Biological Chemistry,* **263**(35), pp. 18815-18820.

SORENSON, M.M., DA SILVA, A.C., GOURVEIA, C.S., SOUSA, V.P., OSHIMA, W., FERRO, J.A. and REINACH, F.C., 1995. Concerted action of the high affinity calcium binding sites in skeletal muscle troponin C. *The Journal of Biological Chemistry,* **270**(17), pp. 9770-9777.

SPIRITO, P., SEIDMAN, C.E., MCKENNA, W.J. and MARON, B.J., 1997. The management of hypertrophic cardiomyopathy. *The New England Journal of Medicine,* **336**(11), pp. 775-785.

SRIKAKULAM, R. and WINKELMANN, D.A., 1999. Myosin II Folding is mediated by a Molecular Chaperonin. *The Journal of Biological Chemistry,* **274**(38), pp. 27265-27293.

STEDMAN, H.H., ELLER, M., JULLIAN, E.H., FERTELS, S.H., SARKAR, S., SYLVESTER, J.E., KELLY, A.M. and RUBINSTEIN, N.A., 1990. The human embryonic myosin heavy chain.

Complete primary structure reveals evolutionary relationships with other developmental isoforms. *The Journal of Biological Chemistry,* **265**(6), pp. 3568-3576.

STEIN, L.A., CHOCK, P.B. and EISENBERG, E., 1981. Mechanism of the actomyosin ATPase: Effect of actin on the ATP hydrolysis step. *Proceedings of the National Academy of Sciences of the United of America*, **78**(3), pp. 1346-1350.

STEVENSON, D.A., CAREY, J.C., PALUMBOS, J., RUTHERFORD, A., DOLCOURT, J. and BAMSHAD, M.J., 2006. Clinical characteristics and natural history of Freeman-Sheldon syndrome. *Pediatrics,* **117**(3), pp. 754-762.

STREHLER, E.E., STREHLER-PAGE, M.A., PERRIARD, J.C., PERIASAMY, M. and NADAL-GINARD, B., 1986. Complete nucleotide and encoded amino acid sequence of a mammalian myosin heavy chain gene. Evidence against intro-dependent evolution of the rod. *Journal of Molecular Biology,* **190**(3), pp. 291-317.

SWENSON, A.M., TRIVEDI, D.V., RAUSER, A.A., WANG, Y., TAKAGI, Y., PALMER, B.M., MALNASI-CSIZMADIA, A., DEBOLD, E.P. and YENGO, C.M., 2014. Magnesium modulates actin binding and ADP release in myosin motors. *The Journal of Biological Chemistry,* **289**(34), pp. 23977-23991.

SYSKA, H., WILKINSON, J.M., GRAND, R.J.A. and PERRY, S.V., 1976. The relationship between biological activity and primary structure of troponin I from white skeletal muscle of the rabbit. *Biochemical Journal,* **153**(2), pp. 35-387.

SZCZESNA, D. and FAJER, P.G., 1995. The tropomyosin domain is flexible and disordered in reconstituted thin filaments. *Biochemistry,* **34**(11), pp. 3614-3620.

TAJSHARGHI, H., 2008. Thick and thin filament gene mutations in striated muscle disease. *International Journal of Molecular Sciences,* **9**(7), pp. 1259-1275.

TAJSHARGHI, H., KIMBER, E., HOLMGREN, D., TULINIUS, M. and OLDFORS, A., 2007. Distal arthrogryposis and muscle weakness associated with a ß-tropomyosin mutation. *Neurology,* **68**, pp. 772-775.

TAJSHARGHI, H., KIMBER, E., KROKSMARK, A.K., JERRE, R., TULINIUS, M. and OLDFORS, A., 2008. Embryonic Myosin Heavy-Chain Mutations Cause Distal Arthrogryposis and Developmental Myosin Myopathy That Persists Postnatally. *Archives of Neurology,* **65**(8), pp. 1083-1090.

TAJSHARGHI, H., THORNELL, L.E., DARIN, N., MARTINSSON, T., KYLLERMAN, M., WAHLSTROM, J. and OLDFORS, A., 2002. Myosin heavy chain IIa gene mutation E706K is pathogenic and its expression increases with age. *Neurology,* **58**(5), pp. 780-786.

TGK SCIENTIFIC, 2016-last update, Stopped-flow [Homepage of TgK Scientific], [Online]. Available: http://www.hi-techsci.com/techniques/stoppedflow/ [April 4th, 2016].

THIERFELDER, L., WATKINS, H., MACRAE, C., LAMAS, R., MCKENNA, W., VOSBERG, H.P., SEIDMAN, J.G. and SEIDMAN, C.E., 1994. α-tropomyosin and cardiac troponin T mutations cause familial hypertrophic cardiomyopathy: A disease of the sarcomere. *Cell,* **77**(5), pp. 701-712.

TOBACMAN, L.S., 1996. This filament-mediated regulation of cardiac contraction. *Annual Review of Physiology,* **58**, pp. 447-481.

TORRICELLI, F., GIROLAMI, F., OLIVOTTO, I., PASSERINI, I., FRUSCONI, S., VARGIU, D., RICHARD, P. and CECCHI, F., 2003. Prevalence and clinical profile of troponin T mutations among patients with hypertrophic cardiomyopathy in Tuscany. *The American Journal of Cardiology,* **92**(11), pp. 1358-1362.

TOSELAND, C. P., and FILI, N., 2014. Fluorescent methods for molecular motors. Basel: Springer pp.87-104

TOYDEMIR, R.M., CHEN, H., PROUD, V.K., MARTIN, R., VAN BOKHOVEN, H., HAMEL, B.C., TUERLINGS, J.H., STRATAKIS, C.A., JORDE, L.B. and BAMSHAD, M.J., 2006. Trismus-pseudocamptodactyly syndrome is caused by recurrent mutation of MYH8. *American Journal of Medical Genetics Part A,* **140**(22), pp. 2387-2393.

TOYDEMIR, R.M., RUTHERFORD, A., WHITBY, F.G., JORDE, L.B., CAREY, J.C. and BAMSHAD, M., 2006. Mutations in embryonic myosin heavy chain (MYH3) cause Freeman-sheldon syndrome and Sheldon-Hall syndrome. *Nature Genetics,* **38**, pp. 561-565.

TRAVERS, F. and BARMAN, T., 1995. Cryoenzymology: how to practice kinetic and structural studies. *Biochimie,* **77**(12), pp. 937-948.

UYEDA, T.Q., RUPPEL, K.M. and SPUDICH, J.A., 1994. Enzymatic activities correlate with chimeric substitutions at the actin-binding face of myosin. *Nature,* **368**(6471), pp. 567-569.

VAN DIJK, J., FURCH, M., DERANCOURT, J., BATRA, R., KNETSCH, M.L., MANSTEIN, D.J. and CHAUSSEPIED, P., 1999a. Differences in the ionic interaction of actin with the motor domains of nonmuscle and muscle myosin II. *European Journal of Biochemistry,* **260**(3), pp. 672-683.

VAN DIJK, J., FURCH, M., LAFONT, C., MANSTEIN, D.J. and CHAUSSEPIED, P., 1999b. Functional characterization of the secondary actin binding site of myosin II. *Biochemistry,* **38**(46), pp. 15078-15085.

VAN DRIEST, S.L., OMMEN, S.R., TAJIK, A.J., GERSH, B.J. and ACKERMAN, M.J., 2005. Sarcomeric genotyping in hypertrophic cardiomyopathy. *Mayo Clinic proceedings,* **80**(4), pp. 463-469.

VAN DRIEST, S.L., VASILE, V.C., OMMEN, S.R., WILL, M.L., TAJIK, A.J., GERSH, B.J. and ACKERMAN, M.J., 2004. Myosin binding protein C mutation and compound

heterozygosity in hypertrophic cardiomyopathy. *Journal of the American College of Cardiology,* **44**(9), pp. 1903-1910.

VARNAVA, A.M., ELLIOTT, P.M., MAHON, N., DAVIES, M.J. and MCKENNA, W.J., 2001. Relation between myocyte disarray and outcome in hypertrophic cardiomyopathy. *The American Journal of Cardiology,* **88**(3), pp. 275-279.

VEUGELERS, M., BRESSAN, M., MCDERMOTT, D.A., WEREMOWICZ, S., MORTON, C.C., MABRY, C., LEFAIVRE, J.F., ZUNAMON, A., DESTREE, A., CHAUDRON, J.M. and BASSON, C.T., 2004. Mutation of the perinatal myosin heavy chain associated with a Carney complex variant. *New England Journal of Medicine,* **351**, pp. 460-469.

WALSH, R., RUTLAND, C., THOMAS, R. and LOUGHNA, S., 2010. Cardiomyopathy: a systematic review of disease-causing mutations in myosin heavy chain 7 and their phenotypic manifestations. *Cardiology,* **115**(1), pp. 49-60.

WATKINS, H., CONNER, D., THIERFELDER, L., JARCHO, J.A., MACRAE, C., MCKENNA, W.J., MARON, B.J., SEIDMAN, J.G. and SEIDMAN, C.E., 1995. Mutations in the cardiac myosin binding protein-C gene on chromosome-11 cause familial hypertrophic cardiomyopathy. *Nature Genetics,* **11**(4), pp. 434-437.

WEISS, A. and LEINWAND, L.A., 1996. The Mammalian Myosin Heavy Chain Gene Family. *Annual Review in Cell Developmental Biology,* **12**, pp. 417-439.

WHALEN, R.G., BUTLER-BROWNE, G.S. and GROS, F., 1978. Identification of a novel form of myosin light chain present in embryonic muscle tissue and cultured muscle cells. *The Journal of Biological Chemistry,* **126**(3), pp. 415-431.

WHALEN, R.G., SCHWARTZ, K., BOUVERET, P., SELL, S.M. and GROS, F., 1979. Contractile protein isozymes in muscle development: Identification of an embryonic form of myosin heavy chain. *Proceedings of the National Academy of Sciences of the United States of America,* **76**(10), pp. 5197-5201.

WHITE, S.P., COHEN, C. and PHILLIPS, G.N.J., 1987. Structure of co-crystals of tropomyosin and troponin. *Nature,* **352**(6107), pp. 826-828.

WU, Y.Z., CRUMLEY, R.L., ARMSTRONG, W.B. and CAIOZZO, V.J., 2000. New perspectives about human laryngeal muscle: single-fiber analyses and interspecies comparisons. *Archives of otolaryngology--head & neck surgery,* **126**(7), pp. 857-864.

WYDRO, R.M., NGUYEN, H.T., GUBITS, R.M. and NADAL-GINARD, B., 1983. Characterization of sarcomeric heavy chain genes. *The Journal of Biological Chemistry,* **258**(1), pp. 670-678.

YAMAMOTO, S., OSUGA, T., OKADA, M., HASHIMOTO, T., SHIGEMATSU, H., SUZUKI, S., FUJITA, K., MATSUMOTO, N. and HORI, T., 1994. Anesthetic management of a patient with Freeman-Sheldon syndrome. *Masui. The Japanese Journal of Anesthesiology,* **43**(11), pp. 1748-1753.

YILMAZ, A., KINDERMANN, I., KINDERMANN, M., MAHFOUD, F., UKENA, C., ATHANASIADIS, A., HILL, S., MAHRHOLDT, H., VOEHRINGER, M., SCHIEBER, M., KLINGEL, K., BÖHM, M. and SECHTEM, U., 2010. Comparative evaluation of left and right ventricular endomyocardial biopsy: differences in complication rate and diagnostic performance. *Circulation,* **122**(9), pp. 900-909.

ZOT, H.G. and POTTER, J.D., 1982. A structural role for the Ca2+-Mg2+ sites on troponin C in the regulation of muscle contraction. Preparation and properties of troponin C depleted myofibrils. *The Journal of Biological Chemistry,* **257**(13), pp. 7678-7683.

Publication list

Walklate, J., Geeves, M. A., Temperature manifold for a stopped-flow machine to allow measurements from -10 to +40°C. Analytical Biochemistry, 2015, **476**, p.11-16.

Walklate, J., Ujfalusi, Z., Geeves, M. A., Myosin isoforms and the mechanochemical cross-bridge cycle. The Journal of Experimental Biology, 2016, **219** (pt 2), p. 168-174.

Walklate, J., Vera, C., Bloemink, M. J., Geeves, M. A., Leinwand, L., The most prevalent Freeman-Sheldon syndrome mutations in the embryonic myosin motor share functional defects. The Journal of Biological Chemistry, 2016, **291**, p.10318-10331.